Karlsruher Institut für Technologie

Modelling the post-yield and post necking behaviour of irradiated F/M steels

Zur Erlangung des akademischen Grades eines

Doktors der Ingenieurwissenschaften (Dr.-Ing.)

von der KIT-Fakultät für Maschinenbau des
Karlsruher Institut für Technologie (KIT)

genehmigte

Dissertation

von

Roshan Ram Rajakrishnan

aus Chennai, Indien

Tag der mündlichen Prüfung:	18. Dezember 2025
Hauptreferent:	Prof. Dr.-Ing. Jarir Aktaa
Korreferent:	Prof. Dr.-Ing. habil. Thomas Seelig
Korreferent:	Prof. Dr.-Ing. Bronislava Gorr

தெய்வத்தான் ஆகா தெனினும் முயற்சிதன்
மெய்வருத்தக் கூலி தரும்.

திருக்குறள் | குறள் 619

Translations:

Though fate-divine should make your labour vain;
Effort its labour's sure reward will gain.

G.U.Pope

Liess auch das Geschick es nicht gelingen — das
Anstreben selbst lohnt des eignen Leibs Anstrengen.

Karl Graul

Thirukkural* | Couplet 619

*The Thirukkural *(திருக்குறள்)* is an ancient Tamil language text composed of 1,330 short couplets of seven words each.

Abstract

EUROFER97 is a Reduced Activation Ferritic Martensitic (RAFM) steel that will be utilized for breeding blanket and first wall applications in future fusion reactors due to its advantageous thermo-mechanical properties and swelling resistance. Despite this, in its irradiated state, its strain hardening, and uniform elongation capabilities are inhibited, rendering it potentially unusable according to current design standards. Nonetheless, the material's strength and the low ratio of uniform elongation to fracture strain necessitate an investigation into its potential for use beyond uniform elongation loss. A component scale continuum mechanics-based material model able to describe the tensile properties of irradiated material would assist in determining the maximum operating limits of reactor components.

Existing frameworks in continuum mechanics do not account for the energy transfers that occur during neutron irradiation and plastic deformation of the material. Therefore, a newly developed thermodynamic framework is constructed to satisfy the first law of thermodynamics by introducing a novel irradiation power term. By separating the contribution of free energy to hardening from the total free energy, it is possible to modify the Clausius-Duhem entropy inequality, which forms the basis for deriving a finite strain model capable of describing the pronounced material and geometrical nonlinearities resulting from the deformation of irradiated materials. The developed framework is used to extend the constitutive equations of an existing small strain viscoplasticity model [1] capable of describing deformation induced by irradiation to finite strains using the Dual Variables Approach [2]. In addition, the conditions required to guarantee thermodynamic consistency are identified and discussed. To describe the observed damage mechanism of accelerated void coalescence, a rate-dependent extension of the GTN ductile damage model [3] is developed. Using a corotational algorithm, the developed coupled deformation-damage model is implemented in a Finite Element code. Model calibration and subsequent validation are applied to tensile test experiments conducted at RT and 300 °C on unirradiated and irradiated material specimens until failure. After demonstrating and establishing the high accuracy of the model, a ductility study is conducted using the model to examine and discuss the predicted effect of irradiation on the development of the material's neck and its ductility. In conclusion, the implications of irradiation's effect on ductile failure design rules are discussed, and suggestions for loosening the failure criteria are provided.

Kurzfassung

EUROFER97, ein reduziert aktivierbarer ferritisch-martensitischer Stahl (RAFM), wird aufgrund seiner vorteilhaften thermomechanischen Eigenschaften und Bestrahlungsschwellbeständigkeit für Blanket Module und die Erste Wand zukünftiger Fusionsreaktoren verwendet. Im bestrahlten Zustand sind jedoch seine Dehnungsverfestigungskapazität und Gleichmaßdehnung eingeschränkt, was ihn nach aktuellen Designstandards potenziell unbrauchbar macht. Dennoch erfordern die Festigkeit des Materials und das niedrige Verhältnis von Gleichmaßdehnung zu Bruchdehnung die Untersuchung seines Potenzials für den Einsatz über die Gleichmaßdehnung hinaus. Ein kontinuumsmechanisches Materialmodell auf Komponentenskala, das die Zugeigenschaften des bestrahlten Materials beschreibt, würde helfen, die maximal erlaubten Betriebsgrenzen von Reaktorkomponenten zu bestimmen.

Bestehende Ansätze der Kontinuumsmechanik berücksichtigen nicht die Energieübertragungen, die während der Neutronenbestrahlung und der plastischen Verformung des Materials auftreten. Daher wird ein neuer thermodynamischer Ansatz entwickelt, bei dem das erste Gesetz der Thermodynamik durch die Einführung eines neuartigen Bestrahlungsleistungsterms erfüllt wird. Durch die Trennung des Verfestigungsbeitrags der freien Energie von der gesamten freien Energie ist es möglich, die Clausius-Duhem-Entropieungleichung zu modifizieren und somit die Grundlage für die Ableitung eines Modells für große Deformationen zu bilden, das die auftretenden, ausgeprägten materiellen und geometrischen Nichtlinearitäten bei großen Verformungen bestrahlter Materialien beschreiben kann. Der entwickelte Ansatz wird verwendet, um die konstitutiven Gleichungen eines bestehenden viskoplastischen Modells zur Beschreibung des Verformungsverhaltens unter Bestrahlung für kleine Dehnungen [1] auf finite Dehnungen unter Verwendung des Konzepts der Dualen Variablen [2] zu erweitern. Zudem werden die zur Gewährleistung der thermodynamischen Konsistenz erforderlichen Bedingungen identifiziert und diskutiert. Zur Beschreibung des beobachteten Schädigungsmechanismus der beschleunigten Porenverschmelzung wird eine ratenabhängige Erweiterung des GTN-Modells für die duktile Schädigung [3] entwickelt. Mit einem Korotationsalgorithmus wird das entwickelte gekoppelte Verformungs-Schädigungsmodell in einen Finite-Elemente-Code implementiert. Die Modellkalibrierung und anschließende Validierung werden an Zugversuchen durchgeführt, die bei Raumtemperatur und 300 °C an unbestrahlten sowie bestrahlten Materialproben bis zum Versagen durchgeführt wurden. Nach der Demonstration der hohen Beschreibungsgenauigkeit des Modells wird eine Duktilitätsstudie durchgeführt, bei der der vorhergesagte Einfluss der Bestrahlung auf die Entwicklung der Einschnürung und Duktilität des Materials untersucht und diskutiert werden. Abschließend werden die Auswirkungen der Bestrahlung auf die Designregeln für das duktile Versagen diskutiert und Vorschlage zur Lockerung der Versagenskriterien vorgestellt.

Acknowledgements

This thesis was possible due to the help and support of several people both within and outside the Institute for Applied Materials – Mechanics of Materials and Interfaces (IAM-MMI) at the Karlsruhe Institute of Technology (KIT).

First and foremost, I would like to express my heartfelt gratitude to Prof. Dr.-Ing. Jarir Aktaa, my doctoral advisor, for allowing me to work on this project and for always being available when I needed him, reviewing my progress constantly, and guiding me through my doctoral studies. Furthermore, I would like to express gratitude to Prof. Dr.-Ing. habil. Thomas Seelig and Prof. Dr.-Ing. Bronislava Gorr for reviewing this thesis and acting as co-referents during my Ph.D. defense. Additionally, I would like to thank Prof. Dr.-Ing. Arne Rönnau for presiding over my defense.

I would also like to thank my supervisor, Dr.-Ing. Ermile Gaganidze, for guiding me throughout this project and reviewing my thesis. The literary resources he provided, and our conversations greatly enhanced my understanding of material properties and helped me to articulate my work. The experimental investigations supporting this thesis were conducted by Dr. Dmitry Terentyev and his team at SCK-CEN, Belgium. Discussions about damage modeling and optimization techniques with Prof. Dr. mont. Christoph Kirchlechner and Dr. Alexander Schowtjak yielded fresh insights that significantly raised the caliber of this work. I am grateful for the stimulating conversations I have had with my colleagues Dr. Mario Walter, Dr. Michael Mahler and Dr. Jie Gao. In addition, I appreciate the helpfulness and professionalism of the institute's staff and fellow researchers, and the pleasant atmosphere we enjoyed while working together.

I am deeply grateful to my parents and my wife, Nandhitha, whose unwavering support, encouragement, and understanding were instrumental in my journey to complete my doctoral degree. Their steadfast presence provided me with the strength and motivation to persevere. I also extend my heartfelt gratitude to my friends and colleagues Mathias Jetter, Dr. Qian Yuan, Dr. Kaiju Lu, Dr. Ankur Chauhan, Dr. Silva Basu, and Dr. Yijing Zheng for the many joyful moments we shared.

Finally, this work was carried out under the financial support of KIT Fusion program and the Euratom research and training program 2014–2018 under Grant agreement No. 755039 (M4F Project).

Karlsruhe, in December 2025 Roshan Ram Rajakrishnan

Table of contents

List of figures

List of tables

List of symbols

General notations

$\boldsymbol{a}, \boldsymbol{A}$	Vectors
a, A	Scalars, constants
$\mathbf{A}$	Tensors
ΔA	Absolute error of A
δA	Relative error of A
$\mathrm{div}(\boldsymbol{A})$	Divergence of vector $\boldsymbol{A}$
$\mathrm{grad}(\boldsymbol{A})$	Gradient of vector $\boldsymbol{A}$
$\mathbf{A}^D$	Deviator of tensor $\mathbf{A}$
$\det(\mathbf{A})$	Determinant of tensor $\mathbf{A}$
$\hat{\mathbf{A}}$	Tensor $\mathbf{A}$ transformed to the $\hat{\mathcal{X}}_t$
$\mathbf{A}^{-1}$	Inverse of tensor $\mathbf{A}$
$\dot{\mathbf{A}}$	Time derivative of tensor $\mathbf{A}$
$\mathbf{A}^T$	Transpose of tensor $\mathbf{A}$
$\bar{\mathbf{X}}$	Bar transformation of tensor $\mathbf{X}$
$\overset{\circ}{(\cdot)}$	Jaumann time derivative
$\frac{\mathrm{d}}{\mathrm{d}t}()$	Time derivative
$\overset{\triangle}{(\cdot)}$	Lower Oldroyd time derivative $\overset{\triangle}{(\cdot)} = \dot{(\cdot)} + \mathbf{L}^T\,(\cdot) + (\cdot)\,\mathbf{L}$
$\overset{\triangledown}{(\cdot)}$	Upper Oldroyd time derivative $\overset{\triangledown}{(\cdot)} = \dot{(\cdot)} - \mathbf{L}\,(\cdot) - (\cdot)\,\mathbf{L}^T$

Roman Symbols

a	Defect density model parameter
$\mathcal{A}$	Consistent tangent modulus variable
$A(p)$	Plasticity driven function
A_0	Initial cross sectional area of gauge section
A_{min}	Minimum cross sectional area of gauge section
$\mathbf{A}$	Almansi strain tensor
b	Defect density model parameter
$\mathcal{B}$	Consistent tangent modulus variable
B	Bridgman correction factor
$\mathfrak{B}$	Material body
$\mathbf{B}$	Right Cauchy Green tensor
$\mathcal{C}$	Consistent tangent modulus variable
c	Isotropic softening parameter
c_s	Isotropic softening parameter
C	Kinematic hardening parameter

$\mathbf{c}$	Time-dependent translation of the origin
$\mathbf{C}$	Left Cauchy Green tensor
$\mathbb{C}$	Fourth-order elasticity tensor
d	Damage variable
d_0	Initial diameter of gauge section
d_c	Critical damage
d_{min}	Minimum diameter of gauge section
$\mathrm{d}V$, $\mathrm{d}v$	Material volume element
$\mathrm{d}\boldsymbol{A}$, $\mathrm{d}\boldsymbol{a}$	Material surface element
$\mathrm{d}\boldsymbol{X}$, $\mathrm{d}\boldsymbol{x}$	Material line element
$\mathbf{D}$	Spatial strain rate tensor
$\mathbf{D}_{HW}$	Spatial strain rate calculated by Hughes Winget method
$\mathbb{D}$	Consistent tangent modulus
e	Specific internal energy per unit mass
e_1	Portion of defects removed before rate of defect removal drops.
E_{int}	Internal energy
E_{kin}	Kinetic energy
$\boldsymbol{\varepsilon}_m$	Inelastic strain rate in matrix material
E	Theoretical Young's modulus
E_{exp}	Slope of experimental curve
$\mathbf{E}$	Green strain tensor
$\mathbf{E}_e$	Elastic part of strain tensor
$\mathbb{E}^3$	Euclidean space
$\dot{f}_{growth}$	Growth rate of void volume fraction
$\dot{f}_{nucl}$	Nucleation rate of void volume fraction
f	Void volume fraction
f^*	Effective void volume fraction
f_u^*	VVF when load bearing capacity is lost
f_c	Critical void volume fraction
f_N	Void fraction of nucleating particles
f_v	Porosity
f_{CTM}	Plasticity function variable
F	Dissipative potential function
F_d	Damage potential of dissipation
F_y	Yield function
$F_{\boldsymbol{\Omega}}$	Plastic potential of dissipation
$\mathbf{F}$	Deformation gradient tensor
$\mathbf{F}_e$	Elastic part of the deformation gradient
$\mathbf{F}_p$	Plastic part of the deformation gradient
$\boldsymbol{g}$	Spatial temperature gradient
h	Isotropic softening parameter
h_N	Temperature-dependent dislocation pile-up strength.
$H(\mathfrak{B},t)$	Entropy supply
H	Kinematic hardening parameter
$\mathbb{I}$	Symmetric part of the fourth-order identity tensor
$\mathbf{I}$	Second order identity tensor
J	Jacobian determinat
k	Initial yield stress
K	Viscous parameter
$\mathcal{K}$	Set of all configurations

$\boldsymbol{k}$	Force vector acting on the material body volume
$\mathbf{K}$	Orientation mapping tensor
δl	Cross head displacement
l_0	Initial length of gauge section
$l_{N,i}$	Portion of defects removed before rate of defect removal drops.
L	Load applied
$\mathbf{L}$	Spatial velocity gradient
$\mathrm{m}(\mathfrak{B},t)$	Mass of the body
m_ψ	Isotropic softening parameter
m	Kinematic hardening parameter
n	Viscous parameter
N	Defect density variable
N_l	Defect density available for removal by plastic deformation
N_r	Defect density model parameter
N_s	Saturation value of defect density
$\boldsymbol{n}$	Normal vector to the area
p	Accumulated plastic strain
P_a	Total energy of the material body
P_{irr}	Irradiation power
$\mathcal{P}$	Material points
q_1	GTN model parameter
q_2	GTN model parameter
q_N	Defect density model parameter
q	Heat flux density
Q	Non-mechanical energy exchange
$\boldsymbol{q}$	Cauchy heat flux vector
$\mathbf{Q}$	Orthogonal tensor
$\mathbf{Q}_{HW}$	Orthogonal tensor calculated by Hughes Winget method
r	Isotropic hardening state variable
r_N	Defect density model parameter
R_{curv}	Radius of curvature of neck profile
r_ψ	Isotropic softening parameter
$\mathcal{R}$	Isotropic hardening variable
R	Kinematic hardening parameter
$\mathbf{R}$	Orthogonal rotation tensor
$\mathbb{R}^3$	Real coordinate space
s_N	Standard deviation of void nucleation distribution
s	Heat supply per unit mass
$\mathcal{S}$	Surface
$\mathcal{S}_d$	Damage surface
S	Entropy
$\mathbf{S}$	Weighted Cauchy stress tensor
t	Time
Σ_v	Hydrostatic part of over stress
$\boldsymbol{t}$	Cauchy stress vector
$\hat{\mathbf{T}}$	Stress tensor from $\hat{\mathcal{X}}_t$
$\mathbf{T}$	Cauchy stress tensor
$\mathbf{T}_R$	First Piola-Kirchhoff stress tensor
$\tilde{\mathbf{T}}$	Second Piola-Kirchhoff stress tensor
$\boldsymbol{u}$	Displacement vector

$\mathbf{U}$	Left stretch tensor
V	Volume
$\mathbf{v}$	Velocity field
$\mathbf{V}$	Right stretch tensor
WA	Weighted Average method parameter
w_d	Damage threshold stored energy density
w_s	Stored energy density
W	Stress power per unit volume
$\mathbf{W}$	Spin tensor
$\mathbf{W}_{HW}$	Spin tensor calculated by Hughes Winget method
$\hat{\mathcal{X}}_t$	Intermediate configuration
$\mathcal{X}_{t_0,}$	Reference configuration
x^k	Spatial coordinates
X^L	Material coordinates
$\mathcal{X}_t$	Current configuration
$\ddot{\boldsymbol{x}}$	Acceleration vector (=$\dot{\boldsymbol{v}}$)
$\boldsymbol{X}$	Position vector in $\mathcal{X}_{t_0}$
$\boldsymbol{x}$	Position vector in $\mathcal{X}_t$
y	List of model variables
Y	Damage conjugate variable

Greek Symbols

$\boldsymbol{\alpha}$	Kinematic hardening state variable
β	Material parameter for isotropic softening free energy function
ε_N	Mean strain for nucleation of void
ε_t	Mean true strain
η	Specific entropy per unit mass
$\boldsymbol{\varepsilon}$	Total strain tensor
$\boldsymbol{\varepsilon}^p$	Plastic strain tensor
$\boldsymbol{\varepsilon}_e$	Elastic strain tensor
$\boldsymbol{\varepsilon}_{in}$	Inelastic strain tensor
Γ	Entropy production
γ	Specific rate of entropy production
γ_N	Material parameter for irradiation defect density free energy function
$\boldsymbol{\Gamma}$	Strain tensor from $\hat{\mathcal{X}}_t$
$\frac{d\bar{\sigma}_t}{d\varepsilon_t}$	Hardening modulus
$\dot{\lambda}$	Plasticity multiplier or viscosity function
$\boldsymbol{\Omega}$	Back stress tensor and kinematic hardening variable
ϕ	Irradiation damage dose
Φ	Gurson yield function
ψ	Isotropic softening variable $\psi = \psi_1 + \psi_2$
ψ_i	Components of isotropic softening variable ψ
$\psi_{s,\infty}$	Isotropic softening parameter
$\boldsymbol{\Phi}_{t_0}$	Mapping function
Ψ	Free energy function

ψ_s	Load history variable for isotropic softening
ψ_r	Isotropic softening parameter
ρ	Density of body in $\mathcal{X}_t$
ρ_R	Density of body in $\mathcal{X}_{t_0}$
σ_A	Tensile flow stress for hydrostatic part of GTN yield function
σ_s	Effective yield stress for GTN yield function
σ_A	Yield stress for hydrostatic part of yield function
$\bar{\sigma}_t$	Bridgman true stress
σ_H	Irradiation hardening
Σ_{eq}	von-Mises equivalent of Over stress tensor
σ_M	Yield stress in the matrix material
σ_s	Effective yield stress in the matrix material
σ_t	Mean true stress
σ_{vis}	Viscous stress
σ_v	Hydrostatic stress
$\boldsymbol{\sigma}$	General stress tensor
$\tilde{\boldsymbol{\sigma}}$	Effective stress tensor
$\boldsymbol{\Sigma}$	Over stress tensor
Θ	Absolute temperature
ς	Volume distributed entropy supply
ξ	Irradiation hardening per unit dose
ζ	Surface distributed entropy supply
$\boldsymbol{\zeta}$	Surface distributed entropy supply vector

Acronyms / Abbreviations

CTM	Consistent tangent modulus
DBH	Dispersed Barrier Hardening
ESS	Engineering stress and strain
ISV	Internal state variables
MTSS	Mean true stress and true strain
TF	Triaxiality factor
TSS	True stress and true strain
GTN	Gurson-Trevgaard-Needleman
VVF	Void volume fraction
WA	Weighted Average method

Chapter 1

Background and motivation

The task of thesis was completed as a part of the Multiscale modeling for fusion and fission materials (M4F) project [18]. The purpose of the project was to predict the effects of irradiation on the mechanical behaviour of ferritic/martensitic (F/M) steels by combining modeling and experiments at different scales. This multidisciplinary project used modeling and experiments at various scales to better understand the complex phenomena of irradiation-induced defect formation and evolution, as well as their effects on macroscopic material behaviour. This would allow us to predict the origin of localized deformation in F/M steels during irradiation and its effects on the mechanical behaviour of future fission and fusion reactor components, improving the modeling of component's mechanical behaviour and hence leading to a more robust design.

For the fabrication of the test blanket modules (TBM) in the experimental fusion reactor ITER and of the breeding blankets of future fusion reactors like the DEMOnstration reactor DEMO, reduced activation ferritic martensitic (RAFM) steel has been selected as the reference structural material in Europe. The European RAFM steel Eurofer97 [19–21] (nominal composition Fe-9Cr-1.1W-0.2V-0.12Ta) was developed with this goal in mind, and it possesses both promising resistance to irradiation-induced swelling and excellent thermo-mechanical properties. After being exposed to low-temperature neutron irradiation [22, 14], however, the material exhibits a significant change in its nonlinear mechanical behaviour, such as a strong material hardening accompanied by a significantly reduced uniform elongation and total elongation. There is a marked increase in the irradiated material's yield stress (YS) and ultimate tensile stress (UTS) compared to the unirradiated state, followed by a steep softening. According to the reported comprehensive studies [23, 24], this is the result of localized dislocation movements interacting with irradiation-induced defects such as defect clusters, dislocation loops, voids, etc. formed in the material lattice as a result of irradiation-induced cascades. The number of displacements per atom (dpa) caused by these cascades is used to measure radiation damage. The fig. 1.1 illustrates the evolution of irradiation defects in the material. The thermodynamics of this phenomenon is further discussed in section 3.2. Dislocation pinning by irradiation defects is responsible for the hardening that is observed after irradiation [25]. When a certain level of stress is reached, dislocations begin to move, clearing defects in their path. The resulting channels are characterized as soft, defect-free material that is surrounded by defect-rich, hard

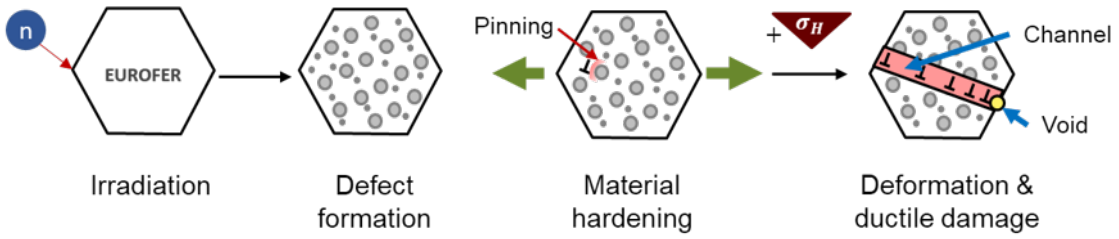

(a) Defect formation (b) Defect removal

Figure 1.1: Illustration of (a) irradiation defect formation with neutron irradiation and (b) defect removal by plastic deformation.

material, as described in [26, 27]. Micro-cracks begin when dislocations cluster near grain boundaries, interact, and create voids that grow and coalesce. It has been determined that void nucleation, growth, and coalescence are the primary damage mechanisms responsible for the ductile damage of irradiated F/M steels [26], while channeling is the primary deformation mechanism.

Loss of uniform elongation renders components unsafe per current nuclear industry design rules [28]. With the high cost of component replacement and the potential downtime of the reactor, it is advantageous to accurately estimate the maximum operating range of the components after they have lost their uniform elongation/deformation. A description of the material's post-yield and flow softening behaviour would greatly aid in estimating the component life and support the development of advanced design criteria for breeding blanket components, both of which are made possible by continuum approaches for modeling the material's behaviour at the component scale. The continuum-based models that are currently available are primarily micro-mechanical. These models make use of crystal plasticity to explain the initiation and destruction of each type of defect in grains [29], single crystals [30, 31], poly-crystals [32, 33], and self-consistent plasticity theory [34] to explain the connection between macroscopic and local strain/stress rates. These approaches combine micro-structure observations and computationally expensive simulations at different length scales to capture the dominant physical mechanisms within a finer length scale (nm) and pass the relevant information to a higher length scale (μm) model until an appropriate level of coarse Finite Element (FE) mesh can predict the macroscopic mechanical property observable with physical fidelity. Damage initiation and grain boundary effects may require even more advanced multiscale techniques due to the high mesh refinement needed for convergence. These methods can study the micro-structural evolution of materials after irradiation and deformation.

This work focuses on continuum modeling using constitutive equations to describe macroscopic material behaviour. These models can be reliably calibrated using data from mechanical tests, without the need for computationally-expensive simulations at lower scales. They can be used with most Finite Element Method (FEM) codes to simulate component deformation and damage under operating conditions, making them essential for design and development. To define a well-posed initial value problem (IVP) and keep the field equations hyperbolic, a viscoplastic framework is used. This allows faster calculations and reduced mesh dependency. Since it uses constitutive equations for

the nucleation and annihilation of defects to describe the influence of irradiation on the material behaviour for small-strains (below 5%), the elasto-viscoplastic model by Aktaa and Petersen [1] is the most appropriate base model for this work. In order to simulate diffuse and localized necking, large deformations and rotations must be handled. Therefore, the constitutive system of equations by Aktaa and Petersen [1] is expanded to the finite strain framework. To ensure the formulation of a thermodynamically consistent model, the Dual Variables concept [35, 2, 36] is used. Thermodynamic modeling of the mechanisms involved in defect formation during irradiation and the removal of defects during plastic deformation is required to ensure the consistency of the model because the irradiation defects in the material are what cause the irradiation-induced changes in material properties. Since there is currently no thermodynamic framework to explain the energy transactions involved in these events, a modified thermodynamic framework is suggested in this work to explain the changes in the material's internal energy. Irradiation defect density is added as an internal variable to the material's free energy function in this regard. The phenomena of void nucleation, growth, and coalescence mechanism are responsible for the experimentally observed ductile damage of the material under large deformations. Many researchers are still interested in this topic who use rate-independent plasticity to define pressure dependent models [3, 37], which are frequently used to describe this mechanism. Due to its simplicity of use, the well-known Gurson-Tvergaard-Needleman (GTN) model [3] is chosen among them and extended to viscoplasticity by considering an appropriate viscoplastic potential.

The thesis is structured as follows: In chapter 2, the fundamentals of continuum mechanics are covered. In chapter 3, experimental results from tensile tests on unirradiated and irradiated materials are presented to illustrate the material behaviour under various loading conditions. The thermodynamic framework for modeling irradiated materials is presented and thoroughly discussed, then the finite strain model is formulated. Finally, the evolution of the GTN viscoplastic model is discussed. Chapter 4 discusses model integration and implementation in the FE-software ABAQUS. Chapter 5 deals with model calibration and validation using available experimental data. In addition, an investigation into the impact of temperature and irradiation dose on the model's predictions is presented. In chapter 6, the simulation results and model predictions are discussed in depth, and the work is concluded in chapter 7.

Chapter 2

Fundamentals of continuum mechanics

Continuum mechanics is a branch of mechanics, which deals with the mathematical description of the motion and deformation of material bodies under thermo-mechanical loads. Here the material body is considered to be a continuous assembly of material points forming a continuous mass, instead of discrete particles. Thus, all physical quantities can be described as continuous fields related to either the material point or the spatial location using a scalar when direction-independent or a tensor when direction-dependent. While a scalar is used for temperature, spatial displacement $\mathbf{u}$ is a tensor of order one (vector), while stress $\mathbf{T}$ is usually represented as a tensor of order two.

The continuum mechanics is fundamentally built on three main pillars. The first is *kinematics*, which describes the motion and deformation that a material body may undergo. The second is the formulation of balancing relations for the conservation of mass, momentum, and energy. These two pillars lay the fundamental assumptions based on space, time, and the principles of mechanics which are valid for all materials. The final/third pillar is the material theory, which is concerned with the modeling of material behaviour using constitutive equations. Constitutive equations are meant to represent the behaviour of only the material under investigation. Material theory provides recommendations for constructing constitutive models in order to ensure that the equations do not contradict any fundamental physical laws. The material behaviour of solids can be separated into four classes: elasticity, plasticity, viscoelasticity, and viscoplasticity [35]. Since this work deals with thermo-elasto-viscoplasticity, the focus will be placed on this behaviour.

The said fundamentals which are essential for understanding the related and sometimes advanced topics in this work, like *conjugate variables*, *finite strain framework*, *Dual Variables* concept, are discussed in this chapter.

2.1 Kinematics

The mathematical description of the motion of material points, i.e. the deformation of material bodies, is the goal of kinematics. The concepts of motion and configuration in kinematics are briefly described here.

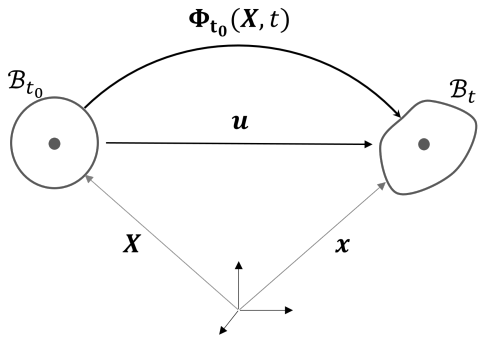

Figure 2.1: Schematic representation of configurations.

2.1.1 Motion

In continuum theory [35, 38–41], the concept of material body $\mathfrak{B}$ is introduced which constitutes a set of material points $\mathcal{P}$ ($\mathfrak{B}$=$\{\mathcal{P}\}$) for which a set of one-to-one mappings $\mathcal{K} = \{\mathcal{X}\}$ exists, where each mapping $\mathcal{X}$ is called a *configuration*.

$$\begin{aligned} \mathcal{X} : \mathfrak{B} &\longrightarrow \mathcal{X}[\mathfrak{B}] \subset \mathbb{R}^3 \\ \mathcal{P} &\longmapsto \mathcal{X}(\mathcal{P}) = \left(x^1, x^2, x^3\right) \Leftrightarrow \mathcal{P} = \mathcal{X}^{-1}\left(x^1, x^2, x^3\right) \end{aligned} \tag{2.1}$$

For any two of such configurations $\mathcal{X}_1, \mathcal{X}_2$, their composition $\mathcal{X}_2 \circ \mathcal{X}_1^{-1}$ is continuously differentiable. The motion of the material body is described using a sequence of configurations identified by time t.

$$\begin{aligned} t \mapsto \mathcal{X}_t : \mathfrak{B} &\longrightarrow \mathcal{X}_t[\mathfrak{B}] \subset \mathbb{R}^3 \\ \mathcal{P} &\longmapsto \mathcal{X}_t(\mathcal{P}) = \left(x^1(t), x^2(t), x^3(t)\right) \end{aligned} \tag{2.2}$$

The configuration at time t, $\mathcal{X}_t$ is known as the *current configuration*. From the numerous possible configurations of the set $\mathcal{K}$, one is emphasized to describe the motion of a material body. This is the *reference configuration*. Usually, the initial configuration at t_0, $\mathcal{X}_{t_0}$ is chosen to be the reference configuration

$$\begin{aligned} \mathcal{X}_{t_0} : \mathfrak{B} &\longrightarrow \mathcal{X}_{t_0}[\mathfrak{B}] \subset \mathbb{R}^3 \\ \mathcal{P} &\longmapsto \mathcal{X}_{t_0}(\mathcal{P}) = \left(X^1, X^2, X^3\right) \end{aligned} \tag{2.3}$$

which identifies each material point from $\mathcal{P} \in \mathfrak{B}$ by the triplet $\left(X^1, X^2, X^3\right)$. The triplets $X^L = \left(X^1, X^2, X^3\right)$ and $x^k = \left(x^1, x^2, x^3\right)$ are called *material* and *spatial coordinates* of the point $\mathcal{P}$ respectively. For physical observation, it is necessary to identify the points in a space as illustrated in the fig. 2.1. Thus, the material body is represented in the Euclidean space $\mathbb{E}^3$. With this arrangement, the motion of the body is given by the mapping

$$\mathbf{x} = \mathbf{\Phi}_{t_0}(\boldsymbol{X}, t) \tag{2.4}$$

where, $\boldsymbol{x}$ and $\boldsymbol{X}$ are the position vectors of the point $\mathcal{P}$ in the current and reference configurations respectively. The displacement vector $\boldsymbol{u}$ is used to describe motion between the position vectors and given by:

$$\boldsymbol{u}(\boldsymbol{X},t) = \boldsymbol{x} - \boldsymbol{X} = \boldsymbol{\Phi}_{t_0}(\boldsymbol{X},t) - \boldsymbol{X}. \tag{2.5}$$

2.1.2 Deformation

Deformation of a body can be described as its transformation from the reference to current configuration. Since the transformation of the body in eq. (2.4) is continuously differentiable, its differentiation with respect to the position vector $\boldsymbol{X}$ is referred to as the *deformation gradient* [35, 39]

$$\mathbf{F} = \mathrm{Grad}\, \boldsymbol{\Phi}_{t_0}(\boldsymbol{X},t) = \frac{\partial \boldsymbol{x}}{\partial \boldsymbol{X}}. \tag{2.6}$$

If $\mathrm{d}\boldsymbol{X}$ and $\mathrm{d}\boldsymbol{x}$ represent the tangent vectors of material line elements in the reference and actual configurations, respectively, the important property of the deformation gradient is to map the line$(\mathrm{d}\boldsymbol{X}, \mathrm{d}\boldsymbol{x})$, surface $(\mathrm{d}\boldsymbol{A}, \mathrm{d}\boldsymbol{a})$ and volume elements $(\mathrm{d}V, \mathrm{d}v)$ from the reference to the current configurations using the Jacobian determinant J.

$$\begin{aligned} \mathrm{J} &= \det \mathbf{F} \\ \mathrm{d}\boldsymbol{x} &= \mathbf{F}\, \mathrm{d}\boldsymbol{X} \\ \mathrm{d}\boldsymbol{a} &= \mathrm{J}\, \mathbf{F}^{-\mathrm{T}}\, \mathrm{d}\boldsymbol{A} \\ \mathrm{d}v &= \mathrm{J}\, \mathrm{d}V \end{aligned} \tag{2.7}$$

Although, the deformation gradient is non-symmetric, due to its irreversibility and the continuity of motion, the determinant $\det \mathbf{F} > 0$ is valid. In general, all the information about local deformation is contained in $\mathbf{F}$. However, it is not directly used in constitutive equations since $\mathbf{F}$ is not independent of rigid body motions and therefore to circumvent this, it is used to formulate suitable strain tensors. Since $\mathbf{F}$ is not singular $(\det \mathbf{F} \neq 0)$, the deformation gradient can be decomposed multiplicatively into the orthogonal rotation tensor $\mathbf{R}$ $\left(\mathbf{R}^{\mathrm{T}} = \mathbf{R}^{-1},\ \det \mathbf{R} = +1\right)$ and a symmetric stretch tensor $\mathbf{U}$ (or $\mathbf{V}$)

$$\mathbf{F} \;=\; \mathbf{R}\mathbf{U} \;=\; \mathbf{V}\mathbf{R} \tag{2.8}$$

where, $\mathbf{U}$ is the right stretch tensor, $\mathbf{V}$ is the left stretch tensor. This is referred to as the *polar decomposition* of $\mathbf{F}$ and is unique in nature.

2.1.2.1 Strain

Strain describes deformation by quantifying the relative displacement of material points that excludes rigid body motion. Different measures of strain can be made with respect to reference and current configurations. In a body, strains may result from force applied or temperature changes of the

body. Constitutive relations are used to establish the relationship between stress and strain. These relations are discussed further in section 2.4. Reversible deformations are described by elastic strains, where the body returns to its original state once the force or stress field is removed. Irreversible deformations described by inelastic or plastic strains, are those, where a part of the deformation remains even after the removal of the stress field. Based on the extent of strain, the description of deformation is classified into small strain and finite strain theories. The infinitesimal strain or small strain theory describes deformations where strains and rotations are small. Here, the undeformed and deformed configurations of the body are assumed to be close. The finite strain theory or the large strain/deformation theory describes deformations with large rotations and strains, where undeformed and deformed configurations of the body are significantly different.

In small strain theory, deformation is measured by the engineering strain as a ratio of total deformation to the undeformed dimension of the body.

$$\varepsilon_{eng} = \frac{\Delta l}{l_0} \tag{2.9}$$

Here, Δl and l_0 are the change in length and initial length of the line element, respectively. In the finite strain theory, the tensors $\mathbf{U}$ and $\mathbf{V}$ are used to formulate strain tensors which describe the deformation, independent of rigid body motions [39, 42]. This includes the Green strain tensor $\mathbf{E}$ which operates in the reference configuration

$$\mathbf{E} \;=\; \frac{1}{2}\big(\mathbf{F}^{\mathrm{T}}\,\mathbf{F} \,-\mathbf{I}\big) \;=\; \frac{1}{2}(\mathbf{C} \,-\mathbf{I})\,, \quad \text{with} \quad \mathbf{C} \,=\mathbf{F}^{\mathrm{T}}\mathbf{F} \;=\; \mathbf{U}^2 \tag{2.10}$$

and the Almansi strain tensor, which operates in the current configuration

$$\mathbf{A} \;=\; \frac{1}{2}\big(\mathbf{I}-\mathbf{F}^{-1}\,\mathbf{F}^{-\mathrm{T}}\big) \;=\; \frac{1}{2}\big(\mathbf{I} \,-\mathbf{B}^{-1}\big) \quad \text{with} \quad \mathbf{B} \,=\mathbf{F}\mathbf{F}^{\mathrm{T}} \;=\; \mathbf{V}^2. \tag{2.11}$$

Here, $\mathbf{C}$ and $\mathbf{B}$ are the right and left Cauchy Green tensors. While $\mathbf{C}$ operates on the reference configuration, $\mathbf{B}$ operates on the current configuration. The strain tensors are related by the *push forward* $\mathbf{F}^{-\mathrm{T}}(\cdot)\mathbf{F}^{-1}$ and *pull back* $\mathbf{F}(\cdot)\mathbf{F}^{\mathrm{T}}$ operations

$$\begin{aligned}\mathbf{A} \;&=\; \mathbf{F}^{-\mathrm{T}}\,\mathbf{E}\,\mathbf{F}^{-1}\\ \mathbf{E} \;&=\; \mathbf{F}^{\mathrm{T}}\,\mathbf{A}\,\mathbf{F}\end{aligned}$$

2.1.2.2 Stress

The stress state present at material point $\mathcal{P}$ is represented by the tensor $\mathbf{T}$, known as the Cauchy stress tensor that has the property $\boldsymbol{t} = \mathbf{T}\,\boldsymbol{n}$, where $\boldsymbol{n}$ is the normal vector. The tensor $\mathbf{T}$ describes the force acting on a material surface element in the current configuration and holds the dimension force per area. Although the action of force acts in the current configuration, its intensity is also relevant in the reference configuration. The first *Piola-Kirchhoff* stress tensor $\mathbf{T}_R$ with the property $\boldsymbol{t}_R = \mathbf{T}_R\,\boldsymbol{n}_R$ is

related to $\mathbf{T}$ by the transformation

$$\mathbf{T}_R = (\det \mathbf{F})\ \mathbf{T}\ \mathbf{F}^{-\mathrm{T}}, \tag{2.12}$$

where $\boldsymbol{n}_R$ is the normal vector in the reference configuration. However, due to the symmetry of $\mathbf{T}$, the tensor $\mathbf{T}_R$ is not symmetric. Definition of additional stress tensors are possible, such as:

$$\mathbf{S} \ = \ (\det \mathbf{F})\ \mathbf{T} = \ \tfrac{\rho_R}{\rho}\mathbf{T} \tag{2.13}$$

$$\tilde{\mathbf{T}} \ = \ \mathbf{F}^{-1}\ \mathbf{S}\ \mathbf{F}^{-\mathrm{T}} = \ (\det \mathbf{F})\ \mathbf{F}^{-1}\ \mathbf{T}\ \mathbf{F}^{-\mathrm{T}} \tag{2.14}$$

where $\mathbf{S}$ is the weighted *Cauchy* tensor and $\tilde{\mathbf{T}}$ is the second *Piola-Kirchoff* tensor which are both symmetric.

2.1.2.3 Deformation velocities

The *spatial velocity gradient* $\mathbf{L}$ describes the rate of change of material line, area and volume elements. It is related to the time derivative of $\mathbf{F}$ and the velocity field $\mathbf{v}(\boldsymbol{x},t) = \dot{\boldsymbol{x}}$.

$$\mathbf{L} \ = grad\ \mathbf{v} \ = \ \dot{\mathbf{F}}\ \mathbf{F}^{-1} \tag{2.15}$$

This can be decomposed additively into its symmetric and skew-symmetric parts

$$\text{with} \quad \mathbf{D} \ = \ \frac{1}{2}(\mathbf{L} \ + \ \mathbf{L}^{\mathrm{T}}) \tag{2.16}$$

$$\text{and} \quad \mathbf{W} \ = \ \frac{1}{2}(\mathbf{L} \ - \ \mathbf{L}^{\mathrm{T}}), \tag{2.17}$$

where $\mathbf{D}$ is the symmetric spatial strain rate tensor and $\mathbf{W} = -\mathbf{W}^T$ is the skew symmetric spin tensor. The dot denotes material time derivative. In section 2.3.1.1, the corotational deformation rates are discussed.

2.2 Balance relations

The balance relations establish a link between the effect of the outside world and the current state of the material body by employing appropriate physical quantities.

Thermomechanics extends the list of mechanical quantities like mass, moment, and angular momentum with thermodynamic quantities like temperature, energy, and entropy which are influenced by the environment. Physical quantities are attributed to the body $\mathfrak{B}$ itself, based on assumptions that they are additive and continuous with respect to the volume dv. Additive quantities and the effects of surroundings are represented by volume integrals using density functions in the current or reference configuration, each consisting of a single volume and surface integral. Thereby the temporal change

of a wide list of physical quantities relating to the current state of a material body is brought into a relationship with the effect of the outside world by means of a balance relation. *Global* and *local* formulations of the balance relations are possible with either being equivalent as long as the physical quantities possess continuity properties. The balance relations are well documented in literature [39, 35] and briefly summarized here.

2.2.1 Balance of mass

The mass of a material body measures the gravitational force acting on it as well as the resistance of the body to changes in velocity. The balance of mass relation which states that the mass of any given material body remains constant is given by:

$$\dot{\mathrm{m}}\left(\mathfrak{B},t\right) \;=\; \frac{\mathrm{d}}{\mathrm{d}t}\int_V \rho_R\left(\boldsymbol{X},t\right)\,\mathrm{d}V \;=\; \frac{\mathrm{d}}{\mathrm{d}t}\int_v \rho\left(\boldsymbol{x},t\right)\,\mathrm{d}v \;=\; 0 \tag{2.18}$$

where $\rho_R,\ \rho$ are mass densities in the reference and current configurations. The relation in the current configuration is transferred to the reference configuration using eq. (2.7) to obtain a local form.

$$\begin{aligned}\dot{\mathrm{m}}\left(\mathfrak{B},t\right) \;&=\; \frac{\mathrm{d}}{\mathrm{d}t}\int_v \rho\left(\boldsymbol{x},t\right)\,\mathrm{d}v \;=\; \frac{\mathrm{d}}{\mathrm{d}t}\int_V \rho\,\det\mathbf{F}\,\mathrm{d}V\\ &=\; \int_V \left(\dot{\rho}\,\det\mathbf{F} \;+\; \rho\,\det\mathbf{F}\,\mathbf{F}^{-\mathrm{T}}\cdot\dot{\mathbf{F}}\right)\,\mathrm{d}V\\ &=\; \int_v (\dot{\rho} \;+\; \rho\,\mathrm{div}(\mathbf{v})\,)\,\mathrm{d}v \;=\; 0\end{aligned}$$

The local balance of mass relation is written as

$$\dot{\rho} \;+\; \rho\,\mathrm{div}(\mathbf{v}) \;=\; 0. \tag{2.19}$$

Since mass conservation requires $\rho_R \mathrm{d}V \;=\; \rho \mathrm{d}v$, eq. (2.7) is used to obtain the relation

$$\rho_R \;=\; (\det\mathbf{F})\,\rho \;=\; \mathrm{J}\,\rho. \tag{2.20}$$

2.2.2 Balance of momentum and angular momentum

The momentum of a material body is got from the product of the mass density and the velocity. The balance of momentum states that the time derivative of the material body's momentum is equal to the sum of all external forces acting on the body

$$\frac{\mathrm{d}}{\mathrm{d}t}\int_v \mathbf{v}\left(\boldsymbol{x},t\right)\;\rho\left(\boldsymbol{x},t\right)\;\mathrm{d}v \;=\; \int_a \mathbf{T}\left(\boldsymbol{x},t\right)\boldsymbol{n}\,\mathrm{d}a \;+\; \int_v \rho\left(\boldsymbol{x},t\right)\;\boldsymbol{k}\left(\boldsymbol{x},t\right)\;\mathrm{d}v. \tag{2.21}$$

With the rate of momentum on the left side of the relation, the terms on the right represent the external forces. The term $\mathbf{T}\left(\boldsymbol{x},t\right)$ is the Cauchy stress tensor with $\boldsymbol{n}$ being the normal vector to the area. The term $\rho\left(\boldsymbol{x},t\right)\boldsymbol{k}\left(\boldsymbol{x},t\right)$ represents the volume distributed force density acting on the material body, which

usually represents the gravitational forces. With the application of balance of mass $\rho_R \mathrm{d}V = \rho \mathrm{d}v$, the first term in eq. (2.21) becomes

$$\begin{aligned} \frac{\mathrm{d}}{\mathrm{d}t}\int_v \mathbf{v}\,\rho\,\mathrm{d}v = \frac{\mathrm{d}}{\mathrm{d}t}\int_V \mathbf{v}\,\rho\,\mathrm{J}\,\mathrm{d}V &= \int_V [\dot{\boldsymbol{v}}\,\rho + \mathbf{v}\,\dot{\rho} + \mathbf{v}\,\rho\,\mathrm{div}(\mathbf{v})]\,\mathrm{J}\,\mathrm{d}V \\ &= \int_v [\dot{\boldsymbol{v}}\,\rho + \mathbf{v}\,\dot{\rho} + \mathbf{v}\,\rho\,\mathrm{div}(\mathbf{v})]\,\mathrm{d}v \\ &= \int_v \rho\,\ddot{\boldsymbol{x}}\,\mathrm{d}v. \end{aligned} \tag{2.22}$$

Using the above relation and the divergence theorem in eq. (2.21), the final global and local forms for the balance of momentum in the current configuration is got as

$$\int_v [\mathrm{div}\,\mathbf{T} + \rho\,(\boldsymbol{k} - \ddot{\boldsymbol{x}})]\,\mathrm{d}v = 0 \tag{2.23}$$

$$\mathrm{div}\,\mathbf{T} + \rho\,(\boldsymbol{k} - \ddot{\boldsymbol{x}}) = 0, \tag{2.24}$$

and in the reference configuration as

$$\int_V [\mathrm{Div}\,\mathbf{T}_R + \rho_R\,(\boldsymbol{k}_R - \ddot{\boldsymbol{x}})]\,\mathrm{d}V = 0 \tag{2.25}$$

$$\mathrm{Div}\,\mathbf{T}_R + \rho_R\,(\boldsymbol{k}_R - \ddot{\boldsymbol{x}}) = 0, \tag{2.26}$$

where $\mathbf{T}_R$ is the *first Piola Kirchhoff* stress tensor which acts on the surface in the reference configuration.

2.2.2.1 Balance of angular momentum

According to the balance of angular momentum (moment of momentum), the temporal change of rotational momentum with respect to any fixed point in space equals the sum of external angular momentum due to forces operating on the material body. The local form of this relation together with the balance of mass and momentum leads to

$$\mathbf{T}^T = \mathbf{T} \tag{2.27}$$

which establishes the symmetry of the Cauchy stress tensor.

2.2.3 Balance of energy

From the balance of the mass and momentum, the concepts of *balance of mechanical power* and *energy* are derived. This implies that a mechanical process entails not only the interchange of force and motion but also the conversion of mechanical power and work into energy. According to the balance of mechanical power, the work done by a system of forces on the material is partially transformed into kinetic energy and the rest remains as *stress power*. Stress power holds the dimension

of power per unit mass and it constitutes the products of stresses and strain rates. Stress power stores a part of the work done by the stresses on strain rates in the material body and transforms the rest into non-mechanical energy. The latter process is known as dissipation, which either increases the non-mechanical energy content or dissipates it as heat. Thermodynamics aims at describing the energy transformations linked with mechanical processes. It proposes two main laws [43–46]. The *first law of thermodynamics* is the *balance of energy* which postulates the equivalence of mechanical and non-mechanical work. The *second law of thermodynamics* establishes essential boundaries for the conversion of thermal energy into mechanical work. Commonly known as the principle of *irreversibility*, the second law suggests that natural processes cannot be reversed without altering the environment of the considered material system.

The energy content of a material body is composed of *kinetic energy* E_{kin} and *internal energy* E_{int}. The internal energy of the material is given by the volume integral

$$E_{int} = \int_v \rho \; e \; \mathrm{d}v, \tag{2.28}$$

where e is the *specific internal energy* per unit mass. The kinetic energy E_{kin} is given by

$$E_{kin} = \int_v \frac{\rho}{2} \mathbf{v}^2 \mathrm{d}v. \tag{2.29}$$

Therefore, the total energy of the material body is given by the sum of internal energy and kinetic energy. The temporal change of this energy content arises from the power of external forces acting on the body

$$P_a \; = \; \int_a \mathbf{v} \cdot (\mathbf{T}\boldsymbol{n}) \; \mathrm{d}a \; + \; \int_v \rho \boldsymbol{k} \cdot \mathbf{v} \; \mathrm{d}v \tag{2.30}$$

and the non-mechanical energy exchange, i.e. Q, the heat flux given by

$$Q \; = \; \int_a q \; \mathrm{d}a \; + \int_v s \; \rho \; \mathrm{d}v \tag{2.31}$$

where, q represents the heat flux density and s denotes a volume distributed heat supply. Therefore the balance of energy is now written as

$$\frac{\mathrm{d}}{\mathrm{d}t}(E_{kin} \; + \; E_{int}) = \; P_a \; + \; Q. \tag{2.32}$$

With $q = -\boldsymbol{q} \cdot \boldsymbol{n}$ and the Cauchy heat flux vector $\boldsymbol{q}$, the global form of the energy balance in the current configuration is written as

$$\frac{\mathrm{d}}{\mathrm{d}t} \int_v \left(\frac{\mathbf{v}^2}{2} + \; e \; \right) \rho \mathrm{d}v = \int_v \rho \; (\boldsymbol{k} \cdot \mathbf{v} \; \; + \; s \;) \, \mathrm{d}v + \; \int_a \left[(\mathbf{T}^T \; \mathbf{v}) \cdot \boldsymbol{n} - \boldsymbol{q} \cdot \boldsymbol{n} \; \right] \mathrm{d}a. \tag{2.33}$$

By applying the product rule and the divergence theorem to the terms in surface integrals from the above relation, the relation $\mathrm{div}(\mathbf{T}^T \mathbf{v}) \; = (\mathrm{div}\mathbf{T}) \cdot \mathbf{v} + \mathbf{T} \cdot \mathrm{grad} \; \mathbf{v} = (\mathrm{div}\mathbf{T}) \cdot \mathbf{v} + \mathbf{T} \cdot \mathbf{L}$ is got. Since

$\mathbf{L} = \mathbf{D} + \mathbf{W}$, with $\mathbf{D} = \mathbf{D}^{\mathrm{T}}$ while $\mathbf{W} = -\mathbf{W}^{\mathrm{T}}$, it results in $\mathbf{T} \cdot \mathbf{W} = 0$. Thus, the spin tensor $\mathbf{W}$ does not contribute to the stress power and $\mathbf{T} \cdot \mathbf{L} = \mathbf{T} \cdot \mathbf{D}$. Furthermore, along with the help of eq. (2.27), the eq. (2.33) is simplified to

$$\int_v [\rho \dot{e} + \mathrm{div}\boldsymbol{q} - \rho\, s - \mathbf{T} \cdot \mathbf{D} - \underbrace{(\mathrm{div}\mathbf{T} + \rho \boldsymbol{k} - \rho \dot{\mathbf{v}})}_{\text{Balance of momentum}} \cdot \mathbf{v}] \mathrm{d}v = 0. \tag{2.34}$$

This can be simplified further using the balance of momentum eq. (2.23) to obtain the local form of the energy balance in the spatial representation

$$\dot{e} = \frac{1}{\rho} \mathbf{T} \cdot \mathbf{D} - \frac{1}{\rho} \mathrm{div}\, \boldsymbol{q} + s = 0. \tag{2.35}$$

Here the term $\mathbf{T} \cdot \mathbf{D}$ represents the stress power, which can also be represented using other types of stresses and strain rates. Using the weighted Cauchy stress tensor and eq. (2.20), eq. (2.35) becomes

$$\dot{e} = \frac{1}{\rho_R} \mathbf{S} \cdot \mathbf{D} - \frac{1}{\rho} \mathrm{div}\, \boldsymbol{q} + s = 0. \tag{2.36}$$

In the material representation, the local form for the balance of energy is given as

$$\dot{e} = \frac{1}{\rho_R} \tilde{\mathbf{T}} \cdot \dot{\mathbf{E}} - \frac{1}{\rho_R} \mathrm{Div}\, \boldsymbol{q}_R + s = 0. \tag{2.37}$$

2.2.4 Balance of entropy

The second law of thermodynamics is intimately linked to the fundamental notions of temperature and entropy. In continuum mechanics, there is a unique formulation for irreversibility called the *entropy inequality*, from which the *Clausius Duhem* inequality follows [39], which is based on the idea of using *entropy production* as a measure of thermomechanical process irreversibility. Entropy production is the difference between the change in entropy held by a body and the entropy absorbed by the body from its surroundings, known as *entropy supply*.

Entropy is an additive physical quantity that is present in every material body at all times and may be represented by a volume integral.

$$S(\mathfrak{B}, t) = \int_v \eta\, \rho \mathrm{d}v = \int_V \eta\, \rho_R \mathrm{d}V \tag{2.38}$$

where η represents *specific entropy* per unit mass. The idea of entropy supply is analogous to mechanical power or heat being an energy source. It is got from the sum of the integrands

$$H(\mathfrak{B}, t) = \int_a \zeta\, \mathrm{d}a + \int_v \varsigma\, \rho \mathrm{d}v \tag{2.39}$$

of surface-distributed entropy supply vector $\zeta = -\boldsymbol{\zeta} \cdot \boldsymbol{n}$ and volume-distributed entropy supply ς. Additionally, the term for entropy production within the body is introduced [35]

$$\Gamma(\mathfrak{B},t) = \int_v \gamma \rho \mathrm{d}v. \tag{2.40}$$

where γ is specific rate of entropy production.

The balance of entropy states that the temporal change of entropy is equal to the sum of entropy supply and entropy production [35] $\dot{S} = H + \Gamma$. As per the second law of thermodynamics, the entropy production is never negative. Therefore the entropy inequality

$$\Gamma = \dot{S} - H \geq 0 \tag{2.41}$$

is valid. Applying the *Gauß* theorem, it is possible to obtain the local formulation

$$\begin{aligned} \dot{\eta}(\boldsymbol{x},t) &= -\frac{1}{\rho} \operatorname{div} \boldsymbol{\zeta} + \varsigma + \gamma \\ \dot{\eta}(\boldsymbol{X},t) &= -\frac{1}{\rho_R} \operatorname{Div} \boldsymbol{\zeta}_R + \varsigma + \gamma \end{aligned} \tag{2.42}$$

in the spatial representation and material representation, respectively.
To substantiate the entropy supply in the formulation of entropy balance, the entropy supply is taken to be the quotient of the heat transport and absolute temperature. This is considered as a good approximation for processes close to equilibrium. Therefore, the surface- and volume-distributed entropy supply can be represented as

$$\boldsymbol{\zeta} = \frac{1}{\Theta} \boldsymbol{q}, \quad \varsigma = \frac{1}{\Theta} s. \tag{2.43}$$

where Θ represents absolute temperature. The *Clausius-Duhem* inequality is thus derived from the global form of the second law [35] as

$$\Gamma = \frac{\mathrm{d}}{\mathrm{d}t} \int_v \eta \, \rho \, \mathrm{d}v + \int_a \frac{\boldsymbol{q} \cdot \boldsymbol{n}}{\Theta} \, \mathrm{d}a - \int_v \frac{s}{\Theta} \, \rho \, \mathrm{d}v \geq 0, \tag{2.44}$$

which can also be expressed by the local formulation

$$\gamma = \dot{\eta} + \frac{1}{\rho \, \Theta} (\operatorname{div} \boldsymbol{q} - \rho s) - \frac{1}{\rho \, \Theta^2} \boldsymbol{q} \cdot \boldsymbol{g} \geq 0. \tag{2.45}$$

Here, $\boldsymbol{g}(\boldsymbol{x},t) = \operatorname{grad} \Theta(\boldsymbol{x},t)$ is the spatial temperature gradient. The free energy function is defined in terms of specific internal energy [35] as

$$\Psi = e - \Theta \, \eta \tag{2.46}$$

Employing the Balance of energy from eq. (2.35) and the eq. (2.46) the eq. (2.45) becomes

$$\Theta\,\gamma \;=\; -\,\dot{\Psi} \;-\; \dot{\Theta}\,\eta \;+\; \frac{1}{\rho}\,\mathbf{T}\cdot\mathbf{D} \;-\; \frac{\boldsymbol{q}}{\rho\,\Theta}\cdot\boldsymbol{g} \geq\; 0 \tag{2.47}$$

where the product $\delta \;=\; \Theta\,\gamma$ is called the *internal dissipation* ($\delta \geq 0$ for *dissipation*) and is equivalent to $\gamma \geq 0$

$$-\,\dot{\Psi} \;-\; \dot{\Theta}\,\eta \;+\; \frac{1}{\rho}\,\mathbf{T}\cdot\mathbf{D} \;-\; \frac{\boldsymbol{q}}{\rho\,\Theta}\cdot\boldsymbol{g} \geq\; 0. \tag{2.48}$$

Later, we'll use the Clausius-Duhem inequality to build a constitutive model that obeys the second law of thermodynamics in all processes and thus thermodynamically consistent a priori. In the case of a process that is isothermal $(\dot{\Theta} = 0)$ and with a uniform temperature distribution ($\boldsymbol{g} = 0$), the eq. (2.48) reduces to

$$\mathbf{T}\cdot\mathbf{D} \;-\; \rho\,\dot{\Psi} \;\geq\; 0. \tag{2.49}$$

Replacing $\mathbf{T}$ with the *weighted Cauchy* stress tensor $\mathbf{S}$ and with the help of eq. (2.20) the above relation can also be written as

$$\mathbf{S}\cdot\mathbf{D} \;-\; \rho_R\,\dot{\Psi} \geq\; 0. \tag{2.50}$$

2.3 Material theory

Finally, the third pillar of continuum mechanics, constitutive modeling, is discussed in this section. Among the concepts included is the principle of *material objectivity*, which is a prerequisite for constitutive relations. Then the concepts of finite strain framework, continuum damage mechanics, and thermodynamics of irreversible process are also discussed.

2.3.1 Objectivity

Objectivity refers to the invariance of physical quantities under superposed rigid body motions. Consistent with this requirement, the *principle of material objectivity* or *material frame-indifference* demands that constitutive equations be invariant with respect to changes of observer, ensuring that the predicted material response is frame-independent [35].

The mapping of position vectors representing the same point with respect to two different frames of reference is

$$\boldsymbol{x}^*(t^*) \;=\; \mathbf{Q}(t)\,\boldsymbol{x}(t) \;+\; \boldsymbol{c}(t), \quad t^* \;= t \;-\; a, \tag{2.51}$$

where t^* represents the time measured by the transformed observer. This transformation describes a time-dependent change of the observer and is known as the *Euclidean* transformation. The time t and spatial coordinates $\boldsymbol{x}$ of any arbitrary event in the primary coordinate system (unstarred) are moved into a second frame of reference (starred) system using the transformation in eq. (2.51). While $\mathbf{c}(t)$ represents the time-dependent translation of the origin, $\mathbf{Q}(t)$ is an orthogonal tensor ($\mathbf{QQ}^T = \mathbf{I}$) that defines a time-dependent rotation.

To verify the material objectivity of the constitutive equation, it is important to understand the behaviour of various quantities under transformation. Based on their behaviour, the quantities can be classified as objective and non-objective. Scalar (s), vector($\mathbf{v}$) and tensor ($\mathbf{T}$) quantities are objective if they obey the rules [35]

$$\begin{aligned} s^*(\mathcal{P},t^*) &= s(\mathcal{P},t), \\ \mathbf{v}^*(\mathcal{P},t^*) &= \mathbf{Q}(t)\,\mathbf{v}(\mathcal{P},t), \\ \mathbf{T}^*(\mathcal{P},t^*) &= \mathbf{Q}(t)\,\mathbf{T}(\mathcal{P},t)\,\mathbf{Q}^T(t). \end{aligned}$$

The objectivity of a quantity can either be established through its definition a priori or be evaluated based on the discussed rules. The transformation properties of some of the frequently used quantities such as

$$\begin{aligned} \mathrm{d}\boldsymbol{x}^* &= \mathbf{Q}\,d\boldsymbol{x}, & \mathrm{d}\boldsymbol{a}^* &= \mathbf{Q}\,d\boldsymbol{a}, & \mathrm{d}v^* &= \mathbf{Q}\,dv, \\ \mathbf{V}^* &= \mathbf{QVQ}^T, & \mathbf{B}^* &= \mathbf{QBQ}^T, & \mathbf{A}^* &= \mathbf{QAQ}^T, \\ \mathbf{D}^* &= \mathbf{QDQ}^T, & \mathbf{T}^* &= \mathbf{QTQ}^T, & \mathbf{S}^* &= \mathbf{QSQ}^T \end{aligned}$$

are objective, while others are non-objective and have special transformations:

$$\begin{aligned} \mathbf{F}^* &= \mathbf{QF}, & \mathbf{R}^* &= \mathbf{QR} & & \\ \mathbf{U}^* &= \mathbf{U}, & \mathbf{C}^* &= \mathbf{C}, & \mathbf{E}^* &= \mathbf{E}, \\ \tilde{\mathbf{T}}^* &= \tilde{\mathbf{T}}, & \mathbf{T}_R^* &= \mathbf{QT}_R, & & \\ \mathbf{L}^* &= \mathbf{QLQ}^T + \mathbf{QQ}^T, & \mathbf{W}^* &= \mathbf{QWQ}^T + \mathbf{QQ}^T. & & \end{aligned}$$

Under these conditions, the material objectivity of constitutive equations can be ensured if all constituting quantities are objective themselves and are related by functions that preserve objectivity.

2.3.1.1 Objective time derivatives of objective tensors

Material time derivatives of objective quantities are however not objective. To illustrate this, the transformation of the objective tensor $\mathbf{X}$ is considered:

$$\mathbf{X}^* = \mathbf{QXQ}^T, \tag{2.52}$$

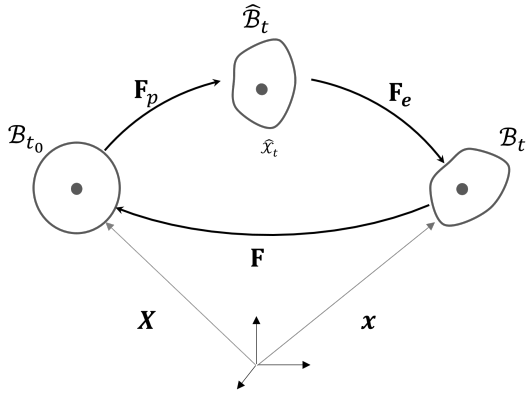

Figure 2.2: Finite strain framework.

and thus, its material time derivative is given by:

$$\dot{\mathbf{X}}^{*} = \mathbf{Q}\dot{\mathbf{X}}\mathbf{Q}^{T} + \dot{\mathbf{Q}}\mathbf{X}\mathbf{Q}^{T} + \mathbf{Q}\mathbf{X}\dot{\mathbf{Q}}^{T} \tag{2.53}$$

which is non-objective since it consists of terms $\dot{\mathbf{Q}}\mathbf{X}\mathbf{Q}^{T}$ and $\mathbf{Q}\mathbf{X}\dot{\mathbf{Q}}^{T}$. To circumvent this, the time derivatives of objective tensors are shown in Haupt [35] using the system of *Oldroyd* time derivative [47]

$$\overset{\triangle}{\mathbf{X}} = \dot{\mathbf{X}} + \mathbf{L}^{T}\,\mathbf{X} + \mathbf{X}\,\mathbf{L} \tag{2.54}$$

$$\overset{\triangledown}{\mathbf{X}} = \dot{\mathbf{X}} - \mathbf{L}\,\mathbf{X} - \mathbf{X}\,\mathbf{L}^{T} \tag{2.55}$$

has been used in this work, which can be reformulated to obtain the corotational or objective *Zaremba-Jaumann* derivative of $\mathbf{X}$

$$\overset{\triangledown}{\mathbf{X}} = \overset{\circ}{\mathbf{X}} - (\,\mathbf{D}\,\mathbf{X} + \mathbf{X}\,\mathbf{D}), \tag{2.56}$$

$$\overset{\triangle}{\mathbf{X}} = \overset{\circ}{\mathbf{X}} + \mathbf{D}\,\mathbf{X} + \mathbf{X}\,\mathbf{D}. \tag{2.57}$$

Here, the *Jaumann* derivative $\overset{\circ}{\mathbf{X}}$ is defined by

$$\overset{\circ}{\mathbf{X}} = \dot{\mathbf{X}} - \mathbf{W}\mathbf{X} + \mathbf{X}\mathbf{W}. \tag{2.58}$$

The concept of *dual variables* [2] provides further understanding on the type of tensors and tensor rates that should be used in constitutive equations and how they should be related, which is discussed in section 2.3.2.1.

2.3.2 Finite deformation

In the framework of finite deformation, the deformation gradient is subjected to multiplicative decomposition into its thermo-elastic and plastic parts as shown in fig. 2.2.

$$\mathbf{F} \;=\; \mathbf{F}_e\,\mathbf{F}_p \tag{2.59}$$

This decomposition introduces the *intermediate configuration*, $\hat{\mathcal{X}}_t$, which is typically regarded as locally stress-free and serves as the reference for elastic response. The concept of an intermediate configuration is related to the decomposition of total strain into components corresponding to different physical qualities (elastic, plastic). Haupt [35] describes the Intermediate configuration as an incompatible strain field which arises as a result of local unloading process. Or, the intermediate state of strain is the asymptotic limit of the material element's response to a given mechanical process, which is followed by a state of zero stress. Using the eq. (2.59) in eq. (2.2) we can obtain the following:

$$\mathrm{d}\boldsymbol{x} \;=\; \mathbf{F}_e\,\mathrm{d}\hat{\boldsymbol{x}} \quad , \quad \mathrm{d}\hat{\boldsymbol{x}} \;=\; \mathbf{F}_p\,\mathrm{d}\boldsymbol{X}, \tag{2.60}$$

$$\hat{\mathbf{L}}_p \;= \dot{\mathbf{F}}_p \mathbf{F}_p^{-1}, \tag{2.61}$$

$$\hat{\mathbf{D}}_p \;=\; \frac{1}{2}(\hat{\mathbf{L}}_p \;+\; \hat{\mathbf{L}}_p^{\,T}) \tag{2.62}$$

2.3.2.1 Dual Variables approach

Within continuum mechanics, definition of various measures of strain and stress tensors is possible. The *Dual Variables approach* introduced by Haupt and Tsakmakis [2] proposes the guidelines for the selection of strain tensor and it's best associated stress tensor, with the type of time derivatives which can properly describe their evolution. It states:

"*The basic property of dual variables and derivatives is that both the stress power and the incremental stress power have invariance properties with respect to a group of transformations, which corresponds to a set of physically reasonable intermediate configurations.*"

Furthermore, starting with a scalar value defined as form invariant with respect to a desired configuration, we may obtain the associated strain and stress measures along with their appropriate time derivatives. Therefore, we consider the following scalar value to be a difference of the square of the line segments from the reference and actual configurations.

$$\triangle \;= \frac{1}{2}(\mathrm{d}\boldsymbol{x}\cdot\mathrm{d}\boldsymbol{x} \;-\; \mathrm{d}\boldsymbol{X}\cdot\mathrm{d}\boldsymbol{X}) \tag{2.63}$$

and the stress power per unit volume in the current configuration from eq. (2.36) is given as

$$W \;=\; \mathbf{S}\cdot\mathbf{D} \tag{2.64}$$

where $\mathbf{S}$ is the *weighted Cauchy stress tensor*. Stress power is formed as the inner product of a convenient deformation rate and a corresponding stress tensor. We call stress and strain tensors which are naturally associated in this way as conjugate variables. Here again, the cumulative decomposition of the scalar value leads to the following relations

$$\triangle \;=\; \triangle_e \;+\; \triangle_p, \quad \triangle_e \;=\frac{1}{2}(\mathrm{d}\boldsymbol{x}\cdot\mathrm{d}\boldsymbol{x} \;-\mathrm{d}\hat{\boldsymbol{x}}\cdot\mathrm{d}\hat{\boldsymbol{x}}), \quad \triangle_p \;=\frac{1}{2}(\mathrm{d}\hat{\boldsymbol{x}}\cdot\mathrm{d}\hat{\boldsymbol{x}}-\mathrm{d}\boldsymbol{X}\cdot\mathrm{d}\boldsymbol{X}) \tag{2.65}$$

$$\begin{aligned}
\triangle &= \mathrm{d}\boldsymbol{X}\cdot\mathbf{E}\,\mathrm{d}\boldsymbol{X} &&= \mathrm{d}\hat{\boldsymbol{x}}\cdot\hat{\boldsymbol{\Gamma}}\,\mathrm{d}\hat{\boldsymbol{X}} &&= \mathrm{d}\boldsymbol{x}\cdot\mathbf{A}\,\mathrm{d}\boldsymbol{X}, && (2.66)\\
\triangle_e &= \mathrm{d}\boldsymbol{X}\cdot\mathbf{E}_e\,\mathrm{d}\boldsymbol{x} &&= \mathrm{d}\hat{\boldsymbol{x}}\cdot\hat{\boldsymbol{\Gamma}}_e\,\mathrm{d}\hat{\boldsymbol{x}} &&= \mathrm{d}\boldsymbol{x}\cdot\mathbf{A}_e\,\mathrm{d}\boldsymbol{x}, && (2.67)\\
\triangle_p &= \mathrm{d}\boldsymbol{X}\cdot\mathbf{E}_p\,\mathrm{d}\boldsymbol{x} &&= \mathrm{d}\hat{\boldsymbol{x}}\cdot\hat{\boldsymbol{\Gamma}}_p\,\mathrm{d}\hat{\boldsymbol{x}} &&= \mathrm{d}\boldsymbol{x}\cdot\mathbf{A}_p\,\mathrm{d}\boldsymbol{x} && (2.68)
\end{aligned}$$

therefore

$$\mathbf{E}_e \;=\; \frac{1}{2}\big(\mathbf{F}^T\,\mathbf{F} \;-\mathbf{F}_p^T\,\mathbf{F}_p\big)\;, \quad \mathbf{E}_p \;=\; \frac{1}{2}\big(\mathbf{F}_p^T\,\mathbf{F}_p \;-\;1\big)\;, \quad \mathbf{E} \;=\; \mathbf{E}_e \;+\; \mathbf{E}_p \tag{2.69}$$

$$\hat{\boldsymbol{\Gamma}}_e \;=\; \mathbf{F}_p^{-T}\,\mathbf{E}_e\,\mathbf{F}_p^{-1} \qquad , \quad \hat{\boldsymbol{\Gamma}}_p \;=\; \mathbf{F}_p^{-T}\,\mathbf{E}_p\,\mathbf{F}_p^{-1} \quad , \quad \hat{\boldsymbol{\Gamma}} \;=\; \hat{\boldsymbol{\Gamma}}_e \;+\; \hat{\boldsymbol{\Gamma}}_p \tag{2.70}$$

$$\mathbf{A}_e \;=\; \mathbf{F}_e^{-T}\,\hat{\boldsymbol{\Gamma}}_e\,\mathbf{F}_e^{-1} \qquad , \quad \mathbf{A}_p \;=\; \mathbf{F}_e^{-T}\,\hat{\boldsymbol{\Gamma}}_p\,\mathbf{F}_e^{-1} \quad , \quad \mathbf{A} \;=\; \mathbf{A}_e \;+\; \mathbf{A}_p \tag{2.71}$$

where $\mathbf{E}$ is the *Green Lagrange strain tensor* from the reference configuration $\mathcal{X}_{t_0}$ and $\mathbf{A}$ is the *Almansi strain tensor* from the actual or current configuration $\mathcal{X}_t$. $\hat{\boldsymbol{\Gamma}}$ is the strain tensor, which is obtained by the transformation of strain from $\mathcal{X}_{t_0}$ onto the intermediate configuration $\hat{\mathcal{X}}_t$. The time derivatives of the scalar quantities may be devised as

$$\begin{aligned}
\dot{\triangle} &= \mathrm{d}\boldsymbol{X}\cdot\dot{\mathbf{E}}\,\mathrm{d}\boldsymbol{x} &&= \mathrm{d}\hat{\boldsymbol{x}}\cdot\overset{\triangle}{\hat{\boldsymbol{\Gamma}}}\,\mathrm{d}\hat{\boldsymbol{x}} &&= \mathrm{d}\boldsymbol{x}\cdot\overset{\triangle}{\mathbf{A}}\,\mathrm{d}\boldsymbol{x}, && (2.72)\\
\dot{\triangle}_e &= \mathrm{d}\boldsymbol{X}\cdot\dot{\mathbf{E}}_e\,\mathrm{d}\boldsymbol{x} &&= \mathrm{d}\hat{\boldsymbol{x}}\cdot\overset{\triangle}{\hat{\boldsymbol{\Gamma}}}_e\,\mathrm{d}\hat{\boldsymbol{x}} &&= \mathrm{d}\boldsymbol{x}\cdot\overset{\triangle}{\mathbf{A}}_e\,\mathrm{d}\boldsymbol{x}, && (2.73)\\
\dot{\triangle}_p &= \mathrm{d}\boldsymbol{X}\cdot\dot{\boldsymbol{\varepsilon}}_{in}\,\mathrm{d}\boldsymbol{X} &&= \mathrm{d}\hat{\boldsymbol{x}}\cdot\overset{\triangle}{\hat{\boldsymbol{\Gamma}}}_p\,\mathrm{d}\hat{\boldsymbol{X}} &&= \mathrm{d}\boldsymbol{x}\cdot\overset{\triangle}{\mathbf{A}}_p\,\mathrm{d}\boldsymbol{X} && (2.74)
\end{aligned}$$

which suggests that the strain rates are material time derivatives in the reference configuration, but *lower Oldroyd time derivatives* for the other configurations.

$$\begin{aligned}
()^{\triangle} &= ()^{\cdot} + \hat{\mathbf{L}}_p^T\,()+\,()\,\hat{\mathbf{L}}_p \quad \text{for} \quad \hat{\mathcal{X}}_t, && (2.75)\\
()^{\triangle} &= ()^{\cdot} + \mathbf{L}_p^T\,()+\,()\,\mathbf{L}_p \quad \text{for} \quad \mathcal{X}_t && (2.76)
\end{aligned}$$

Therefore, the following relationships are also valid

$$\overset{\triangle}{\mathbf{A}} \;=\; \dot{\mathbf{A}} \;+\; \mathbf{L}^T\,\mathbf{A} \;+\; \mathbf{A}\,\mathbf{L} \quad \;=\mathbf{D}, \tag{2.77}$$

$$\overset{\triangle}{\hat{\mathbf{\Gamma}}}_p = \dot{\hat{\mathbf{\Gamma}}}_p + \hat{\mathbf{L}}^T \hat{\mathbf{\Gamma}}_p + \hat{\mathbf{\Gamma}}_p \hat{\mathbf{L}} = \hat{\mathbf{D}}_p. \tag{2.78}$$

The stress tensor with respect to $\mathcal{X}_t$ is the weighted *Cauchy stress* $\mathbf{S}$, while *Second Piola-Kirchoff stress* $\tilde{\mathbf{T}}$ acts in $\mathcal{X}_{t_0}$. Therefore, we have $\hat{\mathbf{T}}$ with respect to intermediate configuration $\hat{\mathcal{X}}_t$, which is related to the other stress tensors through the pull-back operations

$$\tilde{\mathbf{T}} = \mathbf{F}^{-1}\,\mathbf{S}\,\mathbf{F}^{-T}, \tag{2.79}$$

$$\hat{\mathbf{T}} = \mathbf{F}_e^{-1}\,\mathbf{S}\,\mathbf{F}_e^{-T}. \tag{2.80}$$

Therefore, a variety of formulations for stress power exists.

$$W = \mathbf{S}\cdot\mathbf{D} = \hat{\mathbf{T}}\cdot\overset{\triangle}{\hat{\mathbf{\Gamma}}} = \tilde{\mathbf{T}}\cdot\dot{\mathbf{E}} \tag{2.81}$$

Frame invariance of $\dot{W}, \ddot{W}...$ allows the material time derivatives in the reference configuration $\mathcal{X}_{t_0}$ and the *upper Oldroyd* time derivatives to be derived as corresponding stress rates

$$()^{\triangledown} = ()^{\cdot} - \hat{\mathbf{L}}_p\,() - ()\,\hat{\mathbf{L}}_p^T \quad \text{for} \quad \hat{\mathcal{X}}_t, \tag{2.82}$$

$$()^{\triangledown} = ()^{\cdot} - \mathbf{L}_p\,() - ()\,\mathbf{L}_p^T \quad \text{for} \quad \mathcal{X}_t. \tag{2.83}$$

2.3.3 Continuum damage mechanics

In Lemaitre and Desmorat [48], damage in solid materials is defined as the formation and propagation of microvoids or microcracks. Although these are discontinuities in a medium, on a larger scale, they are taken to be continuous. The concept of Representative Volume Element (RVE) is introduced by mechanics into engineering, where all the properties of the RVE are represented by homogenized variables. From a physical point of view, damage is always related to plastic or irreversible strains and more generally to a strain dissipation either on the mesoscale, the scale of the RVE, or on the microscale.

At mesolevel, if the damage is due to the nucleation and growth of cavities under static loadings, it is termed as ductile damage. If it occurs after repeated loadings at high amplitudes, it is known as low cycle fatigue damage. And lastly, it is known as creep damage if it occurs at elevated temperatures. At microlevel, the damage under monotonic loading is known as brittle failure or quasi-brittle damage. When loading involves a large number of cyclic load, it is termed as high cycle fatigue damage. Damage may occur as volume defects (microcavities) or as surface defects (microcracks), which necessitates different definitions of a damage variable. In case of a ductile damage, it is defined as the volume density or volume fraction of the micro-voids, which is also the basis for the Gurson [49] model. The damage variable is given by

$$d_v = \frac{\delta V_{voids}}{\delta V_{RVE}} \tag{2.84}$$

In a more general case, the surface density of microcracks and intersections of microvoids lying on a plane slicing the RVE cross section $\delta\mathcal{S}$ is used to define the damage variable. For the plane with the normal $\boldsymbol{n}$, the damage variable is

$$d_{\boldsymbol{n}} = \frac{\delta\mathcal{S}_d}{\delta\mathcal{S}}. \tag{2.85}$$

If the damage is taken to be isotropic, eq. (2.84) is independent of $\boldsymbol{n}$ and thereby reducing the damage variable to a scalar. But often damage is non-isotropic since microcracking is perpendicular to the largest principal stress and the damage variable is described as a tensor $\mathbf{d}$ that transforms the microvoid density from surface $\delta\mathcal{S}$ with normal $\boldsymbol{n}$ to a surface $\delta\tilde{\mathcal{S}} = \delta\mathcal{S} - \delta\mathcal{S}_d$ with normal $\tilde{\boldsymbol{n}}$ through the relation

$$(\mathbf{I} - \mathbf{d})\,\boldsymbol{n}\;\delta\mathcal{S} = \tilde{\boldsymbol{n}}_i\;\delta\tilde{\mathcal{S}}. \tag{2.86}$$

In the current work, damage is assumed to be isotropic. From hereon, the discussions regarding damage will be limited to the isotropic case.

The constitutive equations for strain and damage define the plain material as being free from volume and surface discontinuities. Constitutive equations for strain and damage introduce the concept of effective stress based on the stress acting on the area that offers resistance. The mean value of the micro-stresses is simply given by the force equilibrium $\tilde{\boldsymbol{\sigma}}\;\delta\tilde{\mathcal{S}} = \boldsymbol{\sigma}\;\delta\mathcal{S}$. With the help of eq. (2.85), the effective stress is

$$\tilde{\boldsymbol{\sigma}} = \frac{\boldsymbol{\sigma}}{1-d}\,. \tag{2.87}$$

2.3.4 Thermodynamics of viscoplasticity coupled with damage

The thermodynamics of an irreversible process facilitates the modeling of various material behaviour including deformation and damage. This general framework described in Lemaitre and Desmorat [48], is briefly discussed here. This framework permits the definition of *state variables, state potentials* and *dissipation potentials*. The state variables describe the current state of the described mechanism, and are chosen based on observed deformation and damage mechanisms of the material. A list of relevant state variables are shown in table 2.1 [16]. In small-strain plasticity, the general measure of strain $\boldsymbol{\varepsilon}$ is decomposed into elastic and plastic components.

$$\boldsymbol{\varepsilon} = \boldsymbol{\varepsilon}_e + \boldsymbol{\varepsilon}_p \tag{2.88}$$

From state potentials, the state laws and conjugate variables of state variables are derived. The Helmholtz specific free energy function Ψ (2.46) is chosen to be the material's state potential and a function of all state variables. For an isothermal case, Ψ is decomposed into elastic Ψ_e and plastic

Mechanism	Type	State variables	Conjugate
Elasticity	Tensor	$\boldsymbol{\varepsilon}$	$\boldsymbol{\sigma}$
Plastic strain	Tensor	$\boldsymbol{\varepsilon}_p$	$-\boldsymbol{\sigma}$
Kinematic hardening	Tensor	$\boldsymbol{\alpha}$	$\boldsymbol{\Omega}$
Isotropic softening	Scalar	r	$\mathcal{R}$
Damage	Scalar	d	$-Y$

Table 2.1: General set of state variables and their conjugates [16].

Ψ_p components. Therefore, the entropy inequality becomes

$$\frac{1}{\rho}\boldsymbol{\sigma}\cdot\dot{\boldsymbol{\varepsilon}}-\dot{\Psi}=\frac{1}{\rho}\boldsymbol{\sigma}\cdot\dot{\boldsymbol{\varepsilon}}_e-\dot{\Psi}_e+\frac{1}{\rho}\boldsymbol{\sigma}\cdot\dot{\boldsymbol{\varepsilon}}_p-\dot{\Psi}_p \tag{2.89}$$

Ψ_e describes the coupling of elasticity and damage through the effective stress concept $\tilde{\boldsymbol{\sigma}}$ which establishes that the strain of a damaged material and a non-damaged material is derived in a similar manner and only requires the stress to be replaced with the effective stress (principle of strain equivalence). Component Ψ_p represents plastic hardening with $w_s=\rho\Psi_p$ describing the energy stored in the RVE due to the plastic deformation. The state law derived from the state potential is essentially the law of elasticity

$$\boldsymbol{\varepsilon}=\rho\frac{\partial\Psi}{\partial\boldsymbol{\sigma}}=\rho\frac{\partial\Psi_e}{\partial\boldsymbol{\sigma}}+\boldsymbol{\varepsilon}_p \quad\rightarrow\quad \boldsymbol{\varepsilon}_e=\rho\frac{\partial\Psi_e}{\partial\boldsymbol{\sigma}}. \tag{2.90}$$

The conjugate of state variables are the other derivatives

$$\mathcal{R}=-\rho\frac{\partial\Psi}{\partial r},\quad \boldsymbol{\Omega}=-\rho\frac{\partial\Psi}{\partial\boldsymbol{\alpha}},\quad -Y=-\rho\frac{\partial\Psi}{\partial d}. \tag{2.91}$$

The Clausius-Duhem inequality is fulfilled for positive damage rate:

$$\boldsymbol{\sigma}\cdot\dot{\boldsymbol{\varepsilon}}_p+Y\dot{d}-\dot{w}_s\geq 0 \tag{2.92}$$

which indicates that the sum of the dissipation due to plastic power ($\boldsymbol{\sigma}\cdot\dot{\boldsymbol{\varepsilon}}_p$) and damage ($Y\dot{d}$) minus the stored energy rate ($\dot{w}_s=\mathcal{R}\dot{r}+\boldsymbol{\Omega}\cdot\dot{\boldsymbol{\alpha}}$) is transformed into heat. Lastly, the dissipation potential (F) is used to define the evolution laws of state variables based on the appropriate dissipation mechanisms. F is a convex function of conjugate variables to ensure the inequality (2.92):

$$F=F(\boldsymbol{\sigma},\boldsymbol{\Omega},\mathcal{R},Y;d)=F_y+F_{\boldsymbol{\Omega}}+F_{\mathcal{R}}+F_d \tag{2.93}$$

with damage d allowed to only act as a parameter. Here, the terms plastic yield function (F_y), and dissipation potentials of kinematic hardening ($F_{\boldsymbol{\Omega}}$), isotropic softening ($F_{\mathcal{R}}$) and the damage (F_d) are

introduced, based on which the evolution laws are framed as

$$\dot{\boldsymbol{\varepsilon}}_p = -\dot{\lambda}_y \frac{\partial F_y}{\partial(-\boldsymbol{\sigma})}, \quad \dot{\boldsymbol{\alpha}} = -\dot{\lambda}_{\boldsymbol{\Omega}} \frac{\partial F_{\boldsymbol{\Omega}}}{\partial(-\boldsymbol{\Omega})}, \quad \dot{r} = -\dot{\lambda}_{\mathcal{R}} \frac{\partial F_{\mathcal{R}}}{\partial \mathcal{R}}, \quad \dot{d} = -\dot{\lambda}_d \frac{\partial F_d}{\partial(-Y)} \tag{2.94}$$

which are collectively referred to as the *normality rule*. Based on F, the theories of time-independent plasticity and time-dependent viscoplasticity are classified and their respective consistency conditions are defined. The terms $\dot{\lambda}_y$, $\dot{\lambda}_{\boldsymbol{\Omega}}$, $\dot{\lambda}_{\mathcal{R}}$, $\dot{\lambda}_d$ are scalar multipliers which determine the magnitude of the corresponding state variables' time derivative. The first relation in eq. (2.94) is the *associated flow rule*, and establishes that the direction of $\dot{\boldsymbol{\varepsilon}}_p$ to be normal to the yield surface defined by F_y and its magnitude is determined by $\dot{\lambda}_y$ [50]. It is a non-negative, scalar term which needs to be identified from the consistency conditions of the respective classification of plasticity. Under the precondition that hardening and damage evolution is driven by $\boldsymbol{\varepsilon}_p$ [16], the following simplification for λ and eq. (2.94) can be made

$$\begin{aligned} &\dot{\lambda}_y = \dot{\lambda}_{\boldsymbol{\Omega}} = \dot{\lambda}_{\mathcal{R}} = \dot{\lambda}_d = \dot{\lambda} \\ \Rightarrow\ &\dot{\boldsymbol{\varepsilon}}_p = -\dot{\lambda} \frac{\partial F_y}{\partial(-\boldsymbol{\sigma})}, \quad \dot{\boldsymbol{\alpha}} = -\dot{\lambda} \frac{\partial F_{\boldsymbol{\Omega}}}{\partial(-\boldsymbol{\Omega})}, \quad \dot{r} = -\dot{\lambda} \frac{\partial F_{\mathcal{R}}}{\partial \mathcal{R}}, \quad \dot{d} = -\dot{\lambda} \frac{\partial F_d}{\partial(-Y)}. \end{aligned} \tag{2.95}$$

In time-independent plasticity, F is not differentiable and $\dot{\lambda}$ can be got from the plasticity consistency conditions: a) $F_y = 0$ indicates that the stress state fulfills the yield criterion and b) $\dot{F}_y = 0$ states that the yield stress only increases with increasing state of hardening. In case of elastic unloading, $F_y < 0$, $\dot{F}_y < 0$ is valid and the state variables remain unchanged. On the other hand, for viscoplasticity the yield criterion follows $F_y \geq 0$ which allows the strain-rate dependent material behaviour to be described. Here, $\dot{\lambda}(F_y)$ is the known as the viscosity function. Furthermore, according to Haupt [35], the theory of viscoplasticity uses an inelastic strain $\boldsymbol{\varepsilon}_{in}$ in place of $\boldsymbol{\varepsilon}_p$. The associated accumulated plastic strain rate ($\dot{p}$) is defined based on the considered yield criterion. For a criterion based on von-Mises, it is given as

$$\dot{p} = \sqrt{\frac{2}{3}\, \dot{\boldsymbol{\varepsilon}}_p \cdot \dot{\boldsymbol{\varepsilon}}_p}. \tag{2.96}$$

Damage begins on a meso or microscale only once the plastic strain exceeds a threshold, which is linked to the energy required for defect development, according to experimental research. Because this energy comes from stored energy (w_d), the threshold is affected by the material and the type of loading. This allows the loading dependency of the damage threshold to be expressed in terms of accumulated plastic strain. When the density of defects reaches a critical value at which the process of localization and instability develops, $d = d_c$ in the plane where damage is maximal, a mesocrack is initiated. Here, d_c is a material parameter for critical damage.

2.3.4.1 Modelling coupled viscoplasticity and damage

Within the thermodynamic approach, based on experimental findings the dissipation potentials of plasticity and damage evolution are defined to be a non-linear function of their respective conjugate variables. The influence of plastic strain on the evolution of state variables is described through the inclusion of ($\dot{\lambda}$) as shown in eq. (2.95). Constitutive relations of viscoplasticity coupled with damage are derived from the dissipation potential function F (2.93). $\dot{\lambda}$ needs to be derived from these relations. The yield criterion (F_y) define the elastic limit of the material by $F_y < 0$, and differentiate the plastic and viscoplastic theories by the consistency conditions

$$F_y = 0,\ \dot{F}_y = 0 \qquad \text{plasticity} \tag{2.97}$$

$$F_y = \sigma_{vis} > 0 \qquad \text{visco-plasticity} \tag{2.98}$$

respectively, with the term σ_{vis} being the viscous stress describing the viscosity, but $\sigma_{vis} = 0$ for plasticity. Considering kinematic and isotropic hardening, the viscoplastic yield function F_y is given by the von Mises criterion using the effective stress $\tilde{\boldsymbol{\sigma}} = \boldsymbol{\sigma}/(1-d)$

$$F_y = (\tilde{\boldsymbol{\sigma}} - \boldsymbol{\Omega})_{eq} - R - k \tag{2.99}$$

with k representing the yield stress. Here, $(\tilde{\boldsymbol{\sigma}} - \boldsymbol{\Omega})_{eq}$ is the von Mises equivalent of the over stress tensor given by $\tilde{\boldsymbol{\sigma}} - \boldsymbol{\Omega}$. Applying the normality rule (2.95) and (2.93), the flow rule and the inelastic strain rate is derived as

$$\dot{\boldsymbol{\varepsilon}}_{in} = \dot{\lambda}\ \frac{\partial F_y}{\partial \boldsymbol{\sigma}} = \frac{\dot{\lambda}}{1-d}\ \frac{3}{2}\ \frac{\tilde{\boldsymbol{\sigma}}^D - \boldsymbol{\Omega}}{(\tilde{\boldsymbol{\sigma}} - \boldsymbol{\Omega})_{eq}} \tag{2.100}$$

with the accumulated plastic strain rate leading to

$$\dot{p} = \frac{\dot{\lambda}}{1-d}\,. \tag{2.101}$$

The viscosity function $\dot{\lambda}$, is given by the Norton power law

$$\sigma_{vis} = K\ \dot{p}^{\frac{1}{n}} \quad \text{or} \quad \dot{p} = \left(\frac{F_y}{K}\right)^n \tag{2.102}$$

where K, n are viscous material parameters. The viscosity offers a regularizing effect on deformation and damage.

2.4 Constitutive models

In section 2.3.4.1, the general framework for modeling material behaviour using viscoplasticity and damage models has been established. Various models can be defined within this framework based on the choice of the viscoplastic yield function and dissipation potentials of the necessary state variables. In this section, the constitutive models of viscoplasticity and damage chosen to describe the material behaviour of ferritic-martensitic steels in an unirradiated and an irradiated condition are discussed. The Aktaa and Petersen [1] model is capable of describing the deformation of irradiated materials using the irradiation defect density as an internal state variable, which can return the instantaneous irradiation hardening based on the level of irradiation damage and plastic deformation of the material. The models to describe the material damage arising out of fatigue damage and ductile damage are also discussed. In later sections, these models are unified such that the unified model can successfully describe the material behaviour observed under tensile loading.

2.4.1 Viscoplastic deformation model

In this work, the deformation model by Aktaa and Petersen [1] which is based on the unified Chaboche viscoplastic constitutive system of equations has been used. This is a small strain model and has been shown to be capable of describing cyclic plasticity arising from low cycle fatigue in unirradiated and irradiated materials. The salient features of the model includes the use of irradiation defect density to model the irradiation induced material changes and a dimensionless isotropic softening variable. Differing from contemporary hardening laws where the isotropic hardening/softening gives as an absolute measure of the change in the size of yield surface, the dimensionless variable used in the discussed model represents the factor by which the yield surface shrinks under cyclic softening. The isotopic softening variable is combined with the stress tensor in the calculation of the over stress tensor that is introduced in the flow rule. This novel approach allows the model to describe the experimentally observed reduction in the rate-dependent behaviour of the material during the development of fatigue damage [17].

The model formulation begins with the viscoplastic yield potential, which is chosen to be

$$F_y = \quad \Sigma_{eq} \; - \; k - \; \sigma_H \geq 0 \tag{2.103}$$

with k and σ_H representing the initial yield stress of the material and the irradiation hardening, respectively. Σ_{eq} is the von Mises equivalent of the over stress tensor, $\boldsymbol{\Sigma}$

$$\Sigma_{eq} \quad = \quad \sqrt{\frac{3}{2}\boldsymbol{\Sigma} : \boldsymbol{\Sigma}} \tag{2.104}$$

which provides a measure of the material deformation and allows the eq. (2.103) to determine if the material is undergoing inelastic deformation. $\boldsymbol{\Sigma}$ is constructed using the stress tensor $\boldsymbol{\sigma}$, back stress

tensor $\boldsymbol{\Omega}$, isotropic softening variable ψ and the damage variable d as

$$\boldsymbol{\Sigma} = \frac{\boldsymbol{\sigma}^D}{\psi(1-d)} - \boldsymbol{\Omega}, \tag{2.105}$$

$$\text{with} \quad \psi = \psi_1 + \psi_2, \tag{2.106}$$

$$\text{and} \quad \boldsymbol{\sigma}^D = \boldsymbol{\sigma} - \frac{1}{3}\,\sigma_{kk}\,\mathbf{I} \tag{2.107}$$

where, $\boldsymbol{\sigma}^D$ is the deviatoric part of the stress tensor and ψ_1, ψ_2 are components of ψ. The *flow rule* and the inelastic strain rate of the model is derived by applying the normality rule (2.100) and eqs. (2.101) and (2.102) on the viscoplastic yield potential (2.103)

$$\dot{\boldsymbol{\varepsilon}}_{in} = \dot{\lambda}\frac{\partial F_y}{\partial \boldsymbol{\sigma}} = \frac{3}{2}\left\langle \frac{\Sigma_{eq} - k - \sigma_H}{K} \right\rangle^n \frac{\boldsymbol{\Sigma}}{\Sigma_{eq}} \tag{2.108}$$

with the accumulated plastic strain rate being described using the relation

$$\dot{p} = \sqrt{\frac{2}{3}\,\dot{\boldsymbol{\varepsilon}}_{in} : \dot{\boldsymbol{\varepsilon}}_{in}} \quad \text{or} \quad \dot{p} = \left\langle \frac{\Sigma_{eq} - k - \sigma_H}{K} \right\rangle^n. \tag{2.109}$$

The evolution of kinematic hardening variable $\boldsymbol{\Omega}$ follows the Chaboche [51] model which was developed from the original Frederick and Armstrong [52] model to account for strain rate effects and given by

$$\dot{\boldsymbol{\Omega}} = H\,\dot{\boldsymbol{\varepsilon}}_{in} - C\,\dot{p}\,\boldsymbol{\Omega} - R\,|\boldsymbol{\Omega}|^{m-1}\boldsymbol{\Omega} \tag{2.110}$$

with temperature and material dependent parameters H, C, R, m. Here, $|\boldsymbol{\Omega}|$ is the Euclidean norm of the tensor $\boldsymbol{\Omega}$. The isotropic softening variable ψ is used to model the cyclic softening of the material. It must have an initial value of 1 at the onset of inelastic deformation, which signifies no material softening.

$$\psi = 1 \quad \text{at} \quad \mathrm{t} = 0 \tag{2.111}$$

ψ is described by its sub-variables ψ_1, ψ_2, described by the evolution equations [17]

$$\dot{\psi}_1 = -h\dot{p}, \tag{2.112}$$

$$\dot{\psi}_2 = c\,(\psi_s - \psi_2)\,\dot{p} - r_\psi\,|\psi_2 - \psi_r|^{m_\psi - 1}\,(\psi_2 - \psi_r). \tag{2.113}$$

Here, ψ_s describes the increase of the cyclic softening capacity of the material, which is driven by increasing amplitude of inelastic strain

$$\psi_s = 1 - \psi_{s,\infty}\left(1 - exp\left\{-c_s \max_{-\infty<\tau<t} \varepsilon_{in,eq}(\tau)\right\}\right). \tag{2.114}$$

Here, the temperature and material dependent model parameters are h, c, r_ψ, ψ_r and m_ψ. The last terms in eqs. (2.110) and (2.113) of the kinematic hardening and the isotropic softening models respectively account for static recoveries which are observed under creep, relaxation or cyclic loading with hold time.

The irradiation influenced material changes are described using the irradiation defect density variable, N [53], whose evolution for "i" types of defects is given by

$$\dot{N}_i \;=\; a_i\,(N_{s,i} \;-\; N_i)\,\dot{\phi} -\; b_i\left(N_i - N_{l,i}\right)\dot{p} -\; r_{\mathrm{N,i}}\,N_i^{q_{\mathrm{N,i}}}. \tag{2.115}$$

Here, the first term accounts for the increase in irradiation induced defect density and thus hardening as a result of irradiation, and hence is driven by the irradiation dose rate $\dot{\phi}$. The second term accounts for the recombination of defects and thus softening brought about by inelastic deformation and thus is plasticity driven. The third term accounts for the annealing of irradiation induced defects at high temperatures as observed in heat treatment over a period of time. Here $N_{s,i}$ represents the saturation value of defect density while $N_{l,i}$ refers to the amount of defects cleared by plastic deformation

$$N_{l,i} \;=\; \left\langle \sqrt{\max_{-\infty<\tau<t} |N_i(\tau)|} - \sqrt{N_{r,i}} \right\rangle^2. \tag{2.116}$$

The model has $a_i,\ b_i,\ r_{\mathrm{N,i}},\ q_{\mathrm{N,i}}$ and $N_{r,i}$ as other temperature and material dependent model parameters. Finally, the instantaneous measure of irradiation hardening is calculated from N using the *Dispersed Barrier Hardening* (DBH) model [54]

$$\sigma_H = \sum_i^{n_H} \sigma_{H,i} \quad \text{with} \quad \sigma_{H,i} = h_{N,i}\sqrt{N_i}, \tag{2.117}$$

where $h_{N,i}$ describes the temperature dependent strength of the dislocation pileup associated with defect type i.

2.4.2 Ductile damage

In both metals and polymers, ductile damage is essentially due to the nucleation, growth, and coalescence of voids. Void nucleation is attributed to de-cohesion or fracture of inclusions in the matrix material [55]. The ratio of hydrostatic to equivalent stress, also known as the triaxiality factor (TF) of the stress, has big impact on void growth. As loading continues, voids grow and coalesce due to shearing between nearby voids. Coalescence accelerates the specimen's overall ductile damage, resulting in a macroscopic ductile crack and ultimately failure. Continuum Damage Mechanics

treats this as a reduction in the area resisting deformation in any plane of a Representative Volume Element (RVE), driven by elastic energy and accumulated plastic strain. On the other hand, from a micromechanical perspective, it is the formation of a spherical or elliptic hole in a plastic media that is subjected to enormous strains. Large deformations and plastic strains are the factors that contribute to ductile failures in metals. Therefore, the finite strain theory is used in the modeling of ductile damage. They're always linked to instabilities and the phenomenon of strain localization and damage. Presence of holes or notches in reactor components and pressure vessels pose the risk for ductile failure and therefore must be tested for ductile failures in the event of over-loading to ensure the safety of the component and reactor during service.

Numerous works have been carried out by various researchers in an effort to model this phenomenon using a material model, including Tvergaard and Needleman [3], Rousselier [37], Senior et al. [56], Tvergaard [57] to name a few. Gurson [49] considered an ideal plastic matrix material subjected to loading, which surrounds a spherical RVE representing a void of void volume fraction (VVF), f. By solving this mechanical equilibrium problem, he developed the yield condition

$$\Phi = \left(\frac{T_{eq}}{\sigma_M}\right)^2 + 2\, f\, Cosh\left(\frac{3}{2}\frac{T_v}{\sigma_M}\right) - 1 - f^2 = 0 \tag{2.118}$$

to model the deterioration of the material. Here, $\sigma_M(=k)$ is the tensile flow stress of the matrix material. T_v and T_{eq} are the hydrostatic stress and the von-Mises equivalent of the Cauchy stress tensor $\mathbf{T}$. At $f = 0$, the eq. (2.118) represents a damage free material and reduces to the von Mises yield condition. As f increases, the cylindrical von-Mises yield surface changes to an ellipsoid like surface. Assuming the plastic incompressibility of the matrix material, Gurson [49] described the evolution of f using

$$\dot{f} = (1-f)\,\mathbf{I}\cdot\mathbf{D}_p \tag{2.119}$$

where $\mathbf{D}_p$ is got by applying the normality rule. This model's prediction of the theoretical VVF at fracture, $f = 1$, is known to be highly overestimated [58] as it neglects the void nucleation and coalescence. Therefore a suitable nucleation criterion was necessary. Gurson [49] had already concluded that nucleation can be correlated to plastic strain. The nucleation itself is attributed to particle cracking or particle-matrix de-cohesion [55, 59, 56], based on which, the concept of a critical nucleation strain was endorsed by Goods and Brown [55] and Senior et al. [56]. Senior observed that larger voids nucleate at smaller strains while smaller voids nucleate at larger strains. Chu and Needleman [59] suggested that the nucleation rate is influenced by both the accumulated inelastic strain as well as the hydrostatic stress, but neglected the latter to introduce the nucleation criterion

$$\dot{f} = \dot{f}_{nucl} + \dot{f}_{growth}, \tag{2.120}$$

$$\dot{f}_{nucl} = \frac{f_N}{s_N\sqrt{2\pi}} \exp\left[-\frac{1}{2}\left(\frac{\varepsilon_M - \varepsilon_N}{s_N}\right)^2\right], \tag{2.121}$$

$$\dot{f}_{growth} = (1-f)\ \text{trace}(\mathbf{D}_p), \tag{2.122}$$

as an extension to eq. (2.119), assuming that nucleation correlates with a Gaussian distribution of accumulated inelastic strain ε_M in the matrix. Here ε_N is the critical strain that also represents the mean of the distribution which has a standard deviation of s_N. f_N represents the volume fraction of void nucleating inclusions. The development of ε_M is described by the Gurson [49] model using

$$\dot{\varepsilon}_M = \frac{\mathbf{T}\cdot\mathbf{D}_p}{(1-f)\ \sigma_M}, \tag{2.123}$$

which introduces an isotropic hardening behaviour and forces σ_M to depend on the evolution of ε_M instead of remaining constant.

Finally, Tvergaard and Needleman [3][60] proposed the following extension to the original model in eq. (2.118) based on the results from [61, 62] to include the effects of void coalescence

$$\Phi = \left(\frac{T_{eq}}{\sigma_M}\right)^2 + 2\ f^*\ q_1\ Cosh\left(\frac{3\ q_2}{2}\frac{T_v}{\sigma_M}\right) - 1 - (q_1\ f^*)^2 = 0 \tag{2.124}$$

where the term f^* is the effective value of the VVF f, introduced by Tvergaard [62] to better characterize the experimentally observed void coalescence mechanism [3] and the growth of the VVF once it reaches a value above the critical value, f_c,

$$f^* = \begin{cases} f & \text{, if } f \le f_c \\ f_c + \dfrac{f_u^* - f_c}{f_F - f_c}(f - f_c) & \text{, if } f > f_c. \end{cases} \tag{2.125}$$

Here, f_u^* represents the value of f^* at which the load-bearing capacity of the matrix material is lost and is usually taken to be $f_u^* = 1/q_1$. The VVF f at fracture is represented by f_F, which can be experimentally identified. The model described by eqs. (2.120) to (2.125) is popularly known as the GTN model.

For predicting structural damage, constitutive models must be able to describe the influence of non-monotonic loading on the material behaviour and damage. As discussed in sections 2.3.4 and 2.4.1, the cyclic plasticity is used to describe these effects of non-monotonic loading. In homogeneous specimens, progressive localization of the deformation field may alter the loading path. Under hydrostatic pressure, the Gurson model predicts negative void volume growth, or recovery, as it is based on a symmetric yield surface with respect to the deviatoric stress planes. This violates the experimental observations which establish that for constant triaxiality, the VVF does not vary during closed loading cycles [63]. Thus, the model needs to be extended to cyclic or non-monotonic loading. To allow the application of kinematic hardening law, the yield condition of the GTN model was

extended by Mear and Hutchinson [58]

$$\Phi = \left(\frac{(\mathbf{T}-\mathbf{\Omega})_{eq}}{\sigma_s} \right)^2 + 2\, f^*\, q_1\, Cosh\left(\frac{3\, q_2}{2} \frac{(\mathbf{T}-\mathbf{\Omega})_v}{\sigma_s} \right) - 1 - (q_1\, f^*)^2 = 0 \tag{2.126}$$

$$\text{with } \frac{(\mathbf{T}-\mathbf{\Omega})_{eq}}{\sigma_s} = \frac{T_{eq}}{\sigma_M}, \tag{2.127}$$

where $(\mathbf{T}-\mathbf{\Omega})_v$ is the hydrostatic part of $\mathbf{T}-\mathbf{\Omega}$ and σ_s is the effective flow stress. An alternate approach by Leblond et al. [64] introduced two measures Σ_1 and Σ_2 in place of σ_s to account for isotropic hardening resulting from deviatoric and hydrostatic stress states

$$\Phi = \left(\frac{T_{eq}}{\Sigma_1} \right)^2 + 2\, f\, Cosh\left(\frac{3\, T_v}{2\Sigma_2} \right) - 1 - f^2 = 0. \tag{2.128}$$

Following the work of Mear and Hutchinson [58], Leblond et al. [64] obtained the following extension of the Gurson model

$$\Phi = \left(\frac{(\mathbf{T}-r\,\mathbf{\Omega})_{eq}}{r\,\sigma_M + (1-r)\Sigma_1} \right)^2 + 2\, f\, Cosh\left(\frac{3}{2} \frac{(\mathbf{T}-r\,\mathbf{\Omega})_v}{r\,\sigma_M + (1-r)\Sigma_2} \right) - 1 - f^2 = 0 \tag{2.129}$$

where r represents the fraction of total hardening offered by kinematic hardening. Unit cell simulations performed by Klingbeil et al. [65] showed that kinematic hardening influences localization on the mesoscopic level and consequently the damage development, which motivated the extension

$$\Phi = \left(\frac{(\mathbf{M}-b\,\mathbf{\Omega})_{eq}}{\sigma_M} \right)^2 + 2\, f^*\, q_1\, Cosh\left(\frac{3\, q_2}{2} \frac{M_v}{\sigma_A} \right) - 1 - (q_1\, f^*)^2 = 0 \tag{2.130}$$

of the GTN yield condition, following the approaches of [58, 64] to describe material behaviour when subjected to large deformations and cyclic loading with σ_M and σ_A representing the tensile flow stress of the deviatoric and hydrostatic parts of the yield function respectively. Here, $b = 1 - q_1\, f^*$ and $\mathbf{M}$ is the Mandel stress. Based on the idea the hydrostatic part of $\mathbf{M}$ is much larger than the hydrostatic part of $\mathbf{\Omega}$ ($M_v \gg Z_v$), the hydrostatic part of $\mathbf{\Omega}$ is omitted from the triaxiality term.

2.4.3 Consistent tangent modulus

Continuum deformation and damage models are usually developed with the aim of assessing the influence of material behaviour on structures under certain operating and loading conditions. For this, the developed models need to be implemented in a finite element code, where the global equilibrium iterations are solved and the local estimates of displacement and strain are provided as inputs to the material model. In addition to computing the stress response of the material, it is necessary to provide

the Jacobian matrix known as the consistent tangent modulus (CTM) which help in the convergence of the equilibrium iterations.

The tangent modulus is a fourth order tensor, which is originally defined using the base system as

$$\mathbb{D}_{ijkl} = \frac{\partial \Delta \mathbf{T}_{ij}}{\partial \Delta \mathbf{A}_{kl}}. \tag{2.131}$$

However, it can be represented using the Lamé constants as a 6x6 matrix by taking advantage of the symmetric nature of the stress and strain tensors. This reduced system of representation is known as the Voigt notation which is usually applied by FE-programs to tensor variables of orders 2 and 4, that are used in solid mechanics calculations

$$\mathbb{D}_{\alpha\beta} = \frac{\partial \Delta \mathbf{T}}{\partial \Delta \mathbf{A}}. \tag{2.132}$$

As previously discussed, the material subroutine is required to provide a consistent tangent modulus to the FE-program for the easier convergence of the global equilibrium iterations. Due to the ease of convergence, the material subroutine is allowed to operate on larger time steps. For these reasons, the computation effort and time of the FE-calculation is reduced. While many approaches exist for the correct identification of the CTM using implicit integration schemes, fewer explicit approaches exist for the approximation of tangent modulus. Since the common practice of using the elastic tensor for explicit schemes is inefficient for elasto-plastic problems, few approaches exist as an alternative for obtaining a more efficient CTM [66–72]. Among these, the method introduced by Fleig [72] is of interest, primarily due to its simplicity and ease of implementation while ensuring high accuracy which succeeds in reducing the computational effort. Using this method, $\mathbb{D}$ is approximated at the end of the time step as

$$\mathbb{D}_{(t_1)} = \frac{1}{\Delta t}\left(\frac{\partial \mathbf{T}}{\partial \mathbf{A}}\right)_{(t_1)} \approx \frac{1}{\Delta t}\begin{bmatrix} \mathcal{A} & \mathcal{B} & \mathcal{B} & 0 & 0 & 0 \\ \mathcal{B} & \mathcal{A} & \mathcal{B} & 0 & 0 & 0 \\ \mathcal{B} & \mathcal{B} & \mathcal{A} & 0 & 0 & 0 \\ 0 & 0 & 0 & \mathcal{C} & 0 & 0 \\ 0 & 0 & 0 & 0 & \mathcal{C} & 0 \\ 0 & 0 & 0 & 0 & 0 & \mathcal{C} \end{bmatrix}_{(t_1)} \tag{2.133}$$

where the variables $\mathcal{A}, \mathcal{B}, \mathcal{C}$ are described by the evolution equations

$$\dot{\mathcal{A}} = (1-d)\ (2\mu+\lambda) - 4\mu f_{CTM}\,(\mathcal{A}-\mathcal{B}) \tag{2.134}$$

$$\dot{\mathcal{B}} = (1-d)\ \lambda - 2\mu f_{CTM}\,(\mathcal{B}-\mathcal{A}) \tag{2.135}$$

$$\dot{\mathcal{C}} = (1-d)\ \mu - \mu f_{CTM}\,\mathcal{C} \tag{2.136}$$

where the choice of f_{CTM} is made with respect to the flow rule of the model. For e.g, to use this method with the viscoplastic model discussed in section 2.4.1, f_{CTM} is chosen from the flow rule in

eq. (2.108) to be

$$f_{CTM} = \left\langle \frac{\Sigma_{eq} - \sigma_s}{Z} \right\rangle^n \frac{3}{2}\frac{1}{\Sigma_{eq}}. \tag{2.137}$$

The eqs. (2.134) to (2.136) shall be integrated along with the incremental formulation of the constitutive model.

In applications to FE-calculations involving finite deformation and rotations, the transformation of $\mathbb{D}$ to a different orientation becomes necessary. For the increment of rotation represented by the orthogonal tensor $\mathbf{Q}$ during the given time step, the transformation

$$\bar{\mathbb{D}} = \mathbf{Q}\,\mathbf{Q}\,\mathbb{D}\,\mathbf{Q}^T\,\mathbf{Q}^T \tag{2.138}$$

which maps the tensor to the new orientation is applied to obtain the structure of $\bar{\mathbb{D}}$. As a result of the transformation, the zero entries in the original matrix $\mathbb{D}$ may not remain zero in the new matrix $\bar{\mathbb{D}}$. The transformation law (2.138) is for $\mathbb{D}_{ijkl}$ and therefore is not convenient for the 6x6 matrix $\mathbb{D}_{\alpha\beta}$ since the analytical calculations involving tensor operations described in the above relation is complex and highly demanding, a numerical approach introduced by Bond [73][74] to approximate the operation in eq. (2.138)

$$\bar{\mathbb{D}} = \mathbf{K}\,\mathbb{D}\,\mathbf{K}^T \tag{2.139}$$

where $\mathbf{K}$ is a tensor represented by a 6x6 matrix which is constructed using the elements of the orthogonal tensor $\mathbf{Q}$

$$\mathbf{K} = \begin{bmatrix} \mathbf{K}_1 & 2\mathbf{K}_2 \\ \mathbf{K}_3 & \mathbf{K}_4 \end{bmatrix} \tag{2.140}$$

$$\text{with} \quad \mathbf{K}_1 = \begin{bmatrix} \mathbf{Q}_{11}^2 & \mathbf{Q}_{12}^2 & \mathbf{Q}_{13}^2 \\ \mathbf{Q}_{21}^2 & \mathbf{Q}_{22}^2 & \mathbf{Q}_{23}^2 \\ \mathbf{Q}_{31}^2 & \mathbf{Q}_{32}^2 & \mathbf{Q}_{33}^2 \end{bmatrix}, \tag{2.141}$$

$$\mathbf{K}_2 = \begin{bmatrix} \mathbf{Q}_{12}\,\mathbf{Q}_{13} & \mathbf{Q}_{13}\,\mathbf{Q}_{11} & \mathbf{Q}_{11}\,\mathbf{Q}_{12} \\ \mathbf{Q}_{22}\,\mathbf{Q}_{23} & \mathbf{Q}_{23}\,\mathbf{Q}_{21} & \mathbf{Q}_{21}\,\mathbf{Q}_{22} \\ \mathbf{Q}_{32}\,\mathbf{Q}_{33} & \mathbf{Q}_{33}\,\mathbf{Q}_{31} & \mathbf{Q}_{31}\,\mathbf{Q}_{32} \end{bmatrix}, \tag{2.142}$$

$$\mathbf{K}_3 = \begin{bmatrix} \mathbf{Q}_{21}\,\mathbf{Q}_{31} & \mathbf{Q}_{22}\,\mathbf{Q}_{32} & \mathbf{Q}_{23}\,\mathbf{Q}_{33} \\ \mathbf{Q}_{31}\,\mathbf{Q}_{11} & \mathbf{Q}_{32}\,\mathbf{Q}_{12} & \mathbf{Q}_{33}\,\mathbf{Q}_{13} \\ \mathbf{Q}_{11}\,\mathbf{Q}_{21} & \mathbf{Q}_{12}\,\mathbf{Q}_{22} & \mathbf{Q}_{13}\,\mathbf{Q}_{23} \end{bmatrix} \text{ and} \tag{2.143}$$

$$\mathbf{K}_4 = \begin{bmatrix} \mathbf{Q}_{22}\,\mathbf{Q}_{33} + \mathbf{Q}_{23}\,\mathbf{Q}_{32} & \mathbf{Q}_{23}\,\mathbf{Q}_{31} + \mathbf{Q}_{21}\,\mathbf{Q}_{33} & \mathbf{Q}_{21}\,\mathbf{Q}_{32} + \mathbf{Q}_{22}\,\mathbf{Q}_{31} \\ \mathbf{Q}_{32}\,\mathbf{Q}_{13} + \mathbf{Q}_{33}\,\mathbf{Q}_{12} & \mathbf{Q}_{33}\,\mathbf{Q}_{11} + \mathbf{Q}_{31}\,\mathbf{Q}_{13} & \mathbf{Q}_{31}\,\mathbf{Q}_{12} + \mathbf{Q}_{32}\,\mathbf{Q}_{11} \\ \mathbf{Q}_{12}\,\mathbf{Q}_{23} + \mathbf{Q}_{13}\,\mathbf{Q}_{22} & \mathbf{Q}_{13}\,\mathbf{Q}_{21} + \mathbf{Q}_{11}\,\mathbf{Q}_{23} & \mathbf{Q}_{11}\,\mathbf{Q}_{22} + \mathbf{Q}_{12}\,\mathbf{Q}_{21} \end{bmatrix}. \tag{2.144}$$

Using the established integration routine, the material model is applied to experiments performed on unirradiated and irradiated materials to calibrate the set of material parameters. This allows the model to be used for the simulation of the experiments. These activities are discussed in detail in the next chapter.

Chapter 3

Thermodynamic framework for modeling of materials under irradiation

An event of *Radiation* is described as the transmission of energy from energetic particles (neutrons) to a solid, which results in the redistribution of target atoms [75]. From this, it can be deduced that the neutrons introduce energy to a closed system, which in this case is the material. Locally, this energy transfer introduces significant changes in the system and affects the material's elastic and inelastic properties. The thermodynamic approach to describe the material behaviour must account for the irradiation related energy transfers. This is because the constitutive models in continuum mechanics are derived using the fundamental rules of thermodynamic rules governing mass, energy and entropy outlined in section 2.2. A framework to model irradiated materials is not available during the course of this work. This chapter proposes a framework for deriving the thermodynamic modeling of irradiated materials based on the application of the law of energy conservation and the Dual Variables concept.

First, the experiments performed to support the modeling performed in this work are presented. The important information regarding the elastic and inelastic behaviour of unirradiated and irradiated material is discussed. The thermodynamic concerns of radiation and the exposed material are discussed next, followed by recommendations made in this work for satisfying energy conservation. The consequent entropy inequality completes the proposed framework for irradiated materials. The development of a finite strain model using the proposed framework is shown and discussed, culminating in the derivation of conditions that ensure the thermodynamic consistency of the model. Finally, a ductile damage model is extended to viscoplasticity and incorporated into the finite strain deformation model.

3.1 Experimental findings

To provide the valuable information and insight necessary to model the material behaviour in its unirradiated and irradiated condition, experimental and microstructural data were generated by SCK-CEN, Belgium [4]. Camera-monitored tensile tests were performed to capture the neck development and local deformation that provide information to determine the true stress and strain for unirradiated

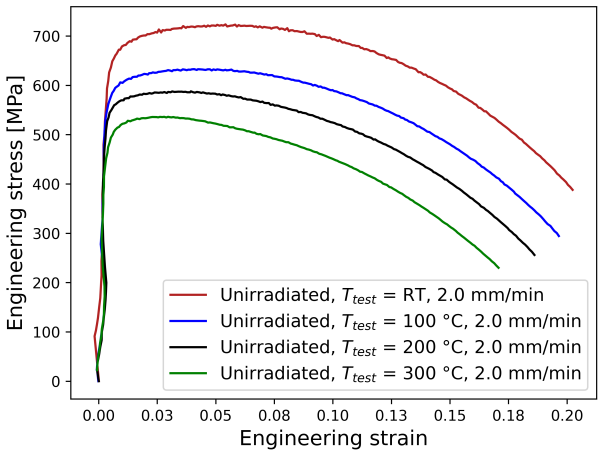

Figure 3.1: Engineering stress-strain curves of unirradiated samples tested at RT - 300 °C [4].

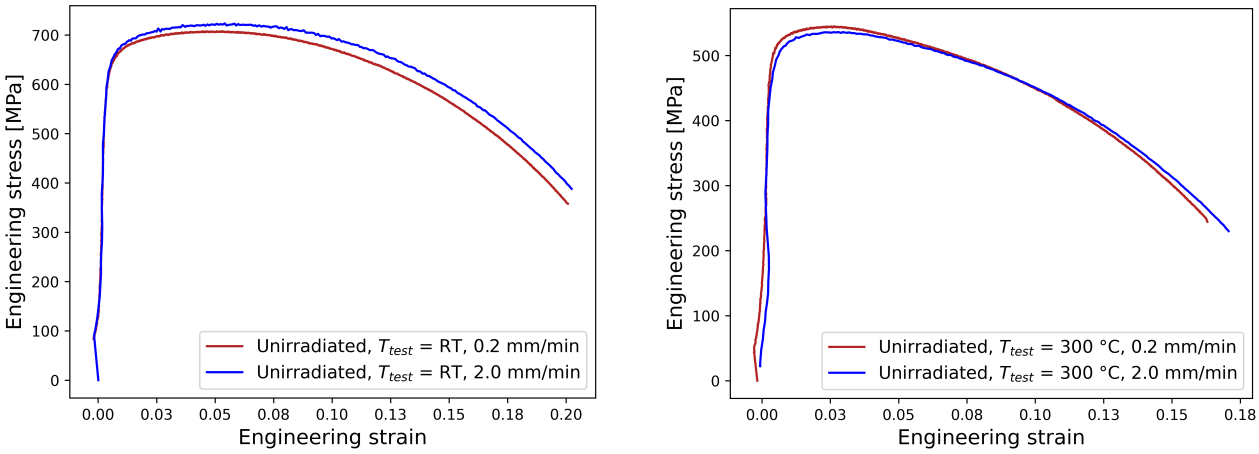

(a) RT (b) 300 °C

Figure 3.2: Engineering stress-strain curves of unirradiated samples tested at different strain rates [4].

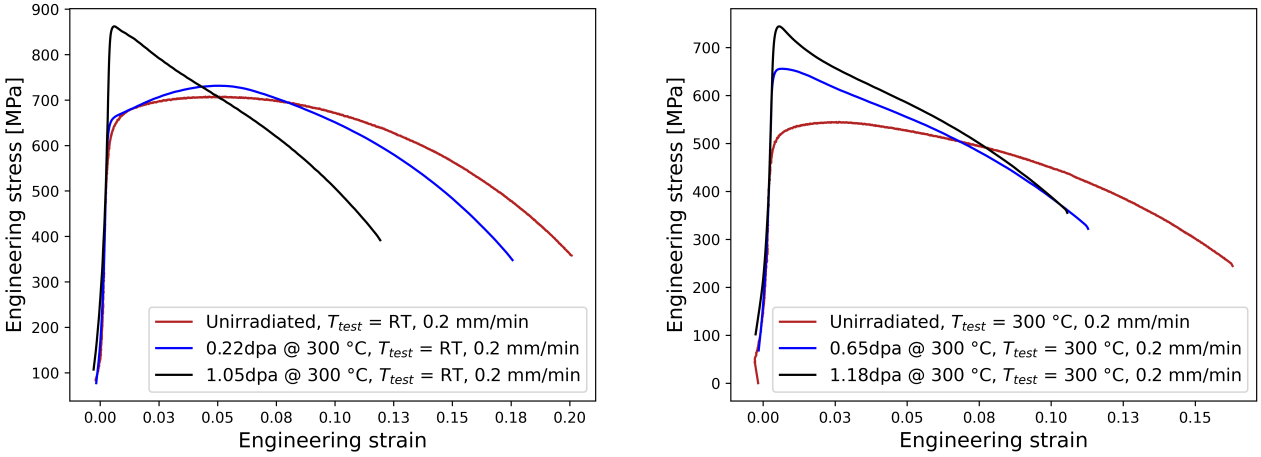

(a) RT (b) 300 °C

Figure 3.3: Engineering stress-strain curves of irradiated samples [4, 5].

T_{test} (°C)	T_{irr} (°C)	Irradiation dose (dpa)	Deformation rate (mm/min)
RT	-	-	0.2
RT	-	-	2.0
RT	300	0.22	0.2
RT	300	1.05	0.2
100	-	-	2.0
200	-	-	2.0
300	-	-	0.2
300	-	-	2.0
300	300	0.65	0.2
300	300	1.18	0.2

Table 3.1: List of tensile tests performed with test temperature T_{test}, irradiation temperature T_{irr}, irradiation dose, and deformation rates.

and irradiated Eurofer97. The material used in this study is Eurofer97 Heat 83699, procured from Böhler Austria GmbH in the form of a cylindrical bar. The heat treatment of the material includes normalization at 979 °C for 1 hour 51 minutes and tempering at 739 °C for 3 hours 42 minutes, with a period of air-cooling succeeding each step. Samples were cut from the cylinder such that their axes are parallel. The standard miniaturized geometry (see fig. A.1) comprising of a gauge length 12 mm and diameter 2.4 mm was used. Neutron irradiation of samples was performed at 300 °C in the Callisto loop of the BR2 reactor. Irradiation damage doses of four irradiated samples were between 0.22 -1.18 dpa. The testing campaign was structured in a way to study the deformation and damage at various conditions: temperature, strain rate, and irradiation damage dose. The details of irradiation and testing conditions are found in Table 3.1. The unirradiated samples were tested in a cold mechanical lab, while the irradiated (active) samples were tested in hot cells. The unirradiated samples were tested in the temperature range of RT-300 °C with a deformation rate of 2 mm/min. The influence of strain rate on material behaviour was investigated through tests at RT and 300 °C with a deformation rate one order of magnitude lower (0.2 mm/min). Due to the difficulty and the high cost of acquiring neutron irradiated samples, the available irradiated samples were divided into 2 groups: a) samples irradiated to 0.22 and 1.05 dpa were tested at RT, b) samples irradiated to 0.65 and 1.18 dpa were tested at 300 °C. A deformation rate of 0.2 mm/min was used for all irradiated samples. The load applied and the sample displacement recorded by the cross head movement are provided by the testing machine. Tests were performed with the deformation and necking of the sample being recorded by a camera.

From the load displacement data provided by SCK-CEN, the engineering stress and strain curves were calculated using the formulae

$$\sigma_{eng} = \frac{L}{A_0}, \quad \varepsilon_{eng} = \frac{\Delta l}{l_0} \tag{3.1}$$

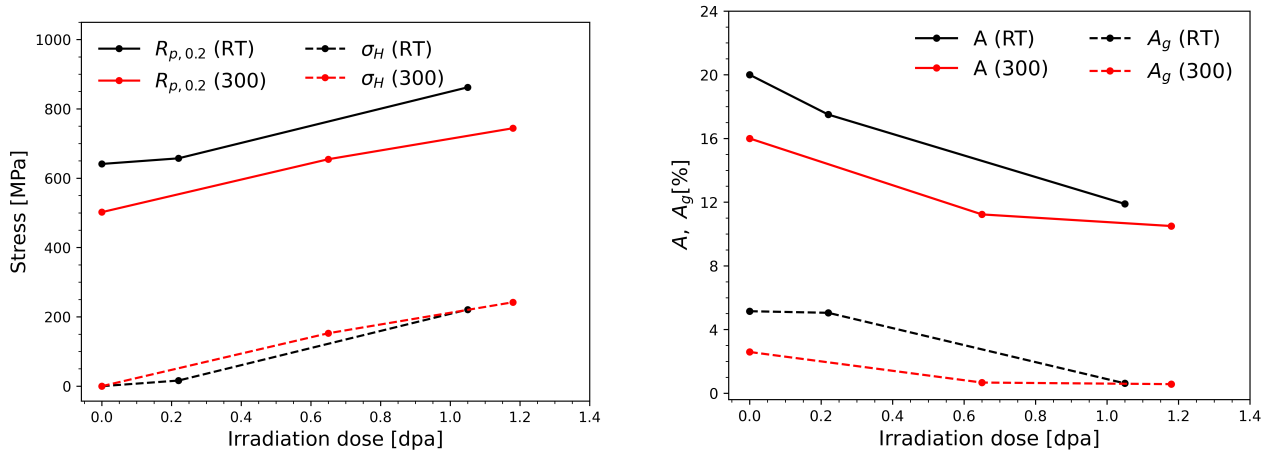

(a) (b)

Figure 3.4: Comparison of tensile properties of samples tested at RT and 300 °C: (a) 0.2% yield strength ($R_{p0.2}$), irradiation hardening (σ_H) and UTS (σ_{UTS}), (b) uniform elongation (A_g) and total elongation (A).

where L is the load applied, Δl is the cross head displacement, while A_0 and l_0 are the initial cross sectional area and length of the gauge section. $A_0 = \pi(d_0/2)^2$ is calculated from the initial gauge diameter d_0. The correction for removing the machine stiffness was applied to determine the specimen strain using the formula

$$\varepsilon_{eng,s} = \varepsilon_{eng} - \frac{\sigma}{E_{exp}} + \frac{\sigma}{E} \tag{3.2}$$

where E_{exp} is the slope of the most linear portion of the elastic region in the engineering stress and strain curve, and E is the Young's modulus of the material at the given temperature which is referred from the literature [17, 1].

The resulting engineering curves of unirradiated samples tested at various temperatures at 2 mm/min are shown in fig. 3.1. The observed reduction of yield stress, uniform elongation and total elongation with increase in the temperature is in agreement with results from literature [17, 76–79]. The strain rate influence on tensile properties is illustrated in fig. 3.2, where the increase in UTS and fracture strain is in agreement with literature [79] at RT. At 300 °C, there are some outlying behaviours seen in fig. 3.2b where the sample tested at higher deformation rate exhibits a lower UTS than the sample tested at lower deformation rate. Since the recorded values are above the minimum UTS expected of the material, this anomaly is attributed to the lack of homogeneity in the bulk material. However, the increase in fracture strain for the higher deformation rate is in agreement with literature [79]. Next, the engineering curves of the tested irradiated samples are shown in fig. 3.3 where they are compared with the unirradiated samples tested at the same deformation rate. The tensile properties of unirradiated and irradiated material are tabulated in table 3.2. A common behaviour of increase in yield stress and UTS, with a reduction in fracture strain is observed for all irradiated samples.

Temp. °C	Dose dpa	$R_{p0.2}$ MPa	R_m MPa	σ_H MPa	A_g (%)	A (%)	$R_{p0.2}/R_m$ (%)
RT	0	641.1	722	0	5.15	20	88.79
RT	0.22	657.3	731	16.19	5.05	17.5	89.91
RT	1.05	862.1	862	220.99	0.62	11.89	100
300	0	502	544	0	2.59	16	92.27
300	0.65	654.7	655	152.68	0.67	11.23	99.95
300	1.18	744.1	744	242.1	0.57	10.5	100

Table 3.2: Tensile properties of tested unirradiated and irradiated specimen.

Figure 3.5: Illustration of Bridgman correction factor B as a function of the neck profile described by the minimum radius $d_{min}/2$ and radius of curvature R_{curv} [6].

However, the loss of uniform elongation is very strong for samples irradiated from upwards of 0.65 dpa.

3.1.1 Calculation of true stress and true strain

The calculation of true stress and strain from experimental data, as well as the uncertainty associated with image-based measurement methodology, is described in detail in [4]. In this work, the data is re-evaluated using the same procedure as in [4] to obtain the refinement needed to articulate the material deformation post-necking. The video acquisition for tests was completed at a frame rate of 25 per second. The procedure for the extraction of data from the video regarding the dimensions and profile of the sample's neck with respect to the load applied, which are essential to the calculation of true stress and strain is discussed in this subsection. Since the testing conditions vary, the procedure of video acquisition and the quality of the video change. Although these procedures are not discussed in this work, the quality of the video and the error they introduce into the determined true stress and strain are discussed. Finally, the observations are drawn based on the results and concerning the influence of irradiation.

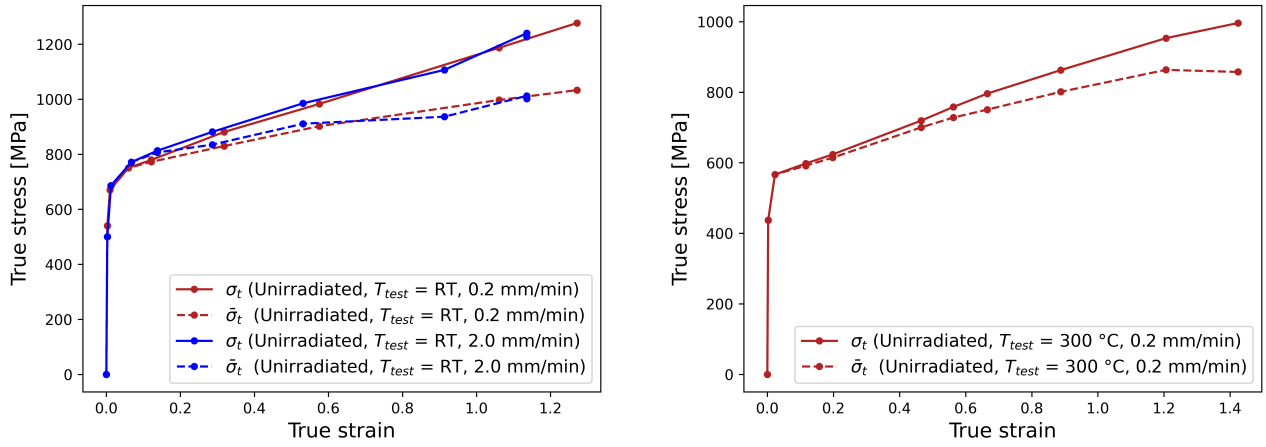

(a) RT (b) 300 °C

Figure 3.6: Mean true stress(σ_t) and Bridgman corrected true stress ($\bar{\sigma}_t$) versus mean true strain for unirradiated samples tested at RT and 300 °C for different deformation rates. The second and third data points correspond to the yield point and the UTS respectively.

3.1.1.1 Extraction of data

The time of fracture in the video is used as reference and with the help of the respective deformation rate and time from the experiment, the load-displacement data is synchronized with the video. With this setup, images are extracted from the video file at different levels of deformation (displacement) and neck development from the entire loading history. From the image of the un-deformed sample from each test, the length and width of the gauge section are measured in pixels and related to the actual dimensions of the sample. For this, the *ImageJ* software [80] was used. Using this method, the pixel measurements are converted to SI units. With these measurements as a reference, the relative local deformation is measured in the other extracted images. From the minimum width of the specimen, the cross-sectional area is estimated and is used to calculate the mean true stress σ_t and strain ε_t

$$\sigma_t = \frac{L}{A_{min}}, \quad \varepsilon_t = ln\left(\frac{A_0}{A_{min}}\right). \tag{3.3}$$

Here, $A_{min} = \pi(d_{min}/2)^2$ and d_{min} are the minimum cross sectional area and diameter of the gauge section. Since the mean true stress holds the influence of triaxial stress state in the neck, it is necessary to apply a suitable correction procedure to determine the uniaxial stress. The Bridgman correction procedure [6] is the widely applied method for smooth and cylindrical samples and has been applied in this work. For this method, the curvature of the neck is also measured from the images and utilized

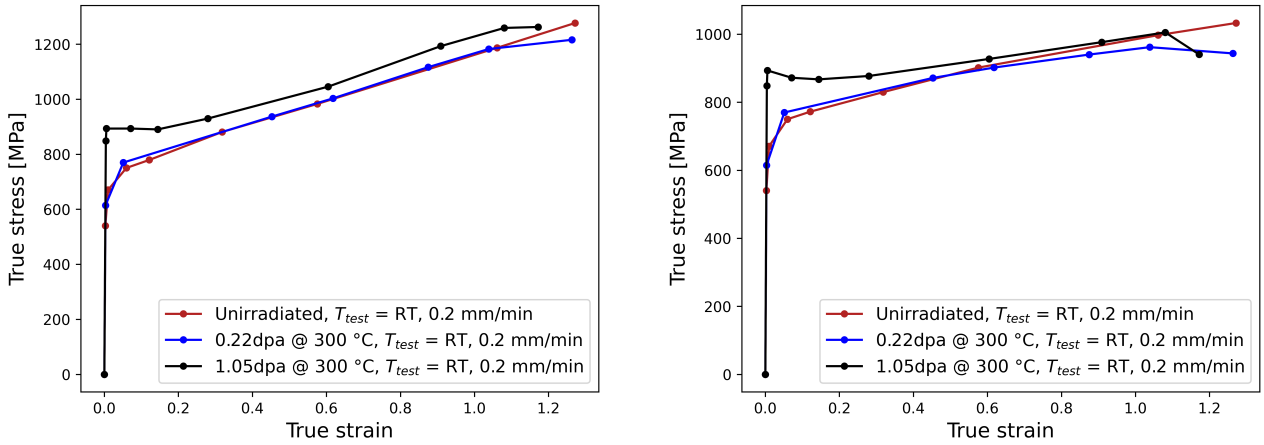

(a) Mean true stress-mean true strain

(b) Bridgman corrected true stress-mean true strain

Figure 3.7: True stress-strain of unirradiated and irradiated samples (T_{irr}=300 °C) at T_{test}=RT. The second and third data points correspond to the yield point and the UTS respectively.

in the calculation of the Bridgman corrected stress $\bar{\sigma}_t$ from the formula

$$\bar{\sigma}_t = \frac{\sigma_t}{\left(1 + \frac{4\,R_{curv}}{d_{min}}\right) ln \left[1 + \frac{d_{min}}{4\,R_{curv}}\right]} = B\sigma_t \tag{3.4}$$

where R_{curv} is the radius of curvature of neck profile and B is the Bridgman correction factor.

3.1.1.2 Calculation of uncertainty

Since the measurements were made from images, the associated uncertainty was calculated using the method in [4]. For a quantity X, its absolute error is taken to be ΔX, while its relative errors as δX. The uncertainty of the calculated quantities originates from a) cross-section diameter d_{min} and b) neck curvature radius R_{curv}. The absolute error Δd_{min} of 1 pixel (px) and relative error δR_{curv} of 20% are assumed. The absolute error of true strain is

$$\Delta\varepsilon_t = \left|\frac{\partial\varepsilon_t}{\partial A_{min}}\right| \Delta A_{min} = \frac{\Delta A_{min}}{A_{min}} = \delta A_{min} = \delta d_{min}. \tag{3.5}$$

Similarly, the relative error of true stress is

$$\delta\sigma_t = \delta A_{min}. \tag{3.6}$$

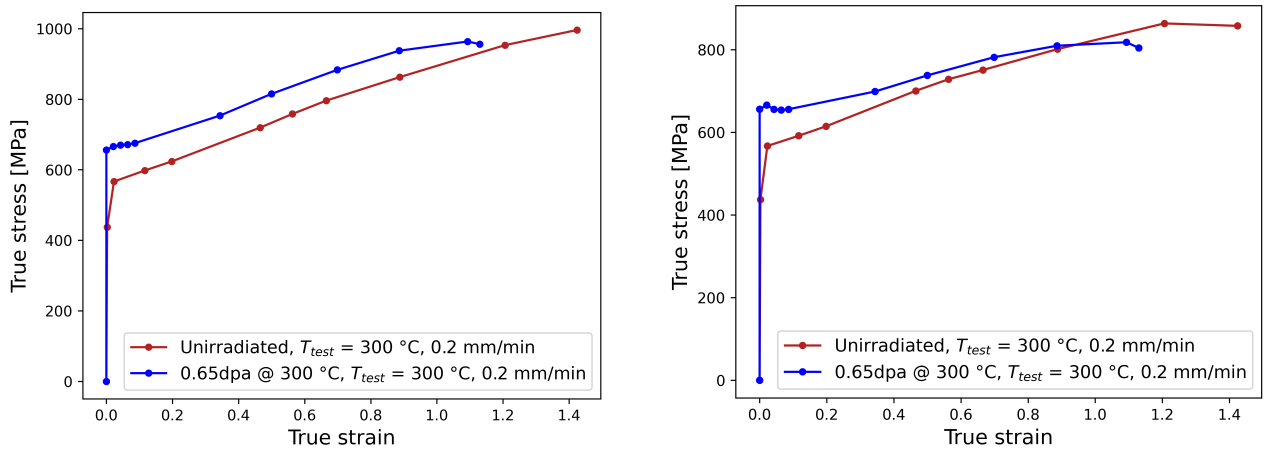

(a) Mean true stress-mean true strain

(b) Bridgman corrected true stress-mean true strain

Figure 3.8: True stress-strain of unirradiated and irradiated samples (T_{irr}=300 °C) at T_{test}=300 °C. The second and third data points correspond to the yield point and the UTS respectively.

With $\beta_B = d_{min}/2R_{curv}$, the Bridgman factor B from eq. (3.4) can be written in the form

$$B = \frac{1}{\left(1+\frac{2}{\beta_B}\right) ln\left[1+\frac{\beta_B}{2}\right]}. \tag{3.7}$$

The relative error of β_B, $\delta\beta_B = \delta d_{min}/2 + \delta R_{curv}$. As the principal contributor is δR_{curv}, $\delta\beta_B \approx \delta R_{curv}$ = 20%. Using the rules of error propagation, the absolute error of the B is calculated as

$$\Delta B = \left|\frac{\partial B}{\partial \beta_B}\right| = \left|\frac{2\ ln\left[1+\frac{\beta_B}{2}\right] - \beta_B}{ln^2\left[\left(1+\frac{\beta_B}{2}\right](\beta_B+2)^2}\right| \delta\beta_B. \tag{3.8}$$

Though $\delta\beta_B \approx$20%, $\delta B \leq 5\%$. After the Bridgman correction is applied, the relative error of stress, $\delta\sigma_B = \delta\sigma_t + \delta B$ was found to remain in the range 3-7% at UTS and 8-16% at the moment of material failure, based on video resolution. Stress and strain relationships with errors due to uncertainty are illustrated in figs. B.1 to B.4

3.1.1.3 Observations

Using the procedure discussed in section 3.1.1.1, the mean true stress and strain are calculated from the images obtained from the tensile test videos. And with the application of the Bridgman correction, the true stress is also estimated. In fig. 3.6, the plots of σ_t and $\bar{\sigma}_t$ versus ε_t for the tests performed on unirradiated samples at RT and 300 °C are shown. At RT, the $\sigma_t - \varepsilon_t$ relation remains linear post

UTS. However, the fracture true strain and the final reduction of the minimum diameter in the neck are shown to be reduced at the higher deformation rate. At 300 °C, the $\sigma_t - \varepsilon_t$ relation is again linear post UTS, but the ability for uniform elongation has visibly reduced in comparison to RT although the reduction of minimum diameter is greater than what was observed for RT. This of course indicates that the material softens at elevated temperatures. The $\bar{\sigma}_t$ shows that material hardening reaches a saturation at fracture, which is likely a result of the onset of ductile damage.

The true stress and strain data calculated for the irradiated samples tested at T_{test} = RT and 300 °C are shown in figs. 3.7 and 3.8. The sample with 0.22 dpa displays a behaviour very similar to unirradiated E97 at RT, only differing by a marginal increase in strain hardening and reduction in fracture strain. Including σ_H, A_g and A from fig. 3.4 into consideration, it is seen that samples with irradiation doses of 0.65 dpa and higher exhibit characteristics that are similar and increasingly independent of T_{test}. The hardening modulus is utilized by Considère [81] to introduce the condition

$$\frac{d\bar{\sigma}_t}{d\varepsilon_t} \leq \bar{\sigma}_t \tag{3.9}$$

for the development of plastic instability and localized deformation in the sample, both of which are responsible for the loss of uniform elongation and neck development. Furthermore, the hardening modulus has an impact on the rate at which the instability and neck develop [82–84]. Because the material normally continues to harden until failure, the hardening modulus of unirradiated ductile materials decreases after yield and tends to stabilize beyond UTS. For instance, the ideal plastic material behaviour is described by a modulus lower bound of zero [82]. The modulus of irradiated materials, on the other hand, drops sharply as the yield turns negative, but then stabilizes to turn positive again as the material continues to harden at higher deformation levels until failure. This is due to the reduction in irradiation-induced hardening caused by the elimination of irradiation-defects during plastic deformation. Because the $\bar{\sigma}_t$ of irradiated samples gradually approaches the curves of unirradiated material at higher deformation levels, it may be assumed that defect removal occurs at a fast rate at first, but then slows down after crossing a threshold to achieve a steady rate after UTS. Even at material failure, it is improbable that all flaws are removed by plastic deformation. An explicit microstructural investigation is required to verify this, which is outside the scope of the current thesis. Because the modulus is negative for the first part of the plastic deformation, it must have a significant role in the accelerated neck development, and explains the steep decline in engineering stress strain curves after UTS. This is owing to the geometrical relaxation provided by the reduction in the minimum cross-sectional area resisting deformation as a result of necking. However, the true stress σ_t at material failure for unirradiated and irradiated material is about the same, which is consistent with findings of Byun [85–88]. A decrease in true strain at fracture is also observed, indicating that the scope for reducing minimum diameter for irradiated samples is limited, and that this limit decreases with increasing irradiation dose. Thus the ductility is reduced for irradiated samples.

Because these changes are caused by irradiation, it is critical to isolate and obtain data describing the evolution of irradiation hardening as a result of irradiation and plastic deformation, which will be used to develop constitutive relations to represent irradiation-induced changes in material behaviour on a continuum scale.

3.2 Thermodynamics of irradiation

The balance law of energy states that the time rate of change of a continuum body's total energy is given by the sum of work done by the surroundings on the body and the heat added to the body. In its traditional form (2.33), the energy transfers made as a result of irradiation are not included. Therefore additional quantities to capture the changes introduced by neutron irradiation into the material have to be identified and included to preserve energy conservation. This would allow the construction of the appropriate free energy functions and entropy inequality that are necessary for the thermodynamic formulation of the finite strain model.

While a large portion of the neutron energy transferred to the system is dissipated as heat, the rest is consumed in the work done on the system. Radiation damage in crystalline materials is measured by the number of displacements per atom (dpa), caused by the irradiation-induced cascades [23, 24]. These changes occur in the form of defect formation in the lattice [23], like defect clusters, dislocation loops, voids, etc. These irradiation induced defects alter the material properties, some of which manifest during mechanical tests in the form of irradiation hardening, loss of ductility, etc. It has been conclusively shown in numerous studies [14, 13, 26] that as a result of neutron irradiation, the material's mechanical properties are significantly altered in essence due to the induced changes in the microstructure of the material matrix. Irradiation-induced hardening arises out of dislocation pinning by defects [89–92]. From tensile tests, it is possible to measure the additional deformation or stress necessary to overcome the pinning and for the onset of plastic deformation [13]. This additional stress is a good measure of irradiation-induced hardening. Plastic deformation of the irradiated material on the other hand, leads to the annihilation or removal of the defects [89, 25, 93]. From these observations, it can be deduced that a portion of the energy from neutrons is transferred to the material and is used as formation energy for the creation of the irradiation defects, thereby altering the material's properties. Since with removal of defects, this portion of energy would dissipate during plastic deformation, it needs to be accounted for the law of energy conservation to be satisfied.

3.2.1 Irradiation Power

Since it has been established that the energy exchanges related to the formation and removal of irradiation defects have to be accounted for the conservation of energy, the ideal approach is to first estimate the formation energy of irradiation induced defects from the summation of the products of defect quantity and the associated formation energy for each defect type. Although numerous studies have been dedicated towards this approach using experimental, modeling, and statistical methodologies, they are not yet conclusive due to the difficulties in determining the quantity of

various defect types. In physics, energy is the stored work performed by a force on a thermodynamic system causing a thermodynamic change. Additionally, power is the rate at which work is performed. Therefore in this work, an alternative approach is adopted to represent or quantify the neutron energy responsible for the formation of the discussed defects.

A conjugate pair of variables is proposed whose product can quantify the amount of energy transferred to the system, which in addition to the material's stress power, is available for dissipation during inelastic deformation and damage of the irradiated material. In this work, it is proposed that the thermodynamic change in the system can be quantified by irradiation damage dose ϕ, an extrinsic quantity measured in dpa. And, the surface distributed thermodynamic force necessary to perform the work for bringing about this thermodynamic change is represented by ξ, which is assumed to be a function of the irradiation dose ϕ and is an intrinsic quantity. The product of this conjugate pair,

$$P_{irr} = \xi \ \dot{\phi} \tag{3.10}$$

is the rate of work or the power and therefore shall be termed *irradiation-induced power* (P_{irr}) in this work [5] which holds the unit of MPa/s or J/s (considering volume). Introduction of the irradiation power term in to the eq. (2.35) helps to satisfy the law of energy conservation

$$\dot{e} \ = \ \frac{1}{\rho}\big(\mathbf{T}\cdot \ \mathbf{D} \ + \ \xi \ \dot{\phi} \ \big) - \ \frac{1}{\rho}\,\mathrm{div}\boldsymbol{q} \ + \ s_{total} \tag{3.11}$$

for an irradiated material with $s_{total} = s + s_{irr}$ [5]. Here, s_{irr} is the heat generated due to neutron-atom and inter-atom interactions as a result of irradiation. Using the eq. (2.45) and (2.46) in the eq. (3.11) and assuming a positive entropy production, the *Clausius-Duhem inequality*

$$-\ \dot{\Psi} \ - \ \dot{\theta}\eta \ + \ \frac{1}{\rho}\big(\mathbf{T}\cdot \ \mathbf{D} \ + \ \xi \ \dot{\phi}\big) \ - \ \frac{\boldsymbol{q}}{\rho \ \Theta}\cdot \boldsymbol{g} \geq \ 0 \tag{3.12}$$

is obtained. Defects of various types contribute differently to material hardening, while certain types, such as point defects, do not contribute at all. Although removal of every defect type dissipates energy, this work will focus on the defect types that contribute to hardening. Hence, the contribution to free energy from defects that do not contribute to hardening is segregated from Ψ and defined as $\Psi_{irr,NH}$ [5]. For an isothermal process with uniform heat distribution, the inequality (3.12) reduces to

$$\begin{aligned} -\rho\left(\dot{\Psi} + \dot{\Psi}_{irr,NH}\right) + \mathbf{T}\cdot\mathbf{D} + \xi \ \dot{\phi} \geq 0, \\ -\rho\dot{\Psi} + \mathbf{T}\cdot\mathbf{D} + \left(\xi \ \dot{\phi} - \rho \ \dot{\Psi}_{irr,NH}\right) \geq 0. \end{aligned} \tag{3.13}$$

where the removal of $\Psi_{irr,NH}$ from the irradiation-induced power makes it possible to isolate the power responsible for irradiation hardening that is available for dissipation during plastic deformation.

This is quantified by introducing the relation [5]

$$\xi\ \dot{\phi} - \rho\ \dot{\Psi}_{irr,NH} = \varphi\ \dot{\phi} \tag{3.14}$$

where the term φ is proposed to be the tangent of the $\sigma_H - \phi$ curve [5]

$$\varphi = \frac{d\sigma_H}{d\phi} \tag{3.15}$$

that links the energy dissipation from the removal of defects, to the amount of irradiation hardening σ_H and the respective irradiation damage ϕ. Therefore, the entropy inequality for irradiated materials in actual configuration $\mathcal{X}_t$ is [5]

$$-\rho\dot{\Psi} + \mathbf{T}\cdot\mathbf{D} + \varphi\ \dot{\phi} \geq 0 \tag{3.16}$$

and in reference configuration $\mathcal{X}_{t_0}$ is

$$-\rho_R\dot{\Psi} + \tilde{\mathbf{T}}\cdot\dot{\mathbf{E}} + J\varphi\ \dot{\phi} \geq 0 \tag{3.17}$$

is henceforth used for determining the constitutive relations and thermodynamic consistency conditions of the finite-strain model that describes the deformation of the material post or during irradiation.

3.2.1.1 Free energy function of irradiated material

The free energy of a system is the portion of its internal energy that can be used to perform thermodynamic work. The free energy function is constructed using a set of internal state variables that are chosen to describe specific material behaviours such as material hardening and softening, as well as material damage. Constitutive equations are used to describe the evolution of the conjugates of these variables. Therefore in this work, to describe the irradiation induced material behaviour, the free energy function is constructed with irradiation defect density N_i as an internal state variable as

$$\Psi\ (t)\ =\ \Psi(\ \mathbf{E}_e,\ H,\ N_i,\ D) \tag{3.18}$$

for 'i' type of defects, in addition to the usual set of variables such as elastic strain $\mathbf{E}_e$, set of variables describing material hardening and softening H, and damage D.

3.3 Finite strain model for irradiated steel

Following the recommendations made in Haupt and Tsakmakis [2] and its implementation works of Lämmer [94], Jansohn [95], the constitutive model is defined in the intermediate configuration $\hat{\mathcal{X}}_t$, to ensure its invariance against any rotations. The transformation from $\mathcal{X}_{t_0}$ to $\hat{\mathcal{X}}_t$ is inelastic, while the transformation from $\hat{\mathcal{X}}_t$ to $\mathcal{X}_t$ is elastic. The formulation of the model starts with the additive

Mechanism	Type	State variables	Conjugate
Elasticity	Tensor	$\mathbf{E}_e \rightarrow \hat{\mathbf{\Gamma}}_e \rightarrow \mathbf{A}_e$	$\tilde{\mathbf{T}} \rightarrow \hat{\mathbf{T}} \rightarrow \mathbf{S}$
Kinematic hardening	Tensor	$\hat{\boldsymbol{\alpha}}_i \rightarrow \boldsymbol{\alpha}_i$	$\hat{\mathbf{Z}}_i \rightarrow \mathbf{Z}_i$
Isotropic softening	Scalar	ψ_i	R_i
Irradiation hardening	Scalar	N_i	$\mathfrak{n}_i$
Damage	Scalar	d	$-Y$

Table 3.3: State variables and their conjugates for the finite strain model.

decomposition of the Green Lagrange strain at $\hat{\mathcal{X}}_t$, into its elastic and plastic parts as seen in eq. (2.70)

$$\hat{\mathbf{\Gamma}} = \hat{\mathbf{\Gamma}}_e + \hat{\mathbf{\Gamma}}_p. \tag{3.19}$$

As discussed in sections 2.3.4 and 2.3.4.1, a free energy function with suitable internal variables is required to describe observed physical phenomena or properties. Internal state variables (ISV) are defined in addition to observable exterior variables like temperature and deformation in order to uniquely define the Helmholtz free energy of a solid system undergoing an irreversible process. ISVs must be based on physically observed behaviour and constrained by thermodynamic rules because they macroscopically average the details of the microscopic organization [96]. To describe the coupled viscoplastic damage model in section 2.4.1, variables of kinematic hardening, isotropic softening, defect density, and damage in addition to the elastic strain are chosen as the internal variables. The conjugate of these terms helps to define the evolution equations for the respective internal variables. The chosen free energy function is:

$$\hat{\Psi}(t) = \hat{\Psi}\left(\hat{\mathbf{\Gamma}}_e,\ \hat{\boldsymbol{\alpha}}_i,\ N_i,\ \psi_i,\ d\right). \tag{3.20}$$

The Clausius Duhem entropy inequality (3.17) with respect to $\hat{\mathcal{X}}_t$ may be rewritten as

$$\hat{\mathbf{T}} \cdot \overset{\triangle}{\hat{\mathbf{\Gamma}}} + \varphi\, \dot{\phi} - \rho_R\, \dot{\Psi} \geq 0. \tag{3.21}$$

Substituting eqs. (3.19) and (3.20) in eq. (3.21), the entropy inequality is written as

$$\hat{\mathbf{T}} \cdot \overset{\triangle}{\hat{\mathbf{\Gamma}}}_e + \hat{\mathbf{T}} \cdot \overset{\triangle}{\hat{\mathbf{\Gamma}}}_p + \varphi\, \dot{\phi} - \rho_R \left(\frac{\partial \Psi}{\partial \hat{\mathbf{\Gamma}}_e} \dot{\hat{\mathbf{\Gamma}}}_e + \frac{\partial \Psi}{\partial \hat{\boldsymbol{\alpha}}_i} \dot{\hat{\boldsymbol{\alpha}}}_i + \frac{\partial \Psi}{\partial N_i} \dot{N}_i + \frac{\partial \Psi}{\partial \psi_i} \dot{\psi}_i + \frac{\partial \Psi}{\partial d} \dot{d} \right) \geq 0. \tag{3.22}$$

Further, with the help of eq. (2.75) the elastic strain rate shall be formulated as

$$\overset{\triangle}{\hat{\mathbf{\Gamma}}}_e = \dot{\hat{\mathbf{\Gamma}}}_e + \hat{\mathbf{L}}_p^T \hat{\mathbf{\Gamma}}_e + \hat{\mathbf{\Gamma}}_e \hat{\mathbf{L}}_p. \tag{3.23}$$

Using eq. (2.62), a relation for $\dot{\hat{\mathbf{\Gamma}}}_e$ is obtained as

$$\begin{aligned}\dot{\hat{\mathbf{\Gamma}}}_e &= \overset{\triangle}{\hat{\mathbf{\Gamma}}}_e - \hat{\mathbf{L}}_p^T \cdot \hat{\mathbf{\Gamma}}_e - \hat{\mathbf{\Gamma}}_e \cdot \hat{\mathbf{L}}_p \quad = \overset{\triangle}{\hat{\mathbf{\Gamma}}}_e - \hat{\mathbf{\Gamma}}_e \left(\hat{\mathbf{L}}_p^T + \hat{\mathbf{L}}_p\right) \\ &= \overset{\triangle}{\hat{\mathbf{\Gamma}}}_e - \hat{\mathbf{\Gamma}}_e \cdot (2\hat{\mathbf{D}}_p)\end{aligned}$$

which is used to simplify eq. (3.22) into

$$\begin{aligned}\rightarrow \left(\hat{\mathbf{T}} - \rho_R \frac{\partial \Psi}{\partial \hat{\mathbf{\Gamma}}_e}\right) \cdot \overset{\triangle}{\hat{\mathbf{\Gamma}}}_e + \left(\hat{\mathbf{T}} + 2\,\rho_R \frac{\partial \Psi}{\partial \hat{\mathbf{\Gamma}}_e}\hat{\mathbf{\Gamma}}_e\right) \cdot \hat{\mathbf{D}}_P + \varphi\,\dot{\phi} \\ - \rho_R \left(\frac{\partial \Psi}{\partial \hat{\boldsymbol{\alpha}}_i}\dot{\hat{\boldsymbol{\alpha}}}_i + \frac{\partial \Psi}{\partial N_i}\dot{N}_i + \frac{\partial \Psi}{\partial \psi_i}\dot{\psi}_i + \frac{\partial \Psi}{\partial d}\dot{d}\right) \geq 0.\end{aligned} \tag{3.24}$$

Here, the first term in eq. (3.24) forms the elastic part and the rest form the plastic part of the entropy inequality. In the elastic state the terms $\hat{\mathbf{D}}_p = \dot{\boldsymbol{\alpha}}_i = \dot{N}_i = \dot{\psi}_i = \dot{d} = 0$, which gives the relation for the stress tensor.

$$\left(\hat{\mathbf{T}} - \rho_R \frac{\partial \Psi}{\partial \hat{\mathbf{\Gamma}}_e}\right) \cdot \overset{\triangle}{\hat{\mathbf{\Gamma}}}_e \geq 0 \quad \Rightarrow \quad \hat{\mathbf{T}} = \rho_R \frac{\partial \Psi}{\partial \hat{\mathbf{\Gamma}}_e} \tag{3.25}$$

As established in section 2.3.3, an effective stress measure considering the relaxation due to the isotropic softening and damage is adopted and used in place of the stress tensor $\hat{\mathbf{T}}$

$$\hat{\mathbf{T}} \rightarrow \frac{\hat{\mathbf{T}}}{\psi(1-d)} \tag{3.26}$$

which leads to the hyperelastic law for finite plasticity using the *Mandel* [97] type stress tensor

$$\hat{\mathbf{P}} = \left(\hat{\mathbf{I}} + 2\,\hat{\mathbf{\Gamma}}_e\right)\,\hat{\mathbf{T}}. \tag{3.27}$$

Replacing the partial derivatives with terms,

$$\hat{\mathbf{Z}}_i = \rho_R \frac{\partial \Psi}{\partial \hat{\boldsymbol{\alpha}}_i}, \quad \mathfrak{n}_i = \rho_R \frac{\partial \Psi}{\partial x_i}, \quad r_i = \rho_R \frac{\partial \Psi}{\partial \psi_i}, \quad Y = \rho_R \frac{\partial \Psi}{\partial d} \tag{3.28}$$

the entropy inequality (3.24) can be simplified into

$$\frac{\hat{\mathbf{P}}}{\psi(1-d)} \cdot \hat{\mathbf{D}}_p + \varphi\,\dot{\phi} - \hat{\mathbf{Z}}_i \cdot \dot{\hat{\boldsymbol{\alpha}}}_i - r_i\dot{\psi}_i - \mathfrak{n}_i\dot{N}_i - Y\dot{d} \geq 0. \tag{3.29}$$

Since the kinematic hardening variable is a stress tensor by nature, it is also converted into a Mandel type stress as already done for the Cauchy stress. With an assumption that

$$\hat{\boldsymbol{\Omega}} \;=\; \left(\hat{\mathbf{I}} \,+\, 2\,\hat{\boldsymbol{\phi}}\right)\cdot\,\hat{\mathbf{Z}} \tag{3.30}$$

is the translation tensor of the kinematic hardening parameter with $\hat{\boldsymbol{\phi}}$ being a strain type tensor, the entropy inequality eq. (3.29) is written as:

$$\frac{\hat{\mathbf{P}}}{\psi(1-d)}\cdot\hat{\mathbf{D}}_p \;+\; \varphi\,\dot{\phi} - \hat{\boldsymbol{\Omega}}_i\cdot\hat{\mathbf{D}}_p + \hat{\boldsymbol{\Omega}}_i\cdot\hat{\mathbf{D}}_p - \hat{\mathbf{Z}}_i\cdot\dot{\hat{\boldsymbol{\alpha}}}_i \;-\; r_i\dot{\psi}_i \;-\; \mathfrak{n}_i\dot{N}_i \;-\; Y\dot{d} \;\geq 0. \tag{3.31}$$

Substituting eq. (3.30), the above dissipation inequality can be decomposed into separate contributions with each term corresponds to a distinct, energetically conjugate mechanism. Thermodynamic consistency is ensured by requiring the individual contributions to be non-negative.

$$\underbrace{\left(\frac{\hat{\mathbf{P}}}{\psi(1-d)} - \hat{\boldsymbol{\Omega}}_i\right)\cdot\hat{\mathbf{D}}_p + \varphi\dot{\phi} - r_i\dot{\psi}_i - \mathfrak{n}_i\dot{N}_i}_{\text{Part A}} \;+\; \underbrace{\left((1+2\hat{\boldsymbol{\phi}})\hat{\mathbf{D}}_p - \dot{\hat{\boldsymbol{\alpha}}}_i\right)\cdot\hat{\mathbf{Z}}}_{\text{Part B}} \;-\; \underbrace{Y\dot{d}}_{\text{Part C}} \;\geq 0. \tag{3.32}$$

3.3.1 Flow rule

The form of viscoplastic potential (2.103) is recalled, where the over-stress tensor $\boldsymbol{\Sigma}$ is replaced by

$$\hat{\boldsymbol{\Sigma}} = \frac{\hat{\mathbf{P}}}{\psi(1-d)} - \hat{\boldsymbol{\Omega}} \quad \text{with} \quad \hat{\Sigma}_{eq} = \sqrt{\frac{3}{2}\hat{\boldsymbol{\Sigma}}^D\cdot\hat{\boldsymbol{\Sigma}}^D}, \tag{3.33}$$

and its von-Mises equivalent is calculated from the deviatoric part of $\hat{\boldsymbol{\Sigma}}$ to eliminate any influence of volumetric stress in multi-axial loading conditions. Thus, using the normality rule (2.100) with eqs. (2.78) and (2.103), the flow rule and the inelastic strain rate is derived as

$$\hat{\mathbf{D}}_p \;=\; \overset{\triangle}{\hat{\boldsymbol{\Gamma}}}_p \;=\dot{\lambda}\;\frac{\partial F_y}{\partial\hat{\mathbf{P}}} = \;\frac{3}{2}\left\langle\frac{\hat{\Sigma}_{eq}-\sigma_H-k}{K}\right\rangle^{n}\frac{\hat{\boldsymbol{\Sigma}}^D}{\hat{\Sigma}_{eq}}, \tag{3.34}$$

which leads to the accumulated plastic strain rate

$$\dot{p} \;=\; \sqrt{\frac{2}{3}\hat{\mathbf{D}}_p\cdot\hat{\mathbf{D}}_p}. \tag{3.35}$$

3.3.2 Kinematic Hardening

To derive the kinematic hardening equations for finite strains, first, a suitable free energy function that is quadratic in nature to ensure positive definiteness is defined

$$\Psi_p^{\text{Kin}}(t) \;=\; \frac{A_i(p)}{2\,\rho_R}\,\hat{\boldsymbol{\alpha}}_i \cdot \hat{\boldsymbol{\alpha}}_i. \tag{3.36}$$

Here, $A(p)$ is a temperature-dependent, plasticity driven function. The conjugate variable of $\hat{\boldsymbol{\alpha}}_i$ is $\hat{\mathbf{Z}}_i$ which is derived by the partial differentiation of Ψ with respect to $\hat{\boldsymbol{\alpha}}$

$$\hat{\mathbf{Z}}_i \;=\; \rho_R \frac{\partial \Psi}{\partial \hat{\boldsymbol{\alpha}}_i} = \; A_i(p)\;\hat{\boldsymbol{\alpha}}_i. \tag{3.37}$$

Therefore, the time derivative of $\hat{\mathbf{Z}}_i$ is written as

$$\overset{\triangledown}{\hat{\mathbf{Z}}}_i = \; \dot{A}(p)\;\hat{\boldsymbol{\alpha}}_i + \; A_i(p)\;\overset{\triangledown}{\hat{\boldsymbol{\alpha}}}_i.$$

Assuming an isothermal process, $\dot{A}(p) = 0$ and therefore the above relation is simplified to

$$\overset{\triangledown}{\hat{\boldsymbol{\alpha}}}_i \;=\; \frac{\overset{\triangledown}{\hat{\mathbf{Z}}}_i}{A_i(p)} \tag{3.38}$$

and on applying eqs. (2.62) and (2.82), the above relation becomes

$$\dot{\hat{\boldsymbol{\alpha}}}_i \;=\; \frac{\overset{\triangledown}{\hat{\mathbf{Z}}}_i}{A_i(p)} \;+\; 2\,\hat{\mathbf{D}}_p \cdot \hat{\boldsymbol{\alpha}}. \tag{3.39}$$

Therefore, the *Part (B)* from the entropy inequality (3.32) is rewritten as:

$$\hat{\mathbf{Z}}_i \cdot \left\{ \hat{\mathbf{D}}_p \;-\; \frac{\overset{\triangledown}{\hat{\mathbf{Z}}}_i}{A_i(p)} \;+\; 2\,\hat{\mathbf{D}}_p \left(\hat{\boldsymbol{\phi}} \;-\; \hat{\boldsymbol{\alpha}}_i \right) \right\} \geq \; 0. \tag{3.40}$$

To remove the inequality, the term κ_p is introduced

$$\hat{\mathbf{D}}_p \;-\; \frac{\overset{\triangledown}{\hat{\mathbf{Z}}}_i}{A_i(p)} \;+\; 2\,\hat{\mathbf{D}}_p \left(\hat{\boldsymbol{\phi}} \;-\; \hat{\boldsymbol{\alpha}}_i \right) = \; \kappa_p\,\hat{\mathbf{Z}}_i. \tag{3.41}$$

Choosing κ_p to be represented by the function

$$\kappa_p \;=\; \frac{b_i}{a_i}\,\dot{p} \;+ \frac{o_i}{a_i}\,|\hat{\mathbf{Z}}_i|^{m_i - 1}, \tag{3.42}$$

the eq. (3.41) is simplified to

$$\overset{\triangledown}{\hat{\mathbf{Z}}}_i \;=\; A_i(p)\left\{\hat{\mathbf{D}}_p \;-\; \frac{b_i}{a_i}\,\dot{p}\,\hat{\mathbf{Z}}_i \;-\; \frac{o_i}{a_i}\,|\hat{\mathbf{Z}}_i|^{m_i-1}\,\hat{\mathbf{Z}}_i \;+\; 2\,\hat{\mathbf{D}}_p\left(\hat{\boldsymbol{\phi}} \;-\; \hat{\boldsymbol{\alpha}}_i\right)\right\}. \tag{3.43}$$

Choosing the plasticity driven function $A(p)$ from Chaboche [98] as

$$A_i(p) = C_i\,a_i\,f_i(p), \tag{3.44}$$

the evolution equation for the kinematic hardening variable is obtained as

$$\overset{\triangledown}{\hat{\mathbf{Z}}}_i \;=\; C_i\,f_i(p)\left\{a_i\,\hat{\mathbf{D}}_p \;-\; b_i\,\dot{p}\,\hat{\mathbf{Z}}_i \;-\; o_i\,|\hat{\mathbf{Z}}_i|^{m_i-1}\,\hat{\mathbf{Z}}_i \;+\; 2\,a_i\,\hat{\mathbf{D}}_p\left(\hat{\boldsymbol{\phi}} \;-\; \hat{\boldsymbol{\alpha}}_i\right)\right\} \tag{3.45}$$

which fulfills the thermodynamic laws. Here, C_i, a_i, b_i, m_i and o_i are temperature dependent material parameters and $f_i(p)$ is a plasticity driven function. The parameters m_i and o_i characterize the static recovery at high temperatures.

3.3.3 Isotropic Softening

Isotropic hardening and softening for an irradiated material can be described by the summation of the unirradiated and irradiated function

$$\Psi^{iso}(t) = \Psi^{iso}_{unirr} \;+\; \Psi^{iso}_{irr}. \tag{3.46}$$

First, the unirradiated material state is considered where the second component can be ignored. The first term Ψ^{iso}_{unirr} is described by a quadratic function, so as to ensure the convexity and positive definiteness of the free energy function. Ψ^{iso}_{unirr} is described by the evolution of two isotropic variables ψ_1 and ψ_2

$$\Psi^{iso}_{unirr}(t) = \;\frac{1}{2\rho_R}\,\beta(\psi_2^2 - \psi_1^2) \tag{3.47}$$

where β is a positive definite, temperature dependent material parameter. The derivatives of the free energy function with respect to the isotropic variables returns the relation for the conjugate variables

$$R_1 \;=\; \rho_R\frac{\partial\Psi^{iso}_{unirr}}{\partial\psi_1} = -\beta\,\psi_1, \quad R_2 \;=\; \rho_R\frac{\partial\Psi^{iso}_{unirr}}{\partial\psi_2} = \beta\,\psi_2. \tag{3.48}$$

Here the first component R_1 describes the linear softening and the second term R_2 is nonlinear in nature and tends to a saturation value. Their time derivatives are

$$\dot{R}_1 \;=\; -\dot{\beta}\,\psi_1 - \beta\,\dot{\psi}_1, \quad \dot{R}_2 \;=\; \dot{\beta}\,\psi_2 + \beta\,\dot{\psi}_2$$

which can be simplified by assuming an isothermal process ($\dot{\beta} = 0$) to

$$\dot{R}_1 \;=\; -\beta\,\dot{\psi}_1, \quad \dot{R}_2 \;=\; \beta\,\dot{\psi}_2. \tag{3.49}$$

Since isotropic softening is plasticity driven, $\dot{R}_1$ shall be proportional to the accumulated plastic strain rate,

$$\dot{R}_1 = \; \kappa_R\,\dot{p}. \tag{3.50}$$

Taking $h = \kappa_R/\beta$ and using eq. (3.50), the evolution equation (2.112) for ψ_1

$$\dot{\psi}_1 \;=\; -\,h\,\dot{p}$$

is attained. Similarly, by choosing the following relation for $\dot{R}_2$ based on the evolution law for isotropic hardening variable from Chaboche [99]

$$\dot{R}_2 \;=\; \frac{1}{\beta}\left[c\;(\psi_s \;-\; \psi_2)\,\dot{p} \;-\; r_\psi|\psi_2 \;-\; \psi_r|^{m_\psi}\;(\psi_2 \;-\; \psi_r)\right], \tag{3.51}$$

the evolution equation of ψ_2 as shown in eq. (2.113) is reached

$$\dot{\psi}_2 \;=\; c\;(\psi_s \;-\; \psi_2)\,\dot{p} \;-\; r_\psi\,|\psi_2 \;-\; \psi_r|^{m_\psi - 1}\;(\psi_2 \;-\; \psi_r).$$

The conditions that ensure thermodynamic consistency of the isotropic softening variables is discussed later in section 3.3.5.

3.3.4 Irradiation influenced hardening-softening

Since irradiation hardening is isotropic in nature, a similar quadratic free energy function is selected

$$\Psi^{iso}_{ir,i}(t) \;= \frac{1}{2\rho_R}\,\gamma_{N,i}\,N_i^2 \tag{3.52}$$

where γ_N is a temperature dependent material parameter. The partial derivative with respect to irradiation variable N fetches the following relation for $\mathfrak{n}_i$

$$\mathfrak{n}_i = \rho_R\,\frac{\partial \Psi^{iso}_{ir,i}}{\partial N_i} = \gamma_{N,i}\,N_i \tag{3.53}$$

and its time derivative is

$$\dot{\mathfrak{n}}_i = \dot{\gamma}_{N,i}\,N_i + \gamma_{N,i}\,\dot{N}_i. \tag{3.54}$$

Assuming an isothermal process ($\dot{\gamma}_{N,i} = 0$), the time derivative reduces to

$$\dot{\mathfrak{n}}_i = \gamma_{N,i}\, \dot{N}_i. \tag{3.55}$$

A suitable evolution function for $\dot{\mathfrak{n}}$ to describe hardening driven by irradiation and softening due to inelastic deformation and annealing is chosen to be

$$\dot{\mathfrak{n}}_i \;=\; \mathfrak{a}_i \left(N_{s,i} \;-\; N_i\right) \dot{\phi} \;-\; \mathfrak{B}_i \left(N_i - N_{l,i}\right) \dot{p} \;-\; \mathfrak{R}_i\, N_i^{q_{\mathrm{N,i}}}. \tag{3.56}$$

in order to obtain the evolution function (2.115) for the irradiation defect density [53] by taking $a_i = \mathfrak{a}_i/\gamma_{N,i},\ b_i = \mathfrak{b}_i/\gamma_{N,i},\ r_{\mathrm{N,i}} = \mathfrak{R}_i/\gamma_{N,i}$. The first term in eq. (2.115) accounts for the formation of irradiation induced defects as a result of irradiation which reaches a saturation density of $N_{s,i}$. The second term accounts for the removal of defects during inelastic deformation, where $N_{l,i}$ refers to the amount of defects which can be cleared by plastic deformation, while $a_i,\ b_i,\ r_{\mathrm{X,i}},\ q_{\mathrm{X,i}}$ are other material parameters. The third term accounts for the annealing effect at high temperatures, e.g. due to heat treatment over a period of time. Finally, the irradiation hardening σ_H is obtained using the Dispersed Barrier Hardening (DBH) model [54, 53] for n_H defect types that contribute to material hardening:

$$\sigma_H = \sum_i^{n_H} \sigma_{H,i} \quad \text{with} \quad \sigma_{H,i} = \sqrt{h_{N,i}^2 N_i}. \tag{3.57}$$

where $h_{N,i}$ is a temperature and material dependent model parameter that quantifies the effectiveness of obstacles of type i in impeding dislocation motion and promoting pile-up formation.

The phenomenon of defect removal is primarily an outcome of the inelastic deformation, and thus depends on the load history. The resulting softening has a strong influence on the hardening modulus, which has been discussed in section 3.1.1.3. Since the term $N_{l,i}$ controls the portion of the defect density that can be removed, it is a function of the accumulated plastic strain, $N_{l,i} = N_{l,i}(p)$. The type of function chosen to describe $N_{l,i}$ will play a major role in determining the model's stress response. In order to address this, this work introduces the relation

$$N_{l,i} = \left\langle \sqrt{\max_{-\infty<\tau<t} N_i(\tau)} \left(1 - l_{N,i}(2 - e^{-e_1\, p})\right) \right\rangle^2 \tag{3.58}$$

that uses the material's accumulated plastic strain to describe $N_{l,i}$. The tensile characteristics of irradiated Eurofer97 are used as the basis for the equation's construction. Here, $l_{N,i}$ and e_1 are dimensionless, temperature and material-dependent parameters. $l_{N,i}$ controls the portion of defects that may be removed before the rate of defect removal drops, but continues to proceed at a steady rate controlled by e_1. Identification of $l_{N,i}$ at various irradiation doses is discussed later in section 5.1.3.2, where $l_{N,i}$ is seen to reduce with increasing levels of irradiation hardening. This indicates that $l_{N,i} = l_{N,i}(\sigma_{H,max}, \theta)$ is a function of the maximum irradiation hardening, $\sigma_{H,max}$, in addition to testing temperature.

As already described in section 3.2.1, establishing the density of each defect type formed as a result of irradiation is extremely difficult. Furthermore, numerous studies have shown that dislocation loops play the largest role in the irradiation induced material hardening [100–103]. Therefore, a reasonable assumption that the phenomena of irradiation hardening is dominated by only one type of defect is made to simplify the model, which limits to $n_H = 1$. Thereby, the subscript i may be omitted from the eqs. (2.115), (3.57) and (3.58).

3.3.5 Consistency conditions for equations of isotropic variables

To prove the thermodynamic consistency of the evolution equations for isotropic softening and irradiation hardening-softening, the part (A) of Clausius Duhem entropy inequality equation (3.32) is recalled here,

$$\left(\frac{\hat{\mathbf{P}}}{\psi(1-d)} - \hat{\mathbf{\Omega}}_i\right)\cdot\hat{\mathbf{D}}_p + \varphi\dot{\phi} - r_i\dot{\psi}_i - \mathfrak{n}\dot{N} \geq 0$$

where by the substitution of eq.(3.34) and eq. (3.35), the above formulation is reduced to:

$$\mathbf{\Sigma}\cdot\frac{3}{2}\dot{p}\frac{\mathbf{\Sigma}}{\Sigma_{eq}} + \varphi\dot{\phi} - r_i\dot{\psi}_i - \mathfrak{n}\dot{N} \geq 0$$

$$\left(\frac{3}{2}\mathbf{\Sigma}\cdot\mathbf{\Sigma}\right)\frac{1}{\Sigma_{eq}}\dot{p} + \varphi\dot{\phi} - r_i\dot{\psi}_i - \mathfrak{n}\dot{N} \geq 0$$

$$\Sigma_{eq}\,\dot{p} + \varphi\dot{\phi} - r_i\dot{\psi}_i - \mathfrak{n}\dot{N} \geq 0 \tag{3.59}$$

$$\Sigma_{eq}\,\dot{p} - R_1\dot{\psi}_1 - R_2\dot{\psi}_2 + \varphi\,\dot{\phi} - \mathfrak{n}\dot{N} \geq 0 \tag{3.60}$$

From the viscoplastic yield potential (2.103), a relation for Σ_{eq} is obtained as

$$\begin{aligned}\Sigma_{eq} - \sigma_{\text{H}} - k \geq 0\\ \Sigma_{eq} \geq \sigma_{\text{H}} + k.\end{aligned} \tag{3.61}$$

Substituting eqs. (2.115), (3.50), (3.51) and (3.61) in eq. (3.59), the following inequality is reached

$$\begin{aligned}\dot{p}(\sigma_H + k) + \varphi\,\dot{\phi} - \beta\,h\,\psi_1\dot{p} - \beta\psi_2\left[c(\psi_s-\psi_2)\dot{p} - r_\psi(\psi_2-\psi_r)^{m_\psi}\right]\\ - \gamma_N N\left[a(N_s-N)\dot{\phi} - b\,(N-N_l)\dot{p} - r_N N^{q_N}\right] \geq 0.\end{aligned} \tag{3.62}$$

Segregating irradiation and inelastic deformation related terms,

$$[k - \beta\,h\,\psi_1 - c\,\beta\,\psi_2(\psi_s-\psi_2)]\,\dot{p} + \beta\,r_\psi\,\psi_2(\psi_2-\psi_r)^{m_\psi}$$

$$+\left[\sigma_H + \gamma_N\, b\, N(N-N_l)\right]\dot{p} + \left[\varphi - \gamma_N\, a\, N\,(N_s-N)\right]\dot{\phi} - \gamma_N\, N\, r_N\, N^{q_N+1} \geq 0 \quad (3.63)$$

an inequality is derived to determine φ. During irradiation $\dot{\phi} \geq 0$, therefore

$$\varphi - \gamma_N\, a\, N\,(N_s-N) \geq 0 \rightarrow \frac{d\,\sigma_H}{d\,\phi} \geq \gamma_N\, a\, N\,(N_s-N).$$

The partial derivative of $N\,(\phi, p)$ in the absence of plastic deformation leads to

$$\dot{N}(\phi) = \frac{dN}{\partial\phi}\dot{\phi}.$$

Comparing the coefficients in this relation with eq. (2.115) helps us obtain the relationship

$$\frac{dN}{d\phi} = a(N_s-N). \quad (3.64)$$

Thereby, the relation for φ can be deduced as

$$\varphi = \frac{d\sigma_H(\phi)}{d\phi} = \frac{d}{d\phi}\sqrt{h_N^2\, N} = \frac{h_N}{2\sqrt{N}}\frac{dN}{d\phi}$$
$$= \frac{h_N}{2\sqrt{N}}\, a(N_s-N). \quad (3.65)$$

In the case of unirradiated condition, with $\dot{p} \geq 0$, the following consistency conditions are deduced from eqs. (3.62) and (3.63):

1. Since β is already assumed to be positive definite,

   $$-\beta\; h\; \psi_1 \geq 0 \quad \rightarrow \quad \psi_1 \leq 0 \quad \text{if} \quad h \geq 0 \text{ or vice versa} \quad (3.66)$$

   are two solutions that exist based on the choice of parameter h.

2. $$-\beta\; r_\psi\; \psi_2(\psi_2-\psi_r)^{m_\psi} \geq 0 \quad \rightarrow \quad r_\psi \geq 0,\; \psi_2 \geq 0\;\&\;\psi_2 \geq \psi_r \quad (3.67)$$

   suggests the limits for the parameter ψ_r to be $\psi_2 \geq \psi_r \geq 0$.

3. Since $\psi_1 \leq 0, \psi_2 \geq 0$ while $\psi \leq 1$, the initial values of the isotropic variables are chosen as

   $$\psi_1 = 0\;\&\;\psi_2 = 1 \text{ at } t = 0. \quad (3.68)$$

4. $$-\beta\; c\; \psi_2(\psi_s-\psi_2) \geq 0 \quad \rightarrow \quad \psi_s \leq \psi_2 \quad \text{if} \quad c \geq 0 \text{ or vice versa}$$

   for which two solutions exist, based on the choice of ψ_s. It is further illustrated by

$$k - \beta\ [h\psi_1 + c\ \psi_2\,(\psi_s - \psi_2)] \geq 0 \quad \rightarrow \quad c \geq \frac{h\psi_1}{\psi_2(\psi_s - \psi_2)} \quad \because k \geq 0,\ \beta \geq 0 \tag{3.69}$$

which indicates that for $\psi_s > \psi_2$, c is positive and for $\psi_s < \psi_2$, c is negative.

Similarly, for the irradiated material the following conditions are deduced with the consideration of $\dot{p} \geq 0,\ \dot{\phi} \geq 0$ using eqs. (3.63) and (3.65):

1. $$a(N_s - N)\left[\frac{h_N}{2\sqrt{N}} - \gamma_N N\right] \geq 0 \quad \rightarrow \quad a \geq 0,\ N_s \geq N,\ \gamma_N \leq \frac{\sigma_H}{2N^2} \tag{3.70}$$

   is necessary for the formation of defects. And since γ_N is positive definite,

$$0 \leq \gamma_N \leq \frac{h_N}{2N\sqrt{N}}. \tag{3.71}$$

2. $$b \geq -\frac{\sigma_H}{\gamma_N\ N(N - N_l)} \tag{3.72}$$

   Since only available flaws can be removed, $N_l \leq N$. Experiments show that N_l is always less than the number of defects of greatest possible hardening [86], implying that $N_l < N_s$. As a result, the right-hand side of the relationship will always be less than or equal to 0. This means that, the only constraint for the parameter is that $b \geq 0$.

3. $$\gamma_N\ r_N\ N^{q_N+1} \geq 0 \tag{3.73}$$

   Since $\gamma_N > 0, N \geq 0$, the condition that r_N must always be positive, i.e $r_N \geq 0$ is obtained.

3.4 Viscoplastic extension for ductile damage model

The following viscoplastic yield criterion is proposed based on the GTN yield surface (2.130) as similarly done for the viscoplastic yield criterion of the model without ductile damage (2.103)

$$\Phi = \left(\frac{\hat{\Sigma}_{eq}}{\sigma_s}\right)^2 + 2\ f^*\ q_1\ Cosh\left(\frac{3}{2}\,q_2\,\frac{\hat{\Sigma}_v}{\sigma_A}\right) - 1 - (q_1\ f^*)^2 \geq 0. \tag{3.74}$$

Since the plasticity framework of Gurson already accounts for the material deterioration due to the VVF development, $(1 - f)$ is omitted from the over stress formulation (2.105)

$$\hat{\mathbf{\Sigma}} = \frac{\hat{\mathbf{T}}}{\psi} - \hat{\mathbf{Z}}. \tag{3.75}$$

The eqs. (2.103) and (3.74) implies that the stress states fulfilling it may lie outside the yield surface by the so-called viscous stress. While the equivalent value of the viscous stress σ_{vis} is directly given by the left side of eq. (2.103), the inequality eq. (3.74) is modified by updating the yield stresses with

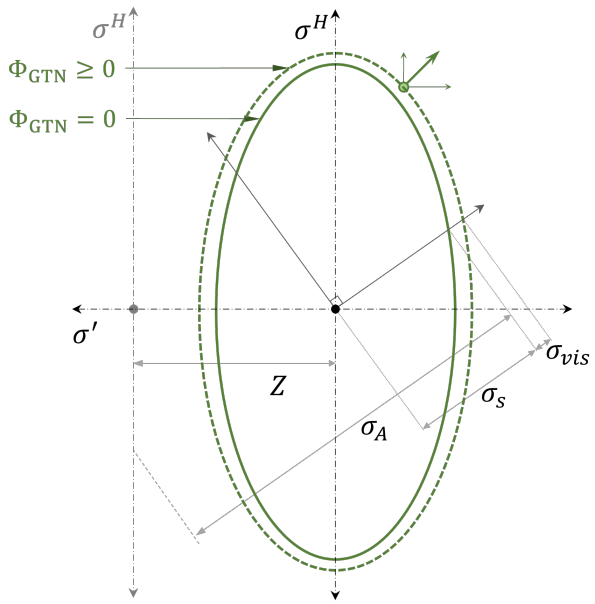

Figure 3.9: Viscoplastic GTN yield potential with kinematic hardening.

the equivalent viscous stress in the matrix material to the following equality which describes all stress states with the same σ_{vis} and hence the same viscoplastic yield potential

$$\Phi = \left(\frac{\hat{\Sigma}_{eq}}{\sigma_s + \sigma_{vis}} \right)^2 + 2\, f^*\, q_1\, Cosh\left(\frac{3}{2}\, q_2\, \frac{\hat{\Sigma}_v}{\sigma_A + \sigma_{vis}} \right) - 1 - (q_1\, f^*)^2 = 0 \tag{3.76}$$

where $\sigma_s = k + \sigma_H$. The GTN yield surface and potential surface are illustrated in the fig. 3.9. To obtain σ_{vis} for a given stress state fulfilling eq. (3.74), the eq. (3.76) needs to be solved and the corresponding inelastic strain rate in the matrix material can be identified as

$$\dot{\varepsilon}_M = \left\langle \frac{\sigma_{vis}}{K} \right\rangle^n . \tag{3.77}$$

Since only the matrix material is considered to undergo kinematic hardening [58, 65], its yield and potential surfaces translate over the deviatoric plane. With this consideration, the history-dependent term σ_A was introduced to track the hardening behaviour and determines the so-called limiting surface. In this work, σ_A is proposed to be given by

$$\sigma_A = \max_{-\infty<\tau<t} \left(\sigma_s(\tau)\right) + \max_{-\infty<\tau<t} \left(\hat{Z}_{eq}(\tau)\right) \tag{3.78}$$

which corresponds to the farthest stress state achieved by the yield surface during the load history.

The inelastic strain rate for the considered stress state is derived by applying the normality rule on the corresponding viscoplastic potential surface given by eq. (3.76)

$$\hat{\mathbf{D}}_p = \dot{\lambda}\hat{\mathbf{N}} \quad \text{where} \quad \hat{\mathbf{N}} = \frac{\partial \Phi}{\partial \hat{\mathbf{\Sigma}}} = \left(\frac{\partial \Phi}{\partial \hat{\Sigma}_v} \frac{\partial \hat{\Sigma}_v}{\partial \hat{\mathbf{\Sigma}}} + \frac{\partial \Phi}{\partial \hat{\Sigma}_{eq}} \frac{\partial \hat{\Sigma}_{eq}}{\partial \hat{\mathbf{\Sigma}}} \right). \tag{3.79}$$

The first term in eq. (3.79) is related to the hydrostatic stress

$$\frac{\partial \Phi}{\partial \hat{\Sigma}_v} \frac{\partial \hat{\Sigma}_v}{\partial \hat{\mathbf{\Sigma}}} = \frac{3\, f^*\, q_1\, q_2}{\sigma_A + \sigma_{vis}} Sinh\left(\frac{3}{2} q_2 \frac{\hat{\Sigma}_v}{\sigma_A + \sigma_{vis}} \right) \frac{\partial \hat{\Sigma}_v}{\partial \hat{\mathbf{\Sigma}}} \tag{3.80}$$

where $\dfrac{\partial \hat{\Sigma}_v}{\partial \hat{\mathbf{\Sigma}}} = \dfrac{1}{3}\hat{\mathbf{I}}$ and the second term is related to the deviatoric part of stress tensor

$$\frac{\partial \Phi}{\partial \hat{\Sigma}_{eq}} = \frac{2\,\hat{\Sigma}_{eq}}{(\sigma_s + \sigma_{vis})^2} \quad \text{and} \quad \frac{\partial \hat{\Sigma}_{eq}}{\partial \hat{\mathbf{\Sigma}}^D} = \frac{3}{2} \frac{\hat{\mathbf{\Sigma}}^D}{\hat{\Sigma}_{eq}}. \tag{3.81}$$

Using eqs. (3.80) and (3.81), the inelastic strain rate is written as

$$\begin{aligned} \hat{\mathbf{D}}_p &= \dot{\lambda} \left[\frac{1}{3} \frac{3\, f^*\, q_1\, q_2}{\sigma_A + \sigma_{vis}} Sinh\left(\frac{3}{2} q_2 \frac{\hat{\Sigma}_v}{\sigma_A + \sigma_{vis}} \right) \hat{\mathbf{I}} + \frac{3\hat{\mathbf{\Sigma}}^D}{2\,\hat{\Sigma}_{eq}} \left(\frac{2\,\hat{\Sigma}_{eq}}{(\sigma_s + \sigma_{vis})^2} \right) \right] \\ &= \dot{\lambda} \left[\frac{f^*\, q_1\, q_2}{\sigma_A + \sigma_{vis}} Sinh\left(\frac{3}{2} q_2 \frac{\hat{\Sigma}_v}{\sigma_A + \sigma_{vis}} \right) \hat{\mathbf{I}} + \frac{3\hat{\mathbf{\Sigma}}^D}{(\sigma_s + \sigma_{vis})^2} \right]. \end{aligned} \tag{3.82}$$

Considering that the power dissipated by inelastic deformation of the considered damaged volume element is that dissipated in its matrix material, the following relation (also seen in eq. (2.123)) can be derived

$$\hat{\mathbf{\Sigma}} \cdot \hat{\mathbf{D}}_p = (1-f)\,(\sigma_s + \sigma_{vis})\,\dot{\varepsilon}_M. \tag{3.83}$$

The inelastic multiplier ($\dot{\lambda}$) to be identified by substituting the relations eqs. (3.77) and (3.82) into eq. (3.83)

$$\begin{aligned} \dot{\lambda} &= (1-f)\, \frac{\sigma_s + \sigma_{vis}}{\hat{\mathbf{\Sigma}} \cdot \hat{\mathbf{N}}} \left\langle \frac{\sigma_{vis}}{K} \right\rangle^n \\ \text{where} \quad \hat{\mathbf{\Sigma}} \cdot \hat{\mathbf{N}} &= \frac{2\,\hat{\Sigma}_{eq}^2}{(\sigma_s + \sigma_{vis})^2} + \hat{\Sigma}_v \frac{f^*\, q_1\, q_2}{\sigma_A + \sigma_{vis}} Sinh\left(\frac{3}{2} q_2 \frac{\hat{\Sigma}_v}{\sigma_A + \sigma_{vis}} \right) \end{aligned} \tag{3.84}$$

Therefore the inelastic strain rate of the damaged material is given by

$$\hat{\mathbf{D}}_p = (1-f) \left\langle \frac{\sigma_{vis}}{K} \right\rangle^n \frac{\sigma_s + \sigma_{vis}}{\hat{\mathbf{\Sigma}} \cdot \hat{\mathbf{N}}} \left[\frac{f^*\, q_1\, q_2}{\sigma_A + \sigma_{vis}} Sinh\left(\frac{3}{2} q_2 \frac{\hat{\Sigma}_v}{\sigma_A + \sigma_{vis}} \right) \hat{\mathbf{I}} + \frac{3\,\hat{\mathbf{\Sigma}}^D}{(\sigma_s + \sigma_{vis})^2} \right] \tag{3.85}$$

which reduces to eq. (3.34) for $f = f^* = 0$.

3.5 Simplified model for small elastic deformation

For large plastic deformation of materials, the elastic part of the strain is much smaller in comparison to the plastic strain. Based on this, the derived finite strain model is simplified. First, the elastic behaviour which is linear in nature can be described for isotropic materials using the free energy function

$$\hat{\Psi}_e(\hat{\mathbf{\Gamma}}_e) = (1-f^*)\left[\frac{\mu}{\rho_R}\hat{\mathbf{\Gamma}}_e\cdot\hat{\mathbf{\Gamma}}_e + \frac{\lambda}{2\,\rho_R}\left(\operatorname{tr}\hat{\mathbf{\Gamma}}_e\right)^2\right], \tag{3.86}$$

which ensures that the elastic relationship is compatible with Hooke's law. Here, $(1-f^*)$ is included to account for the reduction of stiffness in the volume element due to VVF. Here $\mu(\Theta), \lambda(\Theta)$ are the Lamé constants. Using eqs. (3.25) and (3.86), the hyperelastic law to describe stress evolution

$$\hat{\mathbf{T}} = \rho_R\frac{\partial\Psi}{\partial\hat{\mathbf{\Gamma}}_e} = (1-f^*)\left[2\,\mu\hat{\mathbf{\Gamma}}_e + \lambda\operatorname{tr}\hat{\mathbf{\Gamma}}_e\mathbf{I}\right] = \mathbb{C}\cdot\hat{\mathbf{\Gamma}}_e \tag{3.87}$$

$$\text{with}\quad \mathbb{C} = (1-f^*)\left[2\mu\mathbb{I} + \lambda(\mathbf{I}\otimes\mathbf{I})\right] \tag{3.88}$$

in the damaged element is obtained. Here, $\mathbb{C}$ is a fourth order elasticity tensor of the volume element. $\mathbb{I}$ is the symmetric part of the fourth-order identity tensor. For the consideration of small elastic deformations, Jansohn [95] showed that the transformation of tensor variables from $\hat{\mathcal{X}}_t$ to $\mathcal{X}_t$ only amounts to rigid body motion ($\mathbf{V}_e \approx \mathbf{I},\ \mathbf{F}_e = \mathbf{R}_e$). Furthermore, the model can be simplified to constitute the variables defined in $\mathcal{X}_t$, while still maintaining the original structure. As a result, the transformation of Mandel stress in eq. (3.27) to $\mathcal{X}_t$ results in the weighted Cauchy stress, $\mathbf{S}$.

$$\hat{\mathbf{P}} = \hat{\mathbf{F}}_e^T\ \hat{\mathbf{F}}_e\hat{\mathbf{T}} = \hat{\mathbf{T}} \tag{3.89}$$

$$\rightarrow\quad \mathbf{S} = \hat{\mathbf{R}}_e\ \hat{\mathbf{T}}\ \hat{\mathbf{R}}_e^T = \mathbb{C}\left[\mathbf{A}_e\right] = \mathbb{C}\left[\mathbf{A}-\mathbf{A}_p\right] \tag{3.90}$$

Application of the Oldroyd derivatives (2.75), (2.82) to $\hat{\mathbf{T}}$ and $\hat{\mathbf{\Gamma}}_e$ leads to

$$\overset{\triangledown}{\hat{\mathbf{T}}} - \mathbb{C}\cdot\overset{\triangle}{\hat{\mathbf{\Gamma}}}_e = \frac{\partial\mathbb{C}}{\partial\theta}\cdot\hat{\mathbf{\Gamma}}_e\ \dot{\theta}\ - \mathbb{C}\left[\mathbf{L}_p^T\hat{\mathbf{\Gamma}}_e + \hat{\mathbf{\Gamma}}_e\mathbf{L}_p\right] - \mathbf{L}_p\mathbb{C}\cdot\hat{\mathbf{\Gamma}}_e - \mathbb{C}\cdot\hat{\mathbf{\Gamma}}_e\mathbf{L}_p^T. \tag{3.91}$$

For an isothermal process, $\dot{\theta}$=0. And, since $|\hat{\mathbf{\Gamma}}_e| \ll 1$, the terms on the right side can be neglected. Therefore, the hyper-elastic relations in eq. (3.90) can be approximated through the hypo-elastic law

$$\overset{\triangledown}{\hat{\mathbf{T}}} = \mathbb{C}\cdot\overset{\triangle}{\hat{\mathbf{\Gamma}}}_e = \mathbb{C}\cdot\left[\overset{\triangle}{\hat{\mathbf{\Gamma}}} - \overset{\triangle}{\hat{\mathbf{\Gamma}}}_p\right] \quad \text{or} \quad \overset{\triangledown}{\hat{\mathbf{T}}} = \mathbb{C}\cdot\left[\hat{\mathbf{D}} - \hat{\mathbf{D}}_p\right]. \tag{3.92}$$

Transforming the above hypo-elastic law to $\mathcal{X}_t$ and using eq. (2.77), the following relation to describe the evolution of weighted Cauchy stress is obtained, where the deformation rate $\hat{\mathbf{D}}$ is co-rotational.

$$\overset{\triangledown}{\mathbf{S}} = \frac{\partial \mathbb{C}}{\partial \Theta} \cdot \mathbf{A}_e \, \dot{\Theta} \, + \, \mathbb{C} \cdot \overset{\triangle}{\mathbf{A}}_e \tag{3.93}$$

Here, for an isothermal process and small elastic deformations, the first term reduces to zero.

$$\overset{\triangledown}{\mathbf{S}} = \mathbb{C} \cdot [\mathbf{D} - \mathbf{D}_p] \tag{3.94}$$

Similarly, the kinematic hardening can also be simplified with the consideration of

$$\hat{\boldsymbol{\phi}} \; = \; \hat{\boldsymbol{\alpha}}_i \tag{3.95}$$

for small elastic deformations, leading to a relationship very similar to Frederick and Armstrong [52]:

$$\overset{\triangledown}{\mathbf{Z}}_i \; = \; \hat{\mathbf{R}}_e \, \overset{\triangledown}{\hat{\mathbf{Z}}}_i \, \hat{\mathbf{R}}_e^T \; = \; C_i \, f_i(p) \left\{ a_i \, \mathbf{D}_p^D \; - \; b_i \, \dot{p} \, \mathbf{Z}_i \; - \; o_i \, |\mathbf{Z}_i|^{m_i - 1} \, \mathbf{Z}_i \right\}. \tag{3.96}$$

When the GTN damage model is used, $\mathbf{D}_p$ (3.85) is influenced by the hydrostatic stress for $f^* > 0$. Therefore, $\mathbf{D}_p^D$ is used in place of $\mathbf{D}_p$ to ensure the deviatoric nature of the kinematic hardening variable. In addition, the parameters for each term are combined for simplicity, to form the relation

$$\overset{\triangledown}{\mathbf{Z}}_i \; = \; H_i \, \mathbf{D}_p^D \; - \; Q_i \, \dot{p} \, \mathbf{Z}_i \; - \; R_i \, |\mathbf{Z}_i|^{m_i - 1} \, \mathbf{Z}_i. \tag{3.97}$$

Transformation of $\hat{\boldsymbol{\Sigma}}$ to $\mathcal{X}_t$, leads to the over-stress tensor $\boldsymbol{\Sigma}$ that is calulated from

$$\boldsymbol{\Sigma} = \frac{\mathbf{S}}{\psi} - \mathbf{Z}. \tag{3.98}$$

The elastic and inelastic components of the Almansi strain are obtained from the transformations in eqs. (2.69) to (2.71). The constitutive equations that describe scalar state variables will remain unchanged. To integrate the model, a suitable integration algorithm capable of maintaining the model objectivity is adopted and discussed in the next chapter.

3.5.1 Summary

The evolution equations describing all model variables are summarized in section 3.5.1. A suitable integration algorithm that can handle the potential rigid body rotations and ensure the frame-indifference or material objectivity needs to be used for solving the formulated set of constitutive equations. Such a procedure is discussed in section 4.2.

Stress a) Elasticity b) Hypo-elasticity

$$\mathbf{S} = \mathbb{C} \cdot [\mathbf{A} - \mathbf{A}_p] \qquad \overset{\triangledown}{\mathbf{S}} = \mathbb{C} \cdot \left[\overset{\triangle}{\mathbf{A}} - \overset{\triangle}{\mathbf{A}}_p \right] \tag{3.99}$$

Flow rule

$$F = \Sigma_{eq} - \sigma_s \quad \text{with } \sigma_s = \begin{cases} \sigma_{vis} + k & \text{unirradiated} \\ \sigma_{vis} + k + \sigma_H & \text{irradiated} \end{cases} \tag{3.100}$$

$$\mathbf{\Sigma} = \frac{\mathbf{S}}{\psi} - \mathbf{Z} \quad \text{and} \quad \Sigma_{eq} = \sqrt{\frac{3}{2}\, \mathbf{\Sigma}^D \cdot \mathbf{\Sigma}^D} \tag{3.101}$$

Inelastic strain rate

$$\begin{aligned} \mathbf{D}^p &= \overset{\triangle}{\mathbf{A}}_p \\ &= (1-f) \left\langle \frac{\sigma_{vis}}{K} \right\rangle^n \frac{\sigma_s + \sigma_{vis}}{\mathbf{\Sigma} \cdot \mathbf{N}} \left[\frac{f^*\, q_1\, q_2}{\sigma_A + \sigma_{vis}} Sinh\left(\frac{3}{2}\, q_2\, \frac{\Sigma_v}{\sigma_A + \sigma_{vis}} \right) \mathbf{I} + \frac{3\, \mathbf{\Sigma}^D}{(\sigma_s + \sigma_{vis})^2} \right] \end{aligned} \tag{3.102}$$

Accumulated plastic strain rate

$$\dot{p} = \sqrt{\frac{3}{2}\, \mathbf{D}_p \cdot \mathbf{D}_p} \tag{3.103}$$

Kinematic hardening

$$\overset{\triangledown}{\mathbf{Z}}_i \;=\; H_i\, \mathbf{D}_p^D \;-\; Q_i\, \dot{p}\, \mathbf{Z}_i \;-\; R_i\, |\mathbf{Z}_i|^{m_i - 1}\, \mathbf{Z}_i, \quad \mathbf{Z} = \sum_i^{m_\mathbf{Z}} \mathbf{Z}_i \tag{3.104}$$

Isotropic softening

$$\dot{\psi}_1 \;=\; -\, h\, \dot{p} \tag{3.105}$$

$$\dot{\psi}_2 \;=\; c\, (\psi_s \;-\; \psi_2)\, \dot{p} \;-\; r_\psi\, |\psi_2 \;-\; \psi_r|^{m_\psi - 1}\, (\psi_2 \;-\; \psi_r) \tag{3.106}$$

Irradiation defect density

$$\dot{N} \;=\; a\,(N_s \;-\; N)\, \dot{\phi} - \; b\,(N - N_l)\, \dot{p} - \; r_{\mathrm{N}}\, N^{q_{\mathrm{N}}}, \quad \sigma_H = h_N \sqrt{N} \tag{3.107}$$

$$\text{with} \quad N_l = \left\langle \sqrt{\max_{-\infty < \tau < t} N(\tau)}\, \left(1 - l_N (2 - e^{-e_1\, p})\right) \right\rangle^2 \tag{3.108}$$

Viscoplastic GTN ductile damage

$$\dot{f} \;=\; \frac{f_N}{s_N \sqrt{2\pi}} \exp\left[-\frac{1}{2} \left(\frac{\varepsilon_M - \varepsilon_N}{s_N} \right)^2 \right] + \; (1-f)\; \mathrm{trace}(\mathbf{D}_p) \tag{3.109}$$

$$f^* = \begin{cases} f & , \text{if } f \le f_c \\ f_c + \dfrac{f_u^* - f_c}{f_F - f_c}\, (f - f_c) & , \text{if } f > f_c \end{cases} \tag{3.110}$$

$$\dot{\varepsilon}_M = \left\langle \frac{\sigma_{vis}}{K} \right\rangle^n \tag{3.111}$$

Table 3.4: Constitutive system of equations for coupled finite deformation and ductile damage.

Chapter 4

Model integration

This chapter deals with the implementation of the material model in a finite element method code. To do this, it is necessary to understand the implementation of the finite strain framework in finite element method and the type of contribution between the material model and the global FEM calculation. Since finite strain framework describes material deformation across a series of configurations with potential finite rotations, the concept of frame-indifference has to be upheld by both the FEM code as well as the material model.

First the basics of FEM formulation is discussed, followed by the integration approaches available for finite strain and rotations. Later, the integration scheme and integration algorithm used to solve the model is discussed in detail.

4.1 Finite element formulation

4.1.1 Weak form of the balance of momentum

For mechanical problems, the FE method is based on variational methods and virtual displacements, which are derived from the local form of the balance of momentum (2.23)

$$\operatorname{div} \mathbf{T} + \rho\,(\boldsymbol{k} - \ddot{\boldsymbol{x}}) = 0. \tag{4.1}$$

In the intermediate configuration, displacement and stress boundary conditions are applied on the surface of the body ∂R_t.

$$\boldsymbol{u} = \boldsymbol{u}_R(\boldsymbol{x},t), \quad \mathbf{T}\,\boldsymbol{n} = \boldsymbol{t}_R(\boldsymbol{x},t) \tag{4.2}$$

An initial value problem is defined based on the field equations (4.1), boundary conditions (4.2) and initial conditions for displacement $\boldsymbol{x}$ and velocity $\dot{\boldsymbol{x}}$. A weak form of the initial value problem is derived by multiplying the eq. (4.1) by a test function $\boldsymbol{\chi}$ and integrating it over the volume of the

body.

$$\int_{R_t} [\boldsymbol{\chi} \cdot \operatorname{div} \mathbf{T} + \rho \boldsymbol{\chi} \cdot (\boldsymbol{k} - \ddot{\boldsymbol{x}})] \, \mathrm{d}v = 0 \tag{4.3}$$

Test functions act as weight functions, with $\boldsymbol{\chi}$ being a virtual displacement. The virtual state is constrained by the boundary condition $\boldsymbol{\chi}_R = 0$. Applying the product rule and the Gaussian integral theorem to the first term in eq. (4.3) leads to

$$\int_{R_t} \mathbf{T} \cdot \operatorname{grad} \boldsymbol{\chi} \, \mathrm{d}v - \int_{R_t} \rho \boldsymbol{\chi} \cdot (\boldsymbol{k} - \ddot{\boldsymbol{x}}) \, \mathrm{d}v - \int_{\partial R_t} \mathbf{T} \boldsymbol{\chi}_R \cdot \boldsymbol{n} \, \mathrm{d}a = 0 \tag{4.4}$$

Alternatively, applying constraints of the initial boundary and loading conditions leads to the equilibrium system

$$\mathcal{G}(\boldsymbol{u}, \boldsymbol{\chi}) = \int_{R_t} \mathbf{T} \cdot \operatorname{grad} \boldsymbol{\chi} \, \mathrm{d}v - \int_{R_t} \rho \boldsymbol{\chi} \cdot (\boldsymbol{k} - \ddot{\boldsymbol{x}}) \, \mathrm{d}v - \int_{\partial R_t} \mathbf{T} \boldsymbol{\chi}_R \cdot \boldsymbol{n} \, \mathrm{d}a = 0 \tag{4.5}$$

which satisfies the balance of momentum (4.1) and the loading constraints in its integral form. The stress, $\mathbf{T}$ in these equations is provided by the material model. Spatial discretization of this weakform is used by finite element method. And for n degrees of freedom used in the FE models, the initial value problem is described by a system of n non-linear equations. The ansatz functions fulfilling the essential boundary conditions approximate the unknown variables.

4.1.2 General non-linear problem

The finite element calculations involving non-linear constitutive models deal with the challenge of calculating the stress for an estimated displacement of a body, which satisfies the spatially discretized weak form of the momentum balance eq. (4.5). This is accomplished through an incremental method, where the displacement is revised until the stress satisfies the weak form.

Consider the motion of a physical body $\mathcal{B}$ relative to a fixed Cartesian coordinate system (see fig. 4.1). The equilibrium configurations of $\mathcal{B}$ are evaluated at discrete time instances. Assuming that the equilibrium at t is already known, the aim is to find the equilibrium configuration for a given time increment Δt, at time $t + \Delta t$, which defines a strain-controlled problem. Variables referring to time t are identified by the subscript '0', while those corresponding to time $t + \Delta t$ are identified by the index '1'. In addition, the variables associated with intermediate configurations have the subscript 'i'. Therefore, at the times t_i, t_0, and t_1, the body $\mathcal{B}$ occupies spatial configurations $\mathcal{X}_i, \mathcal{X}_0$, and $\mathcal{X}_1$ with the position vectors $\boldsymbol{X}$, $\boldsymbol{x}_0$, and $\boldsymbol{x}_1$.

While the displacement vector $\boldsymbol{u}(\boldsymbol{X}, t) = \boldsymbol{x}_0 - \boldsymbol{X}$ determines the equilibrium state at time t, the ideal equilibrium state at time $t + \Delta t$ is defined by the incremental displacement vector $\Delta \boldsymbol{u} = \boldsymbol{x}_1 - \boldsymbol{x}_0$. The deformation gradients $\mathbf{F}_0$, $\mathbf{F}_1$, and $\Delta \mathbf{F}$ operate between the vector spaces of points in $(\mathcal{X}_i - \mathcal{X}_0)$, $(\mathcal{X}_i - \mathcal{X}_1)$, and $(\mathcal{X}_0 - \mathcal{X}_1)$, respectively, where $\mathbf{F}_1 = \Delta \mathbf{F} \, \mathbf{F}_0$. An updated Lagrangian formulation is used, where the reference configuration is updated for each time step.

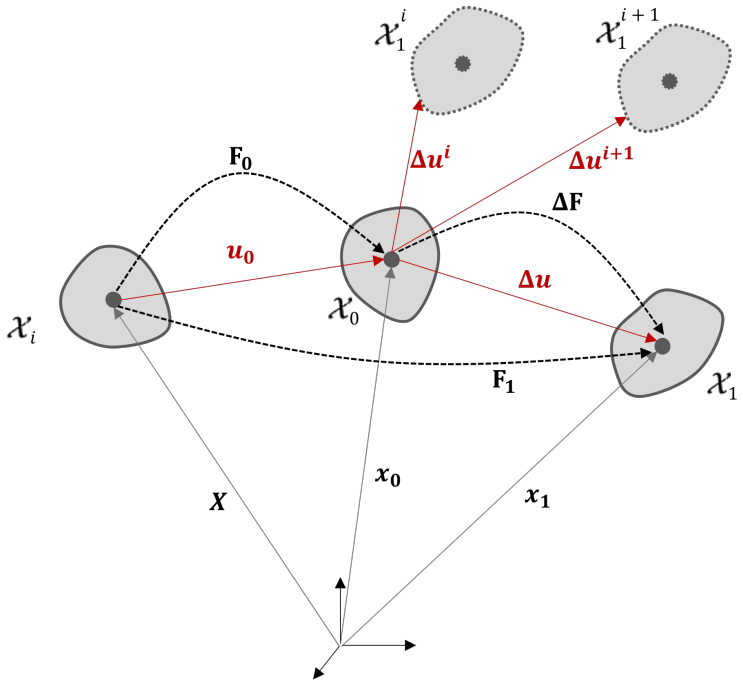

Figure 4.1: Finite element calculation of equilibrium points.

4.1.3 Incremental objectivity

The method adopted to integrate the non-linear constitutive material laws have certain requirements to fulfill. In addition to the usual consistency and stability of the integration scheme, algorithms must ensure that the calculation of stress and all internal variables is frame-indifferent or objective. For this, the corotational Jaumann derivative is used and the elasticity is modeled using the hypo-elasticity law. Different interpretations of incremental objectivity and several time objective integration methods can be found in literature [104–109]. The interpretation of Hughes [110] which is used by the FE program ABAQUS, is adopted here. An integration procedure based on this definition, was proposed in the works of Weber [111], Weber and Anand [112], which is discussed here.

The orthogonal tensor $\mathbf{Q}$ is defined by the solution of the initial value problem [110]

$$\begin{aligned} \dot{\mathbf{Q}}(\zeta) &= \mathbf{W}(\zeta)\,\mathbf{Q}(\zeta) \quad ,\zeta \in [t_0, t_1] \\ \dot{\mathbf{Q}}(t_0) &= \mathbf{I}, \end{aligned} \tag{4.6}$$

which is used to transform tensor quantities with respect to rigid body rotations. Based on this, the bar-transformation operation of a tensor $\mathbf{X}$ is defined [111, 112]

$$\bar{\mathbf{X}}(\zeta) = \mathbf{Q}^T(\zeta)\,\mathbf{X}(\zeta)\,\mathbf{Q}(\zeta) \quad \text{with} \quad \bar{\mathbf{X}}(t_0) = \mathbf{X}(t_0) \tag{4.7}$$

which can be described as a "rotation-neutralizing" transformation. This is applied to all tensors in the constitutive model. From eqs. (4.6) and (4.7), the time derivative of bar-transformed quantities is

related to the Jaumann derivative

$$\dot{\tilde{\mathbf{X}}}(\zeta) = \mathbf{Q}^T(\zeta)\, \overset{\circ}{\mathbf{X}}(\zeta)\, \mathbf{Q}(\zeta). \tag{4.8}$$

If $\mathbf{Q}$ at the end of time increment t_1 is known, then the interpolation of all kinematic quantities within the time increment $[t_0,\ t_1]$ can be avoided. Thus, the constitutive system of equations can be free of the complex Jaumann derivatives, with derivatives of the form $\dot{\tilde{\mathbf{X}}}$ taking its place.

Since the evolution of stress and the internal variables is driven by the deformation rate $\bar{\mathbf{D}}$, the integration algorithm only requires $\bar{\mathbf{D}}$ and $\mathbf{Q}$ to be objective. To interpolate these two tensors, the incremental deformation gradient is first calculated

$$\Delta\mathbf{F}(t_1) = \mathbf{F}_1\, \mathbf{F}_0^{-1} \tag{4.9}$$

which can be decomposed into the increments of rotation and stretch tensors

$$\Delta\mathbf{F}(t_1) = \Delta\mathbf{R}(t_1)\, \Delta\mathbf{U}(t_1). \tag{4.10}$$

Then, the interpolated forms of $\bar{\mathbf{D}}$ and $\mathbf{Q}$ are shown to be

$$\bar{\mathbf{D}}(\zeta) = \bar{\mathbf{D}}\,(\Delta\mathbf{U}(t_1), \zeta) \quad \text{with} \quad \bar{\mathbf{D}}\,(\mathbf{I}, \zeta) = 0, \tag{4.11}$$

$$\mathbf{Q}(t_1) = \Delta\mathbf{R}(t_1) \tag{4.12}$$

where $\bar{\mathbf{D}}$ is made to be a function of the stretch tensor increment $\Delta\mathbf{U}$ alone. Weber [111] proposed that the interpolants can be held as a constant throughout the time increment, provided they can be approximated by a suitable method. The approximation method of the interpolants from Hughes and Winget [104] is suitable for application here [95]. The midpoint rule [110] is used to calculate the constant value of the deformation rate and swirl tensors as

$$\mathbf{D}_{HW} = \frac{1}{\Delta t}\, sym\left(\frac{\partial \Delta \boldsymbol{u}}{\partial \boldsymbol{x}_{1/2}}\right), \quad \mathbf{W}_{HW} = \frac{1}{\Delta t}\, asym\left(\frac{\partial \Delta \boldsymbol{u}}{\partial \boldsymbol{x}_{1/2}}\right), \tag{4.13}$$

with $\boldsymbol{x}_{1/2} = 0.5\,(\boldsymbol{x}_0 + \boldsymbol{x}_1)$. This algorithm is already implemented in ABAQUS, where the strain increment ($\Delta\boldsymbol{\varepsilon}$) is calculated from the integration of $\mathbf{D}_{HW}$ over the time increment.

$$\Delta\boldsymbol{\varepsilon} = \int_{t_0}^{t_1} \mathbf{D}_{HW}\, d\zeta = \Delta t\, \mathbf{D}_{HW} \tag{4.14}$$

Therefore, the bar transformed strain increment is got by the

$$\Delta\bar{\mathbf{A}} = \int_{t_0}^{t_1} \bar{\mathbf{D}}_\zeta\, d\zeta = \Delta t\, \bar{\mathbf{D}}_\zeta = \mathbf{Q}^T(t_1)\, \Delta t \mathbf{D}_\zeta\, \mathbf{Q}(t_1) = \mathbf{Q}^T(t_1)\, \Delta\mathbf{A}\, \mathbf{Q}(t_1). \tag{4.15}$$

The interpolant $\mathbf{W}_{HW}$ is also used to approximate the increment of the rotation tensor which according to eq. (4.12), provides an approximation $\mathbf{Q}_{HW}$ for $\mathbf{Q}(t_1)$.

$$\Delta\mathbf{R}(t_1) = \left(\mathbf{I} - \frac{\Delta t}{2}\,\mathbf{W}_{HW}\right)^{-1}\left(\mathbf{I} + \frac{\Delta t}{2}\,\mathbf{W}_{HW}\right) \;=\; \mathbf{Q}_{HW}. \tag{4.16}$$

4.1.4 Incremental formulation

The integration routine of the constitutive equations has the task of calculating the stress increment based on the load history, with the values of stress, strain and internal variables known at the start of the time step. Therefore, the desired solution of stress is dependent on the material model as well as the integration routine.

$$\begin{aligned}\Delta\mathbf{S} &= \mathbf{S}_1 - \mathbf{S}_0 \\ &= \mathbb{C}\cdot\left[\mathbf{A}_0 + \Delta\mathbf{A} - \mathbf{A}_{p,0} - \Delta\mathbf{A}_p\right] - \mathbf{S}_0\end{aligned} \tag{4.17}$$

To integrate the constitutive system of equations, the explicit Euler scheme is used in this work, whose stability is ensured with the selection of a suitably sized time step. Here, the incremental formulation for stress is of the form

$$\bar{\mathbf{S}}_1 = \bar{\mathbf{S}}_0 + \Delta t\;\dot{\bar{\mathbf{S}}}. \tag{4.18}$$

Explicit Euler is a simple integration method when sub-increments are not used, as it assumes a linear development of function values, where the model equations can be directly used. Thus, for a system of 'q' evolution equations describing the evolution of the model variables represented by y, the approximation of function Δy described by the derivative $\dot{y}$ at the end of time step, is directly dependent on the initial value of function y_0 and its associated derivative $\dot{y}(y_0)$.

$$y_k^{\,t_1} = y_k^{\,t_0} + \Delta t\;\dot{y}_k^{\,t_0}, \quad k = 1,2...q \tag{4.19}$$

$$\Delta y_k = y_k^{\,t_1} - y_k^{\,t_0} = \Delta t\;\dot{y}_k^{\,t_0}, \quad k = 1,2...q \tag{4.20}$$

This suggests that increments of inner state variables are also a function of $\dot{y}(y_0)$.

$$\begin{aligned}\Delta\bar{\mathbf{A}}_p = \Delta t\;\dot{\bar{\mathbf{A}}}_p, \quad \Delta p = \Delta t\;\dot{p}, \quad \Delta\varepsilon_M = \Delta t\;\dot{\varepsilon}_M, \quad \Delta\bar{\mathbf{Z}}_i = \Delta t\;\dot{\bar{\mathbf{Z}}}_i, \\ \Delta\psi_i = \Delta t\;\dot{\psi}_i, \quad \Delta X = \Delta t\;\dot{X}, \quad \Delta f = \Delta t\;\dot{f}\end{aligned} \tag{4.21}$$

Therefore, the incremental system of equations for the explicit scheme without sub-increments, is known completely. This method is suitable for application to non-stiff and linear problems.

For models which exhibit stiff behaviour, the explicit integration with higher order methods like *Runge–Kutta* is more accurate. These methods are based on subdivision of time steps into sub-increments, which leads to the calculation of the constitutive system at multiple interpolation points

within the time step. For a system of 'q' evolution equations, the function values y_k^s at interpolation points s are determined from the function values and derivatives of the previous point $(s-1)$. The beginning of the time step is indicated by the index (0).

$$y_k^s = y_k^s\left(t^0,...,t^s;\quad y_k^0,...,y_k^{s-1};\quad \dot{y}^{\,0},...,\dot{y}_k^{\,s-1}\right), \tag{4.22}$$

$$\text{with}\quad t^s = t_0+\Delta t,\quad t_0 \le t^s \le t_0+\Delta t\quad k=1,2,...q \tag{4.23}$$

Thus, the solution of the constitutive system of differential equations at the end of the time increment is therefore dependent on all the interpolation points 's' calculated within the time increment. The following is valid for the increments Δy:

$$t^s = t_0+\Delta t \quad \Rightarrow \quad \Delta y_k = y_k^s - y_k^0 = y_k^{t_1} - y_k^{t_0}. \tag{4.24}$$

Since the values for $\dot{p}, \dot{\varepsilon}_M, \dot{\tilde{\mathbf{Z}}}_i, \dot{\psi}_i, \dot{X}$ and $\dot{f}$ depend on the integration method used, they are specified as functions of the previously calculated interpolation points (0, 1,..., $s-1$).

In this work, time integration is performed using the fifth order accurate *Runge–Kutta–Fehlberg* method with time stepping [113, 114]. The explicit Euler scheme described earlier serves only as a conceptual reference.

4.1.5 Requirements of an efficient integration routine

The requirements of the integration method can be drawn based on multiple criteria. Since viscoplastic and damage models have multiple stiff regions especially in the areas of transition between elasticity to plasticity and the onset of plastic instability and damage, the model solution will be dependent on the integration routine. In addition, when the material points are transformed as a result of finite rotations, the model solutions must remain frame-indifferent (see section 4.1.3). This requires the routine to be highly accurate and corotational in nature. Accuracy is also of interest to FE programs, where the use of accurate integration methods allows the use of larger time steps and thereby helps to reduce the computational effort and time. Large time-steps and faster convergence of the global equilibrium iterations can be achieved by supplying a suitably accurate tangent modulus, which is usually easier when implicit methods are used. But for use with explicit methods, an economic method to estimate the tangent modulus with minimal effort would prove highly influential. However, accuracy needs to be accompanied by numerical stability to ensure the consistency and correctness of the produced results. When large FE-models are used, inelastic deformation brought about by loading conditions is usually restricted to regions much smaller compared to the whole model while the rest of the model is still undergoing elastic deformation. Therefore, the integration routine must adapt to these expected scenarios:

(a) Elastic loading/unloading and irradiation, where the model behaviour is linear in nature. Thus, the model is integrated using a simple explicit routine without sub-increments to predict the irradiation hardening as well as the elastic stress response of the material.

(b) Inelastic deformation, where the stiff regions should be handled using an explicit scheme with higher order methods with sub-increments.

(c) Finite rotations or transformations, which are geometrical non-linearities that arise as a result of plastic instability and flow softening. Integration routine must ensure the incremental objectivity of the model.

4.2 Integration routine

As discussed in section 4.1.5, an integration routine is needed to solve the initial value problem posed by the system of constitutive equations developed in section 3.5.1. Based on the requirements of such a routine laid out in section 4.1.5, a suitable integration routine based on the works of Jansohn [95] is constructed and discussed in this section.

The finite strain framework which is used to construct the constitutive equations is already implemented in FE programs like ABAQUS, where it can be accessed through the NLGEOM option. As discussed in sections 4.1.1 and 4.1.2, for a given load the FE-program solves the global problem incrementally to determine the equilibrium points and displacement. For the estimated displacement, the associated kinematic quantities are calculated and given as input to the user. Among the available FORTRAN based user-defined subroutine provided by the program, UMAT which allows user defined material models to be used in FE simulations performed in the program. The UMAT has access to the deformation gradients $\mathbf{F}_0$ and $\mathbf{F}_1$, increments of time Δt, strain tensor $\Delta\boldsymbol{\varepsilon}$ and rotation tensor $\Delta\mathbf{R}$ (or $\mathbf{Q}_{HW}$), given under the names DFGRD0, DFGRD1, DTIME, DSTRAN, DROT, respectively. Using $\mathbf{Q}_{HW}$, which will be identified as just $\mathbf{Q}$, the program transforms the initial value of Cauchy stress $\mathbf{S}_0$ at the beginning of the time step, t_0 to the orientation at the end of the time step, t_1

$$\mathbf{S}_0^* = \mathbf{Q}\,\mathbf{S}_0\,\mathbf{Q}^T \tag{4.25}$$

which are provided as input to the material subroutine. The subroutine structure enables the data of the internal variables calculated from the end of each time step to be saved and be passed to the successive time steps. The user defined field subroutine, USDFLD is used to simulate the neutron-irradiation of the material. In return, the material subroutine is responsible for providing the stress response for the given deformation.

The use of co-rotational Jaumann derivatives is suggested by ABAQUS, to describe the evolution of tensors. Therefore, using the bar transformation of input tensor variables the rigid body transformations are neutralized. Furthermore, the bar transformation of constitutive equations containing Oldroyd derivatives allows the equations to be decomposed and reformulated as Jaumann derivatives. Finally, it is shown that this setup can be integrated using an explicit Euler scheme using values of variables known at the start of the time increment, which allows further simplification of the bar transformed terms.

The material subroutine is responsible for supplying the consistent tangent modulus (CTM) for the given deformation in addition to computing the stress response. A precise estimate of the CTM has a significant impact on the course of the FE-calculation and the needed computation time due to its huge influence on the global equilibrium iteration. As already discussed in section 2.4.3, the common usage of elastic tensor to approximate the CTM for explicit methods is highly inefficient and thus, the method developed by Fleig [72] is utilized in this work to obtain a precise approximation of the CTM using an efficient algorithm.

4.2.1 Bar transformation

The bar-transformation (4.7) of tensor variables stress, strain, deformation rate and kinematic hardening variable is given by

$$\begin{aligned}
\bar{\mathbf{S}}(\zeta) &= \mathbf{Q}^T(\zeta)\,\mathbf{S}(\zeta)\,\mathbf{Q}(\zeta), \quad \zeta \in [t_0, t_1] \\
\bar{\mathbf{D}}(\zeta) &= \mathbf{Q}^T(\zeta)\,\mathbf{D}(\zeta)\,\mathbf{Q}(\zeta), \\
\bar{\mathbf{A}}(\zeta) &= \mathbf{Q}^T(\zeta)\,\mathbf{A}(\zeta)\,\mathbf{Q}(\zeta), \\
\bar{\mathbf{A}}_p(\zeta) &= \mathbf{Q}^T(\zeta)\,\mathbf{A}_p(\zeta)\,\mathbf{Q}(\zeta), \\
\bar{\mathbf{Z}}_i(\zeta) &= \mathbf{Q}^T(\zeta)\,\mathbf{Z}_i(\zeta)\,\mathbf{Q}(\zeta),
\end{aligned} \tag{4.26}$$

where, the initial value of $\mathbf{Q}(t_0) = \mathbf{I}$ establishes that $\bar{\mathbf{S}}(t_0) = \mathbf{S}_0$, $\bar{\mathbf{A}}(t_0) = \mathbf{A}_0$, $\bar{\mathbf{A}}_p(t_0) = \mathbf{A}_{p,0}$, $\bar{\mathbf{Z}}_i(t_0) = \mathbf{Z}_{i,0}$, and $\bar{\mathbf{D}}(t_0) = \mathbf{D}_0 = \mathbf{0}$. Before the integration can be performed, it is necessary to reformulate the constitutive system of relations into a form suitable for a corotational integration routine. For this, the evolution equations of stress (3.99) and kinematic hardening (3.104) are considered, where the decomposition of Oldroyd derivatives using eqs. (2.56) and (2.58) allows the equations to be reformulated in terms of Jaumann derivatives

$$\begin{aligned}
\overset{\triangledown}{\mathbf{S}} &= \mathbb{C} \cdot [\mathbf{D} - \mathbf{D}_p] = \overset{\circ}{\mathbf{S}} - \mathbf{D}\,\mathbf{S} - \mathbf{S}\,\mathbf{D} \\
\Rightarrow \overset{\circ}{\mathbf{S}} &= \mathbf{D}\,\mathbf{S} + \mathbf{S}\,\mathbf{D} + \mathbb{C} \cdot [\mathbf{D} - \mathbf{D}_p],
\end{aligned} \tag{4.27}$$

$$\overset{\circ}{\mathbf{Z}}_i = \mathbf{D}\,\mathbf{Z}_i + \mathbf{Z}_i\,\mathbf{D} + H_i\,\mathbf{D}_p^D - Q_i\,\dot{p}\,\mathbf{Z}_i - R_i\,|\mathbf{Z}_i|^{m_i - 1}\,\mathbf{Z}_i. \tag{4.28}$$

Bar transformation of eqs. (4.27) and (4.28) is related to the time derivatives of $\bar{\mathbf{S}}$ and $\bar{\mathbf{Z}}$ respectively, with the help of eq. (4.8)

$$\dot{\bar{\mathbf{S}}} = \mathbf{Q}^T\,\overset{\circ}{\mathbf{S}}\,\mathbf{Q} = \bar{\mathbf{D}}\,\bar{\mathbf{S}} + \bar{\mathbf{S}}\,\bar{\mathbf{D}} + \bar{\mathbb{C}} \cdot \left[\bar{\mathbf{D}} - \bar{\mathbf{D}}_p\right], \tag{4.29}$$

$$\dot{\bar{\mathbf{Z}}}_i = \mathbf{Q}^T\,\overset{\circ}{\mathbf{Z}}_i\,\mathbf{Q} = \bar{\mathbf{D}}\,\bar{\mathbf{Z}}_i + \bar{\mathbf{Z}}_i\,\bar{\mathbf{D}} + H_i\,\bar{\mathbf{D}}_p^D - Q_i\,\dot{p}\,\bar{\mathbf{Z}}_i - R_i\,|\bar{\mathbf{Z}}_i|^{m_i - 1}\,\bar{\mathbf{Z}}_i. \tag{4.30}$$

However, the evolution equations of the other scalar variables are taken in their existing time derivative forms since scalars are independent of rotations and transformations. These evolution equations of

scalar variables and bar transformed tensor variables needs to be integrated using an efficient and stable method.

4.2.2 Numerical integration

The initial value of the stress tensor is got from the bar-transformation of $\mathbf{S}_0^*$ (4.25), from the orientation at t_1 to the orientation at t_0

$$\bar{\mathbf{S}}_0 = \mathbf{Q}^T \, \mathbf{S}_0^* \, \mathbf{Q} = \mathbf{S}_0. \tag{4.31}$$

Using the step size Δt, the bar transformed strain increment (4.15), and the change in temperature $\Delta\Theta$, the deformation rate tensor and the temperature rate are got.

$$\bar{\mathbf{D}} = \frac{\Delta \bar{\mathbf{A}}}{\Delta t} \tag{4.32}$$

$$\dot{\Theta} = \frac{\Delta \Theta}{\Delta t} \tag{4.33}$$

The irradiation dose rate $\dot{\phi}$ is passed by the user using the USDFLD to the UMAT.

Consider the function representing the model variables and their respective time derivatives be given by

$$y = \left[\bar{\mathbf{S}},\ p,\ \varepsilon_M,\ \bar{\mathbf{Z}}_i,\ \psi_i,\ N,\ f \right], \tag{4.34}$$

$$\dot{y} = \left[\dot{\bar{\mathbf{S}}},\ \dot{p},\ \dot{\varepsilon}_M,\ \dot{\bar{\mathbf{Z}}}_i,\ \dot{\psi}_i,\ \dot{N},\ \dot{f} \right] \tag{4.35}$$

respectively, with the derivatives taken from eqs. (3.103) to (3.111), (4.29) and (4.30). Their initial values are therefore y_0 and $\dot{y}_0$ respectively, with the final values of the variables y_1 being the result of the integration.

$$y_{t_0} = \left[\bar{\mathbf{S}}_0,\ p_0,\ \varepsilon_{M,0},\ \bar{\mathbf{Z}}_{i,0},\ \psi_{i,0},\ N_0,\ f_0 \right] = y_0 \tag{4.36}$$

For the first time step, the initial values in the current time step n are set to 0 with the exception of ψ_2 for which 1 is used. With $\bar{\mathbf{S}}_0$ already known, the solutions of other state variables from the previous time step $n-1$ are used as initial values. Solutions of state variables are stored separately in UMAT's STATEV array and are not transformed in successive steps by ABAQUS to t_1. Therefore, unlike $\mathbf{S}_0^*$, initial values of $\mathbf{A}_p$ and $\mathbf{Z}_i$ do not require bar-transformation.

$$\bar{\mathbf{A}}_{p,0}^n = \mathbf{A}_{p,1}^{n-1},\ \bar{\mathbf{Z}}_{i,0}^n = \mathbf{Z}_{i,1}^{n-1},\ p_0^n = p_1^{n-1},\ \varepsilon_{M,0}^n = \varepsilon_{M,1}^{n-1},\ \psi_{i,0}^n = \psi_{i,1}^{n-1},\ N_0^n = N_1^{n-1},\ f_0^n = f_1^{n-1} \tag{4.37}$$

To summarize, the following quantities are provided as inputs to the integration scheme :

1. rate of deformation $\bar{\mathbf{D}}$, temperature $\dot{T}$, and irradiation dose $\dot{\phi}$

2. initial values of variables y_0 and their respective time derivatives $\dot{y}_0$
3. initial temperature T_0, irradiation dose ϕ_0, initial time t_0 and time increment Δt
4. maximum of equivalent inelastic strain $\varepsilon_{in,eq}$, irradiation defect density N_{max} and kinematic hardening $Z_{eq,max}$
5. list of temperature dependent material parameters

where, $\bar{\mathbf{D}}$ is the primary driving factor of deformation behaviour while $\dot{\phi}$ acts as the primary driver of the irradiation process.

Using a predictor-corrector approach, the routine can be adapted to elastic and elasto-plastic deformations. First, the current temperature Θ_1 is calculated

$$\Theta_1 = \Theta_0 + \dot{\Theta}\Delta t$$

for which, the list of material parameters are interpolated from the available data. Then the value of f^* is determined based on eq. (3.110). Next, the simple explicit method is used as a predictor step to calculate the trial value of stress.

$$\bar{\mathbf{S}}_{1,trial} = \bar{\mathbf{S}}_0 + \mathbb{C} \cdot \Delta\bar{\mathbf{A}} + \Delta\Theta \, \frac{\partial \mathbb{C}}{\partial \Theta} \cdot \mathbf{A}_e. \tag{4.38}$$

Next, the irradiation hardening due to irradiation is estimated by integrating the first term of $\dot{N}$ from eq. (3.107) using the explicit Runge-Kutta-Fehlberg method

$$\dot{N}_{nucl} = a\,(N_s - N)\;\dot{\phi} \quad \text{and} \quad \sigma_H = h_N\sqrt{N}, \tag{4.39}$$

and the yield criterion below is checked to detect inelastic deformation.

$$F = \Sigma_{eq}\left(\bar{\mathbf{S}}_{1,trial}, \bar{\mathbf{Z}}_0, \psi_0\right) - \; k - \; \sigma_H \geq 0$$

If the condition is not satisfied, the deformation is elastic in nature. Thus the initial values of the internal variables and the trial stress $\mathbf{S}_{trial}$ are taken to be the solution of the integration routine for the current time step and are returned to ABAQUS. The elasticity tensor is returned as the consistent tangent modulus.

However, if the criterion is met for the obtained stress, the plastic corrector is carried out as the deformation is inelastic. Here, the stress and other internal variables are reset to the initial values at the start of the time step and the initial value problem of the constitutive equations is solved using the Runge-Kutta-Fehlberg method to estimate the increments of stress and internal variables driven by inelastic deformation. The solution scheme requires the σ_{vis} to be solved for a given stress state fulfilling eq. (3.74), eq. (3.76). The Newton-Raphson method is seen to fail when void coalescence begins. Therefore, the BRENT algorithm [115] which is independent of derivatives is used and found to be reliable. If the effective void volume fraction reaches a value of 0.6 ($0.8 \times 1/q_1$), the routine

considered the material point to have lost its load carrying ability and thus requests to the FE-program for the deletion of the element. However, if the integration is unsuccessful the routine requests the FE-program to reduce the size of the time step.

The inelastic strain is updated using the integration results based on eq. (3.102)

$$\bar{\mathbf{A}}_{p,1} \;=\; \bar{\mathbf{A}}_{p,0} \;+(1-f)\frac{\sigma_s+\sigma_{vis}}{\boldsymbol{\Sigma}\cdot\mathbf{N}}\left[\frac{f^*\;q_1\;q_2}{\sigma_A+\sigma_{vis}}\,Sinh\left(\frac{3}{2}\,q_2\;\frac{\Sigma_v}{\sigma_A+\sigma_{vis}}\right)\;\mathbf{I}\;+\;\frac{3\;\boldsymbol{\Sigma}^D}{(\sigma_s+\sigma_{vis})^2}\right]\Delta\varepsilon_M. \tag{4.40}$$

Since the tensor variables are bar transformed before the integration is performed, they are representative of the deformation alone ($\mathbf{F}_e = \mathbf{U}_e$). However, the rigid body rotations of the material points still needs to be accounted for. Therefore, the tensors variables calculated as solutions of the predictor-corrector integration scheme are rotated or transformed using $\mathbf{Q}$

$$\mathbf{S}_1 = \mathbf{Q}\;\bar{\mathbf{S}}_1\;\mathbf{Q}^T \tag{4.41}$$

$$\mathbf{A}_{p,1} = \mathbf{Q}\;\bar{\mathbf{A}}_{p,1}\;\mathbf{Q}^T \tag{4.42}$$

$$\mathbf{Z}_{i,1} = \mathbf{Q}\;\bar{\mathbf{Z}}_{i,1}\;\mathbf{Q}^T \tag{4.43}$$

before they are returned to ABAQUS. The maximum value of $\varepsilon_{in,eq}$ is updated based on $\mathbf{A}_{p,1}$.

The consistent tangent modulus [72] discussed in section 2.4.3 is used, where the necessary measure of f_{CTM} is chosen to be

$$f_{CTM} \;=\; (1-f)\left\langle\frac{\sigma_{vis}}{K}\right\rangle^n\;\frac{\sigma_s+\sigma_{vis}}{\boldsymbol{\Sigma}\cdot\mathbf{N}}\left[\frac{f^*\;q_1\;q_2}{\sigma_A+\sigma_{vis}}\,Sinh\left(\frac{3}{2}\,q_2\;\frac{\Sigma_v}{\sigma_A+\sigma_{vis}}\right)\;+\;\frac{3}{(\sigma_s+\sigma_{vis})^2}\right]. \tag{4.44}$$

With this approach, the integration routine can be adapted to different material behaviour. In addition, this set-up can also be adapted to large FE-simulations where the inelastic deformations are usually limited to regions much smaller in comparison to the whole system.

Chapter 5

Simulation and results

The developed model needs to be calibrated and validated based on the experimental data at hand. Since strain rate and irradiation softening are temperature dependent and influence plastic instability development, the model needs to be calibrated using data from tests performed on unirradiated and irradiated specimens at different strain rates, irradiation doses at RT and elevated temperatures. Experiments performed to support this work, as reported in section 3.1, are structured with this in mind. The highly nonlinear nature of the model makes the parameter identification highly challenging, which is therefore handled using an optimization procedure following the robust *Simplex* algorithm. The model predictions are validated in section 5.2 with the experimental data reported in this work. Finally, in section 5.2.4, the model is also used to study the influence of various irradiation doses on the material ductility and tensile properties at RT and 300 °C.

5.1 Parameter identification

Using the integration procedure from section 4.2, the constitutive equations of the finite strain deformation and damage model developed in section 3.5.1 are implemented in the FE-program using the UMAT subroutine. The model is applied to the tensile tests described in section 3.1, and experimental data are used to determine the temperature-dependent model parameters. Before the model can be applied, the tested material's uni-axial true stress and strain (TSS) relationship must be established. As described in section 3.1.1, the mean TSS is derived from eq. (3.3), and the Bridgman correction, outlined in eq. (3.4), can be applied to estimate the uni-axial true stress. If the radius of curvature R and the minimum radius a are accurately determined, this method can reliably estimate the TSS relationship in cylindrical specimens beyond the necking point. Application of this method is challenging for a number of reasons. In this work, measurements are taken from images of the deformed specimen rather than the actual specimen. As stated in section 3.1.1.2, the image quality has a substantial effect on the uncertainty of the Bridgman correction factor. Due to the image's low contrast and the presence of shadows, the neck profile is insufficiently distinct for R measurements. Nonetheless, a can be measured with a high degree of certainty. For an accurate and reliable determination of R and a, measurements from a series of load tests must be considered.

Due to the unfeasibility of directly measuring true stresses after necking, however, this method's verification is extremely challenging. When performing tensile test simulations on the FE-program ABAQUS using the data points obtained by the application of the Bridgman method as input for the isotropic hardening model, it is discovered that the engineering stress-strain curves plotted from the simulation results do not match the experimental data. Therefore, a procedure for inverse parameter identification employing an optimization routine is utilized. This optimization procedure described in section 5.1.1 is applied to an inverse FEM method described in section 5.1.2 to estimate the TSS data for unirradiated materials tested at RT and 300 °C, which can be used to estimate the initial values of strain-hardening model parameters. With these values as a starting point, the optimal parameter values are determined. After establishing the model parameters for unirradiated materials, the parameters controlling the irradiation-induced changes in the material are determined. In section 5.1.3, the determination of all model parameters is discussed.

5.1.1 Optimization method

In mathematics, optimization is the selection of a best element, with regard to some criterion, from some set of available alternatives. An optimization problem consists of maximizing or minimizing a real function by systematically choosing input values from within an allowed set and computing the value of the function.

5.1.1.1 Optimization problem

An optimization problem usually begins with a set of parameters or variables, for which the acceptable values are defined by certain restrictions, known as constraints. The solution of the problem is the list of acceptable values, for which the cost function reaches an optimal value. The process of optimization generally involves minimization or maximization methods, through which the characteristics of a mathematical model is able to correspond closely to the reality. The standard form [116, 117] of an optimization problems is defined as

$$\begin{aligned} &\text{minimize } f(x), \quad x \in \mathbb{R} \\ &\text{subject to} \quad c_i(x) = 0, \quad i \in \mathcal{E} \\ &\qquad\qquad\ \ c_i(x) \geq 0, \quad i \in \mathcal{I}. \end{aligned} \tag{5.1}$$

Here, the cost (or objective) function f and constraint functions c_i are real-valued scalar functions, while $\mathcal{E}, \mathcal{I}$ are sets of indices for equality and inequality constraints respectively. The standard form generally defines a minimization problem, while a maximization problem is got by negating the cost function. To produce a meaningful model and implementable optimal solution, the problem formulation is completed by putting some constraints on the values of the design parameters, known as bounds.

Estimates of error are used to determine how well the exact quantity is approximated by a computed value. If x represents the exact quantity and $\hat{x}$ represents the computed value, the non-

negative number $|x-\hat{x}|$ is referred to as the absolute error in $\hat{x}$. The relative error, however, takes into account the size of the exact value and is defined as $|x-\hat{x}|/|x|$ for $x \neq 0$ and undefined if $x = 0$. A feasible point $\hat{x}$ is one that satisfies all requirements of eq. (5.1), while the feasible zone is a collection of all feasible points. Only feasible points are likely to be optimal, while the optimality of a point x^* is defined by its interaction with neighboring points, rather than a $\hat{x}$ where $f(\hat{x}) = 0$.

A function that converts an event into a real number indicating the event's "cost" is known as a cost function and the goal of an optimization problem is the minimization of this cost function. The event in consideration is a function of the difference between estimated and true values for an instance of data. A cost function is typically employed for parameter estimation and may be smooth or non-smooth in nature, depending on the function's derivative. Quadratic functions like the least squares techniques are commonly used for cost functions when solving non-smooth functions. This work uses the Simplex method from Nelder and Mead [7] in fig. 5.1, which is well suited for the multivariate problems that are expected in this work.

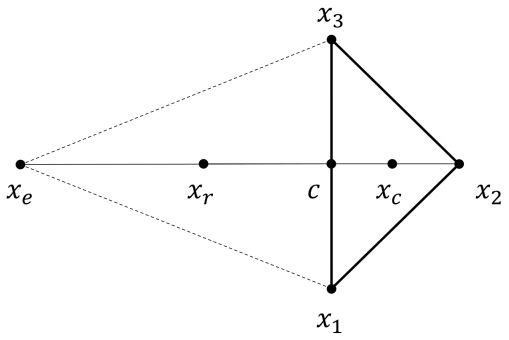

Figure 5.1: Illustration of a single iteration of the Simplex method [7], showing a two dimensional simplex defined by the points x_1, x_2, x_3, the centroid c, the reflection point x_r, the expansion point x_e and the contraction point x_c.

5.1.1.2 Inverse identification

In this work, identification of optimal model parameters is done by solving a suitably framed optimization problem, which allows the computed results given by the integration of the respective material model Y^{sim} to agree with the reference data Y^{exp} obtained from the experiments. For small strain models where geometrical non-linearity is not expected, it is sufficient to integrate the material model locally within environment of the optimization program. However, for finite strain models where the application of the finite strain framework and consideration of geometrical nonlinearities are necessary, dedicated FE-analyses need to be performed where the material response is computed by a material model provided by the FE-program or by a user-defined model. This is necessary because, the development of neck or geometrical softening and the triaxial stress state influences the engineering stress-strain (ESS) and mean true stress-strain (MTSS) relationships.

The FE-program ABAQUS uses the Python programming language for scripting and customization purposes. This allows the usage of an extensive range of open-source Python libraries to perform complex numerical computations. Such a Python-based optimization code developed by Schowtjak

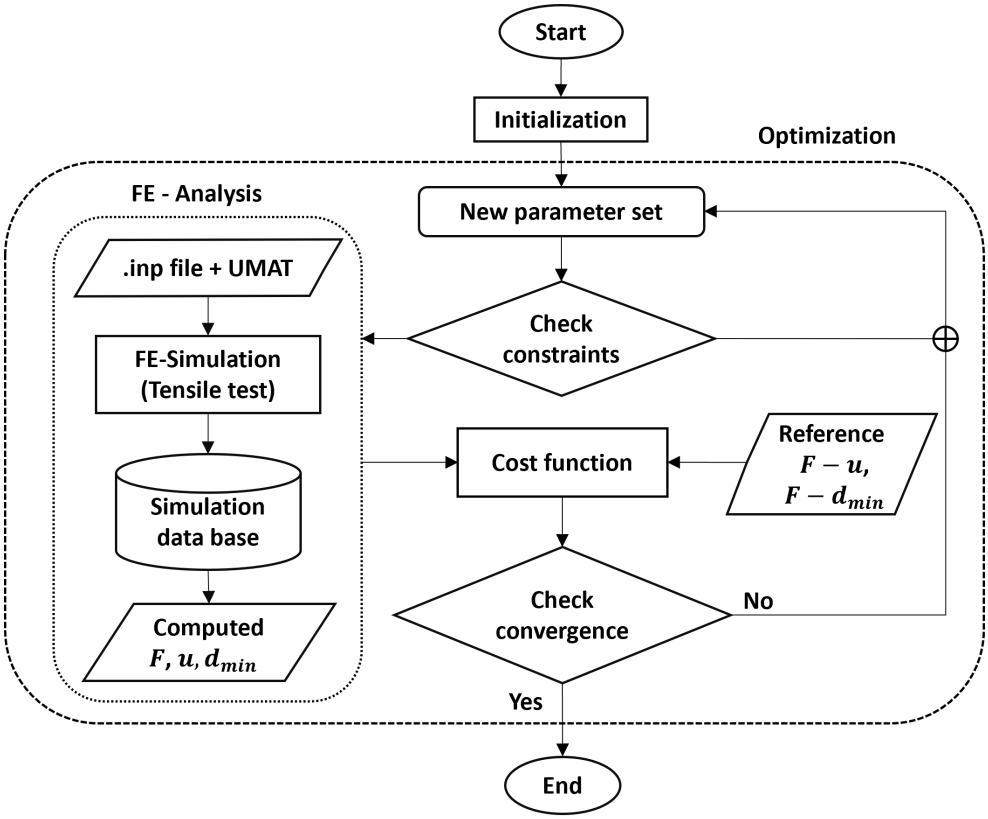

Figure 5.2: Schematic representation of the optimization program [8], where F is the load applied, u is the gauge displacement and d_{min} is the minimum gauge diameter.

et al. [8] is available as open-source. It contains interpolation and cost functions that are suitable for application to FE-analyses. The minimization is performed by *optimize* package of the Python-based *SciPy* libraries [118]. Among the available minimization methods, the Nelder and Mead [7] method (Simplex method) is chosen. The python implementation of *Minuit* optimization package [119, 120] was also found to provide good results. The algorithm of this optimization code is shown in fig. 5.2. For the inverse identification, the optimization problem to be solved is given by the standard form in eq. (5.1), where x is replaced by κ, the parameter set. Here, Y is allowed to represent any desired mechanical quantity. During initialization, the starting values κ_0 of the parameters to be optimized are provided. If the parameters satisfy the constraints, the cost function performs a FE-analysis to compute the Y^{sim} and determines the error between experiment and simulation for a change in the parameter set. Quantification of the error between Y^{exp} and Y^{sim} is performed to determine the cost function $f(\kappa)$ using the root sum of squares method

$$f(\kappa) = \sqrt{\frac{1}{n_{sp}} \sum_{i=1}^{n_{sp}} w_i \left[Y_i^{exp}(\kappa) - Y_i^{sim} \right]^2} \tag{5.2}$$

since it levies penalties on statistical outliers. Here, n_{sp} represents the number of sample points and w_i represents the set of weighting coefficients assigned to the sample points based on their location. The minimization program alters the parameter values κ with the objective of reducing the error until an

error minima or a tolerance limit is reached. For the code's application to the FE-program ABAQUS, information of the specimen geometry and the list material model parameters are passed through the .inp file. The optimization code can be set to pass new parameters through string replacement operations on either the .inp or the UMAT file.

5.1.1.3 Application methodology

The experimentally determined quantities such as load, gauge displacement, and minimum gauge diameter are the reference values. From the simulation entities such as the reaction forces and nodal displacements, relevant quantities can be obtained to draw comparison with the experimentally obtained data. Therefore, the quantities represented by Y would vary based on the following approaches:

(a) To optimize the model parameters based on the load-displacement relation, Y shall represent the force applied on the specimen, while the set of weight coefficients is calculated from the gauge displacement throughout the load history,

$$w_i = \frac{dw_i}{\|dw\|} \quad \text{with} \quad dw_i = \frac{u_{i+1} - u_{i-1}}{2}, \quad i = 1, ..., n. \tag{5.3}$$

This approach is crucial to identifying parameters governing the strain-rate dependent characteristics.

(b) Alternatively, when the parameters governing the material hardening can be identified by using the MTSS relationship as the reference data. Therefore, Y would represent the mean true stress, while the weight coefficients will be calculated from the mean true strain calculated from the reduction in minimum gauge diameter for the applied load.

To identify parameters for material deformation and damage under large strains, it is recommended to start with the approach (b) to identify the parameters governing the material hardening and damage if the MTSS data is available. With these parameters fixed, the viscous parameters and the initial yield stress should be identified using the approach (a). For proper identification of viscous parameters, a multi-cost optimization needs to be performed involving experiments performed at different strain rates and corresponding simulations. Here the n individual cost functions are combined into a single value through the summation

$$f(\kappa) = \sum_{i=1}^{n} w_{f,i}\, f_i(\kappa) \quad \ni \quad \sum_{i=1}^{n} w_{f,i} = 1. \tag{5.4}$$

The weight coefficients $0 \leq w_{f,i} \leq 1$ are applied based on the quality of experimental data, such that experiments with outlying characteristics are assigned a weight $w_{f,i} < 1/n$. For small deformations, the approach (a) is sufficient.

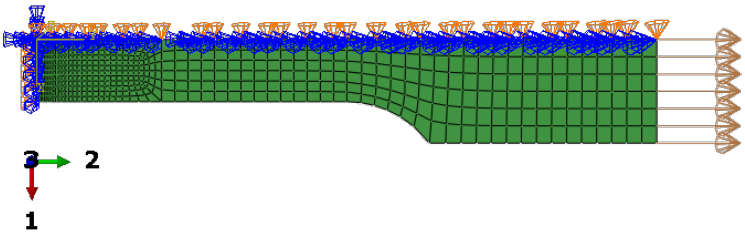

(a) Half longitudinal cross-section of specimen.

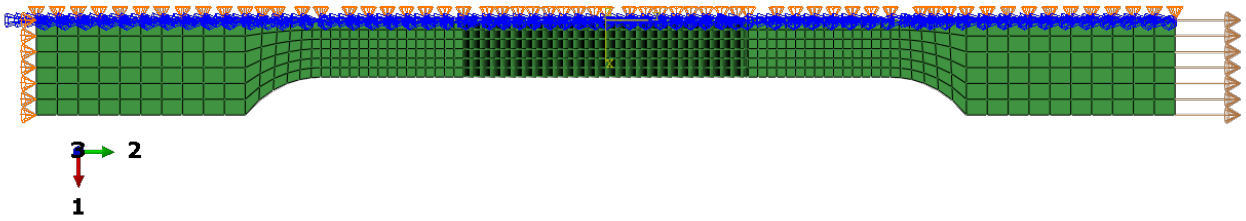

(b) Longitudinal cross-section of specimen.

Figure 5.3: Axisymmetric models of tensile specimen with boundary conditions.

5.1.1.4 FE-Model for tensile tests

To simulate the tensile test, a generic FE-model is constructed based on the experiment described in section 3.1. Taking advantage of the symmetric nature of the specimen geometry, two axisymmetric models are constructed based on the testing conditions. For unirradiated materials, the neck is anticipated at the middle of the gauge length. Therefore, one-fourth of the specimen's cross-section along the tensile axis is used for the geometry as seen in fig. 5.3a. Due to their rapid development, location of the neck is uncertain in irradiated specimens. Thus, half the specimen's cross-section along the tensile axis, as seen in fig. 5.3b is used for the geometry. Within the gauge length region where the neck development subjects the elements to finite deformation and rotations, a finer mesh is required. The aspect ratio is increased upto 4:1 (0.1×0.024) along the gauge length, in order to limit the element's distortion under large deformations. Meshing is done with 4-noded axisymmetric elements (CAX4) that provide four components for the stress ($\sigma_{11}, \sigma_{22}, \sigma_{33}, \sigma_{12}$) and strain ($\varepsilon_{11}, \varepsilon_{22}, \varepsilon_{33}, 2\varepsilon_{12}$) tensors.

For the application of the finite strain framework, NLGEOM is selected. The model is given symmetric boundary conditions along the x (1) and y (2) axes. Using a velocity boundary condition, the strain-controlled loading at the required displacement rate defined in mm/s is applied. Test temperature is applied using the predefined temperature field. However, the irradiation is applied using a user-defined field subroutine, USFLD, which enables the irradiation dose rate to be defined as one of the state variables accessible to the UMAT. Material properties are governed by the UMAT and the associated temperature and material-dependent model parameters. Alternately, the plastic isotropic-hardening model available in ABAQUS can also be applied by providing experimentally obtained true stress versus plastic true strain data. The simulation results are then post-processed to

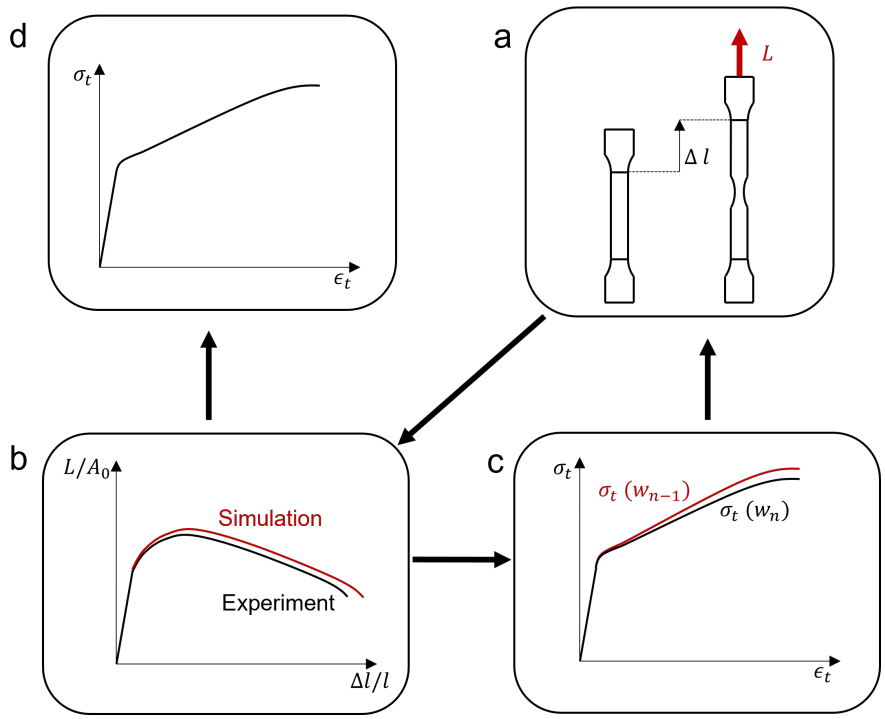

Figure 5.4: Schematic illustration of the inverse method: (a) FE-simulation using WA method, (b) comparison of simulation and experimental results, (c) prediction of new w_n, (d) successful prediction of w_n gives optimal $\sigma_t - \varepsilon_t$.

extract data regarding nodal displacements at the neck surface and the gauge point, von-Mises stress at the top, and state variables from elements with the highest accumulated plastic strain.

5.1.2 True stress-strain correction of unirradiated specimen

To overcome the shortcomings of the Bridgman method, various alternative correction methods have been proposed and can be found in literature [121–128]. Many of these are inverse FEM approaches, first introduced by Zhang [121] based on the consideration that the TSS relationship is mostly linear post the onset of plastic instability identified by eq. (3.9). By iterating FE analyses, Zhang presented a method for simulating the load-displacement of a tensile specimen for both round and flat bars, requiring only the experimental load-extension data. Ling [129] devised a *Weighted Average* (WA) approach, based on the observation that after the onset of plastic instability, the hardening modulus continues to decline with increasing strain. Ling identified that a linear extrapolation of true stress leads to overestimation, while a power law extrapolation leads to an underestimation of true stress. Therefore, by starting with the theoretical true stress (σ_u) and true strain (ε_u) at the onset of plastic instability as the initial values

$$\sigma_u = \sigma(1+\varepsilon_{eng,UTS}), \quad \varepsilon_u = ln(1+\varepsilon_{eng,UTS}), \tag{5.5}$$

the method estimates true stress for given true strain by

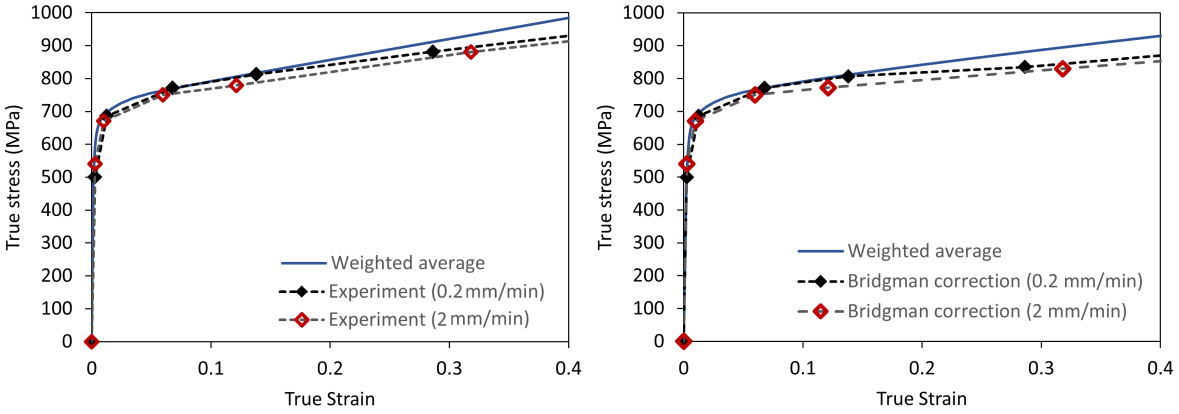

(a) Mean true stress and strain (b) True stress and strain

Figure 5.5: Results of WA method with $w_{WA} = 0.478$ compared with experiments at T_{test}= RT.

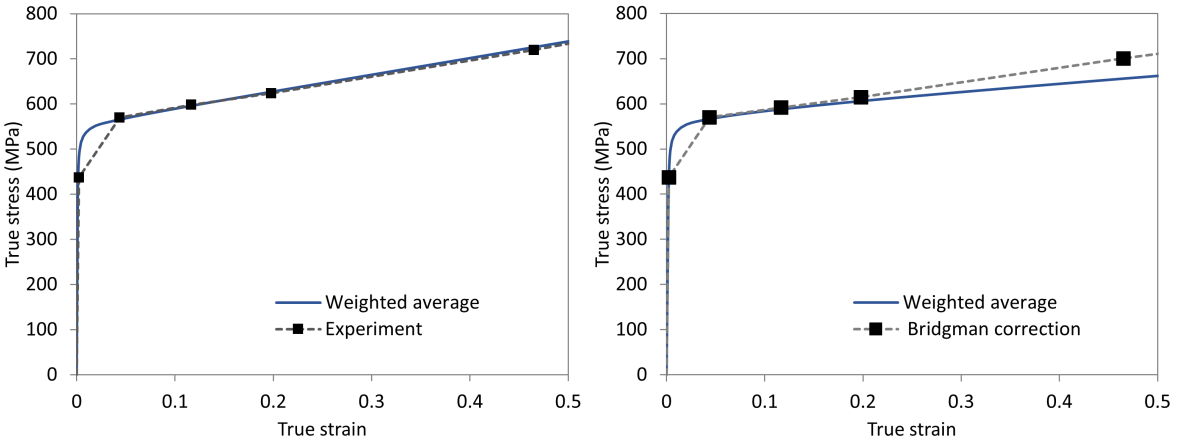

(a) Mean true stress and strain (b) True stress and strain

Figure 5.6: Results of WA method with $w_{WA} = 0.2696$ compared with experiments at T_{test}= 300°C.

$$\sigma = \sigma_u \left[w_{WA} \left(1 + \varepsilon - \varepsilon_u\right) + \left(1 - w_{WA}\right) \left(\frac{\varepsilon}{\varepsilon_u} \right)^{\varepsilon_u} \right] \tag{5.6}$$

where the linear and power law extrapolations are used as the upper and lower bound of the true stress respectively. Here, the parameter $0 \leq w_{WA} \leq 1$ controls the influence of the extrapolation methods, such that the method is purely a linear extrapolation for $w_{WA} = 1$ and purely a power law for $w_{WA} = 0$.

The predicted stress-plastic strain relationship is used to simulate the tensile test in ABAQUS using the FE-model discussed in section 5.1.1.4, whose load-displacement results are later compared with experimental data. By setting an optimization routine, the value of parameter w_{WA} is identified for which the simulation results match the experiment. However, this method does not account for irradiation induced material changes and strain-rate effects. For this reason, it is applied only to

T	E	ν	R	m	h	c	r_ψ	ψ_r	m_ψ	$\psi_{s,\infty}$	c_s
°C	GPa		$\mathrm{MPa}^{1-m}\mathrm{s}^{-1}$				s^{-1}				
RT	208	0.3	10^{-70}	1.00	0.096	1.78	1×10^{-70}	1.0	1.0	0.204	1344
300	200	0.3	8.3×10^{-36}	4.32	0.0347	1.81	7.6×10^{-28}	0.754	1.0	0.262	2269

Table 5.1: List of deformation model parameters from literature [17, 1] at RT and 300 °C.

tests performed on unirradiated specimens with low deformation rates. With the application of the inverse identification method discussed in section 5.1.1.2 along with the WA method as shown in section 5.1.2, the parameter w_{WA} is identified to be 0.478 and 0.2696 for specimens tested at RT and 300 °C respectively.

The results of this method are compared with the experimentally obtained Bridgman corrected TSS data in figs. 5.5 and 5.6. From this comparison, it is sufficiently clear that the WA method provides a reasonably good estimation of TSS until a pronounced neck has developed. Beyond this, an overestimation of the reduction in minimum diameter can be observed. This is due to the absence of viscous effects that predict a faster neck development than expected. As a result, it is safer to use the (MTSS & TSS) data only up to a low strain level ($\leq 5\%$). This is sufficient for obtaining an initial estimate for most of the deformation model parameters using curve fitting, while their final values are obtained by setting up a inverse identification discussed using the approach in section 5.1.1.3.

5.1.3 Identification of the deformation model parameters

During the course of this work, the deformation model was developed first and the associated parameters were identified [5]. This was succeeded by the incorporation of the viscoplastic extension of the GTN ductile damage law and the identification of its parameters. This identification process is discussed here, following the same order. First, the procedure followed to identify the model parameters for describing the unirradiated material behaviour is discussed. This is followed by the identification of parameters governing the influence of irradiation. Finally, the identification of the GTN model parameters for both the unirradiated and irradiated materials are discussed.

5.1.3.1 Unirradiated material

The parameter identification process follows the inverse identification approach aided by an optimization routine to identify the optimal values. Providing sufficiently good initial estimations of the parameters is highly beneficial to improve the efficiency and convergence of the optimization program. To this end, the TSS data of the unirradiated specimens determined in section 5.1.2 using the WA method are utilized to determine the initial estimates of model parameters at RT and 300 °C.

The elastic parameters, Young's modulus E and Poisson's ratio ν are taken from literature [17, 1]. Using the TSS data from figs. 5.5 and 5.6, the plastic strain is calculated using the relation

$$\varepsilon_p = \varepsilon - \frac{\sigma}{E}. \tag{5.7}$$

Since the isotropic softening is used primarily for describing the cyclic softening, the parameters of the other hardening laws must be calibrated such that the influence of ψ during monotonic loading is compensated. The isotropic softening model parameters are already known from literature [17, 1] and listed table 5.1. Therefore, eqs. (3.105) and (3.106), are integrated using a simple explicit scheme and σ/ψ is used instead of the experimental true stress (σ). σ/ψ is decomposed using the one-dimensional formulation of eq. (2.103),

$$\frac{\sigma}{\psi} = Z + k + \sigma_{vis}. \tag{5.8}$$

To describe the total strain hardening of the material under finite strains up to the point of ductile damage, a total of three kinematic hardening variables (i=3) are used. The effective kinematic hardening Z in eq. (5.8) is given by the summation of the three individual kinematic hardening variables and is described by the integral form of the Frederick and Armstrong [52] model

$$Z = \sum_{i=1}^{3} \frac{H_i}{Q_i} \left[1 - exp(-Q_i\, p)\right]. \tag{5.9}$$

With each variable being active during different levels of deformation, their effective value describes the level of material hardening at every point of the load history. The kinematic hardening parameters R, m governing the material's static recovery are taken from literature [17, 1]. However, static recovery in Eurofer97 in the considered temperature range is not significant.

Since Eurofer97 generally holds a low sensitivity towards strain rate at the considered temperatures, the viscous effects offered by the viscoplastic model are initially restricted to a minimum as per the recommendations made by Audoly and Hutchinson [130]. Therefore, with an initial assumption of viscous stress σ_{vis} to be 1 MPa, the initial estimates to the parameters of initial yield stress k and the kinematic hardening H_i, Q_i are obtained by fitting the data of σ/ψ at RT and 300 °C to the eqs. (5.8) and (5.9) using the Trust-Region algorithm. To illustrate the quality of this fit, FE simulations are performed with the developed material model and the obtained parameters at 300 °C. The stress-strain relationships plotted using the result are shown in figs. 5.7 and C.1 and from fig. 5.7b, the underestimation of the engineering curve at higher strains suggests that the strain-rate sensitivity of the material is limited, but becomes more prominent during advanced stages of neck development. Therefore, this method is shown to be reliable and fast in producing initial estimates of the model parameters with minimal effort.

It must be noted that the viscous parameters play a crucial role in ensuring a good accuracy and performance of the viscoplastic material model. They regulate the strain-rate dependent material behaviour, with n governing the model's sensitivity to strain-rate and K controlling the potential

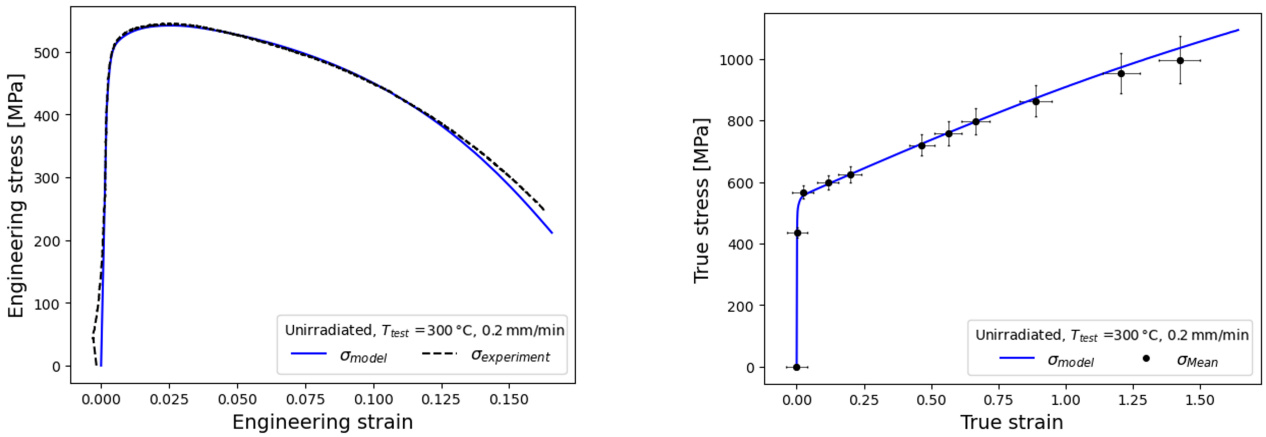

(a) Engineering stress-strain

(b) Mean true stress-strain

Figure 5.7: Comparison of results from tensile test simulation using curve-fit parameters and experimental data.

magnitude of the viscous stress. They also help to improve the computational speed of the model. Therefore, a moderate level of strain rate sensitivity is chosen with the initial value of $n_0 = 2$ for RT and 300 °C. For the assumed σ_{vis} and n_0, the initial value $K = 57.73$ MPa is got from eq. (2.102). Using the initial values of the parameters (denoted by k_0, n_0, K_0, $H_{i,0}$, and $Q_{i,0}$), an optimization problem is designed to determine their optimum values, using the optimization algorithm discussed in section 5.1.1. A highly non-linear optimization problem arises when identifying many parameters simultaneously, making convergence difficult and increasing computational cost. Due to material instabilities at UTS and damage, the numerical problem is stiff, requiring smaller time steps for integration. For these reasons, the load history is split into multiple phases, where each phase optimizes parameters affecting a single instability point while keeping the other parameters constant. This method speeds up the inverse identification process, which would otherwise take much longer or fail to converge. The optimization of the parameters is carried out in the following phases at RT and 300 °C:

1. In the first phase, the optimization problem is defined for the load history up to the Considère instability point (UTS). The specimens tested with the lower deformation rate of 0.2 mm/min are used as the reference data. Starting with the initial values of parameters (k_0, n_0, K_0, $H_{i,0}$ and $Q_{i,0}$), the optimization problem is solved to find their respective optimal values. While the obtained values of k_1, n_1, K_1, and $Q_{3,1}$ are optimal for the chosen phase, they need to be optimized again based on the entire load history. Still, the latest values of n_1, K_1 greatly improve the performance of the model, making it suitable for the successive phases of parameter identification which are more computationally expensive and time consuming.

2. Q_3 helps to describes the material hardening at very high strains along with the neck development and reduction in d_{min} accurately. Here, the experimental MTSS data from fig. 3.6b is used as the reference data where Y for the optimization problem is the mean true stress. By fixing all

T	k	n	K	H_1	Q_1	H_2	Q_2	H_3	Q_3
°C	MPa		MPa $s^{1/n}$	MPa		MPa		MPa	
RT	424.3	10.06	117.76	139042.0	784.85	3814.4	42.84	623.98	0.29
300	334.9	6.62	28.71	332033.65	2166.35	7538.73	125.83	525.46	0.58

Table 5.2: List of parameters for the deformation model determined at RT and 300 °C.

other parameters and providing $Q_{3,1}$ as the starting value, the optimization problem is solved to determine Q_3.

3. To complete the parameter identification for the deformation model, the global optimum values of k, n and K were identified at the end. Viscous parameters (n, K) control the strain-rate influence on the material behaviours like the rise in UTS, neck development and the engineering fracture strain. Accurate estimation of n, K is vital as the local strain rate increases radically as the neck develops. This is done using a multi-cost optimization (5.4) where the ESS data at both deformation rates of 0.2 and 2 mm/min are used as reference data to calculate the cost functions (5.2) using simulations at corresponding loading conditions. When reference data is consistent, like RT, both cost functions receive $w_{f,i} = 0.5$. However, at 300 °C, where one of the datasets (i.e., 2.0 mm/min) shows an outlier behaviour, optimization using this method fails. In this case, $w_{f,i}$ is concurrently increased for the more consistent data and dropped for the outlier, ensuring that $\sum_i w_{f,i} = 1$. With this approach, coefficients of 0.75 (0.2 mm/min) and 0.25 (2.0 mm/min) were found to produce the desired results at 300 °C.

The deformation model parameters thus obtained are listed in table 5.2.

5.1.3.2 Irradiated material

The next step is to identify the model parameters that describe irradiation-induced material behaviour. Since elastic properties parameters are not affected by irradiation, the Young's modulus (E) and Poisson's ratio (v) remain unchanged. Similarly, the material's strain hardening characteristics are independent of irradiation [86] allowing the parameters of the kinematic hardening and isotropic softening laws to remain unchanged. Irradiation defect density (N) evolution with respect to irradiation damage dose ϕ is controlled by the parameters a, N_s, while h_N induces the temperature dependence of the irradiation hardening calculated from the defect density [53, 54, 131]. Defect removal by inelastic deformation reduces irradiation hardening and consequently the material's hardening modulus, which accelerates neck development. The rate of removal controlled by b is high initially, but gradually decreases after a portion of the defects (l_N) are removed and stabilizes at a rate controlled by e_1. The strain rate sensitivity of the material also reduces as a result of irradiation, as per Hashimoto et al. [132] who reported that the hardening strain rate exponent reduced from 0.041 in unirradiated materials to 0.028 in irradiated F82H, which is also a similar RAFM steel. Therefore, it is necessary to re-identify the viscous parameter for irradiated materials (n_{irr}). Values of parameters r_N=10^{-70}

T °C	n_{irr}	h_N MPa	a	$\sqrt{N_s}$ MPa	b	$l_{N,0}$	$l_{N,1}$	e_1
RT	3.62	1.2165	0.1326	526	47.98	0.855	0.42	1.0
300	3.03	1.0	0.1326	526	78.19	0.562	0.18	1.5

Table 5.3: List of defect density evolution parameters determined at RT and 300 °C.

MPa$^{2(1-q_N)}$/s and q_N=1.0 that govern the defect density evolution during annealing, are directly taken from literature [1] for both RT and 300 °C. Therefore, only n_{irr}, a, N_s, h_N, b, l_N and e_1 are required to be identified.

Calibration of a, N_s and h_N can be done using a simple curve fitting method since irradiation was performed prior to deformation. As irradiation hardening σ_H has a quadratic relationship (3.57) with ϕ, it tends to saturate at higher doses (>10-15 dpa) [11, 133, 53, 78]. The experimentally determined relationship between σ_H and ϕ from this work (see table 3.2) and from literature [9–13] are used for the fitting procedure. Since the sample with the damage dose of 0.22 dpa exhibits some outlying behaviour, it is omitted. The integral of the first component in eq. (3.107) (i.e., $\dot{N} = a(N_s - N)\dot{\phi}$) is of the form described by Whapham and Makin [92] and leads to the fitting equation for identifying a, N_s and h_N,

$$\sigma_H = \sqrt{h_N^2 N_s}(1 - exp(-a\ \phi))^{0.5}. \tag{5.10}$$

From literature, σ_H is seen to be greater at lower testing temperatures for the same ϕ and T_{irr}. Therefore, the fitting is done initially using data points where T_{test}=300 °C by holding h_N=1.0. Next, by holding the identified a, N_s constant, h_N is identified from the data points where T_{test}=RT. The fig. 5.8 depicts the results of the fitting procedure. As seen in fig. 5.8, there is a significant amount of scatter between the model-predicted and experimental hardening at low doses [134]. The phenomenon of scattering during irradiation hardening is widely reported in literature [78, 133]. Since σ_H is inferred from tensile tests rather than being directly linked to experimentally measured defect density N, its estimation is subject to uncertainty. Variation in defect evolution could be attributed, in part, to the stochastic nature of the metallographic parameters. Uncertainty in the damage dose received by the specimen is another possible cause of the scattering. Large scatter is observed in the low-dose regime because the $\sigma_H - \phi$ relationship is more sensitive to errors in ϕ estimation at lower doses than at higher doses. However, since these factors tends to stabilize at higher doses of ϕ, the current model's predictions should continue to hold true.

Next, the parameters b, l_N and e_1 that govern the removal of the defect are determined. Defect removal plays a central role in the development of plastic instability in irradiated material and is therefore influential in describing UTS and post-necking behaviour. The experimental ESS data of the irradiated specimen are the sole reference data for parameter identification because of the uncertainty in the experimental TSS data and inapplicability of the WA method to irradiated

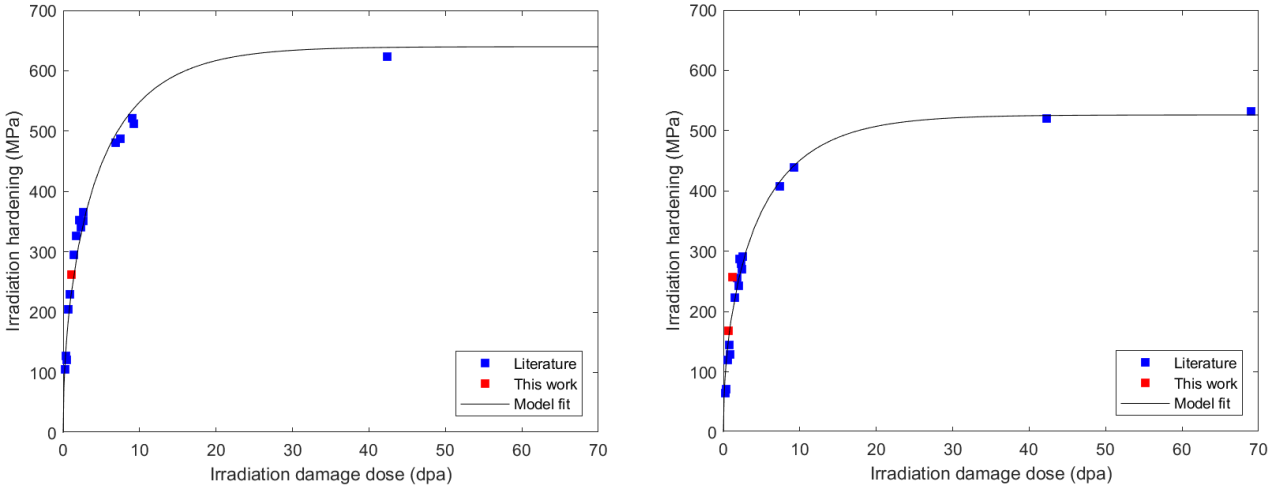

(a) RT (b) 300 °C

Figure 5.8: Curve fitting of irradiation hardening parameters a, N_s and h_N at (a) RT and (b) 300 °C. Hardening values obtained in this work are shown in red and those from literature are in blue [9–13].

materials. Reproducing the experimentally observed UTS and post-neck softening depends on the initial hardening caused by irradiation. However, due to the scatter in σ_H between the model predictions and the experimental data, the effective irradiation dose ϕ is inferred for each irradiated sample by inverting the hardening relation

$$\phi = -\frac{1}{a} \ln\left(1 - \frac{\sigma_{H,exp}^2}{h_N^2 N_s}\right). \tag{5.11}$$

Therefore, the 1.05 dpa @ RT was adjusted to 1.44 dpa. The doses 0.65 and 1.18 dpa @ 300 °C were adjusted to 0.73 and 1.8 dpa, respectively. The optimization process is carried out separately at RT and at 300 °C due to the temperature-dependent nature of the material deformation. At RT, the data from 1.05 dpa specimen is used as the reference data. As the experimental data of 0.65 and 1.18 dpa specimens are available at 300 °C, a multi-objective optimization is performed. For the FE model, the specimen geometry shown in fig. 5.3b is used due to instances of the neck developing away from the middle of the gauge section. At 300 °C, b and e_1 are seen to have higher optimal values, while l_N is larger at RT. At lower doses, these parameters lead to predictions that agree well with experiments, but at higher irradiation doses, they predict excessive post-UTS softening. Therefore, using the load-displacement data of tests performed on materials with higher doses (69.1 dpa @ T_{irr} = 336 °C, at T_{test} = RT and 350 °C) [135, 22, 14] as reference data, and holding all other parameters constant, l_N is re-identified at RT and 300 °C. For this, an axisymmetric model (see fig. A.3) consisting of a quarter of the specimen geometry used in Gaganidze et al. [135] (see fig. A.2) is built and used. Currently, the deformation model is not calibrated for temperatures above 300 °C. Therefore, for the sole purpose of fitting l_N, the initial yield stress k is adjusted to match the UTS from the experimental data for T_{test} = 350 °C. The summary of all l_N identifications is shown in the Appendix (figs. C.2 and C.3). The estimated data $l_N - \sigma_{H,max}$ are curve-fitted to an interpolation function, to determine

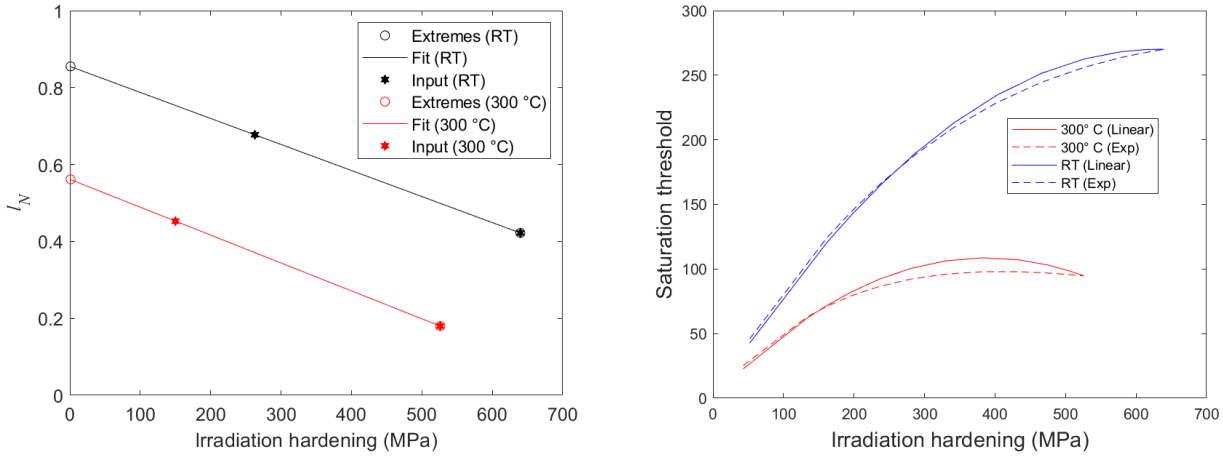

(a) Curve fitting

(b) Saturation threshold

Figure 5.9: Curve fitting of irradiation hardening parameters $l_{N,0}$ and $l_{N,1}$ at RT and 300 °C.

the extremes $l_{N,0}$ and $l_{N,1}$. $l_{N,1}$ is pertinent to $h_N\sqrt{N_s}$ as $\sigma_{H,max}$ saturates at higher doses. On the other hand, $l_{N,0}$ is obtained from extrapolation and therefore serves a numerical purpose, having no physical relevance at $\sigma_H = 0$ MPa. Assuming a linear relationship between l_N and $\sigma_{H,max}$, the associated fitting shown in fig. 5.9a leads to the determination of $l_{N,0}$ and $l_{N,1}$. Although the linear fit works well for most of the dose range, the quadratic relationship between σ_H and ϕ leads to an artificially high saturation threshold ($l_N \times \sigma_H$) at the mid-range (5 dpa $\rightarrow$ 108 MPa) for $T_{test} = 300$ °C which subsequently reduces for higher doses as seen in fig. 5.9b. Using an exponential fitting curve (see fig. H.1) to approximate the second-order trend, this anomaly is seen to disappear. The repercussions of these approaches on the simulation results are discussed in section 6.1. This also suggests that the model has potential for further improvement with the availability of additional data that supports higher-order interpolation functions.

The optimized values of the parameters needed to describe irradiation influenced changes to material properties are shown in table 5.3. Triaxiality development is influenced by the reduction in σ_H, and plays a role in the prediction of ductile damage in irradiated materials. These elements will be taken into account when identifying the parameters for the ductile damage model.

5.1.4 Parameter identification for GTN ductile damage model

The viscoplastic GTN ductile damage model describes material deterioration with the development of porosity due to voids and the influence of strain rate on fracture strain. The model includes seven parameters. The nucleation of the void described in the material is governed by the parameters f_N, ε_N and s_N. Recommended in [59, 3] are the values $f_N = 0.04$, $\varepsilon_N = 0.3$ and $s_N = 0.1$. The model considers the void growth to be hydrostatic stress-dependent, with q_1 and q_2 as the controlling parameters. In addition, the $1/q_1$ value represented by f_u^* estimates the value of f^* at which the material loses its entire load-bearing capacity. Based on their unit-cell calculations using the GTN model, Tvergaard and Needleman [3][60–62] determined that the parameters $q_1 = 1.5$ and $q_2 = 1.0$

T °C	q_1	q_2	ε_N	s_N	f_N	f_c	$f_{c,irr}$	f_F
RT	1.50	1.00	0.3	0.1	0.0018	0.0045	0.00243	0.1
300	1.50	1.00	0.3	0.1	0.0013	0.0045	0.00206	0.1

Table 5.4: List of viscoplastic GTN ductile damage model parameters determined at RT and 300 °C.

are applicable to the majority of cases. However, the original Gurson yield function can be recovered with $q_1 = 1.0$ and $q_2 = 1.0$. Some other choices of these parameters include $q_1 = 1.25$ [58], $q_1 = 1.35$ [64], and $q_1 = 1.46$, $q_2 = 0.931$ [136]. The critical value f_c controls the onset of void coalescence, while f_F represents the value of f at which the material completely loses its load bearing capacity. Therefore, the material failure follows the trend $f \rightarrow f_F,\ f^* \rightarrow f_u^*$, with the restriction $f \ll 1$ proposed by Tvergaard and Needleman [3], who also suggested the values of f_c (= 0.15) and f_F (= 0.25). The parameters $\varepsilon_N = 0.3, s_N = 0.1, q_1 = 1.5$ and $q_2 = 1.0$ from literature [59, 3] are chosen for this work. Stratil et al. [77] determined the critical VVF, f_c for Eurofer97 by examining the material beneath the fracture surface of the specimen that was subjected to tensile testing at RT. This value is adopted in this work. This leaves f_N and f_F to be identified, which can be done using the load displacement data of Eurofer97 at RT and 300 °C. Multi-cost optimization similar to the one used for identifying $n,\ K$ for unirradiated materials in section 5.1.3.1, is reused here to identify f_N and f_F at RT and 300 °C. In contrast to previous instances of optimization where the least-squares cost function was calculated by comparing the entire load-displacement data from simulation results and experiment, relative error of the engineering fracture strain from simulation results and experiment is used here. The value of f_F is bounded between 0.1 and 0.6. For f_N, these are set as 0 and f_c respectively. The optimization identified that $f_F = 0.1$ holds well for both RT and 300 °C. The f_N identified at RT is greater than at 300 °C.

Deformation characteristics of irradiated materials differ from those of unirradiated materials, so the GTN parameters must be adjusted or modified accordingly. Reduced uniform elongation accelerates the onset of plastic instability and hydrostatic stress in the neck area. The critical nucleation strain is reduced, as proposed by Chu and Needleman [59]. Senior et al. [56] also showed experimentally that aging 9Cr-1Mo steel samples at high temperatures causes the critical nucleation strain to decrease. The results of *Senior* are intriguing because the changes in material behaviour induced by material aging, such as an increase in yield stress and a decrease in the true fracture strain, are similar to those induced by irradiation [137]. Irradiation speeds up void growth and reduces the critical VVF needed for the onset of void coalescence, according to studies of unirradiated and irradiated single crystals of FCC materials conducted by Ling et al. [138]. Material instability brought on by the removal of irradiation defects, as described by the constitutive model, accelerates the development of the neck and the associated hydrostatic stress concentration. As a result, there is a dramatic increase in the triaxiality factor (TF). The decrease in σ_H causes softening of the material, which increases the plastic strain rate and, as a result, accelerates the model's calculation

of void nucleation. Furthermore, void growth occurs at a rate consistent with the rapid increase in triaxiality. As a result, the developed model should be able to account for the irradiation-induced reduction in critical strain for nucleation as well as the accelerated void growth. This leaves only the identification of the critical VVF $f_{c,irr}$, which is determined by solving an optimization problem using the load-displacement data of the irradiated samples (0.65 dpa @ $T_{test} = 300\ ^{\circ}C$ and 1.05 dpa @ $T_{test} = RT$) from this work as reference data. The parameters identified at these low doses are found to be suitable for high doses up to 69 dpa. Based on the identified parameters, the following relationships are noticed:

$$\frac{n_{irr}@RT}{n_{irr}@300\ ^{\circ}C} \approx \frac{f_{c,\,irr}@RT}{f_{c,\,irr}@300\ ^{\circ}C} \approx \frac{h_N@RT}{h_N@300\ ^{\circ}C} \tag{5.12}$$

which illustrate that the temperature dependence of irradiated material properties is linked to h_N. Additionally, the ratio of $f_{c,irr}/n_{irr}$ is seen to be the same at both temperatures.

$$\left.\frac{f_{c,irr}}{n_{irr}}\right|_{RT} = \left.\frac{f_{c,irr}}{n_{irr}}\right|_{300\ ^{\circ}C} \tag{5.13}$$

while the same cannot be said for f_c/n in the unirradiated material. These relationships indicate that the critical VVF has a relationship with the strain rate sensitivity of the material, as the latter governs the rate of neck development and thus the T.F which accelerates void growth.

Since these parameters n_{irr} and $f_{c,irr}$ were identified at low doses of 0.65 dpa and 1.05 dpa, the transition of $n \rightarrow n_{irr}$ and $f_c \rightarrow f_{c,irr}$ is expected between 0 dpa and "x" dpa. For irradiation doses above 0.7 dpa at T_{irr} = 300 °C, strain hardening capability is known to vanish [139]. In agreement to this, parameters identified from the data of the sample irradiated to the assumed dose of 0.73 dpa at T_{test} = 300 °C is seen to hold well for doses upto 69 dpa. Therefore, 0.73 dpa is chosen to be the value for "x" and the parameters n and f_c are interpolated between $[n, n_{irr}]$ and $[f_c, f_{c,irr}]$ for the dose range [0, 0.73] dpa. The optimal values of the viscoplastic GTN ductile damage parameters are presented in table 5.4. The optimal values of the set of model parameters can be found in table D.1.

5.2 Simulation results

Simulations are performed to showcase the model's predictive abilities. First, a single element test is performed to verify the model's ability to describe the development of damage under a pure hydrostatic load. Next, the experimental conditions used in this work and listed in table 3.2 are simulated for unirradiated and irradiated specimens at RT and 300 °C. The ESS and MTSS plots are evaluated at specimen level and compared to the experimental data, to assess the predictions. Other quantities, such as state variables, are extracted from the first element to fail, which typically corresponds to the core of the neck region. Finally, a ductility study is performed using the model at these two temperatures for a wide range of irradiation doses, to illustrate its complete predictive

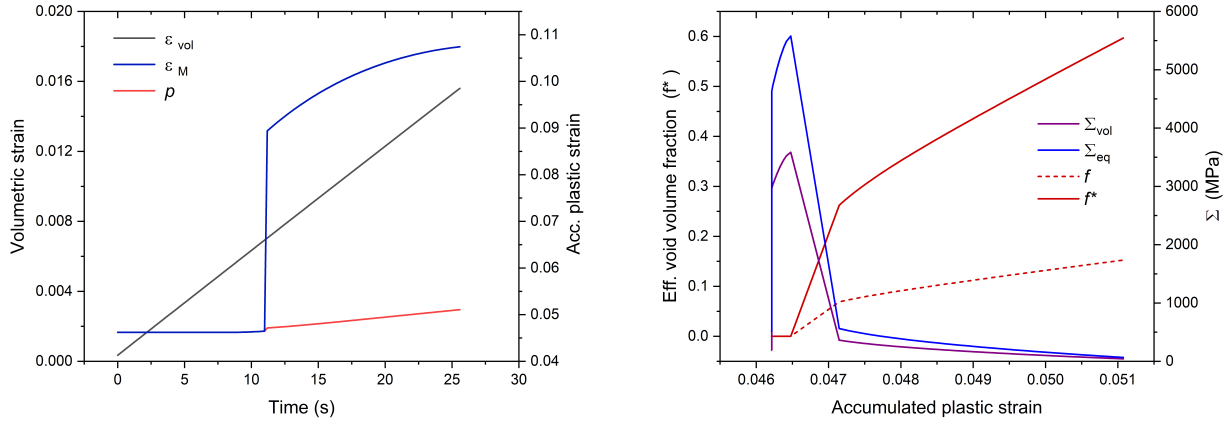

(a) (b)

Figure 5.10: Plot of (a) various strain development under hydrostatic load and (b) development of over-stress and VVF.

capability and to assess the influence of irradiation on the reduction of material ductility. Plots of all internal variables are extracted from the first integration points (IP) to detect material failure or the one with the largest effective VVF (f^*).

5.2.1 Single element test

To verify the proper implementation of the viscoplastic extension of the ductile damage law, the model is used to simulate the VVF development under a hydrostatic load. As the underlying deformation model is already based on the well established viscoplastic framework, validation of the combined deformation and damage model under a hydrostatic load is prioritized. A single, cube element FE model is set up as shown in fig. E.1 where the boundary conditions are placed on the three surfaces adjoining the XY, YZ and XZ planes to only allow displacements tangential to the respective planes. Initially, a uni-axial displacement controlled load is applied in the y-direction, to induce inelastic deformation and for the voids to nucleate and the VVF to reach a low value of 5.5×10^{-5}. Next, displacement controlled loads are applied along X, Y and Z axes to induce a pure-hydrostatic load. The strains applied on the single element are shown in fig. E.2.

Under the hydrostatic load, there is a linear development of volumetric strain as seen in fig. 5.10a. Initially, the deformation is purely elastic with ε_M and p remaining flat. Due to the low value of f^*, void growth is impossible without a very large build-up of local pressure. Therefore, the elastic deformation continues with the over stress growing to a very large value as seen in fig. 5.10b. At Σ_{eq} 4.5 GPa, the material gradually begins to undergo inelastic deformation until VVF reaches 2×10^{-5}. Beyond this, the material experiences rapid inelastic deformation with the void growth rapid growing to a value of 0.07 and induces void coalescence that leads to f^* reaching 0.26. Simultaneously, the hydrostatic over-stress plummets to levels seen at the starting of the load-step. Beyond this, the inelastic deformation and damage develop at a steady rate until the eventual failure

of the material. During this, the over-stress continues to depreciate as the material loses it's load bearing capacity. Therefore, the material model is seen to be capable of describing damage evolution even under a hydrostatic load.

5.2.2 Unirradiated specimen

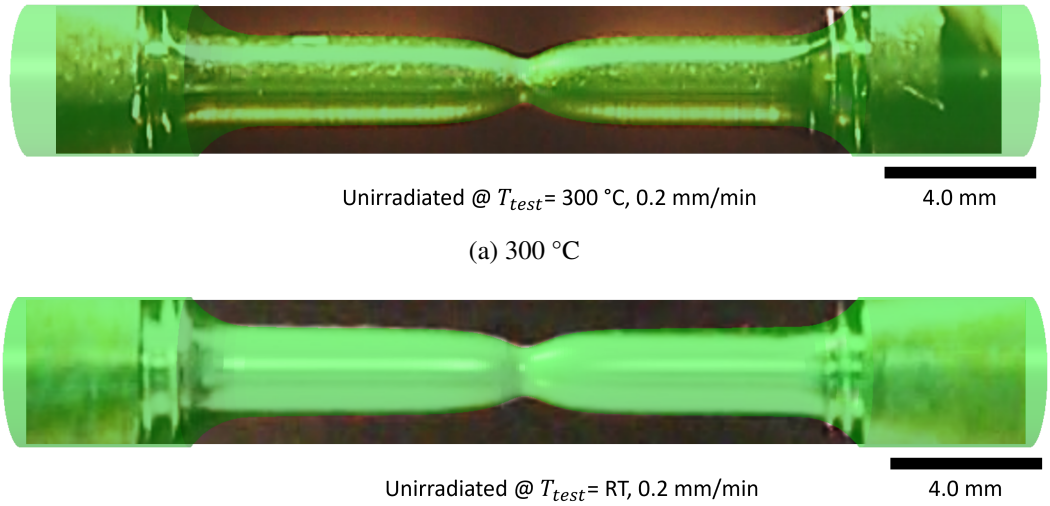

(a) 300 °C

(b) RT

Figure 5.11: Simulated specimen profile (transparent green) compared with images of unirradiated specimens captured just before failure, from experiments performed at (a) 300 °C and (b) RT.

First, a simulation of the tensile test is conducted at 300 °C with two deformation rates of 0.2 and 2 mm/min. The fig. 5.11a compares the model-generated image of the specimen at failure with the image captured during the 0.2 mm/min experiment. The comparison shows good agreement and showcases the model's ability to describe large deformation and ductile damage in a uniaxial loading condition. The simulated deformation is shown in fig. 5.12a, which is supported by the contour plots of gauge displacement (fig. 5.12b) and change in minimum diameter (fig. 5.12c). The von Mises stress in fig. 5.12d, axial stress in fig. 5.12f and the accumulated plastic strain in fig. 5.12h illustrate the localization of large plastic deformation in the neck region. Consequently, a stress minimum is seen just outside the neck region where the maximum pressure stress ($-tr(\boldsymbol{\sigma})/3$) is also seen in fig. 5.12e. This resulting geometric relaxation is responsible for the post-UTS softening seen in the ESS plot (fig. 5.13a). Finally, the shear stress shown in fig. 5.12g indicates that a strong shearing is present at the neck surface due to the strong axial and radial displacements. The stress-strain relationships from the simulation and experiment results are plotted in figs. 5.13a to 5.13d, which share excellent agreement and thus validate the model predictions. The ESS plots demonstrate that the inelastic, post-yield and post-necking behaviours are adequately described. At 2.0 mm/min, the predicted total elongation is conservative and underestimated by 3%. The UTS of the sample tested at a deformation rate of 2 mm/min is lower than that of the sample tested at a lower deformation rate of 0.2 mm/min, indicating that its experimental data exhibits anomalous behaviour. Nonetheless, the model

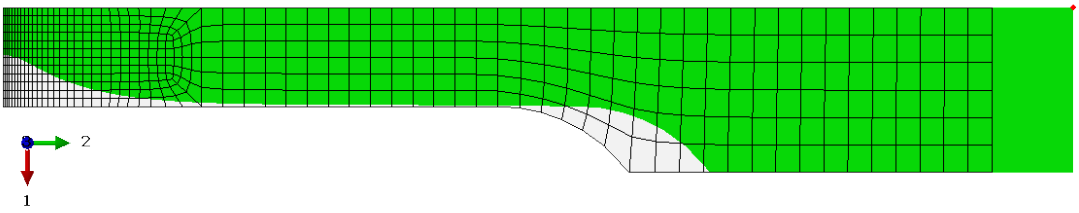

(a) Deformed and undeformed specimen

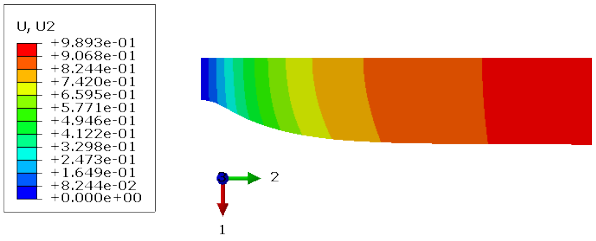

(b) Axial displacement (mm)

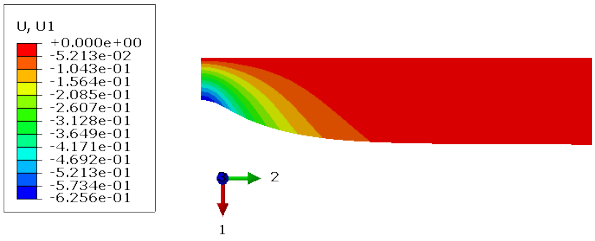

(c) Radial displacement (mm)

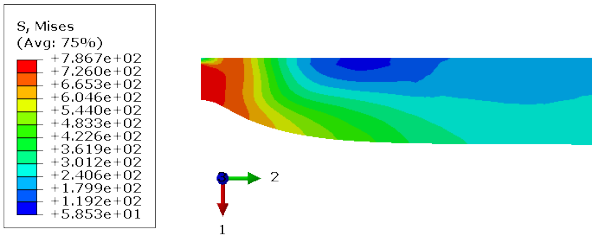

(d) von Mises stress (MPa)

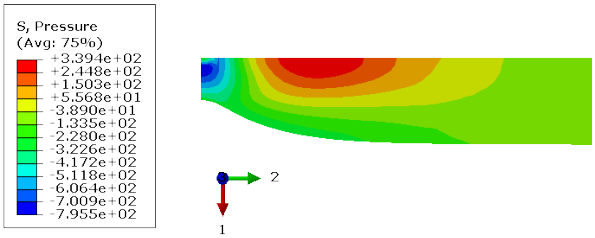

(e) Pressure stress (MPa)

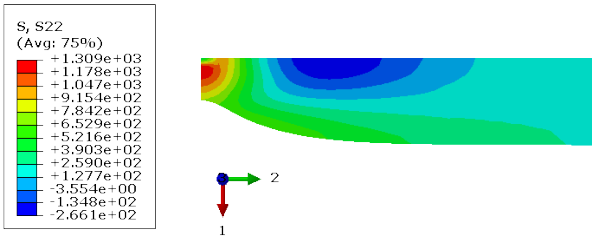

(f) Axial stress (MPa)

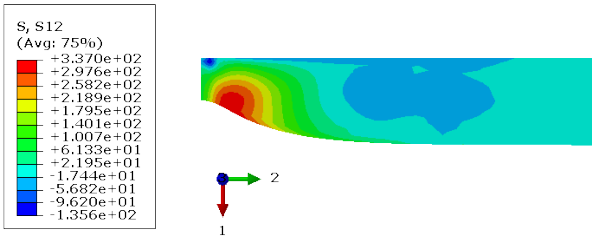

(g) Shear stress (MPa)

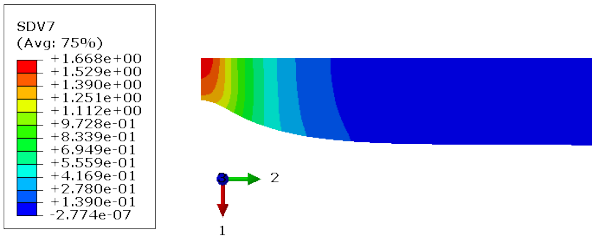

(h) Accumulated plastic strain

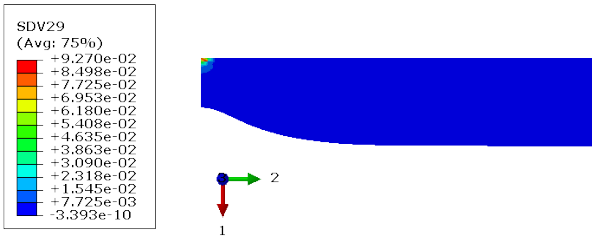

(i) VVF

Figure 5.12: Simulation results for tensile test performed at 300 °C and 0.2 mm/min.

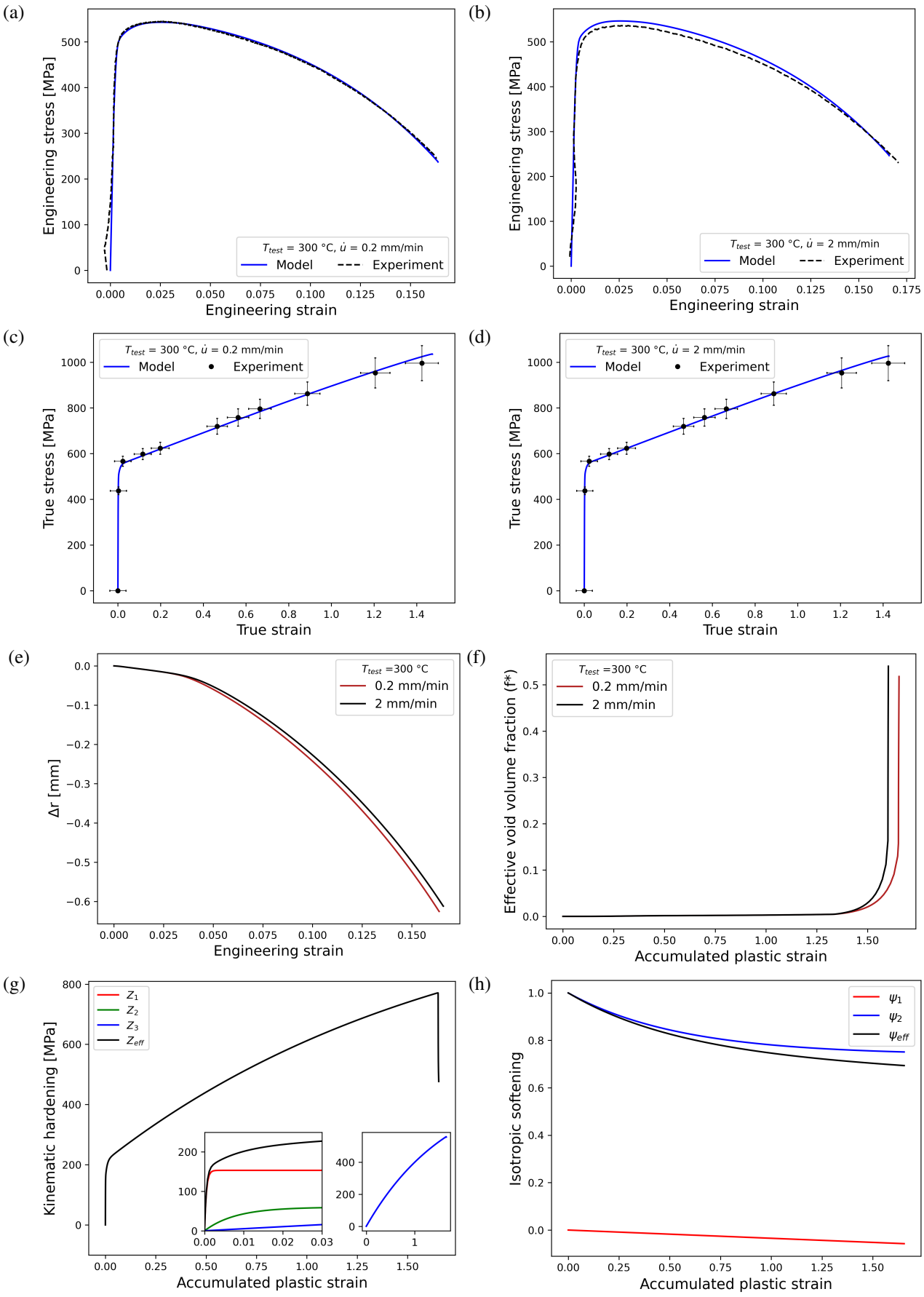

Figure 5.13: Comparison of simulation and experimental results for tensile test performed at 300 °C: (a, b) ESS and (c, d) MTSS. Strain-rate influence on (e) change in neck radius, (f) damage (VVF), (g) kinematic hardening and (h) isotropic softening.

consistently predicts a greater UTS for greater deformation rates. From the MTSS plot, it is evident that the strain hardening of the material develops in a nearly linear fashion after UTS. In addition, the agreement between the mean true strain from the simulation and the experiments indicates that the predicted total reduction of minimum area at the neck is also accurate. The strain hardening is a function of the chosen inner variables. The fig. 5.13g depicts the evolution of the effective kinematic hardening variable, $\mathbf{Z}$, with respect to the accumulated plastic strain, p. $\mathbf{Z}$ is derived from the sum of three kinematic hardening variables, of which two are necessary for describing the hardening up until the point of instability and the third is necessary for describing the strain hardening up until the eventual material damage. The kinematic hardening parameters are calibrated to compensate for the softening provided by the isotropic softening, ψ, as this softening is experimentally observed under cyclic loading and does not appear separately under monotonic uniaxial loading. The fig. 5.13h depicts the evolution of ψ along with the variables ψ_1 and ψ_2 with respect to p. Consequently, $\psi \times \mathbf{Z}$ ultimately represents the effective estimation of strain hardening. The fig. 5.13e illustrates the effect of deformation/strain rate on the reduction of neck radius with respect to engineering strain. After an initial period of linear development, the radius reduction becomes nonlinear, indicating the development of the neck. For the higher deformation rate, a decrease in the rate of radius reduction and fracture strain along both the engineering strain and true strain are observed. The fig. 5.13f provides further insight, showing that the evolution of VVF is also accelerated at a higher deformation rate. The distribution of VVF in the specimen is shown in fig. 5.12i, which when compared with fig. 5.12e shows that maximum VVF is reached at the core of the neck as void growth is driven by the hydrostatic stress.

Next, similar tensile test simulations are repeated at room temperature. In fig. 5.11b, the superimposed image of the simulated specimen at failure over the corresponding image from the experiment performed at 0.2 mm/min shows good agreement on the predicted neck profile and neck radius. This simulated reduction in minimum diameter with respect to total elongation is verified by comparing the ESS and MTSS plots from the simulation and experiment results in figs. 5.14a to 5.14d. The inelastic, post-yield and post-necking behaviours are adequately described. Similar to 300 °C, the material's strain hardening develops in a nearly linear fashion after UTS. Deformation/strain rate influence on the rate of radius reduction is observed to be stronger at RT than 300 °C, as seen in fig. 5.14e where the process is clearly slower at higher rate. However, the decrease in fracture strain seems to be minor as seen in fig. 5.14f. Strain rate influence on the specimen profile at failure, as obtained from simulations and experiments is compared in fig. F.1. The evolution of the hardening variables such as the kinematic hardening in fig. 5.14g, isotropic softening in fig. 5.14h indicate that strain hardening at RT is also stronger than at 300 °C. Simulations are also performed at 100 and 200 °C with a deformation rate of 2 mm/min, using material parameters linearly interpolated with respect to temperature. The simulated stress-strain relationships for the material are compared with experimental results in fig. 5.15, which confirm the model's capability to reliably describe all the desired post-yield and post-necking material behaviour. However, there is a noticeable scatter between the model predictions and experimental data. The temperature influence on total elongation and specimen profile at failure, as obtained from simulations and experiments is illustrated in fig. F.2.

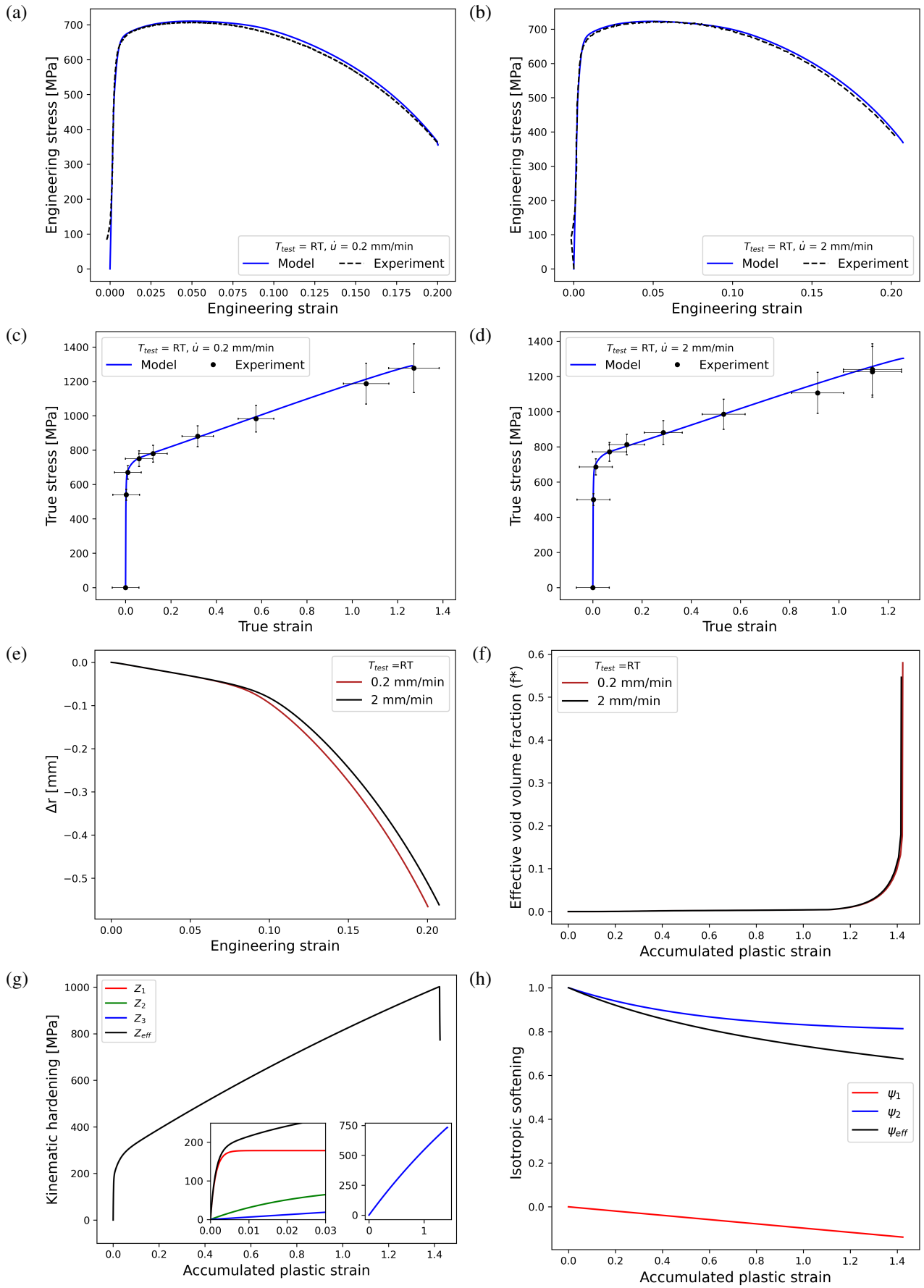

Figure 5.14: Comparison of simulation and experimental results for tensile test performed at RT: (a, b) ESS, (c, d) MTSS. Strain-rate influence on (e) change in neck radius, (f) damage (VVF), (g) kinematic hardening and (h) isotropic softening.

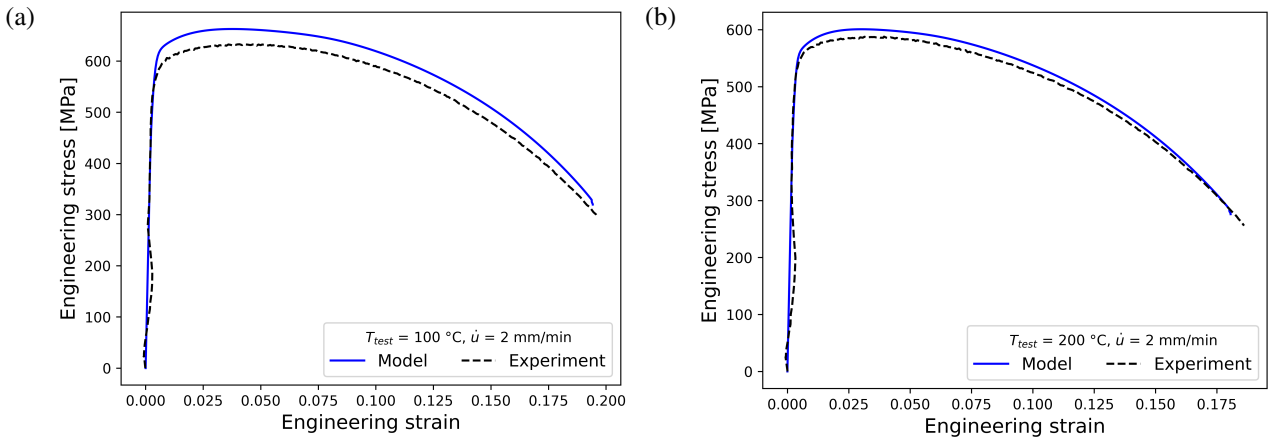

Figure 5.15: Comparison of engineering stress-strain plots from the simulation and experimental results for tensile test performed at 100 and 200 °C.

It is demonstrated that the viscoplastic model can describe the strain-rate sensitivity, deformation, and damage behaviour of the unirradiated material at the reactor's operation temperatures which range between RT and 300 °C. The model accurately predicts the reduction in minimum area and total elongation at failure, thereby validating its ability to describe material ductility in these conditions. The strain-rate sensitivity and strain hardening of the material are seen to reduce with an increase in temperature. It is evident that strain rate sensitivity plays a significant role in the predicted post-necking behaviour and the rate of neck development. The viscous stress linked to the material's strain rate sensitivity can be observed by comparing MTSS plots. Although the viscous stress is much smaller than the material's strain hardening, the former controls the development of instabilities [81], that drive the neck development. In addition, Needleman and Tvergaard [140] corroborated the influence of strain rate on the evolution of the VVF observed in figs. 5.13f and 5.14f. Therefore, it has been demonstrated conclusively that an increase in strain rate contributes to an increase in the total elongation of the specimen (see fig. F.1) by delaying the development of the neck.

5.2.3 Irradiated specimen

Uniaxial tensile testing at 300 °C and a deformation rate of 0.2 mm per min is simulated after irradiating the specimen to 0.65 and 1.18 dpa at 300 °C. Good agreement between the simulated and experimentally fractured images of the specimen at the point of failure is shown in fig. 5.16. The figs. 5.17b and 5.17c shows the axial and radial displacements of the irradiated specimen at the point of failure, which show faster necking than the unirradiated material at 300 °C. The figs. 5.17d, 5.17e and 5.17h shows that the deformation is localized. The figs. 5.18a and 5.18b compare the ESS relationships derived from simulation results and available experimental data. Yield stress, σ_y, increases due to irradiation-induced hardening, σ_H, and this phenomenon is well described. Both the σ_H (fig. 5.18e) and UTS predicted by the model are very close to what has been observed experimentally. There is also a precise description of the material's reduced uniform strain. The rapid decline of the ESS curve post UTS is indicative of the high development rate of the neck and

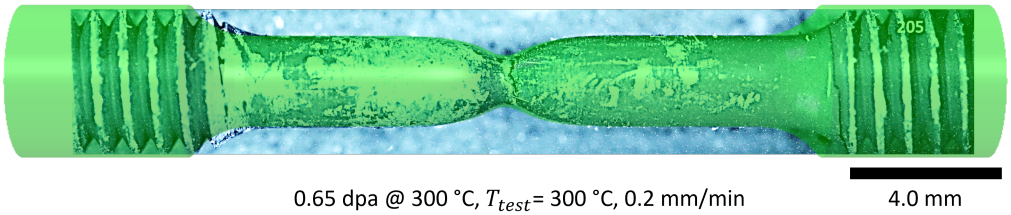

(a) 0.65 dpa @ T_{test}=300 °C

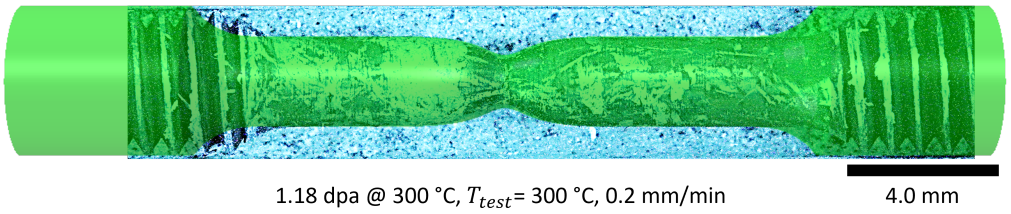

(b) 1.18 dpa @ T_{test}=300 °C

Figure 5.16: Simulated specimen profile (transparent green) compared with images of damaged specimens irradiated to (a) 0.65 dpa and (b) 1.18 dpa, and deformed at 300 °C with a rate of 0.2 mm/min.

the associated geometric relaxation. The predicted engineering fracture strain has good agreement with experimental data and is significantly reduced when compared to the unirradiated specimen, which is consistent with the experimental observations. The MTSS relationships derived from simulation results are displayed in figs. 5.18c and 5.18d. For the 0.65 dpa specimen, the simulation has good agreement with the experimental data, capturing both the material's strain hardening and the specimen's reduction in minimum diameter. In contrast to unirradiated materials, where the MTSS plots show continuous strain hardening up to failure, the irradiated materials exhibit a short period of softening following the UTS. Although this softening is initially pronounced, it reduces eventually for the material to resume hardening. The removal of irradiation defects under plastic deformation accounts for the entirety of this softening. When comparing figs. 5.17f to 5.17h, we see that the largest reduction in irradiation defect density, N, and σ_H occurs in regions of localized deformation. The N at the central position of the specimen is plotted against p in fig. 5.18f, where the rate of defect removal is initially high, resulting in a sharp decrease in N and σ_H. As soon as N falls below the threshold controlled by the parameter l_N the rate of defect removal drops dramatically, reaching a quasi-saturation state where the removal is allowed to continue at a constant rate. A portion of defects remains even at fracture. As shown in figs. 5.18c and 5.18d, the predicted true fracture strain is reduced for irradiated specimens and has good agreement with experimental data. In fig. 5.17i, VVF distribution in the specimen is seen to be concentrated at the core of the neck region, like the unirradiated specimens. The fig. 5.18h shows a plot of VVF versus p, which indicates that void growth is more rapid and void coalescence is hastened in materials subjected to higher doses of radiation. The fig. 5.18g illustrates the effect of irradiation on neck development, by plotting the change in minimum specimen radius at the neck versus the engineering strain derived from the

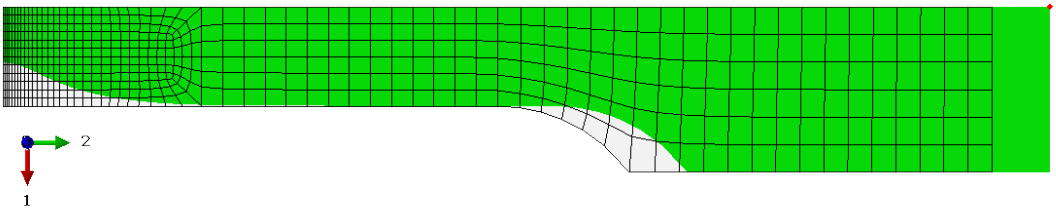

(a) Deformed and undeformed specimen

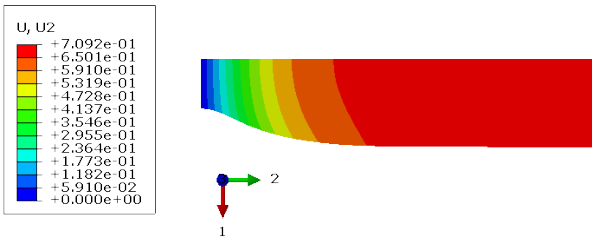

(b) Axial displacement (mm)

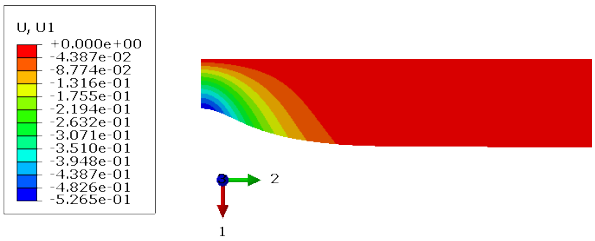

(c) Radial displacement (mm)

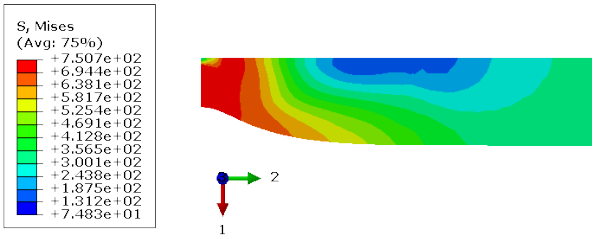

(d) von Mises stress (MPa)

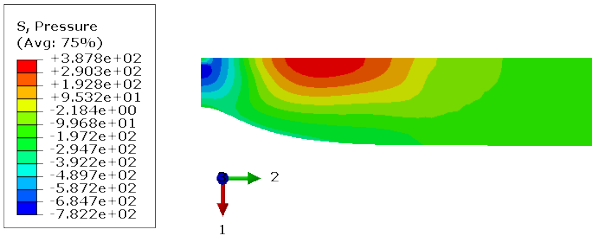

(e) Pressure stress (MPa)

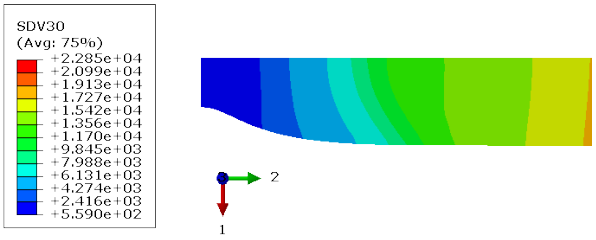

(f) Irradiation defect density (MPa^2)

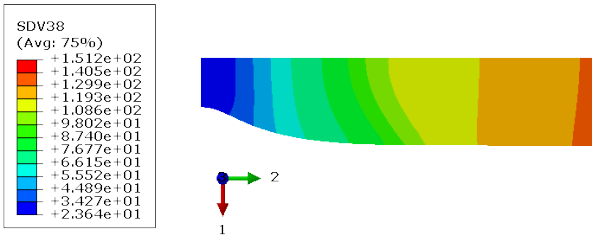

(g) Irradiation hardening (MPa)

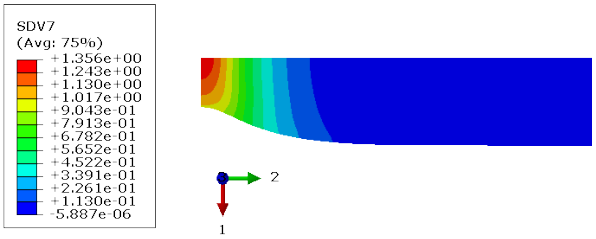

(h) Accumulated plastic strain

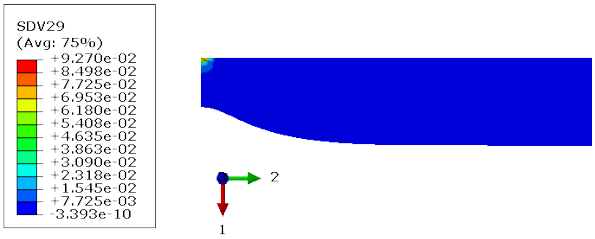

(i) VVF

Figure 5.17: Simulation results for irradiation (0.65dpa @ T_{irr}=300 °C) and tensile test performed on at 300 °C and 0.2 mm/min

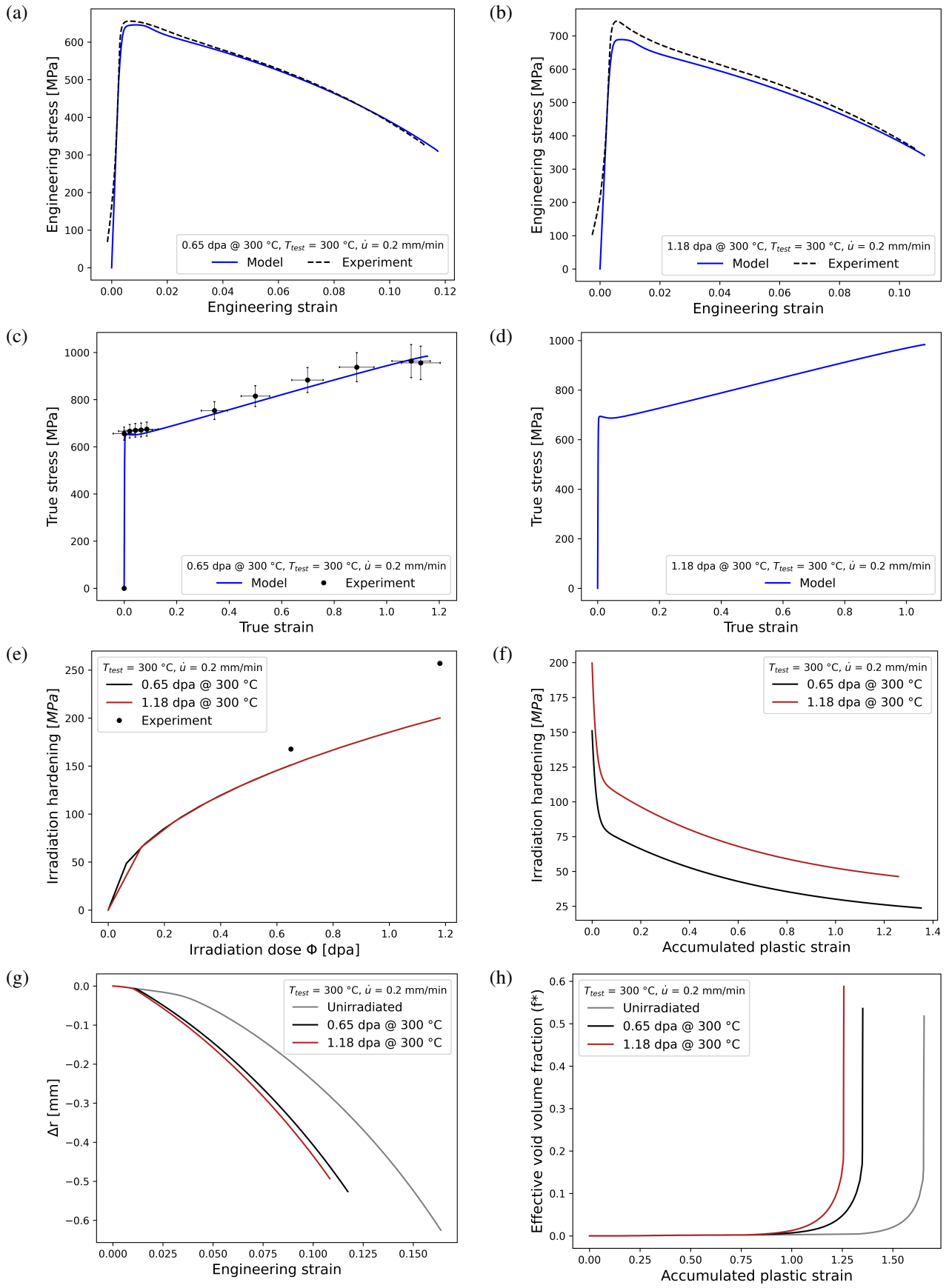

Figure 5.18: Comparison of (a, b) ESS and (c, d) MTSS from simulation and experimental results for irradiation (0.65 and 1.18 dpa) and tensile test of Eurofer97 at $T_{test} = 300$ °C.
Illustration of irradiation hardening evolution with defect (e) nucleation and (f) removal, and irradiation influence on (g) reduction in neck radius and (h) damage (VVF).

gauge displacement. Clearly, the neck develops much faster in irradiated specimens, and the rate of development increases with increasing irradiation doses.

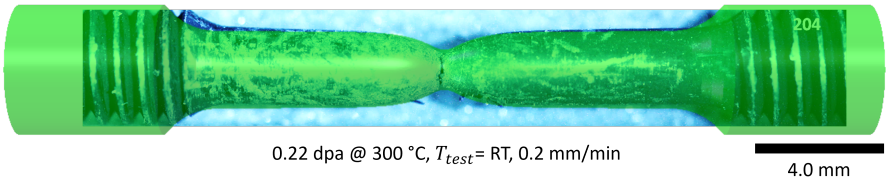

(a) 0.22 dpa @ T_{test}=RT

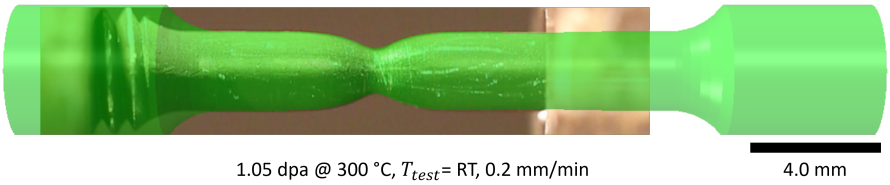

(b) 1.05 dpa @ T_{test}=RT

Figure 5.19: Simulated specimen profile (transparent green) compared with images of damaged specimens irradiated to (a) 0.22 dpa and (b) 1.05 dpa, and deformed at RT with a rate of 0.2 mm/min.

Next, specimen irradiation to 0.22 and 1.05 dpa followed by uniaxial tensile test at room temperature and at the deformation rate of 0.2 mm/min are simulated. In fig. 5.19, the simulated specimen at failure is superimposed over images of the post-test fractured specimens. In contrast to the 0.22 dpa specimen where the neck is seen to have developed in the middle, the neck develops away from the middle in the 1.05 dpa specimen. This phenomenon is discussed in section 6.1.0.3. However, the profile and diameter of the neck is well described. The comparison of ESS relationships from simulations and experiments results in figs. 5.20a and 5.20b show that the increase in yield stress, σ_y is well described. However, the σ_H predicted by the model differs significantly from the experimental observations of the 0.22 dpa specimen. Although scattering of σ_H at low neutron-irradiation doses is expected, as discussed in section 5.1.3.2, the 0.22 dpa specimen exhibits an outlier behaviour, as shown in fig. 5.20e, and can therefore be disregarded. The uniform-elongation regime is drastically reduced and the rapid neck development following UTS is well described. The resulting softening of the ESS curve agrees well with experimental observations. While the predicted decrease in engineering fracture strain is consistent with laboratory findings, there is scatter in the experimental and simulated data due to the scatter in irradiation hardening. The MTSS relationships shown in figs. 5.20c and 5.20d display a trend consistent with the simulations at 300 °C. There is a short period of material softening post UTS, inducing a negative hardening modulus. Eventually, the material's strain hardening becomes more dominant. At first, plastic deformation causes a dramatic drop in N, as shown in fig. 5.20f. When N is below the l_N-controlled threshold, however, removal of N reaches a quasi-saturation state in which it continues at a constant rate. At larger strains (>40 %), all defects contributing to material hardening are eliminated. The predicted true fracture strain is reduced for irradiated specimens and has good agreement with experiments as seen in figs. 5.20c and 5.20d. The fig. 5.20h illustrates the irradiation influenced reduction of the predicted fracture strain, where the VVF reaches the critical value (f_c) more rapidly as the irradiation dose increases. However, there

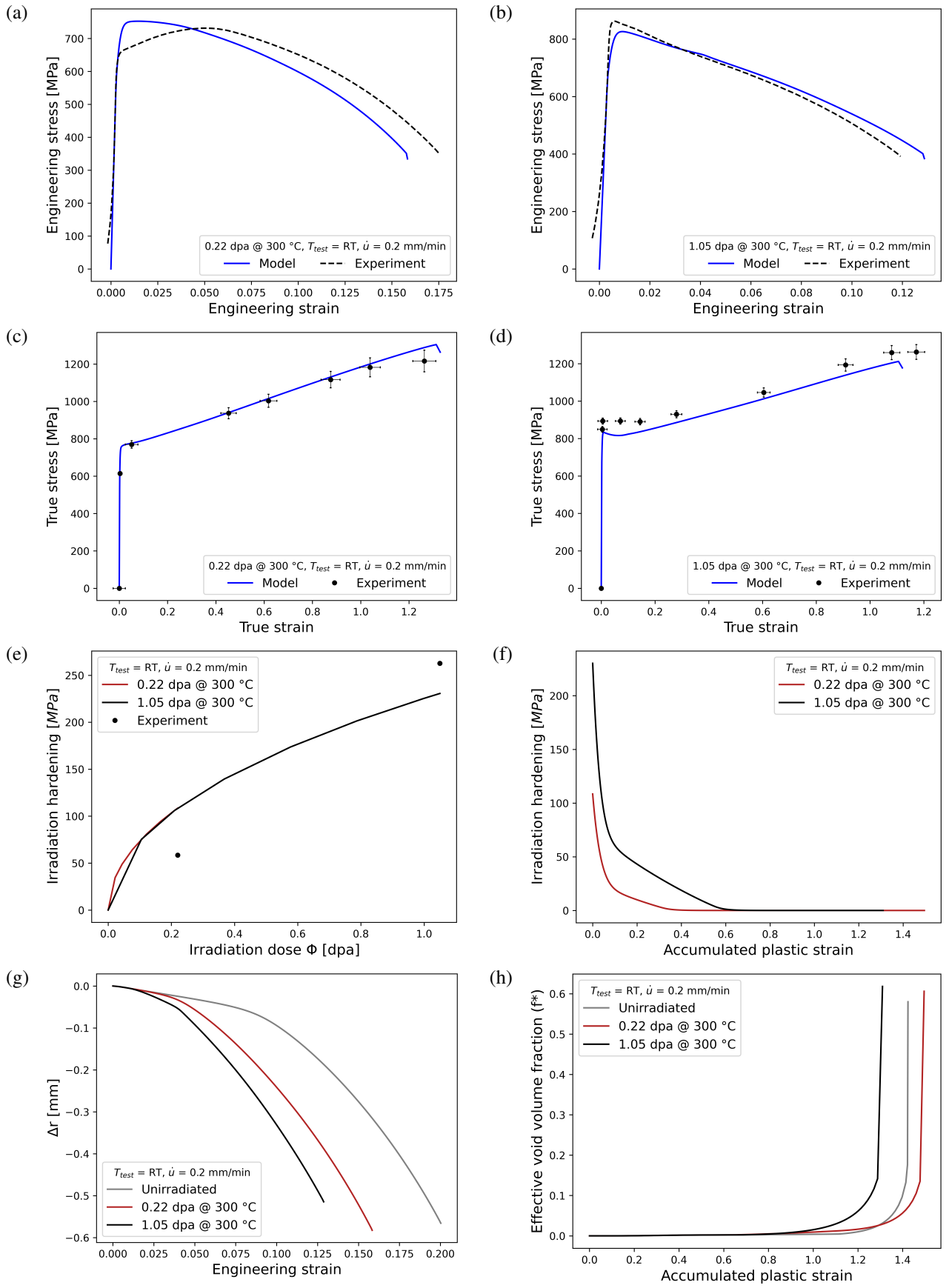

Figure 5.20: Comparison of (a, b) ESS and (c, d) MTSS from simulation and experimental results for irradiation (0.22 and 1.05 dpa) and tensile test of Eurofer97 at T_{test} = RT.
Illustration of irradiation hardening evolution with defect (e) nucleation and (f) removal, and irradiation influence on (g) reduction in neck radius and (h) damage (VVF).

is overestimation of fracture strain for 0.22 dpa due to the reduction in viscous effects originating from the interpolation strategy for n and K. Irradiation influence on neck development is shown in fig. 5.20g, where the faster reduction in neck radius suggests that the neck development is faster with increasing irradiation doses.

5.2.4 Ductility study

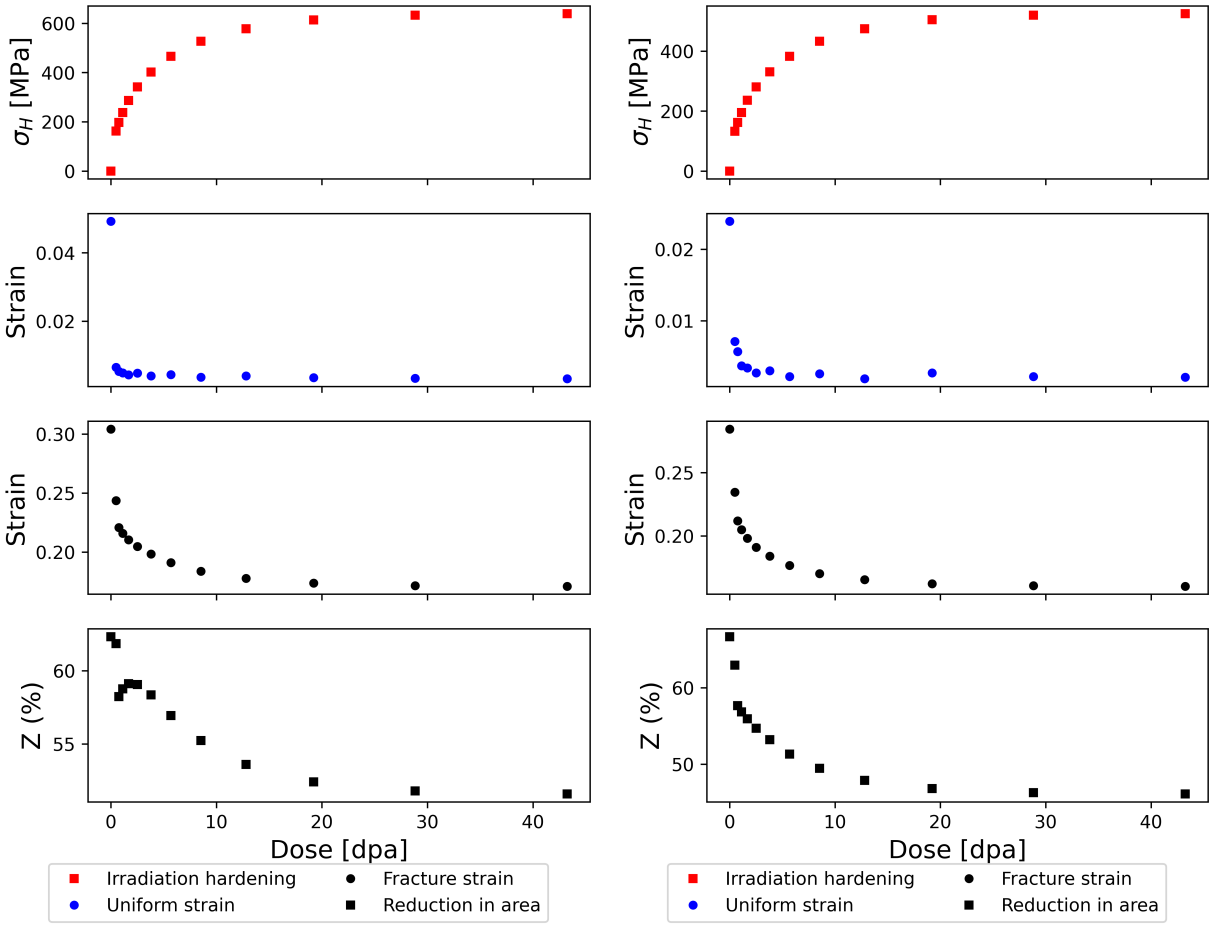

(a) RT

(b) 300 °C

Figure 5.22: Simulated irradiation influence on tensile properties.

Ductility of a material is defined as it's ability to undergo plastic deformation under a tensile load, without failure. Ductility can be quantified by a) elongation and b) percentage reduction of cross-sectional area. A larger fracture strain and reduction of area generally indicates greater ductility. However, the reduction of area is mostly seen as a better measure of ductility. To study the influence of irradiation on ductility reduction predicted by the model, simulations are performed on smooth specimen and notched specimens of notch radius 0.5 and 0.2 mm using specimen geometry adopted from literature [15] which is shown in fig. A.4. Inclusion of the notched specimens allows the study of how initial triaxiality affects the local fracture strain. Axisymmetric FE models (see fig. A.5) are built

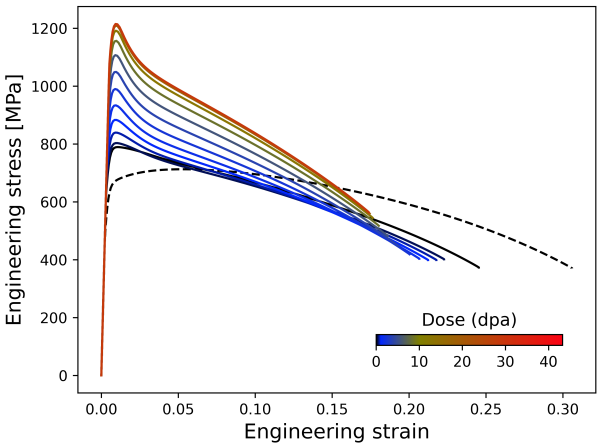

(a) RT - Engineering stress and strain

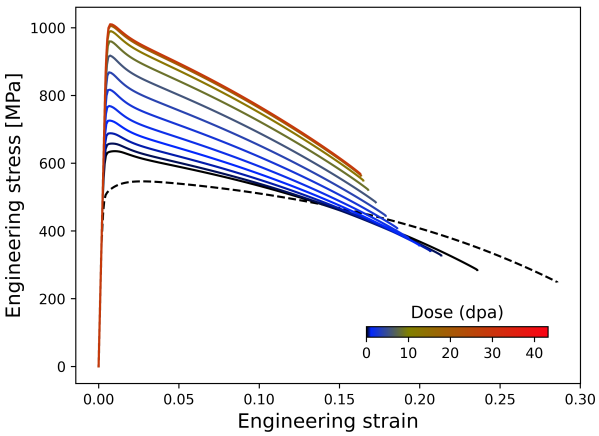

(b) 300 °C - Engineering stress and strain

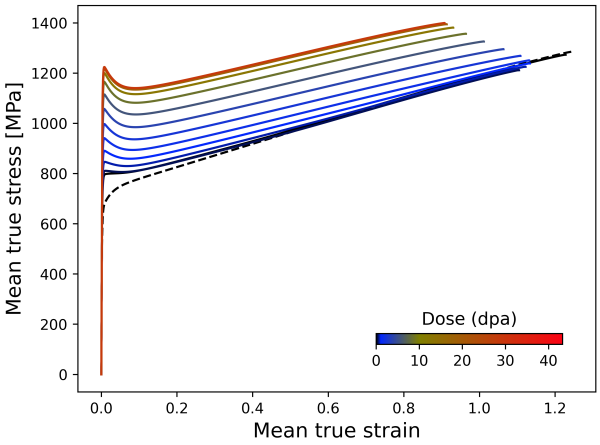

(c) RT - Mean true stress and strain

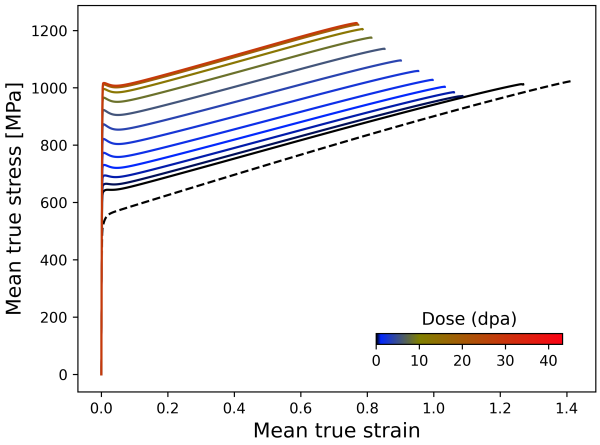

(d) 300 °C - Mean true stress and strain

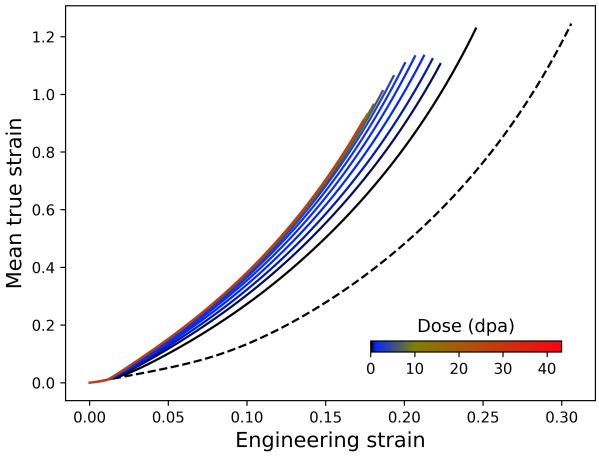

(e) RT - Mean true strain vs. engineering strain

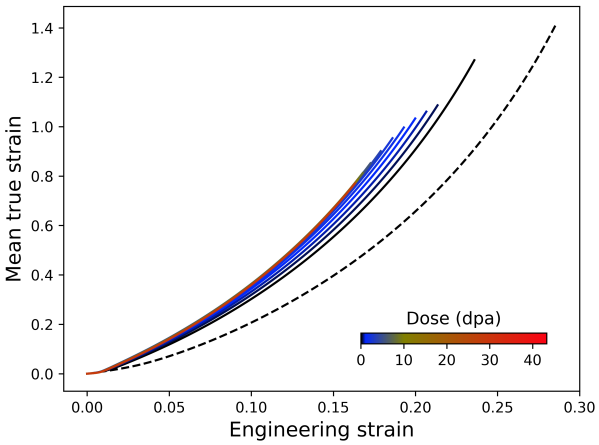

(f) 300 °C - Mean true strain vs. engineering strain

Figure 5.21: Irradiation influence on tensile properties at RT and 300 °C for a smooth specimen, with unirradiated material in dotted lines.

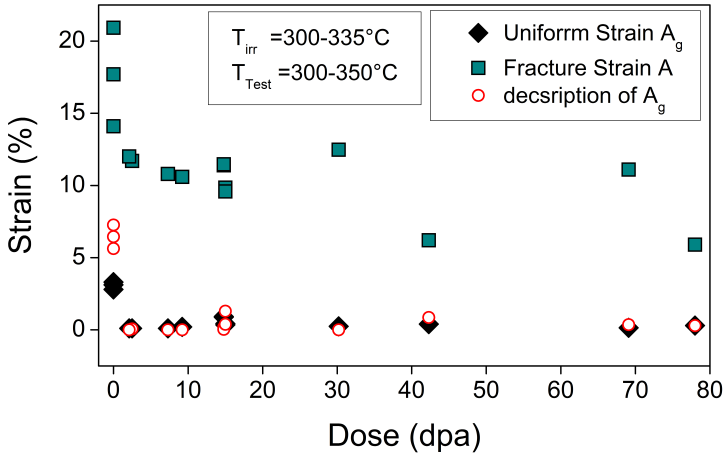

Figure 5.23: Experimental data for different product forms of Eurofer97 [1].

using quarter of the specimen similar to those shown in fig. 5.3a, to perform simulations at a constant T_{irr} = 300 °C, with T_{test} of RT and 300 °C, and a displacement rate of 0.2 mm/min. A set of 13 irradiation doses from zero up to 43 dpa where the predicted σ_H saturates, is chosen to ensure that the predicted irradiation-induced hardening is evenly distributed. This results in a higher concentration at low-doses, which is very beneficial for studying the drastic changes in material properties occurring in this regime.

The engineering stress-strain relationships taken from the simulation results of the smooth specimen are compared in figs. 5.21a and 5.21b. The model predicts a steady rise in yield stress and UTS, with a sharp decline in engineering fracture strain for increasing doses of irradiation. Even though these properties change quite rapidly at low doses, they are seen to gradually stabilize at higher doses. The mean true stress-strain relationships plotted in figs. 5.21c and 5.21d illustrate the irradiation influence on the hardening modulus. The modulus is generally low post-yield, even turning negative for higher doses. But eventually, it stabilizes and strain hardening develops almost at the same modulus of the unirradiated material. At RT, the curves show larger level of softening and align with the unirradiated material plots for low doses. True fracture strain is significantly reduced by irradiation, and this reduction increases as the irradiation dose increases. The figs. 5.21e and 5.21f illustrate how the neck develops in relation to the total gauge displacement by plotting the engineering strain against the true strain. The initial linear relationship seen represents the gauge section's uniform deformation, whereas the nonlinear period represents the gauge section's nonuniform deformation during the formation of the diffused and localized neck. It is evident that neck development begins much earlier in irradiated specimens, and that the rate of development accelerates as the radiation dose increases. It can be determined that the predicted neck development is diffused in nature because there was no sign of an unstable neck development.

[1]This article was published in Gaganidze and Aktaa [141], Copyright Elsevier (2013).

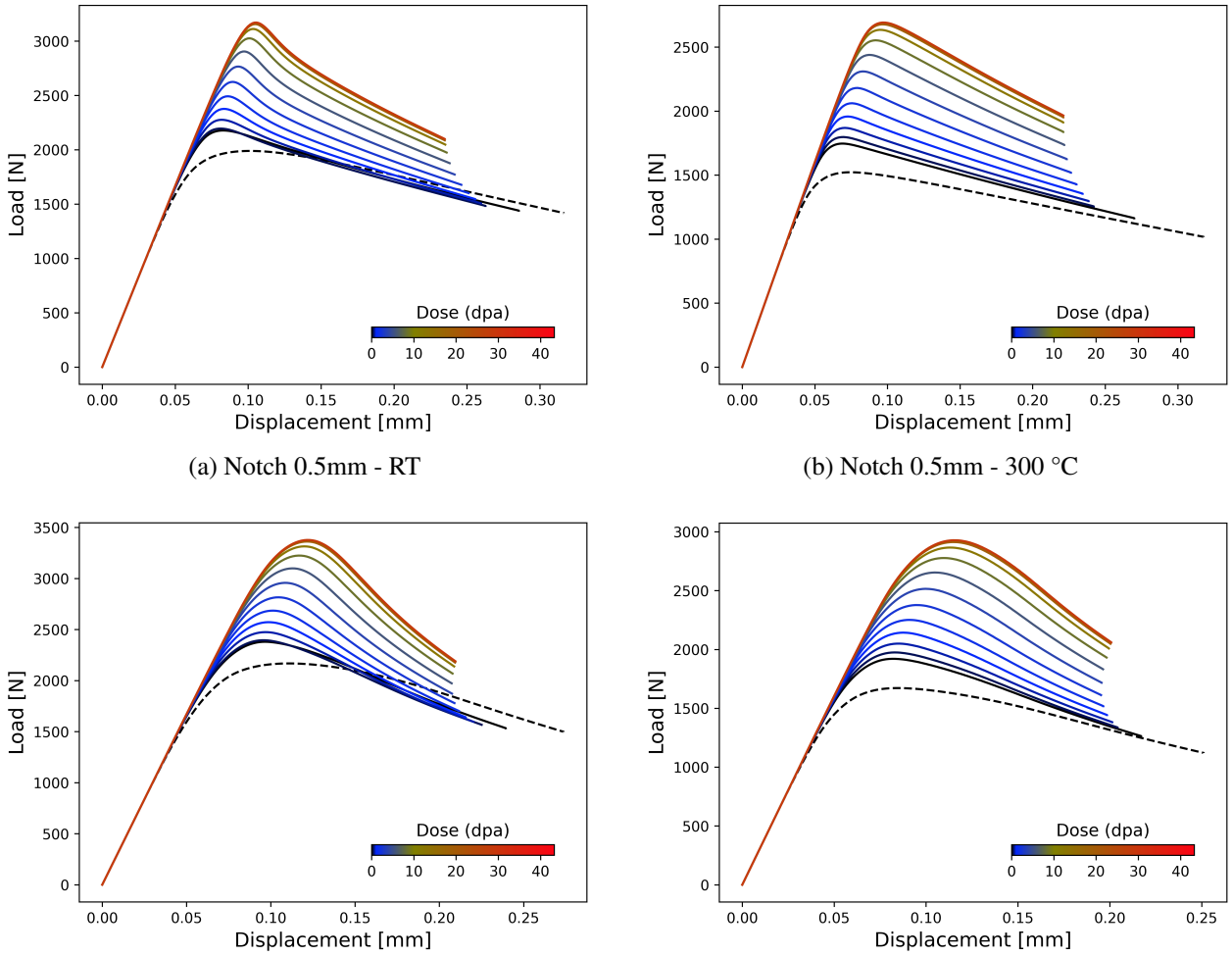

(a) Notch 0.5mm - RT

(b) Notch 0.5mm - 300 °C

(c) Notch 0.2mm - RT

(d) Notch 0.2mm - 300 °C

Figure 5.24: Irradiation influence on load vs displacement at RT and 300 °C for notched specimen, with unirradiated material in dotted lines.

The fig. 5.22 depicts a summary of the temperature-dependent tensile properties of the material predicted by the model at RT and 300 °C with respect to irradiation dose. The hardening is greater at RT than it is at 300 °C for the same dose, as can be seen from the predicted σ_H plot. The uniform strain plot demonstrates how, even at low doses, the uniform elongation is almost completely lost. This trend is in agreement with the published experimental data [141] shown in fig. 5.23, of different forms of Eurofer97 which have marginally different tensile properties to the material used in this work. At RT, it is observed that this loss of uniform elongation is more drastic. The engineering fracture strain is also plotted, displaying a sharp decline at very low doses (30% loss), an initial stabilization just after 2 dpa, and a saturation at roughly 20 dpa (44% loss). This trend is also evident in the data from the literature [141], where it is understandable that there is no further noticeable decrease in fracture strain as a result of an increase in irradiation dose, despite the scatter in the recorded fracture strain at doses above 10 dpa shown in fig. 5.23.

Further information can be obtained by plotting the ductility, or the percentage decrease in the cross-sectional area (Z) at the neck, against the radiation dose. Similar to the previously mentioned metrics, the final reduction in area drops quickly at low doses, but steadily stabilizes as the dose rises and reaches saturation at large doses. At RT, there is an outlier behaviour at low doses between 0.75 and 2 dpa, where there is a significant fall in Z initially, but increases until 2 dpa and then begins to decrease with dose increase. This most likely results from parameter interpolation at low doses, which disappears at higher doses. However, using an exponential fit for l_N appears to alleviate this anomaly, as seen in figs. H.2 and H.3. This suggests that the $l_N - \sigma_H$ relationship is non-linear in nature. The model predicts a 17% and 30% drop in ductility at RT and 300 °C respectively, based on the area reduction.

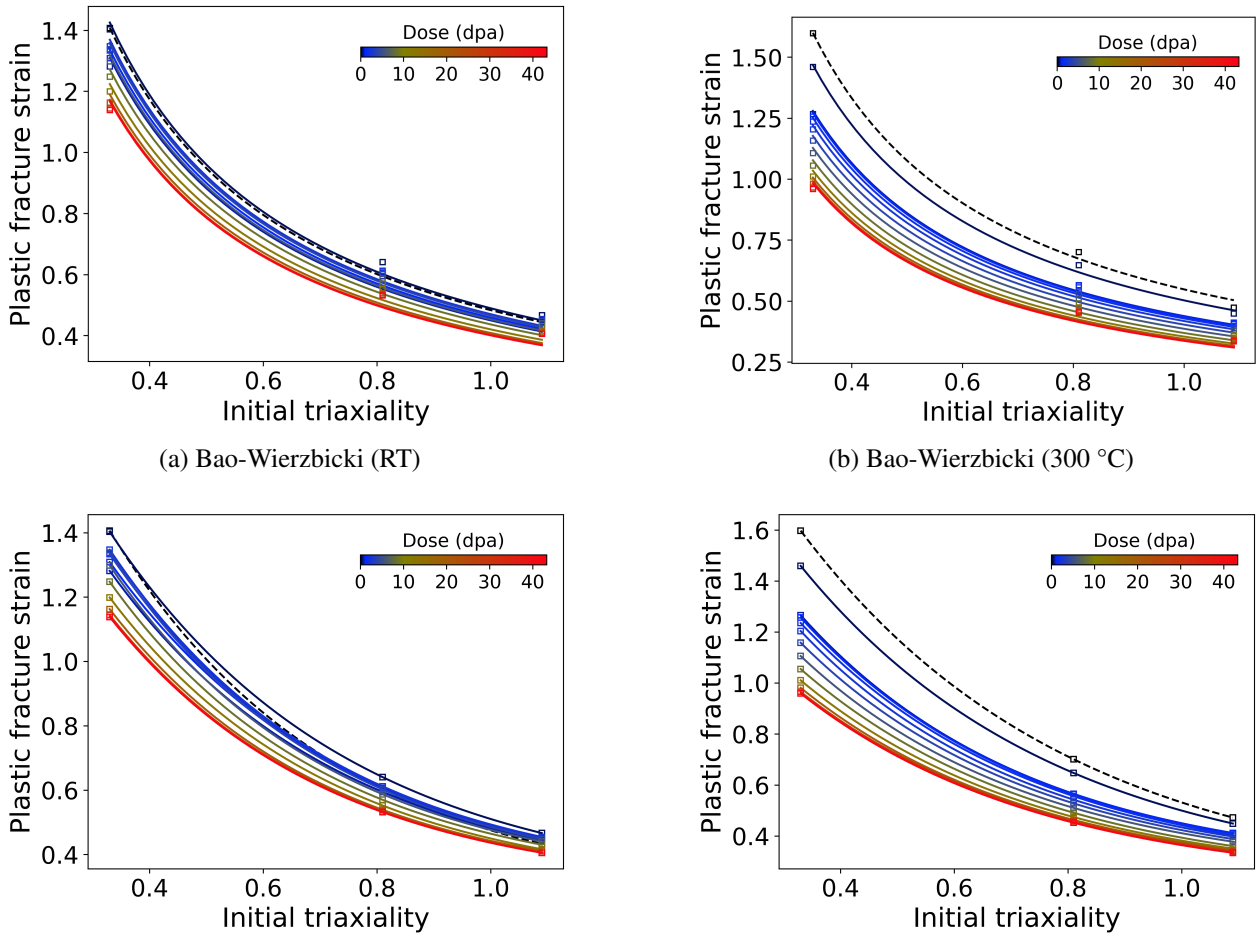

(a) Bao-Wierzbicki (RT)

(b) Bao-Wierzbicki (300 °C)

(c) Johnson-Cook (RT)

(d) Johnson-Cook (300 °C)

Figure 5.25: Comparison of irradiation influence on true plastic fracture strain with respect to initial triaxiality at RT and 300 °C, with best fits obtained with Bao-Wierzbicki and Johnson-Cook models. The dashed lines mark the results for the unirradiated state.

The load displacement results of the two notched specimens are shown in fig. 5.24. The material behaviour is consistent with the smooth specimen, with the increased peak load due to the increased hydrostatic stress and irradiation hardening being well represented. The total elongation continuously reduces with an increase in dose across all test cases. The fig. 5.25 plots true plastic strain at fracture

against initial triaxiality factor (TF) of smooth and notched specimens for the set of irradiation doses. Individual plots are shown later in fig. 6.4. For unirradiated specimens, the fracture strain is highest for smooth specimens with an initial TF of 0.33. This decreases by 57% and 69% for specimens with notch radius of 0.5 mm and 0.2 mm, which correspond to triaxiality values of 0.81 and 1.09, respectively. As dose increases, this decline eases to 53% and 64% at ≈20 dpa and saturates thereafter. At RT, an out-lying behaviour in the fracture strain is seen which follows a similar trend to the reduction in minimum area (Z) for doses below 2 dpa. While fracture strain decreases more at 300°C than at RT, the trend in the reduction of fracture strain remains nearly similar. The out-lying behaviour under 2 dpa at RT is absent at 300 °C. Therefore, the material model predicts that an increase in triaxiality and irradiation dose reduces fracture strain. This is consistent with Rice and Tracey [142], who established an inverse relationship between the fracture strain and initial triaxiality factor ($\varepsilon_f \approx 1/TF$). Among the several models found in literature that describe this relationship, the Bao-Wierzbicki (BW) model [143] for high triaxiality ($TF \geq 0.4$)

$$\varepsilon_f = \frac{A}{TF}, \tag{5.14}$$

and the Johnson-Cook (JC) fracture model [144, 145] for constant strain rate and temperature

$$\varepsilon_f = D_1 + D_2 \cdot \exp(D_3 \cdot TF) \tag{5.15}$$

are widely used due to their simplicity. Here, A and D_i are temperature and irradiation dose dependent model parameters that need to be identified for each temperature and each dose. The fig. 5.25 shows the best fit curves obtained for the two models. While the BW model which uses a single parameter gives good description of the material's $\varepsilon_f - TF$ relationship in the unirradiated condition, considerable scatter is seen as the dose increases. On the other hand, the reduced JC model which requires three parameters provides very good description.

Based on the results of this ductility study at both temperatures, it is evident that the change in material properties occurs rapidly in the low dose range (<5 dpa), stabilizing between (5 and 15 dpa), and reaching general saturation beyond this range. These results are discussed in section 6.1 with additional data from these simulations summarized in appendix G.

Chapter 6

Discussion and remarks

The developed coupled finite strain viscoplastic and ductile damage model is validated in sections 5.2.2 and 5.2.3 using available experimental data. Additional simulations were performed on various irradiation damage doses in section 5.2.4 to analyze the predicted irradiation influence on the material's tensile properties. Based on these simulation results, a discussion on the model's characteristics and other factors that play a role in modeling the post-yield and post-necking behavior of unirradiated and irradiated materials is made in this chapter. Studying the influence of irradiation on material failure, the possibility and scope of relaxing the damage criteria in the design rules of nuclear fusion power plant components is investigated in this chapter.

6.1 Discussion on simulation results

To support this discussion, the ESS and MTSS plots are determined globally whereas other data computed by the model is extracted at integration points suffering the highest amount of plastic deformation which is typically the core of the neck region.

6.1.0.1 Stress-Strain relationships

The ESS and MTSS plots in figs. 5.21a to 5.21d, 6.1a and 6.1b provide an overview on the predicted tensile properties for the unirradiated and irradiated material at RT and elevated temperatures. As seen in figs. 6.1a and 6.1b, yield stress and therefore, the elastic regime of the unirradiated material is the highest at RT and reduces with increase in temperature, which is consistent with the experimental data in fig. 3.1. The predictions for irradiated specimens are fundamentally dependent on the predicted irradiation defect-density/hardening evolution during irradiation. As already discussed in section 3.2.1, there is significant experimental scatter in irradiation hardening at low irradiation doses (fig. 5.8) [78, 133]. Therefore, there is less likelihood that the model's predicted irradiation hardening will match experimental data at small doses, as seen in figs. 5.18e and 5.20e figs. 5.18 and 5.20. However, the predictions will be more in line with experiments done on specimens exposed to higher irradiation doses because irradiation hardening stabilizes and saturates at higher doses (> 10 dpa) [78, 133, 141].

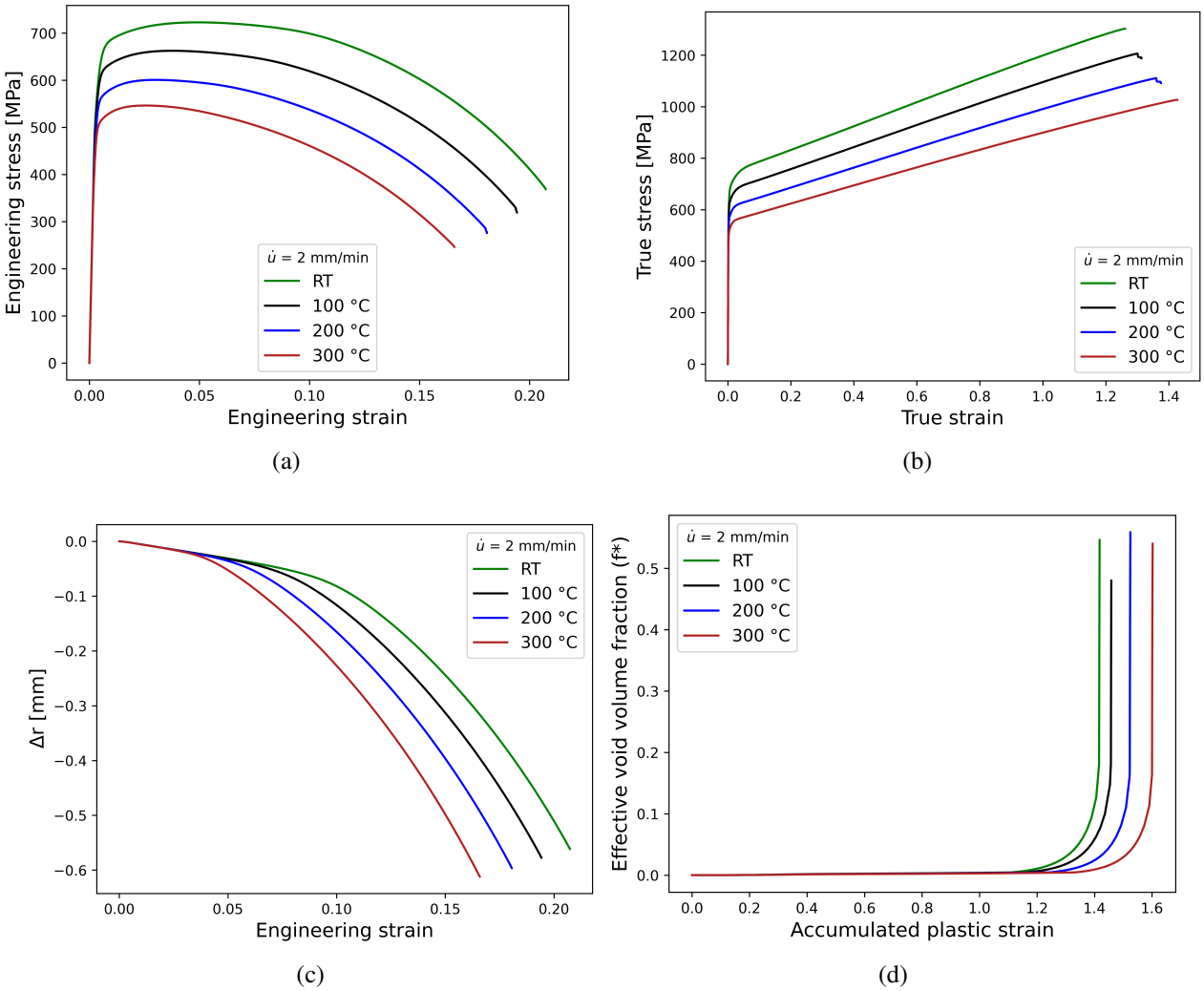

Figure 6.1: Comparison of simulations performed on unirradiated material at RT, 100, 200 and 300 °C: (a, b) stress-strain relationships, (c) change in neck radius and (d) evolution of VVF.

Yet, the steep softening post-UTS is consistently well described by the model. In instances where the predicted hardening is close to experimental data, the steep softening post UTS has good agreement with experiments.

6.1.0.2 Uniform elongation and UTS

The uniform and total elongation of the unirradiated material is the highest at RT and reduces with increase in temperature, which is consistent with the experimental data in fig. 3.1. The predicted true fracture strain remains almost the same across these temperatures. As seen in figs. 5.15a and 5.15b, the predicted UTS at 100 and 200 °C are marginally overestimated in comparison to the experiments. However, the predictions are acceptable as the deviations are minimal (<5%) and fall within the experimental scatter range (15%). In irradiated specimens, the uniform elongation is almost completely lost as seen in figs. 5.21a, 5.21b and 5.22. Therefore, the UTS is very close to the yield stress and highly dependent on the predicted irradiation hardening.

6.1.0.3 Neck development

The post-necking behaviour and neck development is governed by the plastic instability condition (3.9), which is primarily influenced by the change in the hardening modulus, determined by material's strain hardening characteristics. The specimen's non-uniformity causes instabilities. As material matrix is mostly homogeneous, stress concentrations in regions where the cross-section is non-uniform, such as where specimen's shoulder meets gauge section, cause instability. Instabilities manifest themselves and become more severe as the hardening modulus computed by the integration points associated with consecutive nodes on the gauge section's surface satisfies the condition (3.9). A lower hardening modulus favors stronger instability development. Strain hardening is in turn described by the set of hardening models. For unirradiated material, the kinematic hardening and the isotropic softening model are used. The MTSS of unirradiated materials shown in fig. 6.1b illustrates the reduction in hardening modulus with increase in temperature. A higher strain rate sensitivity increases the total elongation [81, 60, 140]. Due to the extremely high local strain and strain rates at the neck, the associated rise in viscous stress (2.102) increases the hardening modulus and plays an important role in regulating the instability development. When instabilities coalesce, they grow dramatically stronger and develop into a diffused neck. With the non-homogeneity from either ends of the gauge section acting as sources, instabilities combine usually at the middle of the specimen. Due to this, most simulations in this work predict a neck development at the middle. The plot of reduction in neck radius Δr against the engineering strain in fig. 6.1c illustrates the neck development in unirradiated materials, where the combination of larger strain hardening and strain rate sensitivity of the material at RT leads to a slow rate of neck development. The identified model parameters indicate that both these characteristics grow weaker at higher temperatures, allowing the neck to develop faster.

In irradiated materials, the defect removal driven by plastic deformation leads to localized softening. This softening reduces the hardening modulus and forces a rapid development of the neck. The TSS computed by the model for increasing levels of irradiation dose is plotted in figs. 6.2a and 6.2b and shows a strong softening post-yield which is a result of the reduction in irradiation hardening shown in figs. 6.2c and 6.2d. In comparison to unirradiated material, the true stress at high plastic strains is lower for low doses at RT. This is caused by the stark contrast between the high and low strain-rate sensitivity of the unirradiated and irradiated material respectively at RT. Due to the unirradiated material's already low sensitivity at 300 °C, this difference is hardly noticeable at this temperature. The model predicts that a major portion of the defect density is removed rapidly with the onset of plastic deformation. As seen in figs. G.1c and G.1d where defect density reduction in the damaged element of smooth specimens is plotted against accumulated plastic strain, once the threshold controlled by l_N is reached, defect removal stabilizes and proceeds further at a steady rate controlled by e_1. At 300 °C, a residual amount of irradiation hardening remains even at the time of failure. This suggests that not all defects are removed. Since l_N estimated at RT is much greater, all defects are completely removed for low doses. With increasing levels of defect density at higher doses, however, some portion of the initial defect density remains left over at the time of fracture.

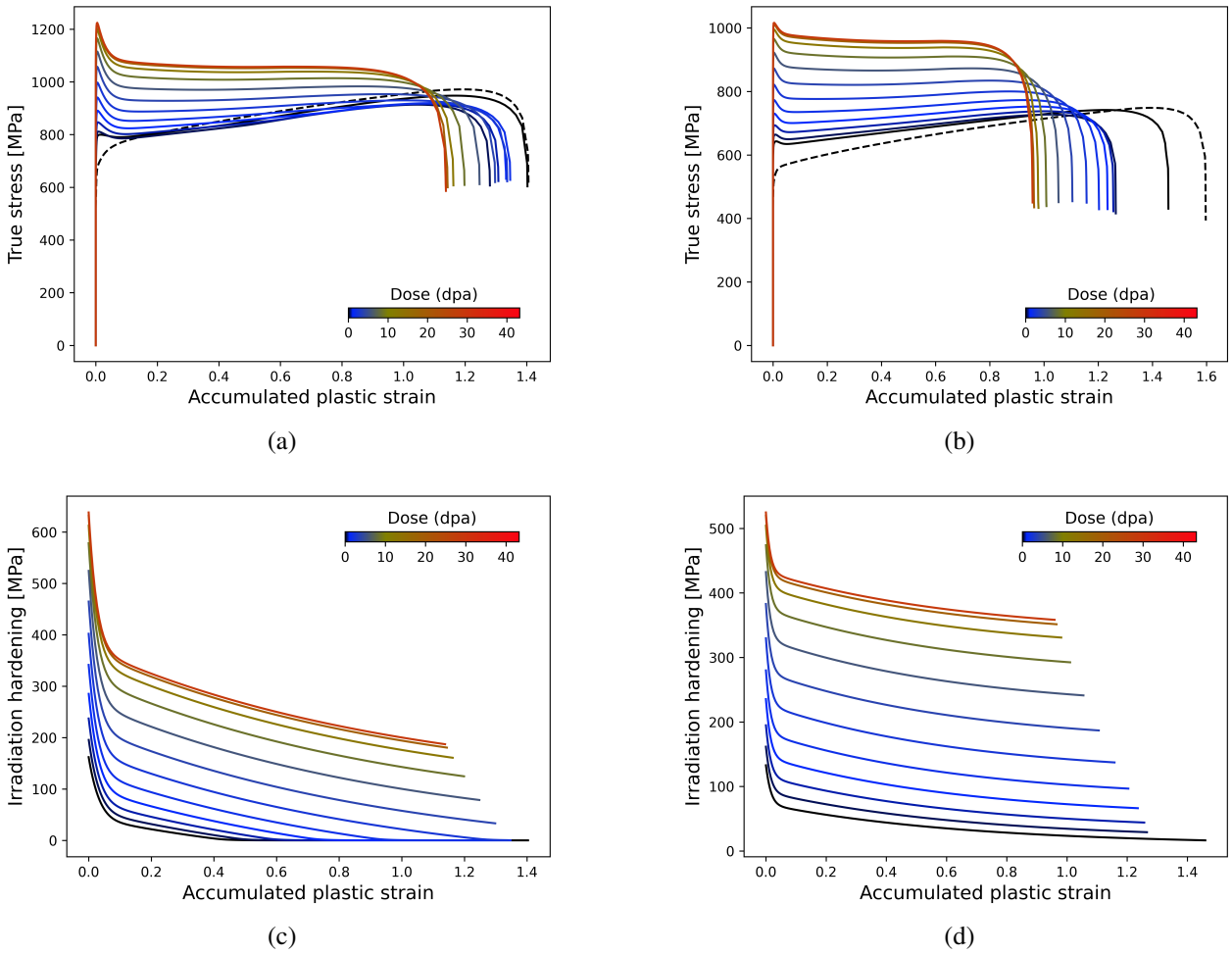

Figure 6.2: Comparison of the true stress-strain and reduction of irradiation hardening computed by the model as a function of irradiation dose, at (a, c) RT and (b, d) 300 °C.

In contrast to other simulations, irradiated specimens of the geometry in fig. A.1 show an offset of the neck from the middle at RT. Similar simulations using the geometry in figs. A.2 and A.4 do not produce this offset. It is likely due to the former's gauge section being larger than the other two. The identified model parameters at RT predict a drastic decrease in the hardening modulus and rate dependence of the irradiated material, which are important in describing the rapid neck development and steep softening seen in the experimental ESS curves following the UTS. This inhibits instability development in consecutive nodes and causes the diffused neck to develop closer to the non-uniformity and away from the middle. Due to these factors, the predicted neck development in irradiated specimens is significantly accelerated and temperature dependent, with localization progressing more rapidly at RT than at 300 °C.

As necking induces a triaxial stress state in the specimen, irradiation defect removal plays a vital role in the triaxiality development. This is illustrated in figs. G.1e and G.1f where triaxiality development in the damaged element of a smooth specimen is plotted against irradiation hardening.

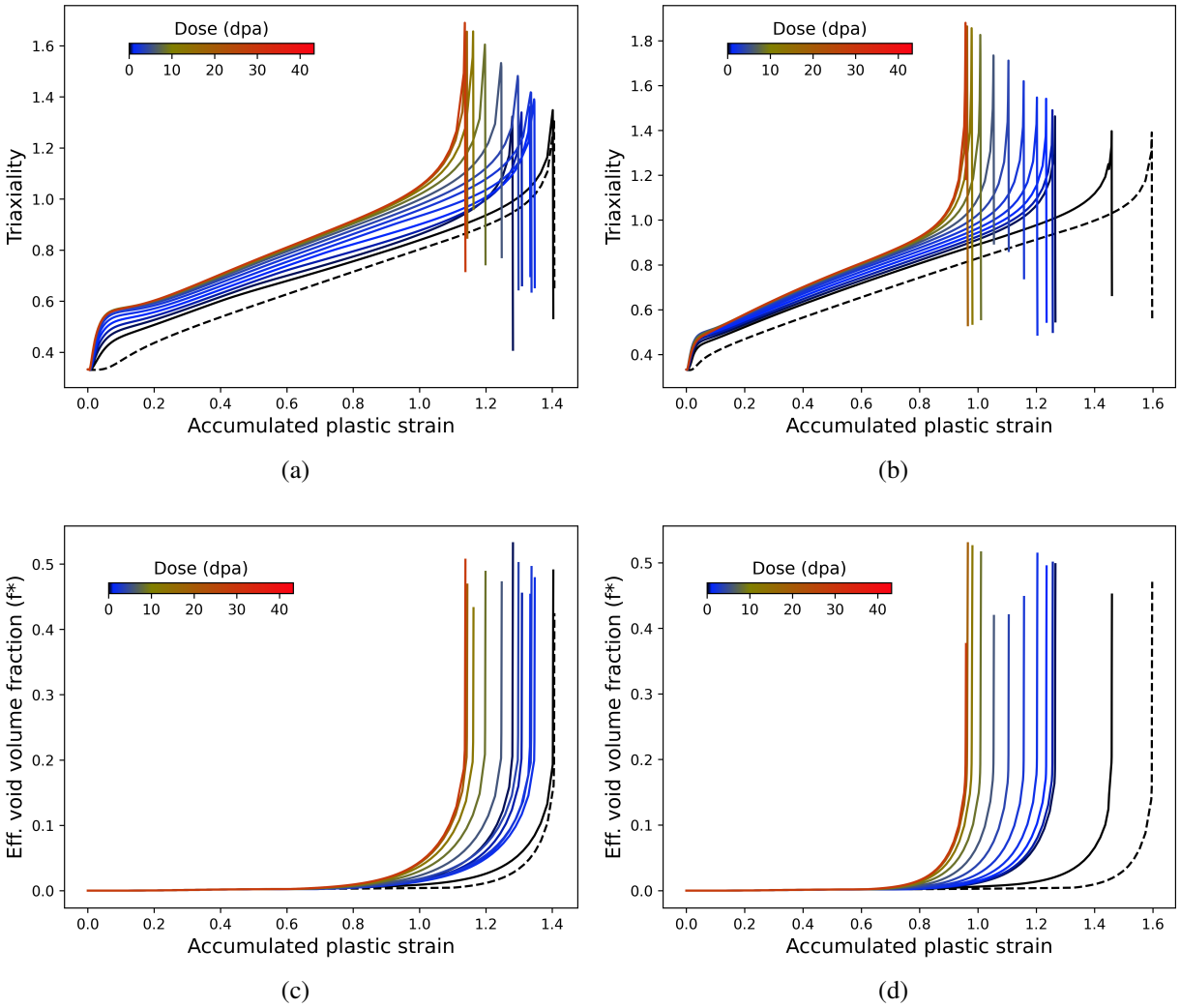

Figure 6.3: Comparison of the triaxiality factor and VVF computed by the model as a function of irradiation dose, at (a, c) RT and (b, d) 300 °C. Unirradiated material in shown in dotted lines.

6.1.0.4 Ductile damage

Effective VVF, f^* from the smooth specimens is plotted against accumulated plastic strain in figs. 6.3c and 6.3d. Development of the respective VVF, f is shown in figs. G.1a and G.1b where the void nucleation reaches a maximum at ε_N. Although void nucleation is plasticity driven and peaks at ε_N, void growth is primarily hydrostatic stress dependent. The GTN model uses triaxiality factor (TF) to describe the growth of VVF. In smooth cylindrical specimens, the TF is initially 0.33 throughout the specimen volume. As the neck develops, the pressure or the volumetric stress grows proportionally within the neck region. Consequently, the TF in the neck regions grows as seen in figs. 6.3a and 6.3b, and drives the void growth. When the VVF reaches the critical values, void coalescence is initiated. The material loses all load bearing capability when f reaches f_F. The local fracture strain and the TF at fracture is higher for unirradiated specimens at 300 °C, when compared to RT. Irradiation influence on ductile damage is characterized by an accelerated void growth and coalescence. As the rate of neck development in the specimens increases proportionally with irradiation hardening, the triaxiality

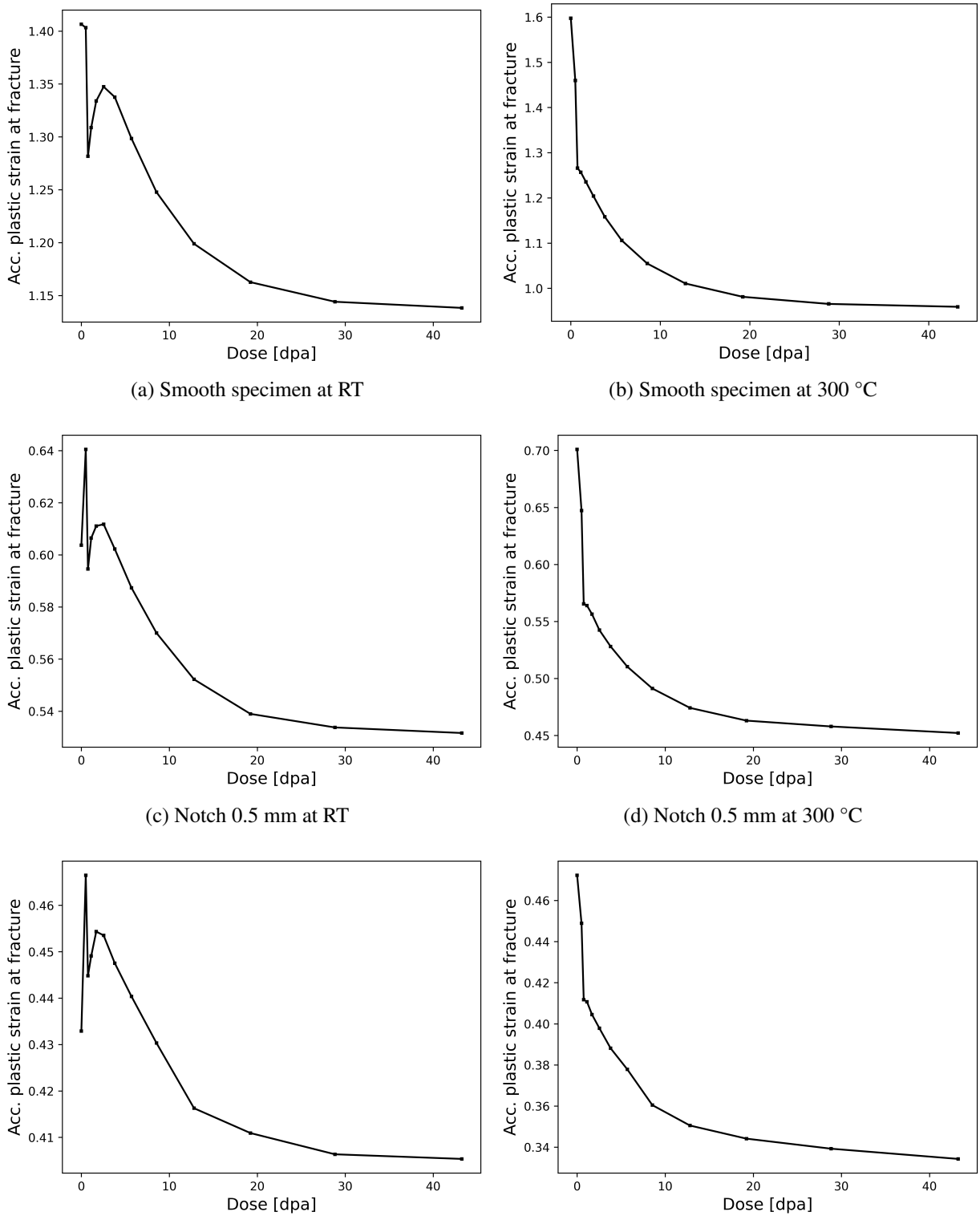

(a) Smooth specimen at RT

(b) Smooth specimen at 300 °C

(c) Notch 0.5 mm at RT

(d) Notch 0.5 mm at 300 °C

(e) Notch 0.2 mm at RT

(f) Notch 0.2 mm at 300 °C

Figure 6.4: Temperature and dose dependent fracture strain predicted for smooth and notched specimens.

development is faster as seen in figs. 6.3a and 6.3b and favors void growth. Void coalescence is also accelerated by a reduction of the critical VVF, f_c. As the material stiffness deteriorates with the onset of coalesce, the equivalent true stress computed by the model shows strong relaxation as seen in figs. 6.2a and 6.2b. This also leads to an exponential rise in the triaxiality as they have an inverse relationship, which is seen in the figs. 6.3a and 6.3b. As the material begins to lose its load bearing capacity for high values of f^*, there is a drop in hydrostatic stress and triaxiality.

In notched specimens, the initial triaxiality is much higher than the smooth specimen as shown in figs. G.4 and G.7. As a result, the void growth is accelerated and the fracture strain is reduced for the given testing condition. The plots of f and f^* for the specimens with notch radius 0.5 mm and 0.2 mm are shown in figs. G.4 and G.7, respectively. Here, the integration algorithm is seen to fail prematurely at lower values of f^* for irradiated specimens at RT. However, this does not affect the predicted tensile properties, which remain consistent, as seen in figs. G.3 and G.6.

True fracture strains estimated for the smooth and notched specimens with respect to dose and temperature are shown in fig. 6.4. At 300 °C, the fracture strain continuously decreases with increase in dose. At RT, however, there is repetition of the outlying behaviour previously mentioned in section 5.2.4, where between 0 dpa and 2 dpa the fracture strain and reduction in cross-sectional area (Z) tends to be inconsistent. It is speculated that this is due to the linear interpolation used for parameters l_N, n and f_c at low doses. In addition, the use of an exponential fit for l_N tends to mitigate these outlying behaviour as seen in figs. H.2 and H.3, although it doesn't completely remove it. This indicates that the $l_N - \sigma_H$ and $n - \phi, f_c - \phi$ relationships might be non-linear in nature, which needs to be validated with experimental data from lower doses when they become available. There is only a minimal change in the results at 300 °C, where this inconsistency is generally absent.

6.1.0.5 Integration scheme

Since the implemented damage model follows a local approach, there is difficulty in simulating the damage propagation across the elements. Although this doesn't affect the prediction of the fracture strain, this approach is not optimal for simulating crack development. A non-local approach such as a strain-gradient based formulation may be considered. Apart from internal quantities, external factors like the integration scheme and the meshing strategy plays an important role in the quality of the model predictions. The corotational integration scheme is influential in handling finite rotations and produces considerable stress relaxation when the diffused neck develops to a localized neck. The fifth order Runge-Kutta explicit integration scheme is used, in order to obtain a result asymptotic to the analytical result. The disadvantage of this method is that time increments are limited to a small value, to ensure convergence of the global Newton iterations. However, an economical estimation of the tangent modulus allows the use of larger time increments. These are still limited to suitable values based on the displacement rate applied, with the aim to limit the inelastic strain rate.

6.1.0.6 Mesh dependency

One of the advantages of using the viscoplastic framework is the reduction of mesh dependency. Due to the viscous effects generated by the model, the mesh dependency is avoided at small strains where geometrical changes and geometrical non-linearity are limited. However the mesh size and aspect ratio play an important role when finite strains and rotations are handled. Elements chosen with a more even aspect ratio tend to undergo larger elongation along the loading direction. When such elements are present in the neck region and undergo rigid body rotations, they poorly describe the diameter reduction and are unable to capture the geometrical changes of the neck profile. Use of larger element sizes worsens this problem and lead to overestimation of total elongation. Therefore, considerable mesh dependency is brought into effect at large strains. To mitigate this problem and to accurately capture the changes in the neck profile, small elements of the size 0.1 mm$\times$0.024 mm with the aspect ratio of 4:1 are used in the the gauge section where the neck development is expected. A transition mesh in the rest of the gauge section allows the use of larger element sizes outside the neck where deformation is limited. In irradiated specimens, the location of the neck is uncertain as an offset from the center of the gauge length is seen when larger irradiation doses are used. Therefore, the entire gauge section of the axisymmetric model is meshed with elements of the size 0.1 mm$\times$0.024 mm. Benchmarks were performed using both the discussed axisymmetric models on unirradiated specimens and the difference in total elongation were identified to be minimal (<0.5%).

Computational cost of the model can be quantified from the CPU and user time taken for each simulation. Based on this, the cost is observed to consistently reduce with an increase in the strain rate sensitivity of the material.

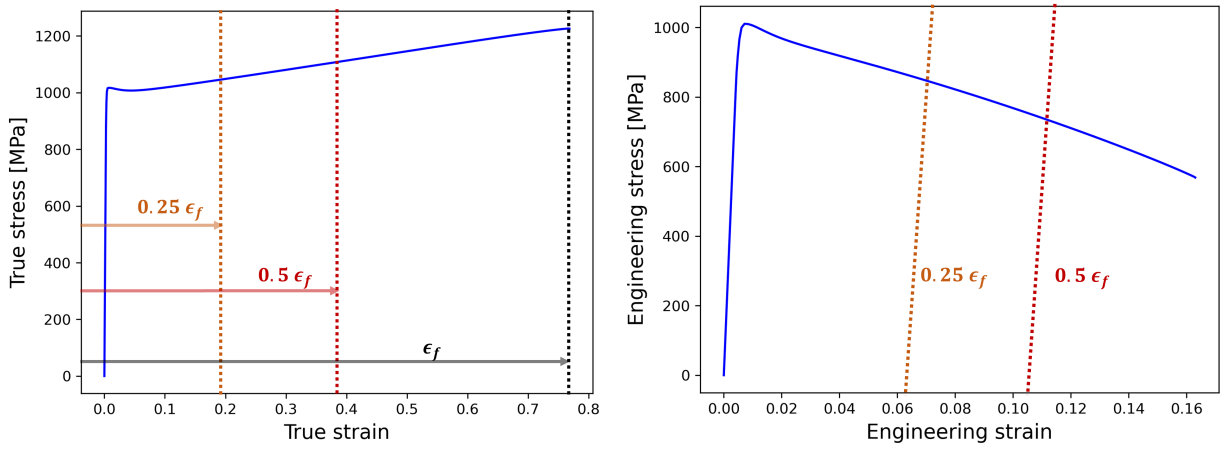

(a) (b)

Figure 6.5: Example of safe limit determination for two levels of safety factor using the stress-strain data generated for 43.5 dpa @ T_{irr}=300 °C and T_{test}=300 °C.

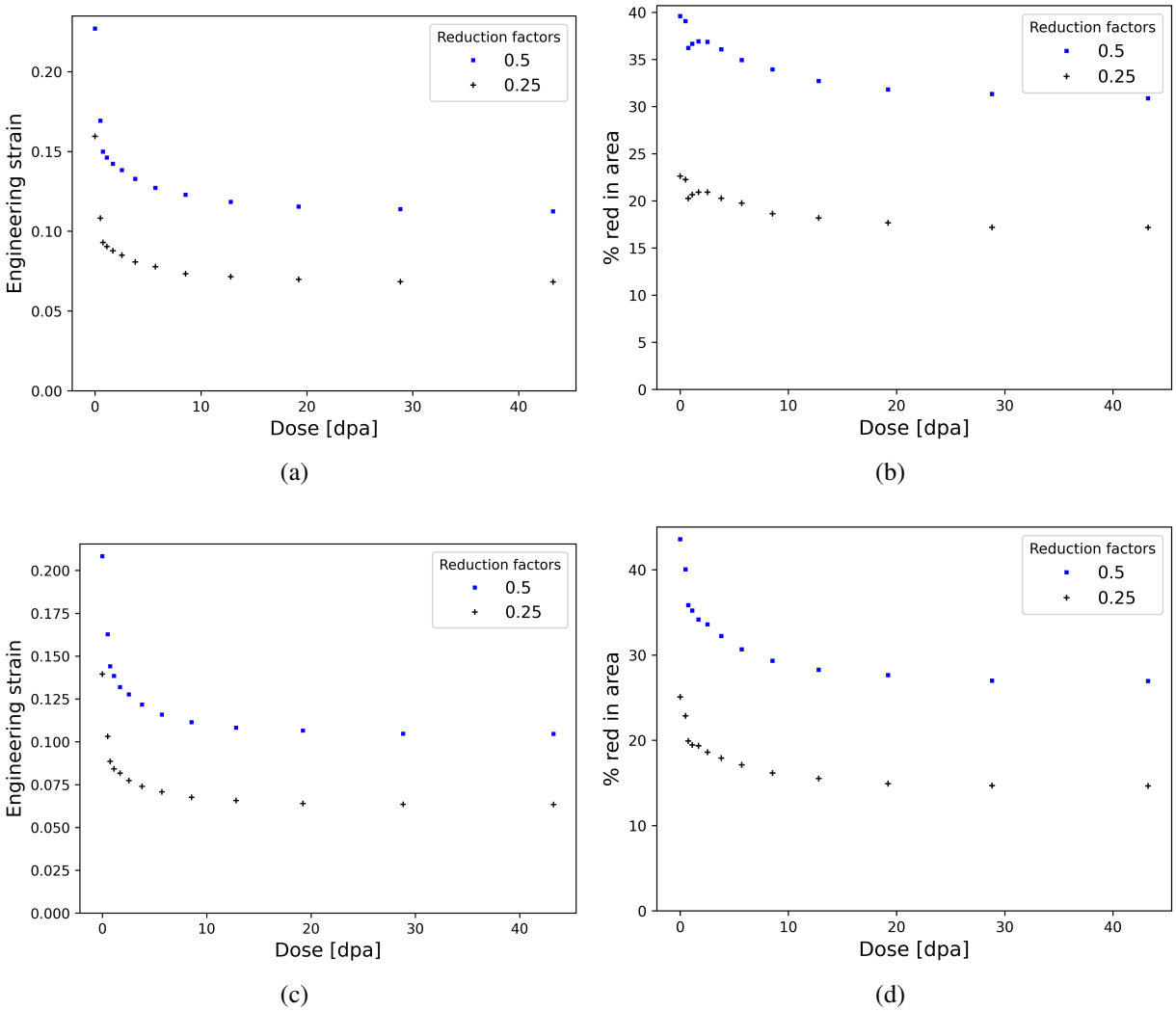

Figure 6.6: Comparison of the safe level of deformation and the corresponding reduction in minimum area for two reduction factors at (a, b) RT and (c, d) 300 °C.

6.2 Influence on design rules

Current design rules for nuclear power plant components use the loss of uniform elongation as the damage criteria, which is a very conservative approach. Nuclear components are expected to have an operating temperature of 300 °C and during a full power year (fpy), they would sustain high irradiation damage (≈20-30 dpa per fpy) [146]. The lifetime of the first DEMO blanket will be limited to 20 dpa, and the second one to 50 dpa. After attaining such high levels of damage, the material is shown to experience a high level of hardening where the yield stress doubles in magnitude. Although the uniform elongation is completely lost and the softening as a result of geometrical relaxation at the neck is rapid, the engineering stress at the time of damage is larger than the UTS of the unirradiated material. This suggests that the irradiated material holds considerable load-bearing capability throughout its deformation under non-uniform elongation. As already mentioned in section 5.2.4, total elongation and reduction in minimum area of cross-section is used to measure the material's ductility or it's

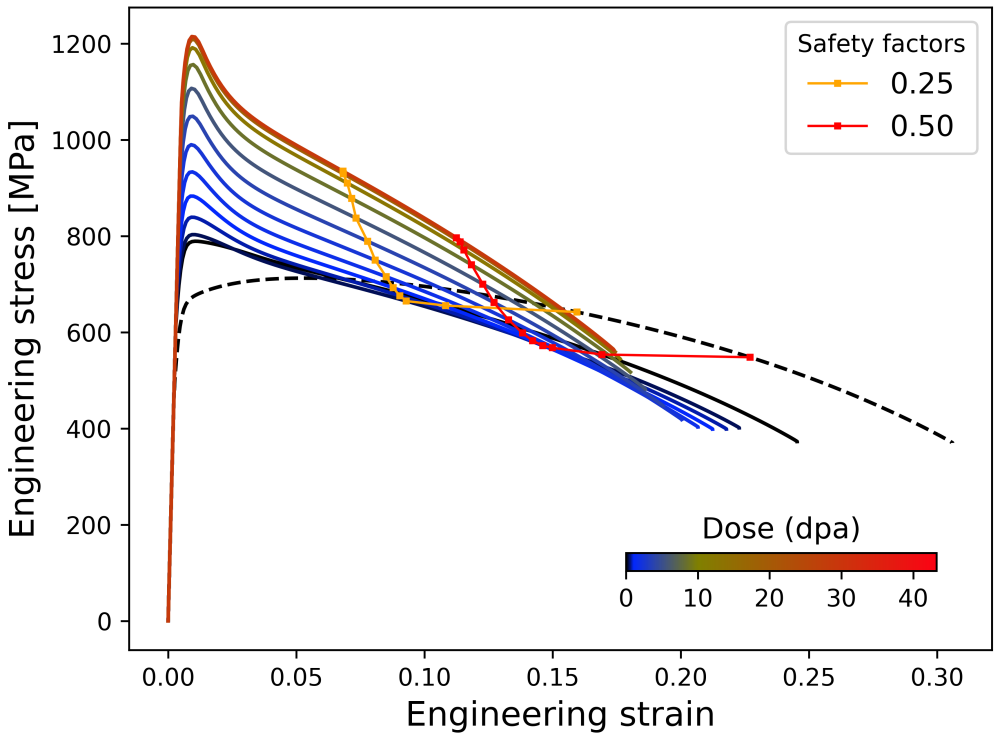

(a) RT

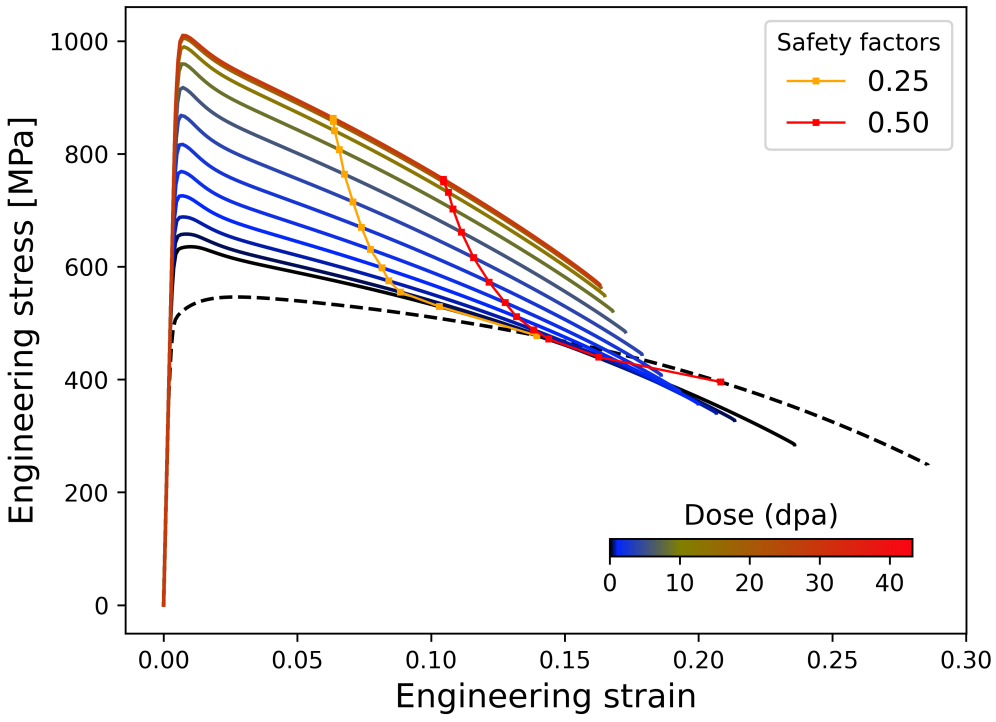

(b) 300 °C

Figure 6.7: Irradiation influence on safe strain for safety factors 0.25 and 0.5.

reduction. Since the latter is the better approach, and as the model is also shown to be capable of simulating the post-necking behaviour along with the resulting reduction in minimum area of cross-section, the simulation results obtained in this work present the possibility to identify the scope for relaxing the current design rule for material failure. Therefore, a proposal in this direction is made based on engineering stress-strain, since design rules are primarily used by design engineers who prefer the engineering curve instead of the mean true stress-strain relationship.

The idea is to identify a safe deformation level based on the reduction of minimum area, which can be translated to a safe level of total elongation. It is proposed that the mean true fracture strain is reduced by a reduction factor and taken as the safe limit. The engineering strain and reduction of minimum area at this safe limit is taken to be the damage criteria. This is still a conservative estimation when compared to the actual damage, however it provides considerable relaxation to the existing rules. Two levels of reduction factors : a) 0.25 and b) 0.50, are proposed to be applied for determination of safe deformation level. This proposal is demonstrated in fig. 6.5 utilizing the results from the simulated irradiation (43.5 dpa @ 300 °C) and deformation at 300 °C from section 5.2.4. Furthermore, the safe level of total strain for irradiated materials at RT and 300 °C are shown in fig. 6.6, where the corresponding percentage reduction in minimum area is also illustrated. Based on this, for the safety factors 0.25 and 0.5, the safe strain at 300 °C for the smooth specimen used in section 5.2.4 ranges between 0.14 and 0.20 for an unirradiated material and between 0.06 and 0.10 for a material irradiated to 43.25 dpa. Correspondingly, the permissible reduction in minimum area for the unirradiated material is between 25 and 43.6%, and between 14.65 and 26.94% for the irradiated material. At RT, the safe strain ranges between 0.16 and 0.23 for the unirradiated material and between 0.07 and 0.11 for high irradiation doses. The permissible reduction in minimum area is between 22.6 and 39.6% for the unirradiated material, and between 17.17 and 30.86% for the irradiated material. The obtained safe limits on the ESS plots are shown in fig. 6.7.

These figures are preliminary proposals made based on uniaxial tensile tests and intended to illustrate the scope for relaxing the damage criteria in the design rules of reactor components, which are extremely conservative. This opens the door to further discussions into the practical feasibility of such relaxations based on the operating conditions of the components, which must still remain conservative and not threaten the safety of the reactor. Future work should consequently focus on systematic experimental studies under controlled multiaxial loading conditions, enabling rigorous scrutiny of the model predictions and assessment of the proposed safe limits across relevant irradiation and temperature regimes.

Chapter 7

Conclusion

7.1 Summary

This work proposes a model to describe the tensile behaviour of unirradiated and irradiated RAFM steels, focusing on irradiation-induced changes in material properties like yield strength, uniform elongation, and fracture strain. The existing computational mechanics framework does not consider thermodynamic interactions between highly energetic neutrons and target atoms, making thermodynamic modeling of the irradiated material difficult. Thus, a thermodynamic framework (section 3.2) was developed to account for the fact that energy transfer into the system during neutron irradiation causes irradiation defect formation and raises the material's internal energy, which is partly dissipated during plastic deformation. In this framework, the novel irradiation-induced power term is introduced, and the associated contribution to free energy is broken down into two parts: the term contributing to hardening, and an additional term that does not. The first law of thermodynamics is satisfied by the introduction of the irradiation power, and the framework is simplified by excluding the types of irradiation defects that do not contribute to hardening.

Following the Dual Variables approach, the modified Clausius-Duhem entropy inequality is derived and employed to formulate the constitutive laws of a finite strain viscoplastic model (section 3.3). To properly account for finite strains and finite rotations while ignoring the rigid body motions, constitutive framework is formulated in terms of appropriate work-conjugate stress and strain measures, together with objective time derivatives for tensorial quantities. The stress state and inelastic deformation of the material are governed by a viscoplastic yield potential, which is a function of internal variables such as kinematic hardening, isotropic softening, void volume fraction (VVF), and irradiation defect density. The key ingredient of this model is a new function to describe the irradiation defect removal based on the material's plastic strain memory. To describe the material damage, the hydrostatic stress-dependent GTN ductile damage model is incorporated into the deformation model by proposing an extension to viscoplasticity by proposing a novel idea of mapping the viscous response of the matrix material to the volume element through an estimation of the viscous stress. The model is simplified by assuming small elastic deformation and implementing an effective integration algorithm to guarantee incremental objectivity. To get asymptotic to analytical results and keep the

integration algorithm stable, an explicit Runge-Kutta integration scheme of order five is employed. The temperature and strain-rate dependent characteristics of both unirradiated and irradiated materials are obtained through a suitably structured testing strategy that employs camera-monitored tensile tests. The developed model is applied to the obtained data and high quality calibration is ensured using a robust optimization routine.

Model validations match experimental data for unirradiated and irradiated materials up to 70 dpa. Plastic instability development and strain-rate sensitivity are observed to drive the material's post-yield and post-necking behaviour, which controls the sample's diffused and localized necking. Reduced strain-rate sensitivity and hardening modulus post yield in irradiated specimens accelerate neck development and reduce ductility. As irradiation defect removal reduces hardening modulus, the introduced plastic strain memory based function for controlling defect removal accurately predicts post-necking behaviour. Defect removal softens the material, and accelerates the necking which accelerates the ductile damage. The potential for relaxing the current failure criterion in the design rules is discussed in light of the simulation results. There are also suggestions for applying the model to developing new failure criteria.

7.2 Outlook

Although the model produces accurate results for loading conditions involving different strain rates, temperature, and irradiation doses, this work recognizes several limitations and areas for further development. Modeling the material's strain-rate sensitivity and plastic instability development is essential for describing its tensile properties. The model's strain rate sensitivity must be validated at high strain rates since it's only validated at quasi-static strain rates currently. Since only one defect type is assumed to contribute to hardening at the moment, the model can be expanded once sufficient understanding is gained in the future, on the statistical distribution of various defect type and their respective population formed as a result of irradiation. Despite the model's strong performance in describing irradiation defect removal, it needs to be verified for various loading scenarios with appropriate experimental data.

Ductile damage modeling remains an active area of study, with existing methods having limitations. Although the local approach used in this work reliably predicts material damage in terms of fracture strain with high accuracy, it is still limited in modeling crack propagation which is not within the scope of this work. To address this, a global approach can be used instead of the local approach for the damage model. The strain gradient approach is a popular global approach, in which the deformation gradient is replaced by a strain gradient as an additional quantity for calculating the strain and stress tensors. Cohesive zone modeling is another option, but it requires additional fracture mechanical tests for calibration. However, since this is a unique model constructed in a finite viscoplasticity framework and is capable of describing defect removal for a wide range of irradiation doses, it holds great potential for studying the fracture mechanical properties of irradiated F/M steels.

References

[1] J. Aktaa and C. Petersen. Modeling the constitutive behavior of RAFM steels under irradiation conditions. *J. Nucl. Mater.*, (1-3):1123–1126, oct . ISSN 00223115. doi: 10.1016/j.jnucmat.2010.12.295.

[2] P. Haupt and C. Tsakmakis. On the application of dual variables in continuum mechanics. *Contin. Mech. Thermodyn.*, (3):165–196. ISSN 0935-1175. doi: 10.1007/BF01171378.

[3] V. Tvergaard and A. Needleman. Analysis of the cup-cone fracture in a round tensile bar. *Acta Metall.*, 32(1):157–169, 1984. ISSN 00016160. doi: 10.1016/0001-6160(84)90213-X.

[4] C. Yin, J. Knaeps, D. Bainuk, S.Lebediev, and D. Terentyev. Determination of true stress true strain curves of irradiated F/M steels. Technical report, M4F project, H2020 EURATOM WP 2014-2018.

[5] R. R. Rajakrishnan, E. Gaganidze, D. Terentyev, and J. Aktaa. Macro-scale modeling of finite strain viscoplasticity in irradiated F/M steels: a continuum thermodynamic framework. *Contin. Mech. Thermodyn.*, (2):521–543, mar . ISSN 0935-1175. doi: 10.1007/s00161-023-01193-0.

[6] P. W. Bridgman. *Studies in Large Plastic Flow and Fracture*. Number 2. Harvard University Press, dec . ISBN 9780674731332. doi: 10.4159/harvard.9780674731349.

[7] J. A. Nelder and R. Mead. A Simplex Method for Function Minimization. *Comput. J.*, 1965. ISSN 0010-4620. doi: 10.1093/comjnl/7.4.308.

[8] A. Schowtjak, R. Schulte, T. Clausmeyer, R. Ostwald, A. E. Tekkaya, and A. Menzel. ADAPT — A Diversely Applicable Parameter Identification Tool: Overview and full-field application examples. *Int. J. Mech. Sci.*, (June 2021):106840. ISSN 00207403. doi: 10.1016/j.ijmecsci.2021.106840.

[9] H. Tanigawa, K. Shiba, M. A. Sokolov, and R. L. Klueh. Charpy impact properties of reduced-activation ferritic/martensitic steels irradiated in HFIR up to 20 DPA. *Fusion Sci. Technol.*, 44 (1):206–210, 2003. ISSN 15361055. doi: 10.13182/FST44-206.

[10] E. Lucon, R. Chaouadi, and M. Decréton. Mechanical properties of the European reference RAFM steel (EUROFER97) before and after irradiation at 300 °C. *J. Nucl. Mater.*, 329-333 (1-3 PART B):1078–1082, 2004. ISSN 00223115. doi: 10.1016/j.jnucmat.2004.04.023.

[11] E. Lucon, P. Benoit, P. Jacquet, E. Diegele, R. Lässer, A. Alamo, R. Coppola, F. Gillemot, P. Jung, A. Lind, S. Messoloras, P. Novosad, R. Lindau, D. Preininger, M. Klimiankou, C. Petersen, M. Rieth, E. Materna-Morris, H.-C. Schneider, J.-W. Rensman, B. van der Schaaf, B. Singh, and P. Spaetig. The European effort towards the development of a demo structural material: Irradiation behaviour of the European reference RAFM steel EUROFER. *Fusion Eng. Des.*, (8-14):917–923, feb . ISSN 09203796. doi: 10.1016/j.fusengdes.2005.08.044.

[12] J. B. A. Alamo. Status of irradiation experiments performed in BOR-60 reactor at 325 ○C-post-irradiation examinations (PIE) of materials irradiated up to 42 dpa: Part 1. *Prog. Report-TW2-TTMS-001-D02, CEA report, DMN/SRMA/NT 2004-2679,*, (Dec. 2004), 2004.

[13] E. Gaganidze, C. Petersen, E. Materna-Morris, C. Dethloff, O. J. Weiß, J. Aktaa, A. Povstyanko, A. Fedoseev, O. Makarov, and V. Prokhorov. Mechanical properties and TEM examination of RAFM steels irradiated up to 70 dpa in BOR-60. *J. Nucl. Mater.*, (1-3):93–98. ISSN 00223115. doi: 10.1016/j.jnucmat.2010.12.047.

[14] C. Petersen. Post irradiation examination of RAFM steels after fast reactor irradiation up to 33 dpa and < 340°C (ARBOR 1). Technical report, Forschungszentrum Karlsruhe, 2010.

[15] M. Mahler, S. Fessi, and J. Aktaa. Simplified approach for ductile fracture mechanics SSTT and its application to Eurofer97. *Nucl. Mater. Energy*, 26(September 2020), 2021. ISSN 23521791. doi: 10.1016/j.nme.2020.100799.

[16] J. Lemaitre. *A Course on Damage Mechanics*. Springer Berlin Heidelberg, Berlin, Heidelberg. ISBN 978-3-540-60980-3. doi: 10.1007/978-3-642-18255-6.

[17] J. Aktaa and R. Schmitt. High temperature deformation and damage behavior of RAFM steels under low cycle fatigue loading: Experiments and modeling. *Fusion Eng. Des.*, 81(19): 2221–2231, 2006. ISSN 09203796. doi: 10.1016/j.fusengdes.2006.03.002.

[18] L. Malerba, M. Caturla, E. Gaganidze, C. Kaden, M. Konstantinović, P. Olsson, C. Robertson, D. Rodney, A. Ruiz-Moreno, M. Serrano, J. Aktaa, N. Anento, S. Austin, A. Bakaev, J. Balbuena, F. Bergner, F. Boioli, M. Boleininger, G. Bonny, N. Castin, J. Chapman, P. Chekhonin, M. Clozel, B. Devincre, L. Dupuy, G. Diego, S. Dudarev, C.-C. Fu, R. Gatti, L. Gélébart, B. Gómez-Ferrer, D. Gonçalves, C. Guerrero, P. Gueye, P. Hähner, S. Hannula, Q. Hayat, M. Hernández-Mayoral, J. Jagielski, N. Jennett, F. Jiménez, G. Kapoor, A. Kraych, T. Khvan, L. Kurpaska, A. Kuronen, N. Kvashin, O. Libera, P.-W. Ma, T. Manninen, M.-C. Marinica, S. Merino, E. Meslin, F. Mompiou, F. Mota, H. Namburi, C. Ortiz, C. Pareige, M. Prester, R. Rajakrishnan, M. Sauzay, A. Serra, I. Simonovski, F. Soisson, P. Spätig, D. Tanguy, D. Terentyev, M. Trebala, M. Trochet, A. Ulbricht, M.Vallet, K. Vogel, T. Yalcinkaya, and J. Zhao. Multiscale modelling for fusion and fission materials: The M4F project. *Nucl. Mater. Energy*, 29:101051, 2021. ISSN 23521791. doi: 10.1016/j.nme.2021.101051.

[19] A. Hishinuma, A. Kohyama, R. L. Klueh, D. S. Gelles, W. Dietz, and K. Ehrlich. Current status and future R&D for reduced-activation ferritic/martensitic steels. *J. Nucl. Mater.*, 258-263 (PART 1 A):193–204, 1998. ISSN 00223115. doi: 10.1016/S0022-3115(98)00395-X.

[20] B. van der Schaaf, C. Petersen, Y. De Carlan, J. W. Rensman, E. Gaganidze, and X. Averty. High dose, up to 80 dpa, mechanical properties of Eurofer 97. *J. Nucl. Mater.*, (C):236–240. ISSN 00223115. doi: 10.1016/j.jnucmat.2008.12.329.

[21] M. Schäfer. *Numerik im Maschinenbau*. Springer-Lehrbuch. Springer Berlin Heidelberg, Berlin, Heidelberg. ISBN 978-3-540-65391-2. doi: 10.1007/978-3-642-58416-9.

[22] E. Gaganidze and C. Petersen. *Post irradiation examination of RAFM steels after fast reactor irradiation up to 71 dpa and < 340 °C (ARBOR 2).* Number November. 2010. ISBN 9783866447035.

[23] K. Nordlund, S. J. Zinkle, A. E. Sand, F. Granberg, R. S. Averback, R. E. Stoller, T. Suzudo, L. Malerba, F. Banhart, W. J. Weber, F. Willaime, S. L. Dudarev, and D. Simeone. Primary radiation damage: A review of current understanding and models, 2018. ISSN 00223115.

[24] J. C. Sublet, I. P. Bondarenko, G. Bonny, J. L. Conlin, M. R. Gilbert, L. R. Greenwood, P. J. Griffin, P. Helgesson, Y. Iwamoto, V. A. Khryachkov, T. A. Khromyleva, A. Y. Konobeyev, N. Lazarev, L. Luneville, F. Mota, C. J. Ortiz, D. Rochman, S. P. Simakov, D. Simeone, H. Sjostrand, D. Terentyev, and R. Vila. Neutron-induced damage simulations: Beyond defect production cross-section, displacement per atom and iron-based metrics. *Eur. Phys. J. Plus*, 134(7), 2019. ISSN 21905444. doi: 10.1140/epjp/i2019-12758-y.

[25] P. A. Smidt and B. Mastel. Some observations of dislocation channelling in irradiated iron. *Philos. Mag.*, 20(165):651–656, 1969. ISSN 00318086. doi: 10.1080/14786436908228737.

[26] R. Chaouadi. Effect of irradiation-induced plastic flow localization on ductile crack resistance behavior of a 9Cr tempered martensitic steel. *J. Nucl. Mater.*, 372(2-3):379–390, 2008. ISSN 00223115. doi: 10.1016/j.jnucmat.2007.04.044.

[27] K. Wang, Y. Dai, and P. Spätig. Microstructure and fracture behavior of F82H steel under different irradiation and tensile test conditions. *J. Nucl. Mater.*, 468:246–254, 2016. ISSN 00223115. doi: 10.1016/j.jnucmat.2015.09.031.

[28] G. Aiello, J. Aktaa, F. Cismondi, G. Rampal, J. F. Salavy, and F. Tavassoli. Assessment of design limits and criteria requirements for Eurofer structures in TBM components. *J. Nucl. Mater.*, (1):53–68. ISSN 00223115. doi: 10.1016/j.jnucmat.2011.05.005.

[29] A. Patra and D. L. McDowell. Crystal plasticity investigation of the microstructural factors influencing dislocation channeling in a model irradiated bcc material. *Acta Mater.*, 110: 364–376, 2016. ISSN 13596454. doi: 10.1016/j.actamat.2016.03.041.

[30] D. Rodney, G. Martin, and Y. Bréchet. Irradiation hardening by interstitial loops: Atomistic study and micromechanical model. *Mater. Sci. Eng. A*, 309-310:198–202, 2001. ISSN 09215093. doi: 10.1016/S0921-5093(00)01723-8.

[31] A. Arsenlis, B. D. Wirth, and M. Rhee. Dislocation density-based constitutive model for the mechanical behaviour of irradiated Cu. *Philos. Mag.*, 84(34):3617–3635, 2004. ISSN 14786435. doi: 10.1080/14786430412331293531.

[32] S. Krishna, A. Zamiri, and S. De. Dislocation and defect density-based micromechanical modeling of the mechanical behavior of fcc metals under neutron irradiation. *Philos. Mag.*, 90 (30):4013–4025, 2010. ISSN 14786435. doi: 10.1080/14786435.2010.502150.

[33] N. R. Barton, A. Arsenlis, and J. Marian. A polycrystal plasticity model of strain localization in irradiated iron. *J. Mech. Phys. Solids*, (2):341–351. ISSN 00225096. doi: 10.1016/j.jmps.2012.10.009.

[34] X. Xiao, D. Terentyev, L. Yu, A. Bakaev, Z. Jin, and H. Duan. Investigation of the thermo-mechanical behavior of neutron-irradiated Fe-Cr alloys by self-consistent plasticity theory. *J. Nucl. Mater.*, 477:123–133, 2016. ISSN 00223115. doi: 10.1016/j.jnucmat.2016.05.012.

[35] P. Haupt. *Continuum Mechanics and Theory of Materials*. Number 2 in Advanced Texts in Physics. Springer Berlin Heidelberg, Berlin, Heidelberg, . ISBN 978-3-642-07718-0. doi: 10.1007/978-3-662-04775-0.

[36] P. Haupt. On the concept of an intermediate configuration and its application to a representation of viscoelastic-plastic material behavior. *Int. J. Plast.*, (4):303–316, jan . ISSN 07496419. doi: 10.1016/0749-6419(85)90017-8.

[37] G. Rousselier. Ductile fracture models and their potential in local approach of fracture. *Nucl. Eng. Des.*, 105(1):97–111, 1987. ISSN 00295493. doi: 10.1016/0029-5493(87)90234-2.

[38] K. J. Bathe. *Finite Element Procedures*. Prentice Hall. ISBN 0133014584.

[39] G. A. Holzapfel. Nonlinear Solid Mechanics : a Continuum Approach for Engineering. *Work*, page 205. ISSN 1572-9648. doi: 10.1023/A:1020843529530.

[40] W. Bier. *A Constitutive Model for Metal Powder and its Numerical Treatment using Finite Elements*. PhD thesis, University of Kassel, 2008.

[41] E. W. V. Chaves. *Notes on Continuum Mechanics*. ISBN 978-94-007-5985-5.

[42] J. C. Simo. A framework for finite strain elastoplasticity based on maximum plastic dissipation and the multiplicative decomposition. Part II: Computational aspects. *Comput. Methods Appl. Mech. Eng.*, 68(1):1–31, 1988. ISSN 00457825. doi: 10.1016/0045-7825(88)90104-1.

[43] M. Born. *Natural Philosophy of Cause and Chance*. Oxford University Press, London, apr . doi: 10.1086/287082.

[44] G. H. Bryan. *Thermodynamics, an introductory treatise dealing mainly with first principles and their direct applications*. B. G. Teubner, Leipzig, 1907.

[45] C. Caratheodory. Untersuchungen über die Grundlagen der Thermodynamik. *Math. Ann.*, (3): 355–386, sep . ISSN 0025-5831. doi: 10.1007/BF01450409.

[46] R. Clausius. Ueber die bewegende Kraft der Wärme und die Gesetze, welche sich daraus für die Wärmelehre selbst ableiten lassen. *Ann. der Phys. und Chemie*, (4):500–524. ISSN 00033804. doi: 10.1002/andp.18501550403.

[47] J. G. Oldroyd. On the formulation of rheological equations of state. *Proc. R. Soc. London. Ser. A. Math. Phys. Sci.*, (1063):523–541, feb . ISSN 0080-4630. doi: 10.1098/rspa.1950.0035.

[48] J. Lemaitre and R. Desmorat. *Engineering damage mechanics: Ductile, creep, fatigue and brittle failures*. Number July. Springer-Verlag, Berlin/Heidelberg. ISBN 3540215034. doi: 10.1007/b138882.

[49] A. Gurson. Continuum theory of ductile rupture by void nucleation and growth. Part I. Yield criteria and flow rules for porous ductile media. Technical Report 1, Historical Energy Database (United States), sep .

[50] K. Hashiguchi and Y. Yamakawa. *Introduction to Finite Strain Theory for Continuum Elasto-Plasticity*. John Wiley & Sons, Ltd, Chichester, UK, nov . ISBN 9781118437711. doi: 10.1002/9781118437711.

[51] J.-L. Chaboche. Time-independent constitutive theories for cyclic plasticity. *Int. J. Plast.*, 2(2): 149–188, 1986. ISSN 07496419. doi: 10.1016/0749-6419(86)90010-0.

[52] C. Frederick and P. Armstrong. A mathematical representation of the multiaxial Bauschinger effect. *Mater. High Temp.*, (1):1–26, apr . ISSN 09603409. doi: 10.3184/096034007X207589.

[53] J. Aktaa and C. Petersen. Modeling the influence of high dose irradiation on the deformation and damage behavior of RAFM steels under low cycle fatigue conditions. *J. Nucl. Mater.*, (3): 432–435, jun . ISSN 00223115. doi: 10.1016/j.jnucmat.2009.02.032.

[54] C. Dethloff, E. Gaganidze, and J. Aktaa. Quantitative TEM analysis of precipitation and grain boundary segregation in neutron irradiated EUROFER 97. *J. Nucl. Mater.*, (1-3):323–331. ISSN 00223115. doi: 10.1016/j.jnucmat.2014.07.078.

[55] S. H. Goods and L. M. Brown. Overview No. 1. The nucleation of cavities by plastic deformation. *Acta Metall.*, 1979. ISSN 00016160. doi: 10.1016/0001-6160(79)90051-8.

[56] B. A. Senior, F. W. Noble, and B. L. Eyre. The nucleation and growth of voids at carbides in 9 Cr-1 Mo steel. *Acta Metall.*, 34(7):1321–1327, 1986. ISSN 00016160. doi: 10.1016/0001-6160(86)90019-2.

[57] V. Tvergaard. On localization in ductile materials containing spherical voids. *Int. J. Fract.*, 18 (4):237–252, 1982. ISSN 03769429. doi: 10.1007/BF00015686.

[58] M. E. Mear and J. W. Hutchinson. Influence of yield surface curvature on flow localization in dilatant plasticity. *Mech. Mater.*, 4(3-4):395–407, 1985. ISSN 01676636. doi: 10.1016/0167-6636(85)90035-3.

[59] C. C. Chu and A. Needleman. Void nucleation effects in biaxially stretched sheets. *J. Eng. Mater. Technol. Trans. ASME*, 1980. ISSN 15288889. doi: 10.1115/1.3224807.

[60] A. Needleman and V. Tvergaard. An analysis of ductile rupture in notched bars. *J. Mech. Phys. Solids*, 32(6):461–490, 1984. ISSN 00225096. doi: 10.1016/0022-5096(84)90031-0.

[61] V. Tvergaard. Influence of voids on shear band instabilities under plane strain conditions. *Int. J. Fract.*, 17(4):389–407, 1981. ISSN 03769429. doi: 10.1007/BF00036191.

[62] V. Tvergaard. Material failure by void coalescence in localized shear bands. *Int. J. Solids Struct.*, (8):659–672. ISSN 00207683. doi: 10.1016/0020-7683(82)90046-4.

[63] D. Devaux, M. Gologanu, J.-B. Leblond, and G. Perrin. On continued void growth in ductile metals subjected to cyclic loadings. In *IUTAM Symp. nonlinear Anal. Fract.*, pages 299–310. Springer, 1997.

[64] J.-B. Leblond, G. Perrin, and J. Devaux. An improved Gurson-type model for hardenable ductile metals. *Eur. J. Mech. A. Solids*, 1995. ISSN 0997-7538.

[65] D. Klingbeil, B. Svendsen, and F. Reusch. Gurson-based modelling of ductile damage and failure during cyclic loading processes at large deformation. *Eng. Fract. Mech.*, pages 95–123. ISSN 00137944. doi: 10.1016/j.engfracmech.2016.03.023.

[66] Z. L. Zhang. Explicit consistent tangent moduli with a return mapping algorithm for pressure-dependent elastoplasticity models. *Comput. Methods Appl. Mech. Eng.*, 121(1-4):29–44, 1995. ISSN 00457825. doi: 10.1016/0045-7825(94)00707-T.

[67] W. Sun, E. L. Chaikof, and M. E. Levenston. Numerical Approximation of Tangent Moduli for Finite Element Implementations of Nonlinear Hyperelastic Material Models. *J. Biomech. Eng.*, (6):133–136, dec . ISSN 0148-0731. doi: 10.1115/1.2979872.

[68] D. W. Nicholson and T. W. Silvers. On the stiffness of the tangent modulus tensor in elasto-plasticity. *J. Press. Vessel Technol. Trans. ASME*, 133(6):1–7, 2011. ISSN 00949930. doi: 10.1115/1.4004619.

[69] L. Szabó. Tangent modulus tensors for elastic-viscoplastic solids. *Comput. Struct.*, 34(3): 401–419, 1990. ISSN 00457949. doi: 10.1016/0045-7949(90)90265-4.

[70] D. Peirce, C. F. Shih, and A. Needleman. A tangent modulus method for rate dependent solids. *Comput. Struct.*, 18(5):875–887, 1984. ISSN 00457949. doi: 10.1016/0045-7949(84)90033-6.

[71] R. A. Brockman. Explicit forms for the tangent modulus tensor in viscoplastic stress analysis. *Int. J. Numer. Methods Eng.*, 20(2):315–319, 1984. ISSN 10970207. doi: 10.1002/nme.1620200210.

[72] T. Fleig. *Lebensdaueranalyse unter Berücksichtigung viscoplastischer Verformung und Schädigung mit der Methode der Finiten Elemente*. PhD thesis, Universität Karlsruhe, 1995.

[73] W. L. Bond. The Mathematics of the Physical Properties of Crystals. *Bell Syst. Tech. J.*, 22(1): 1–72, 1943. ISSN 15387305. doi: 10.1002/j.1538-7305.1943.tb01304.x.

[74] B. A. Auld and R. E. Green. Acoustic Fields and Waves in Solids: Two Volumes. *Phys. Today*, 1974. ISSN 0031-9228. doi: 10.1063/1.3128926.

[75] G. S. Was. *Fundamentals of Radiation Materials Science*. Number 95. Springer New York, New York, NY. ISBN 978-1-4939-3436-2. doi: 10.1007/978-1-4939-3438-6.

[76] H. Zimmermann M. Rieth, M. S., A. Falkenstein, P. Graf, S. Heger, H. Kempe, R. Lindau. FZKA 691: EUROFER 97 Tensile, Charpy, Creep and Structural Tests. Technical report, Forschungszentrum Karlsruhe GmbH, Karlsruhe, 2003.

[77] L. Stratil, F. Siska, H. Hadraba, and I. Dlouhy. Modeling of Ductile Tearing for RAFM Steel Eurofer97. *Procedia Mater. Sci.*, pages 1155–1160. ISSN 22118128. doi: 10.1016/j.mspro.2014.06.188.

[78] S. Knitel, P. Spätig, T. Yamamoto, H. Seifert, Y. Dai, and G. R. Odette. Evolution of the tensile properties of the tempered martensitic steel Eurofer97 after spallation irradiation at SINQ. *Nucl. Mater. Energy*, pages 69–77, dec . ISSN 23521791. doi: 10.1016/j.nme.2018.09.002.

[79] E. Cadoni, M. Dotta, D. Forni, and P. Spätig. Strain-rate behavior in tension of the tempered martensitic reduced activation steel Eurofer97. *J. Nucl. Mater.*, (3):360–366, jul . ISSN 00223115. doi: 10.1016/j.jnucmat.2011.05.002.

[80] M. D. Abràmoff, P. J. Magalhães, and S. J. Ram. Image processing with ImageJ. *Biophotonics Int.*, 11(7):36–41, 2004. ISSN 10818693. doi: 10.1201/9781420005615.ax4.

[81] A. Considère. Memoire sur l'emploi du fer et de l'acier dans les constructions. In *Ann. des Ponts Chaussées*, volume 9, chapter 34, pages 574–775. Ch. Dunod, EditeurCh. Dunod, Editeur, Paris, 9 edition, 1885.

[82] L. J. Jia, T. Koyama, and H. Kuwamura. Prediction of cyclic large plasticity for prestrained structural steel using only tensile coupon tests. *Front. Struct. Civ. Eng.*, 7(4):466–476, 2013. ISSN 20952430. doi: 10.1007/s11709-013-0219-5.

[83] L.-J. Jia and H. Kuwamura. Ductile Fracture Simulation of Structural Steels under Monotonic Tension. *J. Struct. Eng.*, 140(5):04013115, 2014. ISSN 0733-9445. doi: 10.1061/(asce)st.1943-541x.0000944.

[84] L. J. Jia and H. Kuwamura. Ductile fracture model for structural steel under cyclic large strain loading. *J. Constr. Steel Res.*, pages 110–121. ISSN 0143974X. doi: 10.1016/j.jcsr.2014.12.002.

[85] T. S. Byun, K. Farrell, and N. Hashimoto. Plastic instability behavior of bcc and hcp metals after low temperature neutron irradiation. *J. Nucl. Mater.*, 329-333(1-3 PART B):998–1002, 2004. ISSN 00223115. doi: 10.1016/j.jnucmat.2004.04.071.

[86] T. S. Byun and N. Hashimoto. Strain Localization in Irradiated Materials. *Nucl. Eng. Technol.*, 38(7):619–638, 2006.

[87] T. S. Byun, K. Farrell, and M. Li. Deformation in metals after low-temperature irradiation: Part II - Irradiation hardening, strain hardening, and stress ratios. *Acta Mater.*, 56(5):1056–1064, 2008. ISSN 13596454. doi: 10.1016/j.actamat.2007.10.056.

[88] T. S. Byun, K. Farrell, and M. Li. Deformation in metals after low-temperature irradiation: Part I - Mapping macroscopic deformation modes on true stress-dose plane. *Acta Mater.*, 56 (5):1044–1055, 2008. ISSN 13596454. doi: 10.1016/j.actamat.2007.10.061.

[89] B. Mastel, H. E. Kissinger, J. J. Laidler, and T. K. Bierlein. Dislocation Channeling in Neutron-Irradiated Molybdenum. *J. Appl. Phys.*, (12):3637–3638, dec . ISSN 0021-8979. doi: 10.1063/1.1729281.

[90] P. Greenfield and M. B. Bever. The effect of composition on the stored energy of cold work and the deformation behavior of gold-silver alloys. *Acta Metall.*, 5(3):125–130, 1957. ISSN 00016160. doi: 10.1016/0001-6160(57)90016-0.

[91] I. G. Greenfield and H. G. Wilsdorf. Effect of neutron irradiation on the plastic deformation of copper single crystals. *J. Appl. Phys.*, 32(5):827–839, 1961. ISSN 00218979. doi: 10.1063/1.1736114.

[92] A. D. Whapham and M. J. Makin. The hardening of lithium fluoride by electron irradiation. *Philos. Mag.*, 5(51):237–250, 1960. ISSN 00318086. doi: 10.1080/14786436008235839.

[93] R. P. Tucker, M. S. Wechsler, and S. M. Ohr. Dislocation Channeling in Neutron-Irradiated Niobium. *J. Appl. Phys.*, (1):400–408, jan . ISSN 0021-8979. doi: 10.1063/1.1657068.

[94] H. Lämmer. *Thermoplastizit at und Thermoviskoplastizitat mit Schadigung bei kleinen und großen Deformationen*. PhD thesis, Universität Karlsruhe, 1998.

[95] W. Jansohn. Formulierung und integration von stoffgesetzen zur beschreibung großer deformationen in der thermoplastizität und -viskoplastizität. Technical Report FZKA 6002, Forschungszentrum Karlsruhe, Karlsruhe, Germany, 1997.

[96] B. D. Coleman and M. E. Gurtin. Thermodynamics with internal state variables. *J. Chem. Phys.*, 47(2):597–613, 1967. ISSN 00219606. doi: 10.1063/1.1711937.

[97] J. Mandel. Thermodynamics and Plasticity. In *Found. Contin. Thermodyn.*, pages 283–304. Macmillan Education UK, London. doi: 10.1007/978-1-349-02235-9_15.

[98] J.-L. Chaboche. Thermodynamic and Phenomenological Description of Cyclic Viscoplasticity with Damage. | National Technical Reports Library - NTIS.

[99] J.-L. Chaboche. Cyclic viscoplastic constitutive equations, part II: Stored energy-comparison between models and experiments. *J. Appl. Mech. Trans. ASME*, 60(4):822–828, 1993. ISSN 15289036. doi: 10.1115/1.2900990.

[100] A. Chauhan, Q. Yuan, C. Dethloff, E. Gaganidze, and J. Aktaa. Post-irradiation annealing of neutron-irradiated EUROFER97. *J. Nucl. Mater.*, 2021. ISSN 00223115. doi: 10.1016/j.jnucmat.2021.152863.

[101] B. Gómez-Ferrer, C. Dethloff, E. Gaganidze, L. Malerba, C. Hatzoglou, and C. Pareige. Nano-hardening features in high-dose neutron irradiated Eurofer97 revealed by atom-probe tomography. *J. Nucl. Mater.*, 537, 2020. ISSN 00223115. doi: 10.1016/j.jnucmat.2020.152228.

[102] R. Schaeublin, D. Gelles, and M. Victoria. Microstructure of irradiated ferritic/martensitic steels in relation to mechanical properties. *J. Nucl. Mater.*, 307-311(1 SUPPL.):197–202, 2002. ISSN 00223115. doi: 10.1016/S0022-3115(02)01034-6.

[103] O. J. Weiß, E. Gaganidze, and J. Aktaa. Quantitative characterization of microstructural defects in up to 32 dpa neutron irradiated EUROFER97. *J. Nucl. Mater.*, (1-3):52–58, jul . ISSN 00223115. doi: 10.1016/j.jnucmat.2012.03.027.

[104] T. J. R. Hughes and J. Winget. Finite rotation effects in numerical integration of rate constitutive equations arising in large-deformation analysis. *Int. J. Numer. Methods Eng.*, 15(12):1862–1867, 1980. ISSN 10970207. doi: 10.1002/nme.1620151210.

[105] R. Rubinstein and S. N. Atluri. Objectivity of incremental constitutive relations over finite time steps in computational finite deformation analyses. *Comput. Methods Appl. Mech. Eng.*, 36(3):277–290, 1983. ISSN 00457825. doi: 10.1016/0045-7825(83)90125-1.

[106] K. W. Reed and S. N. Atluri. Analyses of large quasistatic deformations of inelastic bodies by a new hybrid-stress finite element algorithm. *Comput. Methods Appl. Mech. Eng.*, 39(3): 245–295, 1983. ISSN 00457825. doi: 10.1016/0045-7825(83)90094-4.

[107] T. J. R. Hughes. Numerical implementation of constitutive models: Rate-independent deviatoric plasticity. pages 29–63, 1984. doi: 10.1007/978-94-009-6213-2_3.

[108] J. C. Nagtegaal and F. E. Veldpaus. Analysis of metal forming problems with an improved finite strain plasticity formulation. 1982. ISBN 0906674204.

[109] J. Fish and K. Shek. Finite deformation plasticity based on the additive split of the rate of deformation and hyperelasticity. *Comput. Methods Appl. Mech. Eng.*, 190(1-2):75–93, 2000. ISSN 00457825. doi: 10.1016/S0045-7825(99)00415-6.

[110] J. Hughes. *Stability of one-step methods in transient nonlinear heat conduction*. 1977.

[111] G. G. A. Weber. *Computational procedures for a new class of finite deformation elastic-plastic constitutive equations*. PhD thesis, Massachusetts Institute of Technology.

[112] G. G. A. Weber and L. Anand. Finite deformation constitutive equations and a time integration procedure for isotropic, hyperelastic-viscoplastic solids. *Comput. Methods Appl. Mech. Eng.*, 79(2):173–202, 1990. ISSN 00457825. doi: 10.1016/0045-7825(90)90131-5.

[113] S. Teukolsky, W. H. Press, and W. T. Vetterling. Adaptive Stepsize Control for Runge-Kutta. *Numer. Recipes*, pages 714–722, 1983.

[114] E. Fehlberg. Low-order classical Runge-Kutta formulas with stepsize control and their application to some heat transfer problems. *NASA Tech. Rep.*, (July):R–315.

[115] R. P. Brent. *Algorithms for Minimization without Derivatives*. Prentice-Hal, Englewood Cliffs, New Jersey, 1973. ISBN 0-13-022335-2.

[116] P. E. Gill, W. Murray, and M. H. Wright. *Practical Optimization*. ACADEMIC PRESS, INC, New York, NY, 1997.

[117] J. Nocedal and S. J. Wright. *Numerical optimization*. ISBN 0387303030 (hd. bd.)\n9780387303031. doi: 10.1007/978-0-387-40065-5.

[118] C. Hill. SciPy. In *Learn. Sci. Program. with Python*. 2020. doi: 10.1017/9781108778039.009.

[119] F. James and M. Roos. Minuit - a system for function minimization and analysis of the parameter errors and correlations. *Comput. Phys. Commun.*, 10(6):343–367, 1975. ISSN 00104655. doi: 10.1016/0010-4655(75)90039-9.

[120] H. Dembinski and P. Ongmongkolkul. scikit-hep/iminuit. doi: 10.5281/zenodo.3949207.

[121] Z. Zhang. A practical micro-mechanical model-based local approach methodology for the analysis of ductile fracture of welded t-joints. Technical Report 34, Lappeenranta University of Technology, Lappeenranta, Finland, 1994.

[122] Z. L. Zhang, M. Hauge, J. Ødegård, and C. Thaulow. Determining material true stress-strain curve from tensile specimens with rectangular cross-section. *Int. J. Solids Struct.*, 36(23): 3497–3516, 1999. ISSN 00207683. doi: 10.1016/S0020-7683(98)00153-X.

[123] J. M. Choung and S. R. Cho. Study on true stress correction from tensile tests. *J. Mech. Sci. Technol.*, 22(6):1039–1051, 2008. ISSN 1738494X. doi: 10.1007/s12206-008-0302-3.

[124] N. Tsuchida, T. Inoue, and K. Enami. Estimations of the true stress and true strain until just before fracture by the stepwise tensile test and bridgman equation for various metals and alloys. *Nippon Kinzoku Gakkaishi/Journal Japan Inst. Met.*, 76(10):579–586, 2012. ISSN 00214876. doi: 10.2320/jinstmet.76.579.

[125] Y. D. Wang, S. H. Xu, S. B. Ren, and H. Wang. An Experimental-Numerical Combined Method to Determine the True Constitutive Relation of Tensile Specimens after Necking. *Adv. Mater. Sci. Eng.*, 2016(c), 2016. ISSN 16878442. doi: 10.1155/2016/6015752.

[126] S. K. Paul, S. Roy, S. Sivaprasad, and S. Tarafder. A Simplified Procedure to Determine Post-necking True Stress–Strain Curve from Uniaxial Tensile Test of Round Metallic Specimen Using DIC. *J. Mater. Eng. Perform.*, (9):4893–4899. ISSN 15441024. doi: 10.1007/s11665-018-3566-5.

[127] J. Chen, Z. Guan, P. Ma, Z. Li, and X. Meng. The improvement of stress correction in post-necking tension of cylindrical specimen. *J. Strain Anal. Eng. Des.*, 54(3):209–222, 2019. ISSN 20413130. doi: 10.1177/0309324719852875.

[128] S. Tu, X. Ren, J. He, and Z. Zhang. Stress–strain curves of metallic materials and post-necking strain hardening characterization: A review. *Fatigue Fract. Eng. Mater. Struct.*, 43(1):3–19, 2020. ISSN 14602695. doi: 10.1111/ffe.13134.

[129] Y. Ling. Uniaxial True Stress-Strain after Necking. *Amp J. Technol. Vol*, (1):37–48.

[130] B. Audoly and J. W. Hutchinson. One-dimensional modeling of necking in rate-dependent materials. *J. Mech. Phys. Solids*, pages 149–171, feb . ISSN 00225096. doi: 10.1016/j.jmps.2018.08.005.

[131] S. Kotrechko, V. Dubinko, N. Stetsenko, D. Terentyev, X. He, and M. Sorokin. Temperature dependence of irradiation hardening due to dislocation loops and precipitates in RPV steels and model alloys. *J. Nucl. Mater.*, pages 6–15. ISSN 00223115. doi: 10.1016/j.jnucmat.2015.04.014.

[132] N. Hashimoto, S. J. Zinkle, R. L. Klueh, A. F. Rowcliffe, and K. Shiba. Deformation Mechanisms in Ferritic/martensitic Steels Irradiated in HFIR. *MRS Proc.*, page R1.10, mar . ISSN 0272-9172. doi: 10.1557/PROC-650-R1.10.

[133] T. Yamamoto, G. R. Odette, H. Kishimoto, J. W. Rensman, and P. Miao. On the effects of irradiation and helium on the yield stress changes and hardening and non-hardening embrittlement of ˜8Cr tempered martensitic steels: Compilation and analysis of existing data. *J. Nucl. Mater.*, 356(1-3):27–49, 2006. ISSN 00223115. doi: 10.1016/j.jnucmat.2006.05.041.

[134] G. R. Odette, M. Y. He, E. G. Donahue, P. Spätig, and T. Yamamoto. Modeling the multiscale mechanics of flow localization-ductility loss in irradiation damaged bcc alloys. *J. Nucl. Mater.*, 307-311(1 SUPPL.):171–178, 2002. ISSN 00223115. doi: 10.1016/S0022-3115(02)01136-4.

[135] E. Gaganidze, C. Petersen, E. Materna-Morris, C. Dethloff, O. J. Weiß, J. Aktaa, A. Povstyanko, A. Fedoseev, O. Makarov, and V. Prokhorov. Mechanical properties and TEM examination of RAFM steels irradiated up to 70 dpa in BOR-60. In *14th Int. Conf. Fusion React. Mater.*, 2009.

[136] J. Faleskog, X. Gao, and C. Fong Shih. Cell model for nonlinear fracture analysis - I. Micromechanics calibration. *Int. J. Fract.*, 89(4):355–373, 1998. ISSN 03769429. doi: 10.1023/A:1007421420901.

[137] S. Jitsukawa, A. Kimura, A. Kohyama, R. L. Klueh, A. A. Tavassoli, B. Van Der Schaaf, G. R. Odette, J. W. Rensman, M. Victoria, and C. Petersen. Recent results of the reduced activation ferritic/martensitic steel development. *J. Nucl. Mater.*, 329-333(1-3 PART A):39–46, 2004. ISSN 00223115. doi: 10.1016/j.jnucmat.2004.04.319.

[138] C. Ling, B. Tanguy, J. Besson, S. Forest, and F. Latourte. Void growth and coalescence in triaxial stress fields in irradiated FCC single crystals. *J. Nucl. Mater.*, pages 157–170. ISSN 00223115. doi: 10.1016/j.jnucmat.2017.04.013.

[139] E. Lucon, A. Leenaers, and W. Vandermeulen. Post-irradiation mechanical properties of three EUROFER97 joints. *Fusion Eng. Des.*, 83(4):620–624, 2008. ISSN 09203796. doi: 10.1016/j.fusengdes.2008.01.008.

[140] A. Needleman and V. Tvergaard. An analysis of dynamic, ductile crack growth in a double edge cracked specimen. *Int. J. Fract.*, 49(1):41–67, 1991. ISSN 03769429. doi: 10.1007/BF00013502.

[141] E. Gaganidze and J. Aktaa. Assessment of neutron irradiation effects on RAFM steels. *Fusion Eng. Des.*, (3):118–128. ISSN 09203796. doi: 10.1016/j.fusengdes.2012.11.020.

[142] J.R. Rice and D.M. Tracey. On the ductile enlargement of voids in triaxial stress fields. *Journal of the Mechanics and Physics of Solids*, 17(3):201–217, June 1969. ISSN 00225096. doi: 10.1016/0022-5096(69)90033-7.

[143] Y. Bao and T. Wierzbicki. On fracture locus in the equivalent strain and stress triaxiality space. *International Journal of Mechanical Sciences*, 46(1):81–98, January 2004. ISSN 00207403. doi: 10.1016/j.ijmecsci.2004.02.006.

[144] G. R. Johnson and W. H. Cook. Fracture characteristics of three metals subjected to various strains, strain rates, temperatures and pressures. *Engineering Fracture Mechanics*, 21(1):31–48, January 1985. ISSN 00137944. doi: 10.1016/0013-7944(85)90052-9.

[145] T. Wierzbicki, Y. Bao, Y.-W. Lee, and Y. Bai. Calibration and evaluation of seven fracture models. *International Journal of Mechanical Sciences*, 47(4-5):719–743, April 2005. ISSN 00207403. doi: 10.1016/j.ijmecsci.2005.03.003.

[146] G. Federici, R. Kemp, D. Ward, C. Bachmann, T. Franke, S. Gonzalez, C. Lowry, M. Gadomska, J. Harman, B. Meszaros, C. Morlock, F. Romanelli, and R. Wenninger. Overview of EU DEMO design and R&D activities. *Fusion Eng. Des.*, (7-8):882–889. ISSN 09203796. doi: 10.1016/j.fusengdes.2014.01.070.

[147] R. R. Rajakrishnan, E. Gaganidze, and J. Aktaa. Modeling the deformation and ductile damage of irradiated EUROFER97 [oral presentation]. CIMTEC 2024, June 2024.

[148] R. R. Rajakrishnan, E. Gaganidze, and J. Aktaa. Modeling finite viscoplasticity and ductile damage in irradiated EUROFER97 [invited contribution]. ICFRM 20, October 2021.

[149] R. R. Rajakrishnan, E. Gaganidze, D. Terentyev, and J. Aktaa. Development of physically based constitutive equations for describing coupled deformation damage behavior of f/m steels [oral presentation]. M4F technical meeting, October 2021.

[150] R. R. Rajakrishnan, E. Gaganidze, and J. Aktaa. Modeling large deformation and ductile damage in irradiated EUROFER97 [oral presentation]. NUMAT 2020, October 2020.

Publications list

- R. R. Rajakrishnan, E. Gaganidze, and J. Aktaa. Modeling the deformation and ductile damage of irradiated EUROFER97 [oral presentation]. CIMTEC 2024, June 2024

- R. R. Rajakrishnan, E. Gaganidze, D. Terentyev, and J. Aktaa. Macro-scale modeling of finite strain viscoplasticity in irradiated F/M steels: a continuum thermodynamic framework. *Contin. Mech. Thermodyn.*, (2):521–543, mar . ISSN 0935-1175. doi: 10.1007/s00161-023-01193-0

- L. Malerba, M. Caturla, E. Gaganidze, C. Kaden, M. Konstantinović, P. Olsson, C. Robertson, D. Rodney, A. Ruiz-Moreno, M. Serrano, J. Aktaa, N. Anento, S. Austin, A. Bakaev, J. Balbuena, F. Bergner, F. Boioli, M. Boleininger, G. Bonny, N. Castin, J. Chapman, P. Chekhonin, M. Clozel, B. Devincre, L. Dupuy, G. Diego, S. Dudarev, C.-C. Fu, R. Gatti, L. Gélébart, B. Gómez-Ferrer, D. Gonçalves, C. Guerrero, P. Gueye, P. Hähner, S. Hannula, Q. Hayat, M. Hernández-Mayoral, J. Jagielski, N. Jennett, F. Jiménez, G. Kapoor, A. Kraych, T. Khvan, L. Kurpaska, A. Kuronen, N. Kvashin, O. Libera, P.-W. Ma, T. Manninen, M.-C. Marinica, S. Merino, E. Meslin, F. Mompiou, F. Mota, H. Namburi, C. Ortiz, C. Pareige, M. Prester, R. Rajakrishnan, M. Sauzay, A. Serra, I. Simonovski, F. Soisson, P. Spätig, D. Tanguy, D. Terentyev, M. Trebala, M. Trochet, A. Ulbricht, M.Vallet, K. Vogel, T. Yalcinkaya, and J. Zhao. Multiscale modelling for fusion and fission materials: The M4F project. *Nucl. Mater. Energy*, 29:101051, 2021. ISSN 23521791. doi: 10.1016/j.nme.2021.101051

- R. R. Rajakrishnan, E. Gaganidze, and J. Aktaa. Modeling finite viscoplasticity and ductile damage in irradiated EUROFER97 [invited contribution]. ICFRM 20, October 2021

- R. R. Rajakrishnan, E. Gaganidze, D. Terentyev, and J. Aktaa. Development of physically based constitutive equations for describing coupled deformation damage behavior of f/m steels [oral presentation]. M4F technical meeting, October 2021

- R. R. Rajakrishnan, E. Gaganidze, and J. Aktaa. Modeling large deformation and ductile damage in irradiated EUROFER97 [oral presentation]. NUMAT 2020, October 2020

Appendices

A Tensile specimen geometries and FE models

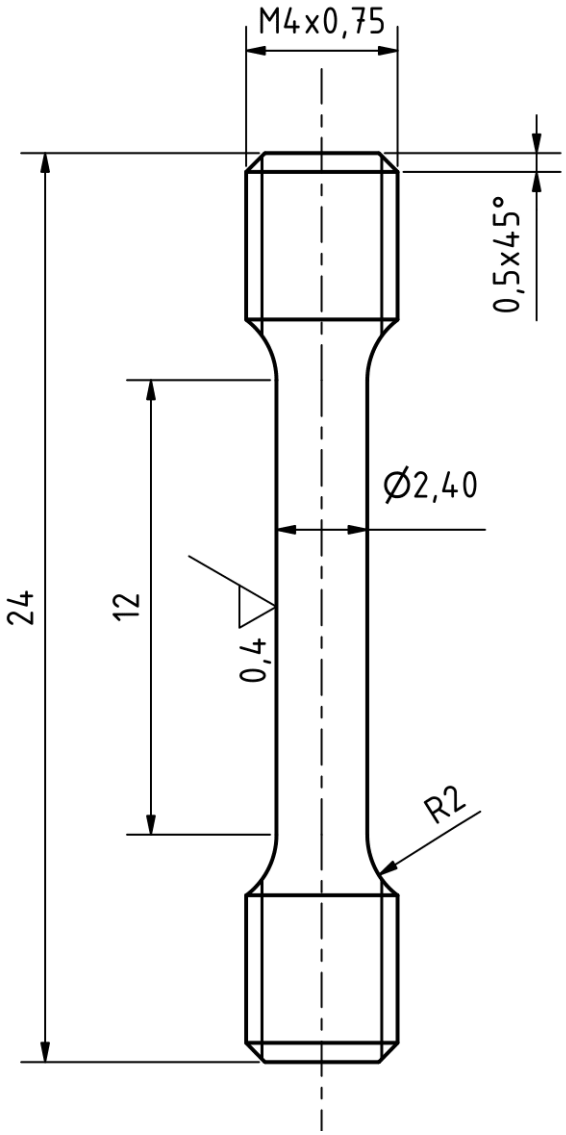

Figure A.1: Smooth tensile specimen geometry used in this work for unirradiated and irradiated specimens (0.22, 0.65, 1.05 and 1.18 dpa) at T_{irr}=300 °C and T_{test}=RT and 300 °C.

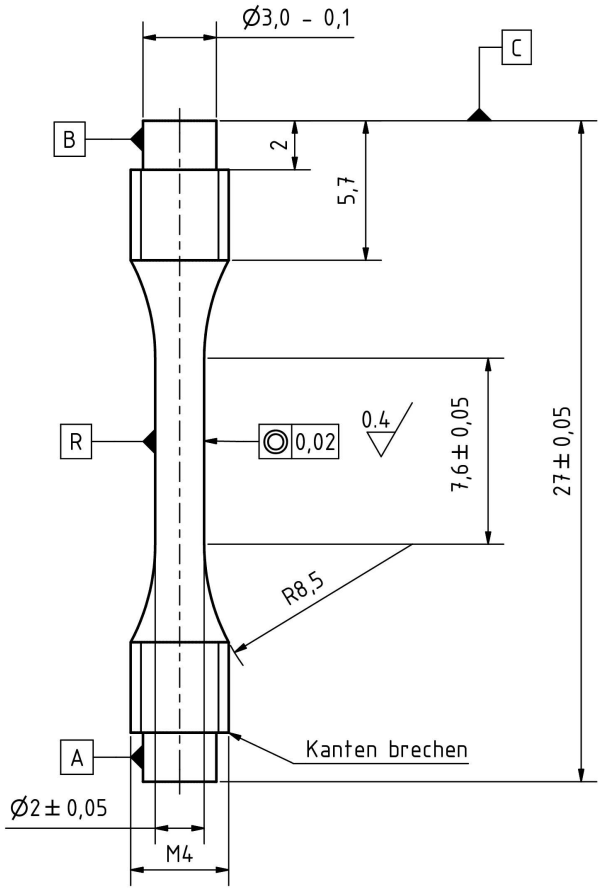

Figure A.2: Smooth tensile specimen geometry used for specimens irradiated to 69.1 dpa at T_{irr}=332 °C and tested at T_{test}=RT and 350 °C [14].

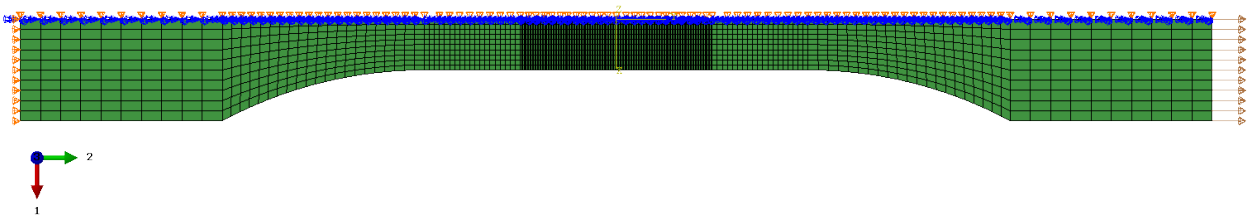

Figure A.3: Axisymmetric model of smooth tensile specimen in fig. A.2.

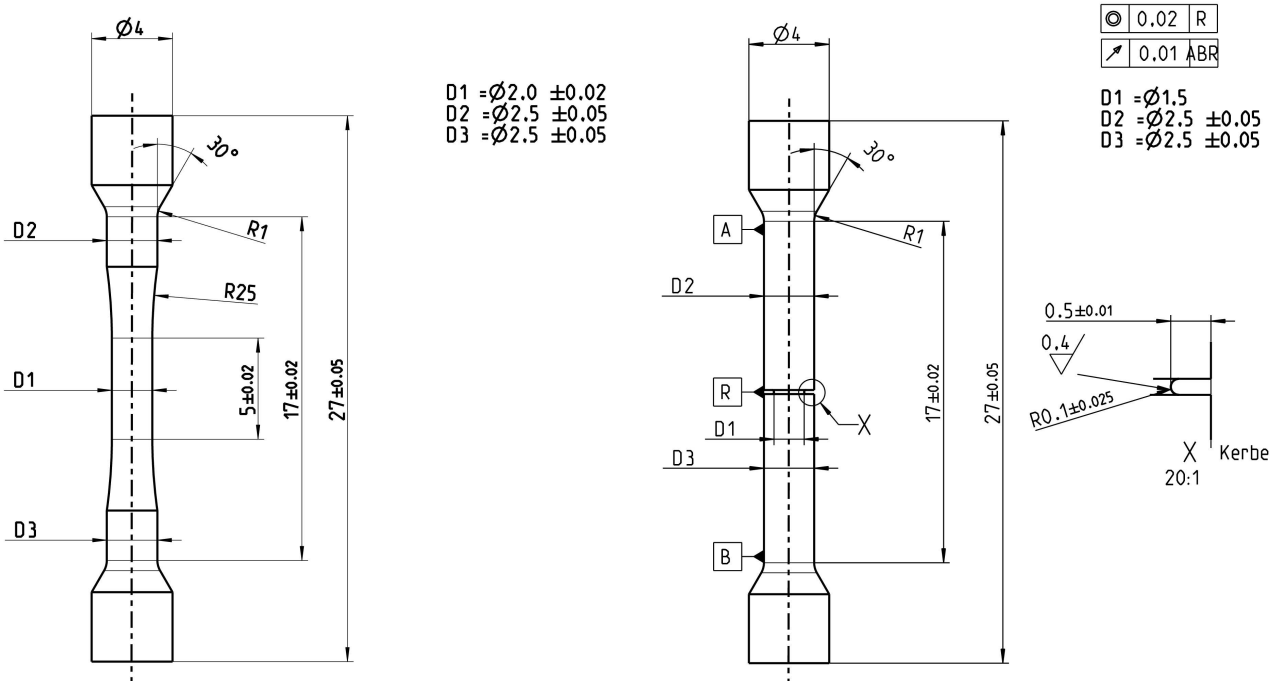

Figure A.4: Smooth and notched tensile specimen geometry used for ductility and triaxiality study at T_{test}=RT and 300 °C [15].

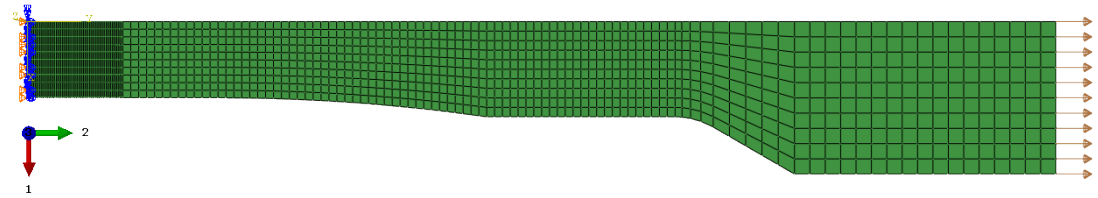

(a) Smooth specimen

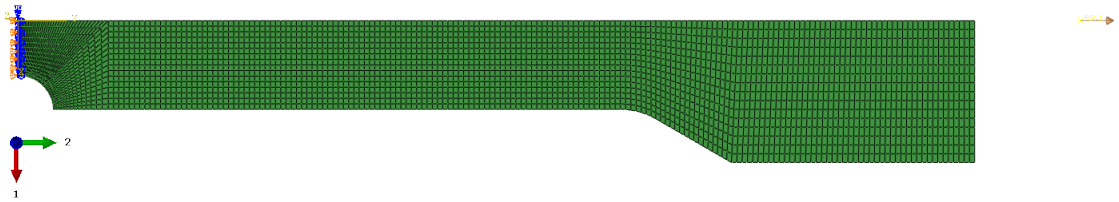

(b) Notch radius 0.5 mm

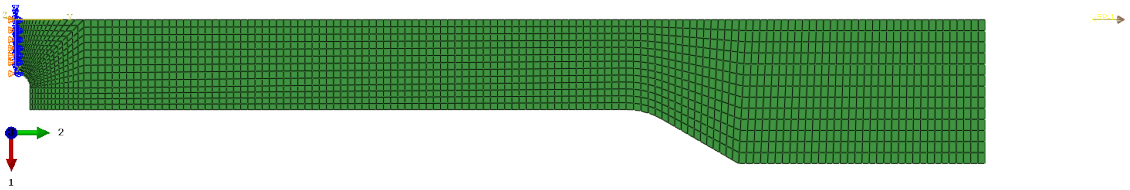

(c) Notch radius 0.2 mm

Figure A.5: Axisymmetric models for ductility study: a) smooth specimen, b) notched specimen with notch radius 0.5mm and c) 0.2 mm. Displacement loads on notched specimens are applied using reference points.

B Uncertainty in true stress and true strain determination

At RT

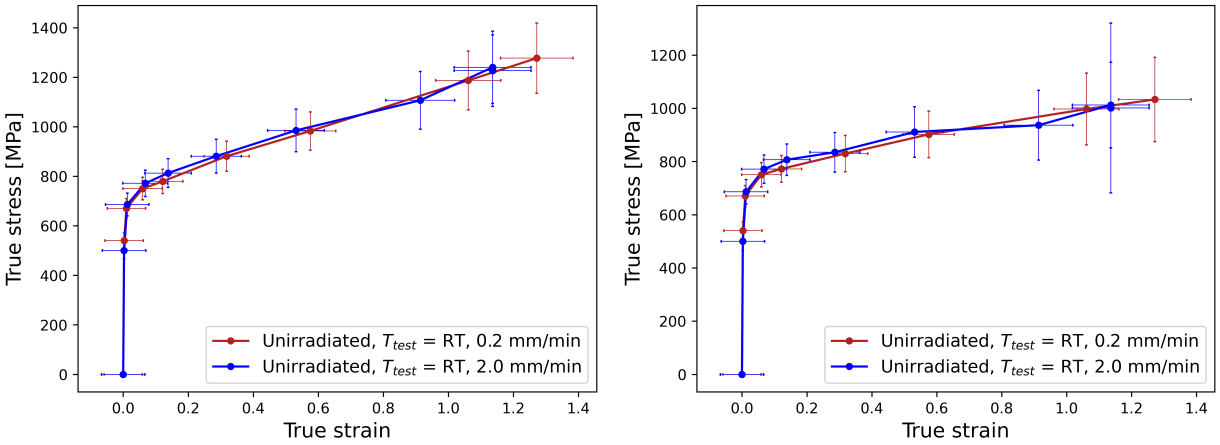

(a) Mean true stress-mean true strain

(b) Bridgman corrected true stress-mean true strain

Figure B.1: True stress-strain relationships for unirradiated samples tested at RT for different deformation rates.

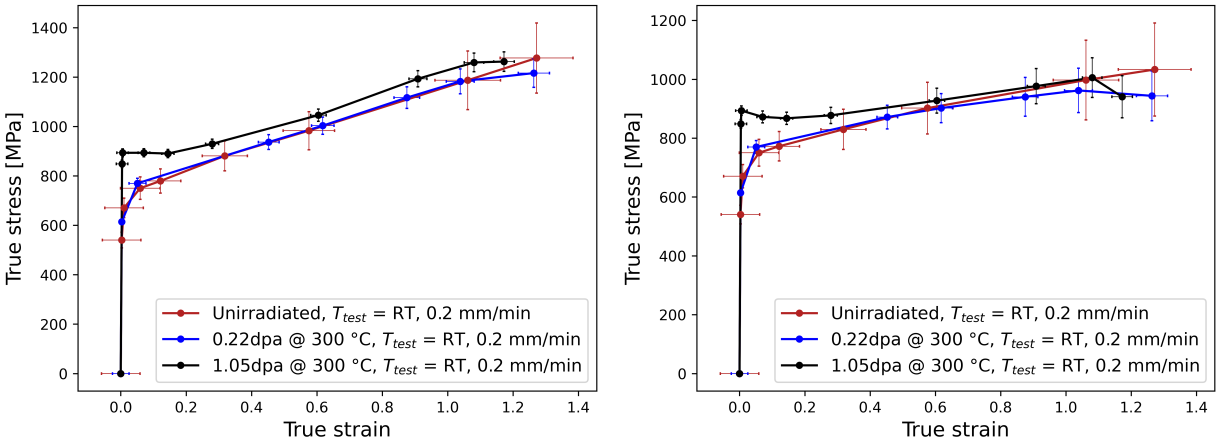

(a) Mean true stress-mean true strain

(b) Bridgman corrected true stress-mean true strain

Figure B.2: True stress-strain relationships for unirradiated and irradiated smooth specimens tested at RT.

At 300 °C

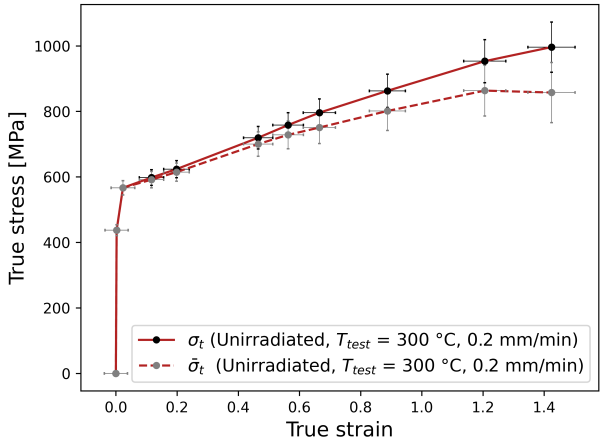

Figure B.3: Mean true stress and Bridgman corrected true stress against mean true strain for unirradiated smooth specimens at 300 °C

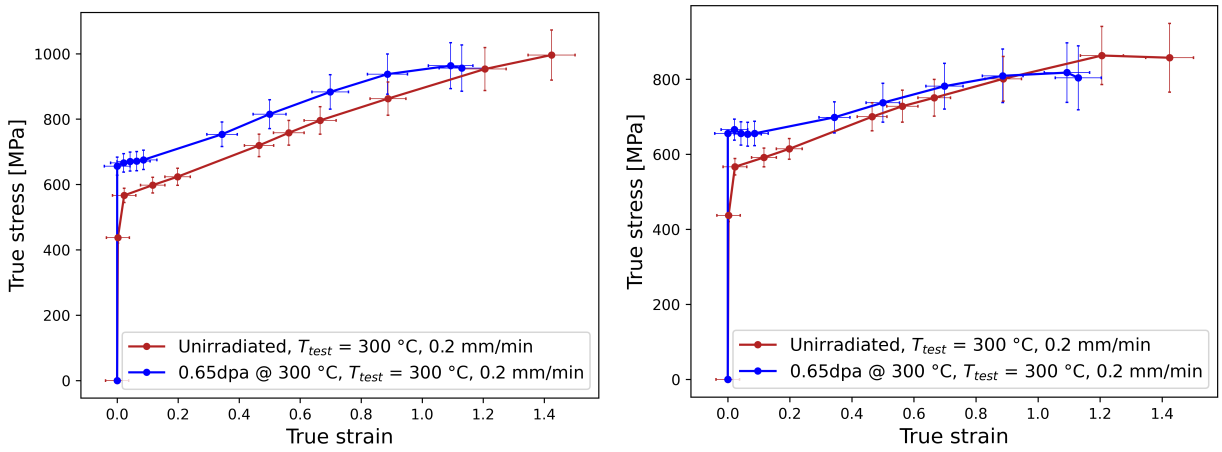

(a) Mean true stress-mean true strain

(b) Bridgman corrected true stress-mean true strain

Figure B.4: True stress-strain relationships for unirradiated and irradiated smooth specimens tested at 300 °C.

C Curve fitting for coupled deformation and damage model parameter identification

Initial estimates of H_i, C_i and k

(a)

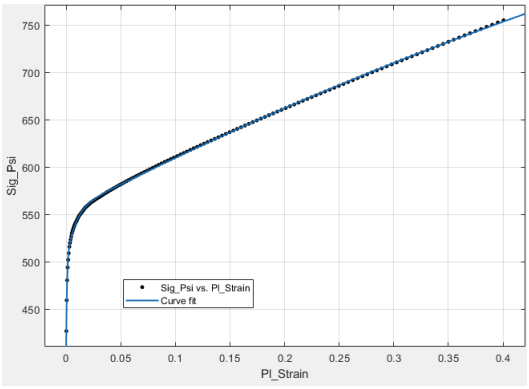

(b)

Coefficients (with 95% confidence bounds):
H1 = 1.257e+05 (1.163e+05, 1.35e+05)
H2 = 6996 (6425, 7566)
H3 = 600 (592.8, 607.2)
Q1 = 1409 (1317, 1502)
Q2 = 131 (124.2, 137.8)
Q3 = 0.9156 (0.8557, 0.9755)
k = 409.9 (407.3, 412.4)

Goodness of fit:
SSE: 92.89
R-square: 0.9999
Adjusted R-square: 0.9999
RMSE: 0.8088

Figure C.1: Results of (a) curve fitting operation, and the (b) initial estimates of parameters at 300 °C.

Identification of l_N at RT

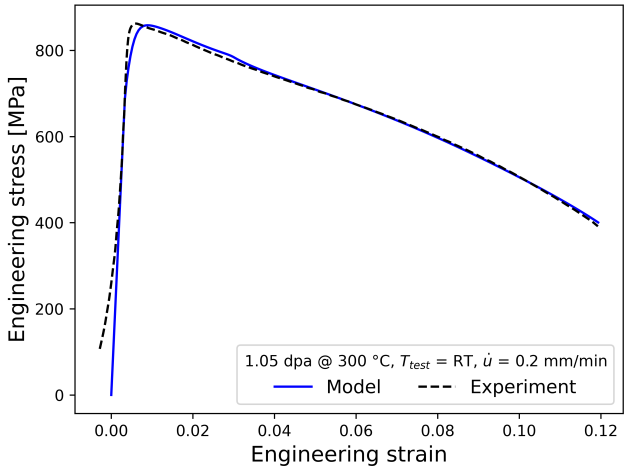

(a) 1.05 dpa @ T_{irr} = 300 °C, T_{test} = RT

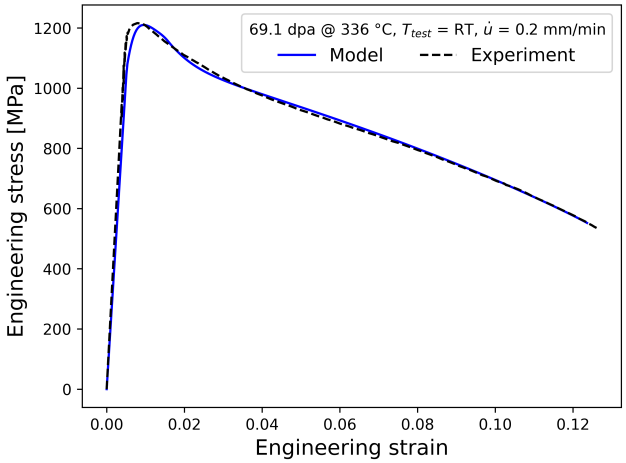

(b) 69.1 dpa @ T_{irr} = 332 °C, T_{test} = RT

Figure C.2: Fitting curves for irradiated smooth specimens at RT.

Identification of l_N at 300 °C

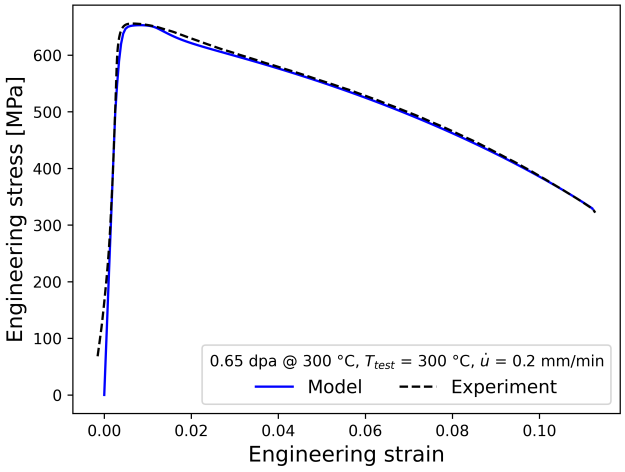

(a) 0.65 dpa @ T_{irr} = 300 °C, T_{test} = 300 °C

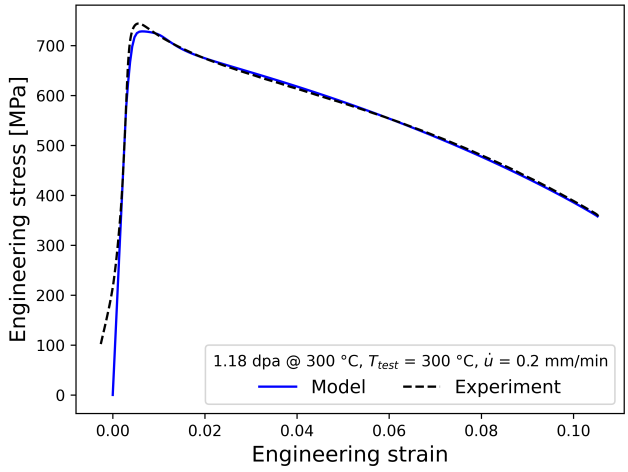

(b) 1.18 dpa @ T_{irr} = 300 °C, T_{test} = 300 °C

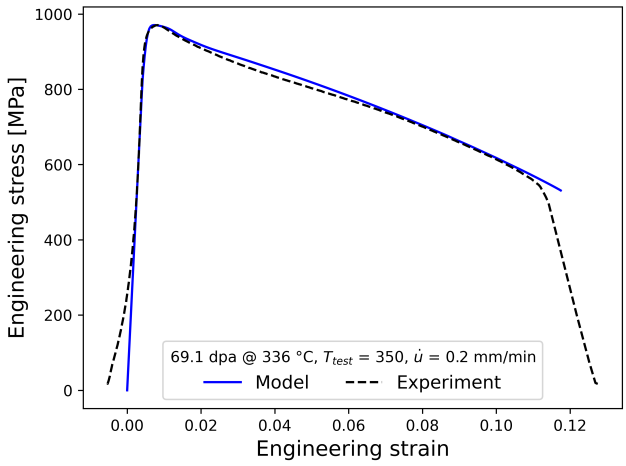

(c) 69.1 dpa @ T_{irr} = 332 °C, T_{test} = 350 °C

Figure C.3: Fitting curves for irradiated smooth specimens at 300 °C.

D Parameters for Eurofer97

Temperature (°C)		RT	300
E	GPa	208	200
v		0.3	0.3
k	MPa	424.3	334.9
n		10.06	6.62
n_{irr}		3.6216	3.03
K	MPa $s^{1/n}$	117.76	28.7136
h		0.096	0.0347
c		1.78	1.81
r_ψ	s^{-1}	1×10^{-70}	7.6×10^{-28}
ψ_r		1	0.754
m_ψ		1	1
$\psi_{s,\infty}$		0.204	0.262
c_s		1344	2269
H_1	MPa	139042	332033.65
Q_1		784.85	2166.35
H_2	MPa	3814.4	7538.73
Q_2		42.84	125.83
H_3	MPa	623.98	525.46
Q_3		0.29	0.58
R	$MPa^{1-m}s^{-1}$	10^{-70}	8.3×10^{-36}
m		1	4.32
h_N	MPa	1.2165	1
a		0.1326	0.1326
$\sqrt{N_s}$		525.9	525.9
b		47.98	78.19
$l_{N,0}$		0.855	0.5615
$l_{N,1}$		0.422	0.18
e_1		1	1.5
r_N	$MPa^{2(1-q_N)}/s$	10^{-70}	10^{-70}
q_N		1	1
q_1		1.5	1.5
q_2		1	1
ε_N		0.3	0.3
s_N		0.1	0.1
f_N		0.0018	0.0013
f_c		0.0045	0.0045
$f_{c,irr}$		0.00243	0.00206
f_F		0.1	0.1

Table D.1: Parameters for the coupled deformation damage model determined for Eurofer97.

E Single element test

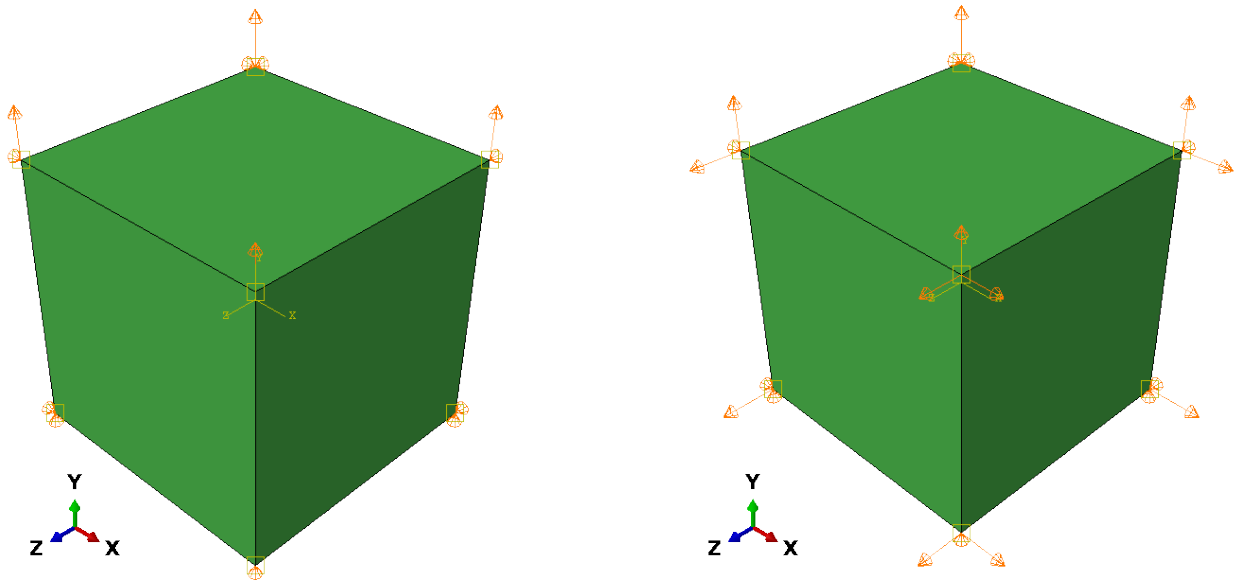

(a) Uni-axial load (b) Volumetric load

Figure E.1: Single element test with displacement controlled load.

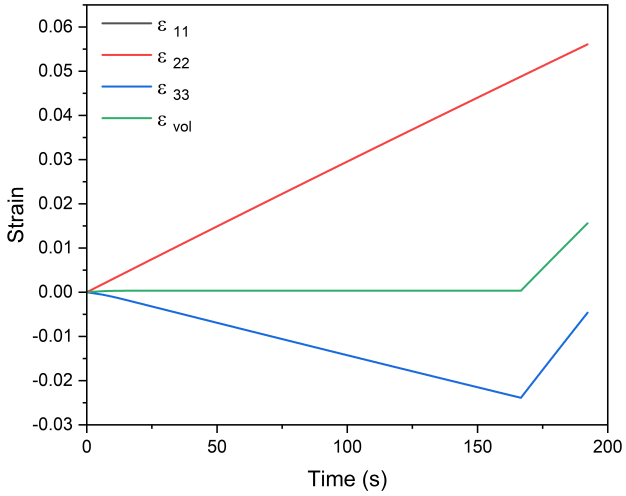

Figure E.2: Plot of strain components and volumetric strain applied on the single element during the uni-axial load ($0 < t < 166.67$s) and pure-volumetric load i.e. $U_x = U_y = U_z$ ($t > 166.67$ s).

F Comparison of simulated specimen and experiment

Strain rate influence

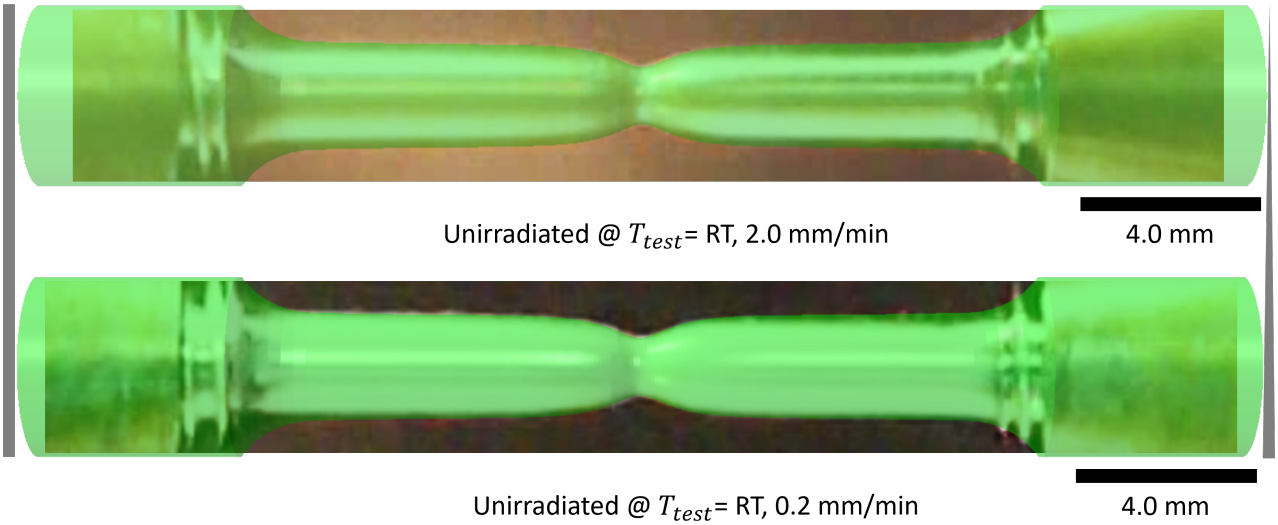

Figure F.1: Strain rate influence: Outline of simulated smooth tensile specimen profile compared with images of unirradiated specimens captured just before failure, from experiments performed at RT. A triangle is used to illustrate the reduction in total elongation with increase in strain-rate.

Temperature influence

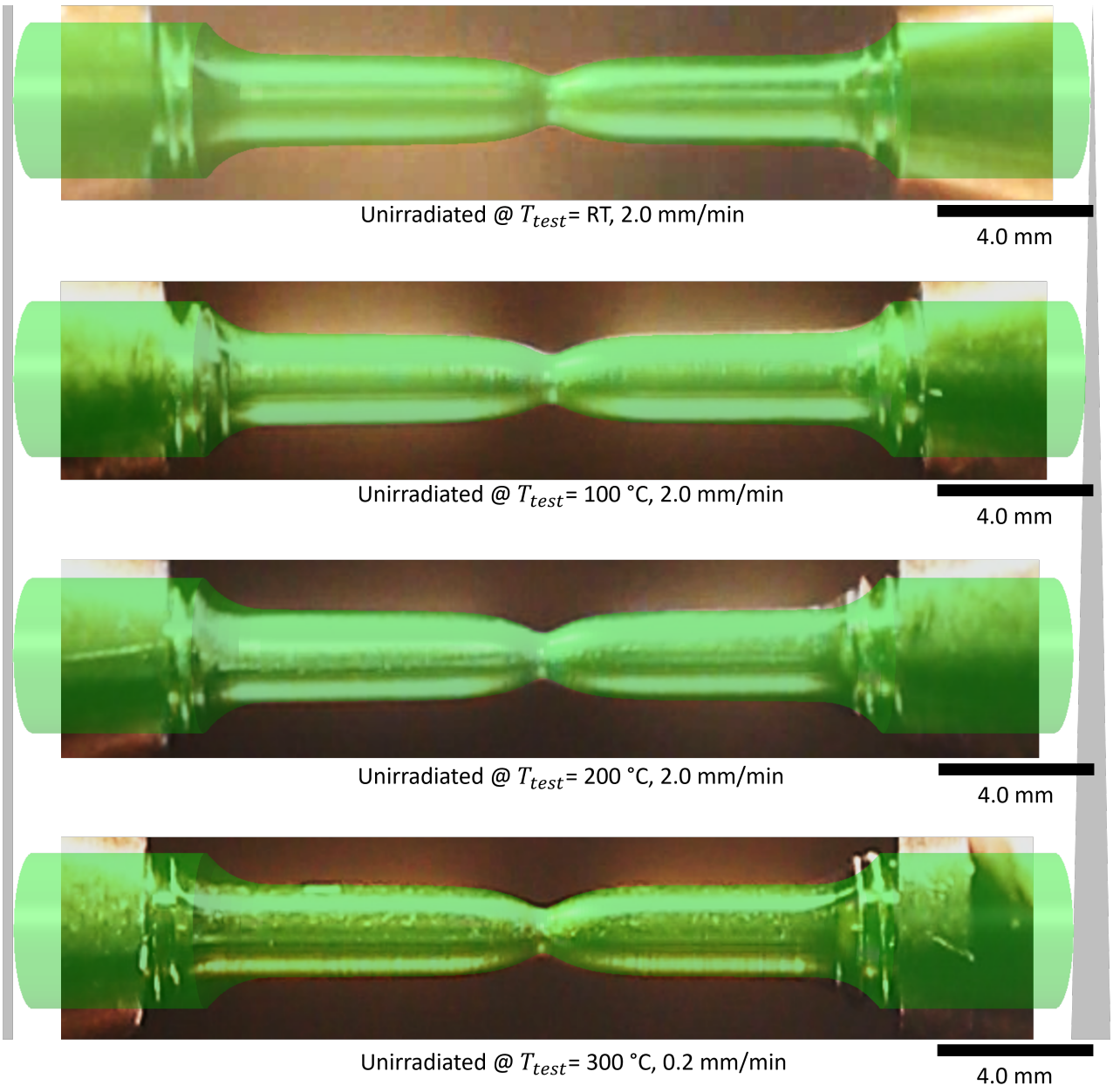

Figure F.2: Temperature influence: Outline of simulated smooth tensile specimen profile compared with images of unirradiated specimens captured just before failure, from experiments performed at RT-300 °C. A triangle is used to illustrate the reduction in total elongation with increase in T_{test}.

G Ductility study results

Smooth specimen

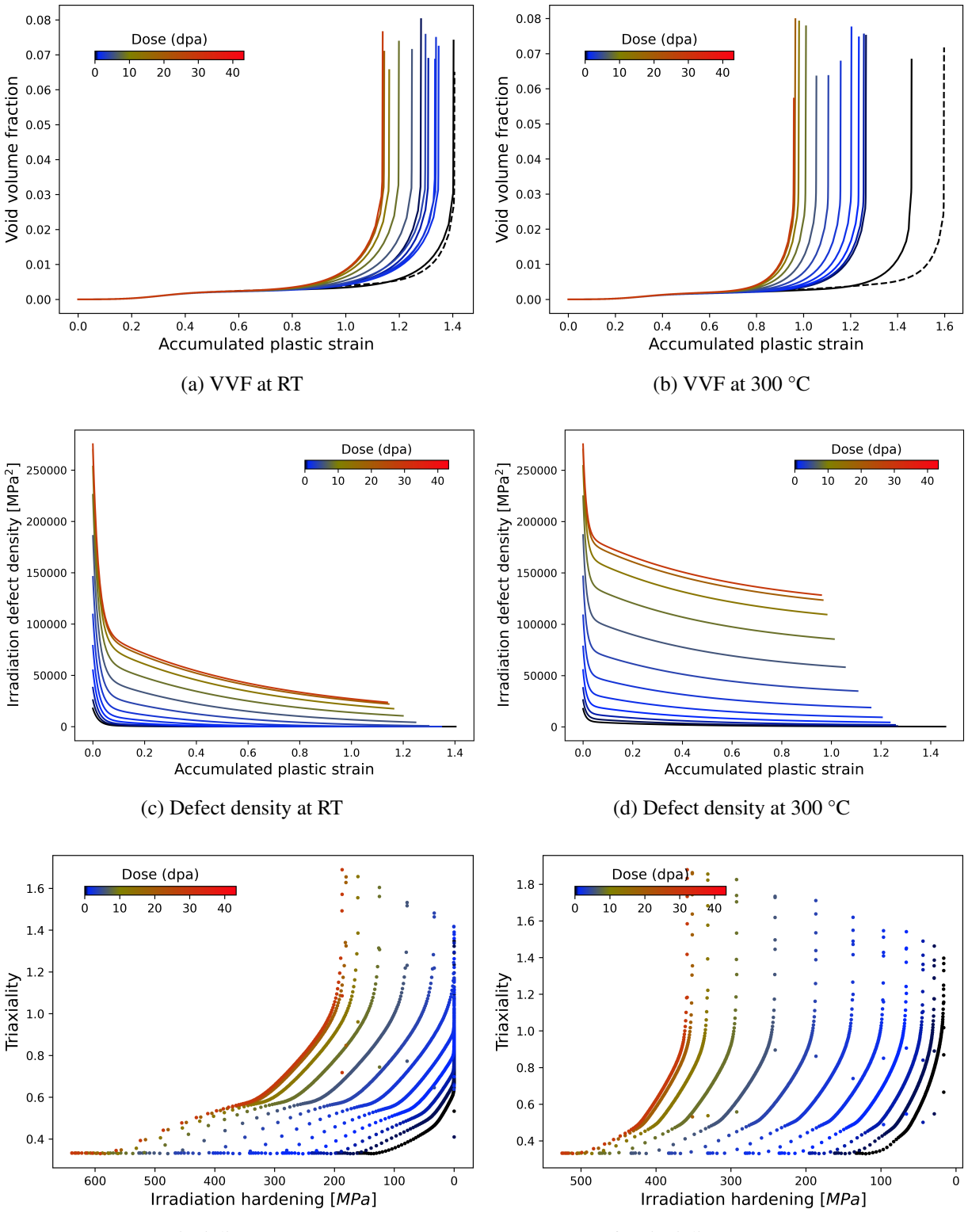

(a) VVF at RT

(b) VVF at 300 °C

(c) Defect density at RT

(d) Defect density at 300 °C

(e) Triaxiality vs σ_H at RT

(f) Triaxiality vs σ_H at 300 °C

Figure G.1: Plot of VVF, defect density against accumulated plastic strain, and triaxiality development w.r.t reduction in σ_H for different doses at the damaged element of smooth specimen.

Notch radius 0.5 mm

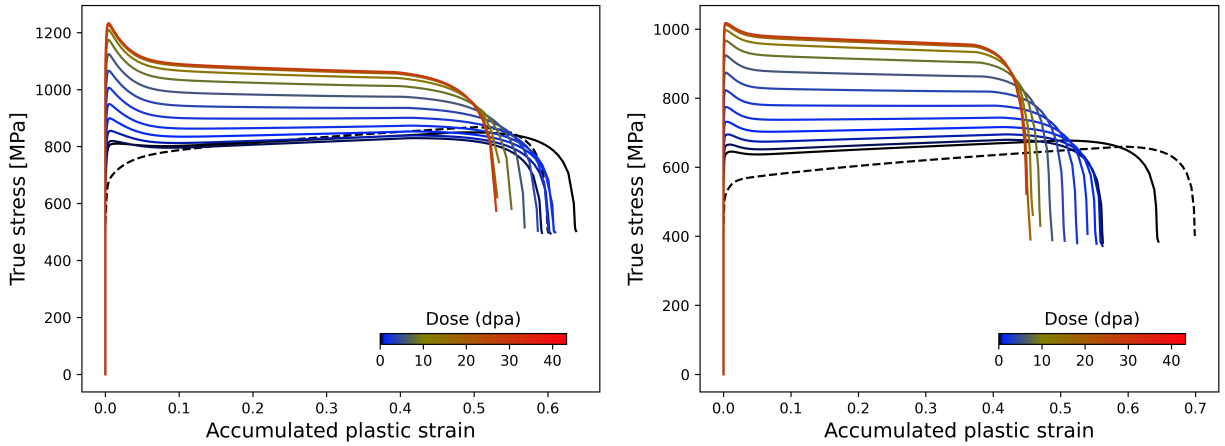

(a) TSS at RT

(b) TSS at 300 °C

Figure G.2: Plot of TSS against accumulated plastic strain for various irradiation doses using data from the damaged element of specimen with notch radius 0.5 mm.

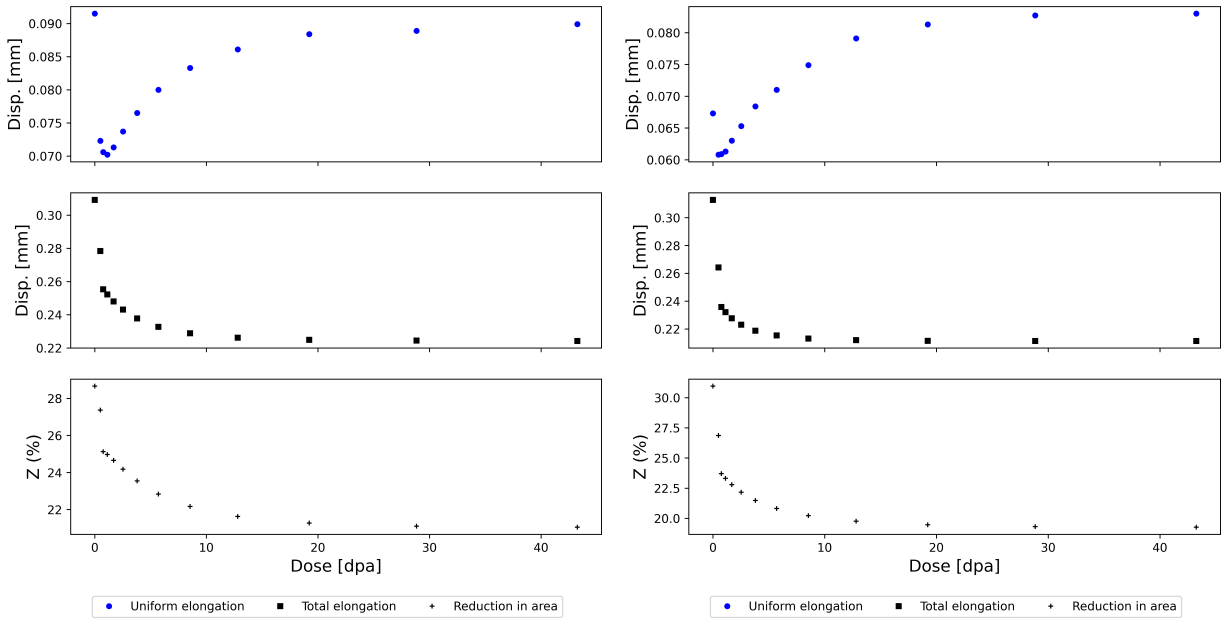

(a) Tensile properties at RT

(b) Tensile properties at 300 °C

Figure G.3: Overview of the simulated tensile properties for specimen with notch radius 0.5 mm.

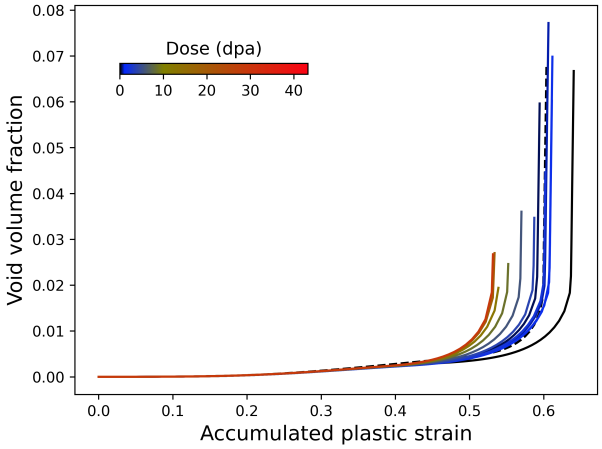

(a) VVF at RT

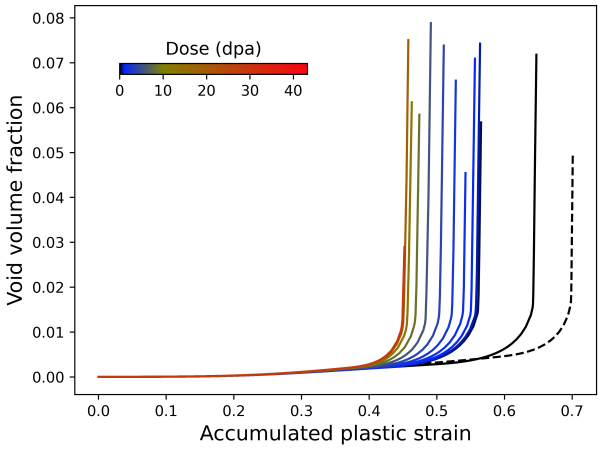

(b) VVF at 300 °C

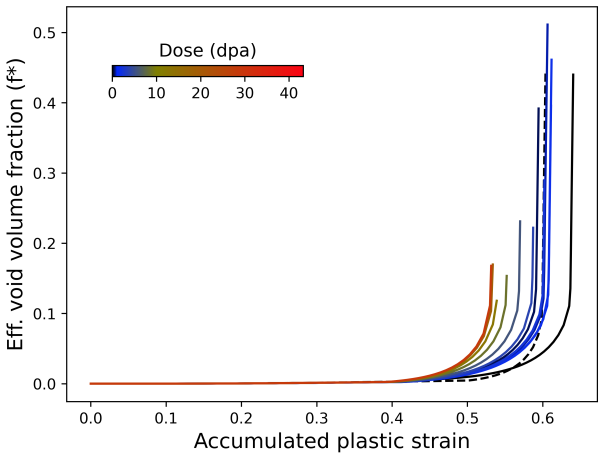

(c) Damage at RT

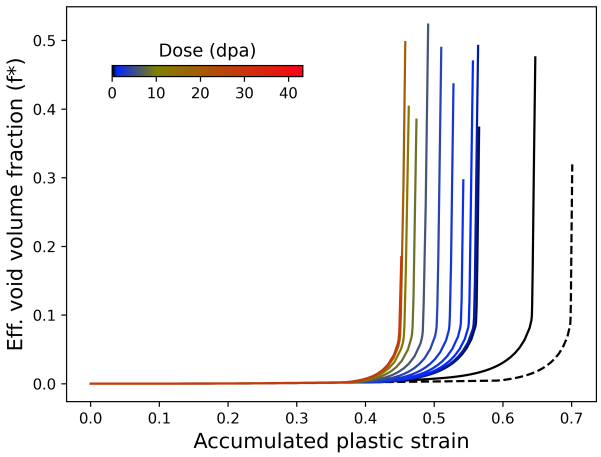

(d) Damage at 300 °C

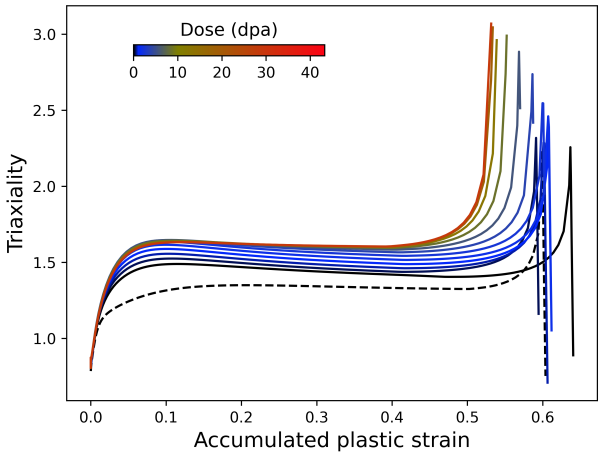

(e) Triaxiality factor at RT

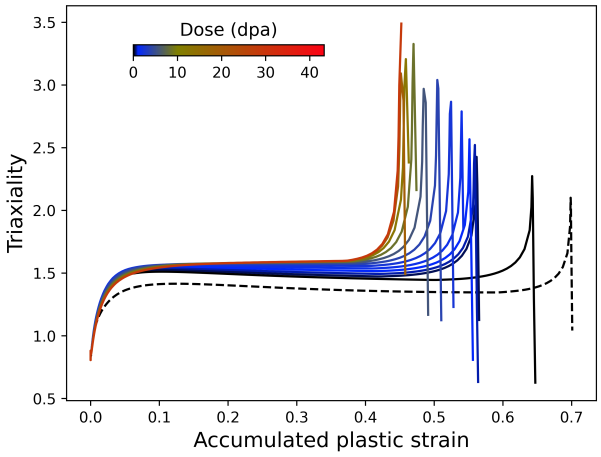

(f) Triaxiality factor at 300 °C

Figure G.4: Plot of VVF, damage and triaxility factor against accumulated plastic strain for different doses at the damaged element of specimen with notch radius 0.2 mm.

Notch radius 0.2 mm

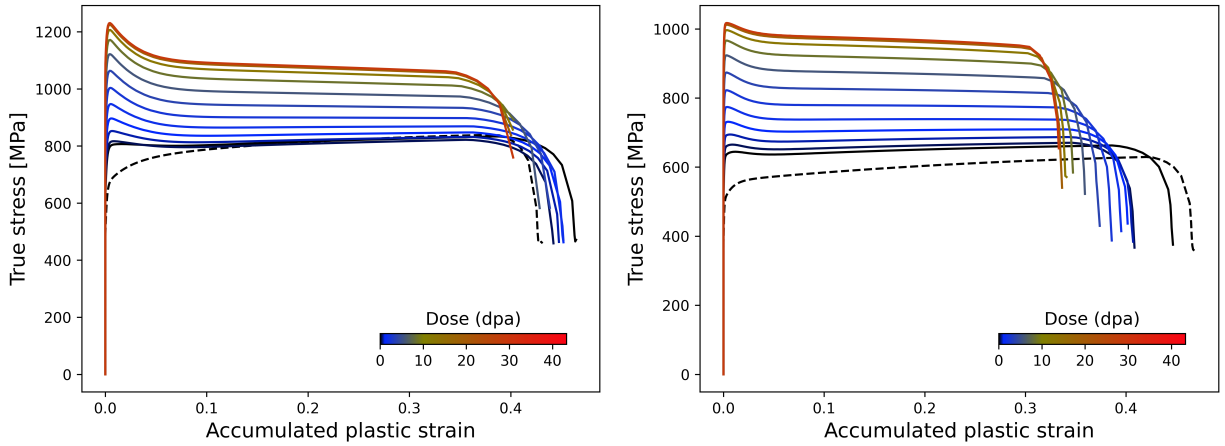

(a) TSS at RT

(b) TSS at 300 °C

Figure G.5: Plot of TSS against accumulated plastic strain for various irradiation doses using data from the damaged element of specimen with notch radius 0.2 mm.

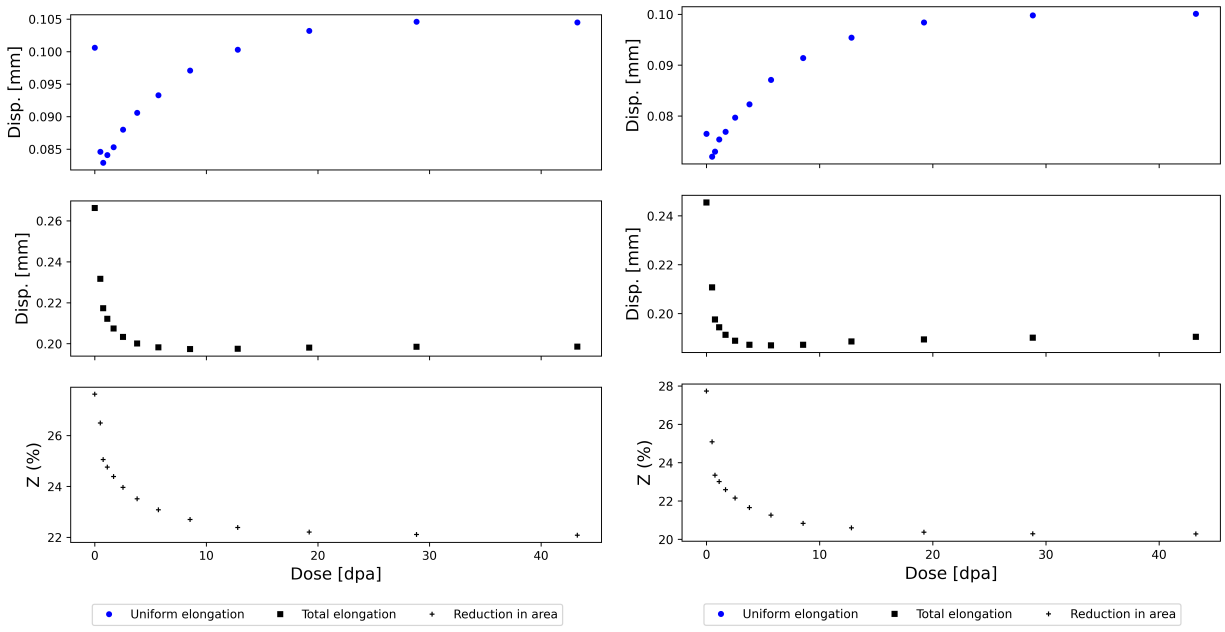

(a) Tensile properties at RT

(b) Tensile properties at 300 °C

Figure G.6: Overview of the simulated tensile properties for specimen with notch radius 0.2 mm.

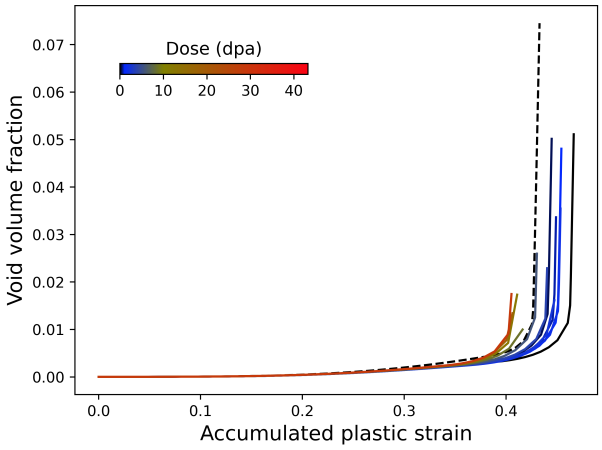

(a) VVF at RT

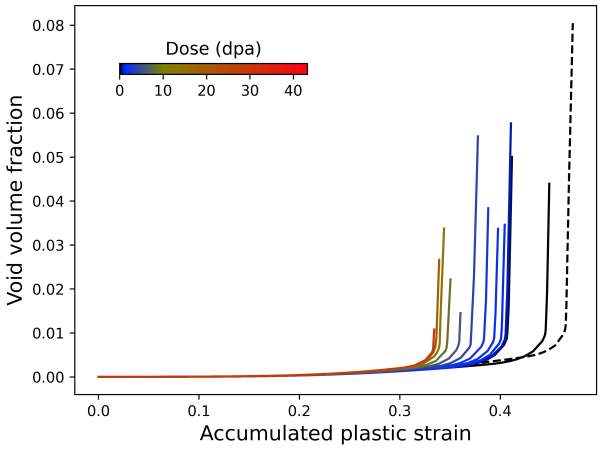

(b) VVF at 300 °C

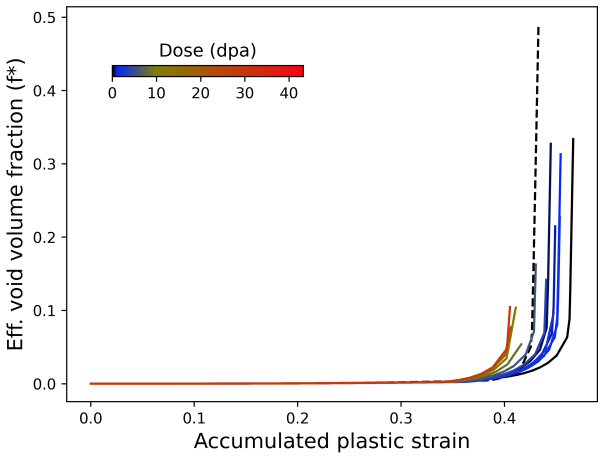

(c) Damage at RT

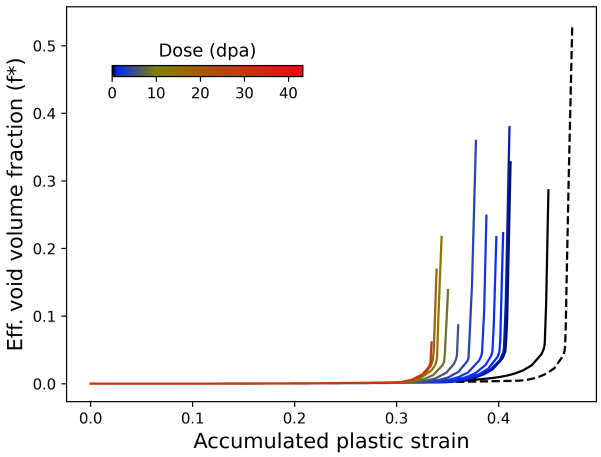

(d) Damage at 300 °C

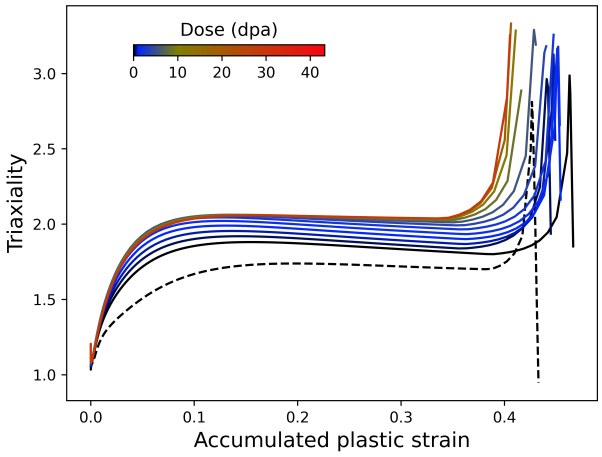

(e) Triaxiality factor at RT

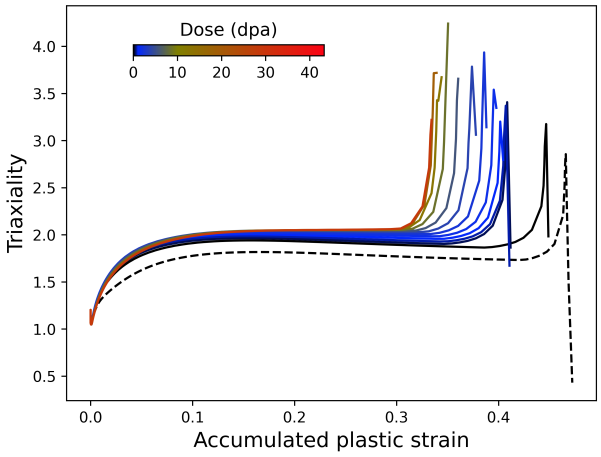

(f) Triaxiality factor at 300 °C

Figure G.7: Plot of VVF, damage and triaxility factor against accumulated plastic strain for different doses at the damaged element of specimen with notch radius 0.2 mm.

H Exponential fit for l_N

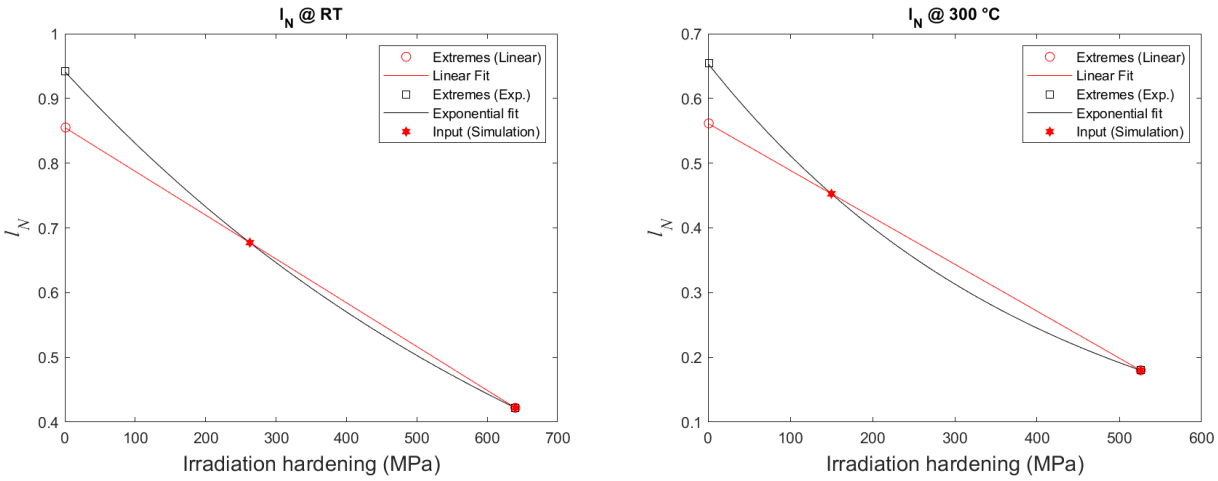

(a) Fit at RT (b) Fit at 300 °C

Figure H.1: Comparison of the linear and exponential fits for l_N.

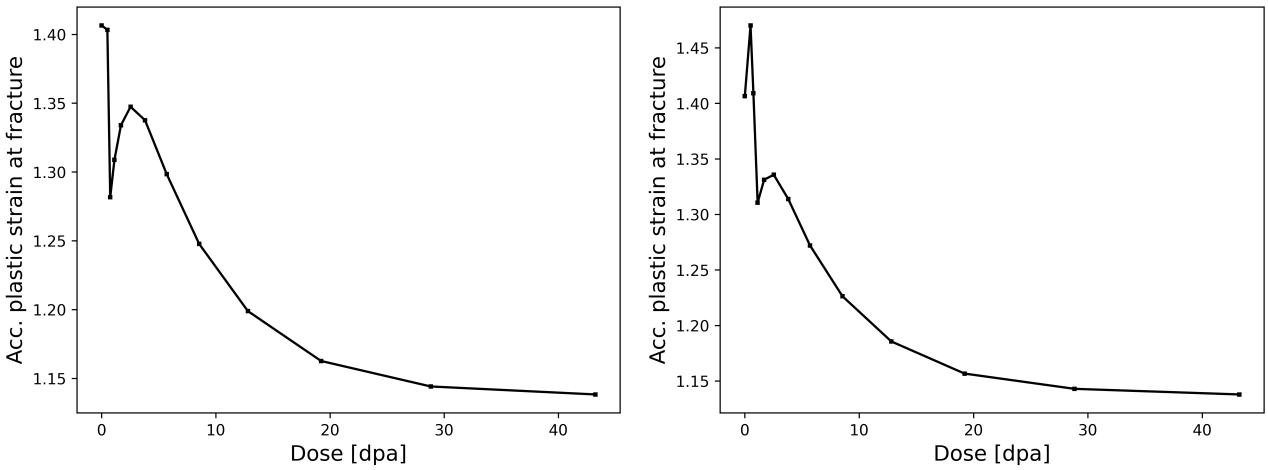

(a) Linear fit (b) Exponential fit

Figure H.2: Impact of linear and exponential fits of l_N on describing the irradiation influence on true-plastic fracture strain for smooth specimen at RT.

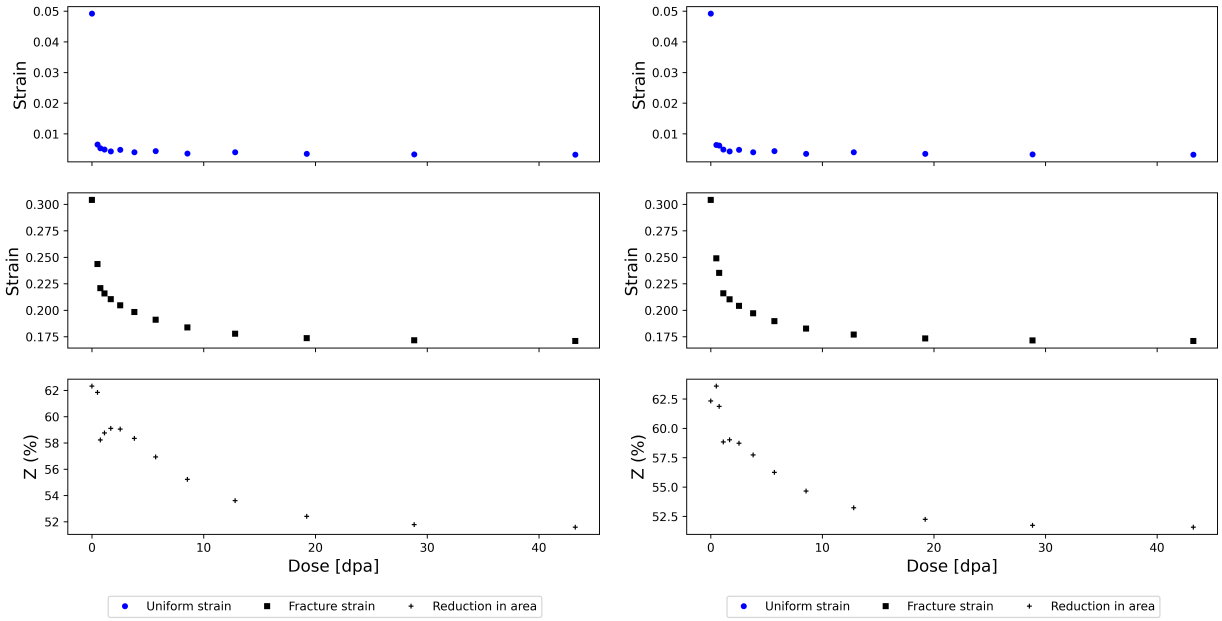

(a) Linear fit (b) Exponential fit

Figure H.3: Comparison of simulated irradiation influence on tensile properties of smooth specimen at RT using a) linear fit and b) an exponential fit for l_N.

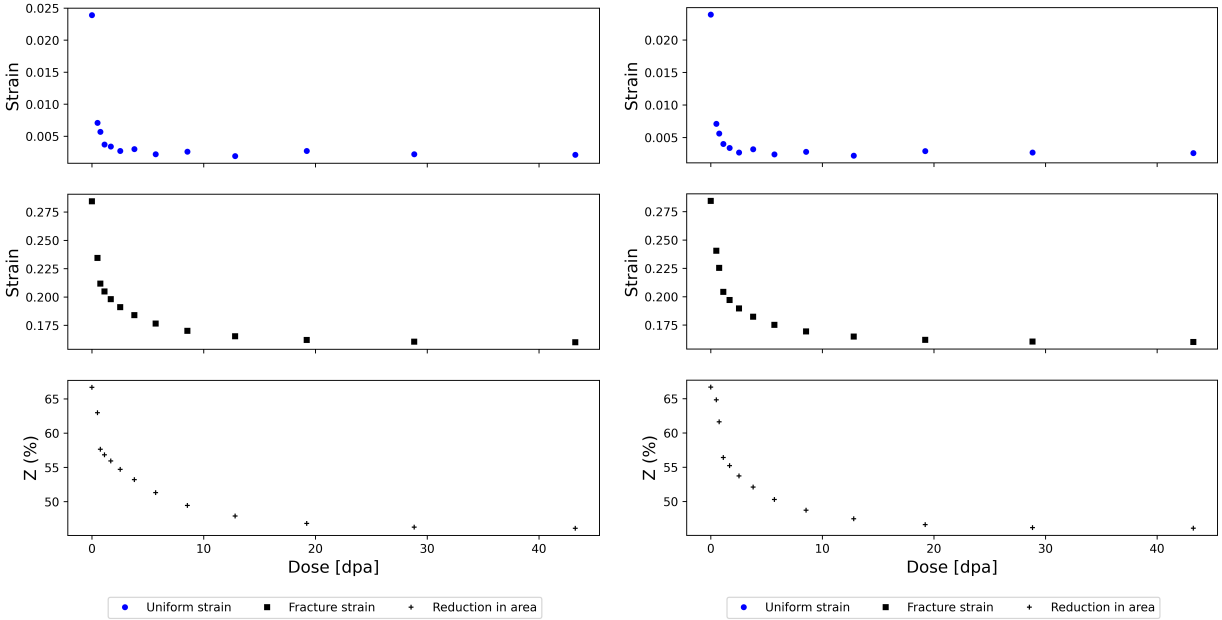

(a) Linear fit (b) Exponential fit

Figure H.4: Comparison of simulated irradiation influence on tensile properties of smooth specimen at 300 °C using a) linear fit and b) an exponential fit for l_N.